Applied Mathematical Modelling of Pulmonary Function Tests

Brody Foy

New College

University of Oxford

Computational Biology Group

Department of Computer Science

Supervisor: Professor David Kay

A thesis submitted for the degree of

Doctor of Philosophy

Trinity 2018

To my parents and siblings...

Acknowledgements

Firstly, to Professor David Kay, thank you for everything. Your guidance throughout the project has been incredible, and means I'm submitting something which I truly believe is valuable. Thank you for the friendship, coffees, and pints. It's been great!

Secondly to Dr Rafel Bordas. You helped on-board me in the initial stages of the project. This work wouldn't have been possible without building upon the foundations you created.

To my friends, both near and far. Thank you for putting up with me during periods of stress, for letting me bore you with technical rants, for sharing coffees, walks, road trips and Skype calls. Jonathan, Kristy, and Sam in particular, your support has been amazing, and helped more than you'd know.

To my family. Mum, Dad, Ben, Davina, Daniel and Frankie, thanks for putting up with me being away for so long. You all kept me believing I could go from a country town to a place like here.

To the Rhodes Trust, and Rhodes community. Being awarded this scholarship has changed my life more than I can really express. I will forever be grateful for the opportunity, and will try to pay forward the good I've received. I've never grown more or grown faster than in this community.

Finally, to Sana. Your love and support throughout has been amazing.

Technical Acknowledgements

This work would not have been possible without a lot of help and support.

AirPROM: Creation of the virtual airway structures, and much of the clinical data collection was funded heavily by the EU AirPROM project.

Dr Rafel Bordas: Who acted as co-supervisor for my first six months. You're insights and guidance were incredibly valuable.

Professor Salman Siddiqui: Who oversaw clinical data collection in Chapters 5 and 6, provided lots of data critique, and designed the clinical study underpinning Chapter 5.

Ms Marcia Soares: Who performed high quality clinical data collection and analysis, which underpins much of the work in Chapter 5.

Mr Alex Bell: Who performed CT scan analysis, and offered lots of insightful thoughts on the airway tree models.

Professor John Owers-Bradley and *Dr Brenda Timmerman*: Who created and ran experiments with the 3D-printed airway.

Professor Christopher Brightling and *Dr Sherif Gonem*: Who were heavily involved in clinical data collection for Chapter 6.

Mr Logan Graham: For countless technical conversations, and rubber-duck debugging.

Mr Jonathan O'Brien, Mr Eamon Conway, and Ms Kristy Van der Vegte: Who all spent countless hours reading my thesis, and offering constructive feedback.

Ms Sanjana Sharma: Who helped turn many of my rough sketches and diagrams into production quality figures.

Abstract

The lungs are an incredibly complex pair of organs, whose function is strongly driven by both shape and structure. However, in standard clinical practice lung function is assessed through analysis of 'at-the-mouth' measurements, which by their nature represent a smoothing of behaviours throughout the lungs. Due to this there is a lack of precision in the understanding of how different pulmonary function test outputs respond to different types of lung disease. Within this thesis we apply mathematical and computational modelling to analyse and improve understanding of these responses, and to generate hypotheses that are suitable for further clinical investigation. In the early chapters physics-based models of ventilation, gas transport and frequency propagation within the lungs are developed, and then implemented in efficient computing environments. These models are then applied to the exploratory analysis of indices derived from three pulmonary function tests: the multiple-breath washout; the forced oscillation technique; and magnetic resonance imaging, under a variety of bronchoconstrictive patterns. Following preliminary analysis, we provide a detailed validation of the washout and frequency propagation models, and then show how these models can help create clinical insight as to how different test indices can be most effectively interpreted. In the later chapters we extend upon earlier models, to incorporate flow and gas transfer processes throughout the pulmonary bloodstream. By embedding these models in high-performance computing environments, we create a tractable way to simulate function of the entire pulmonary system. Following implementation of the pulmonary model, we apply it to analyse how gas choice may affect the multiple-breath washout. Finally, we close the thesis with a discussion of the role of mathematical modelling in clinical medicine, of the clinical relevance of results within this thesis, and of the potential for future work.

Contents

List of Figures

Nomenclature

Acronyms

BiCGStab	Stabilised biconjugate gradient method
CF	Cystic fibrosis
COPD	Chronic obstructive pulmonary disorder
CPU	Central processing unit
CT	Computed tomography
DAE	Differential algebraic equation
ERV	Expiratory reserve volume
FEF	Forced expiratory flow
FOT	Forced oscillation technique
FRC	Functional residual capacity
FVC	Forced vital capacity
GINA	Global initiative for asthma
GMRES	Generalised minimal residual method
GPU	Graphics processing unit
HPC	High-performance computing
IC	Inspiratory capacity
IOS	Impulse oscillometry
IRV	Inspiratory reserve volume
LLL	Left-lower lobe

LUL	Left-upper lobe
MBW	Multiple-breath washout
ODE	Ordinary differential equation
PDE	Partial differential equation
PET	Positron emission tomography
PFT	Pulmonary function test
RLL	Right-lower lobe
RML	Right-middle lobe
RUL	Right-upper lobe
RV	Reserve volume
SBW	Single-breath washout
TLC	Total lung capacity
VC	Vital capacity
VH	Ventilation heterogeneity

Symbols

$\mathbb{C}$	Total lung compliance
C, C_{acin}, C_b	Gas concentration in airway, acinus, and bloodstream
$\mathcal{D}_{\text{cap}}$	Diffusing capacity of a gas through the alveolar-capillary membrane
D	Diffusion rate of tracer gas in air
G, H	Constant-phase acinar impedance model parameters
g_{strength}	Strength of gravitational ventilation gradient
$\mathcal{J}$	Jacobian matrix for Newton solver
P, Q, A	Airway pressure, flow rate and cross-sectional area
P_b, Q_b, A_b	Bloodstream pressure, flow rate, and cross-sectional area
P_{pl}	Pleural pressure
$\bar{Q}_b$	Mean pulmonary artery flow rate

r	Inspiration-expiration ventilation ratio
$R(Q)$	Flow resistance (Pedley's model)
$\mathcal{R}_1, \mathcal{R}_2, \mathcal{C}_T$	Windkessel element parameters
$R_{\text{acin}}, V_{\text{acin}}$	Radius and volume of an acinus
Re	Reynold's number
r_v, δ	Boundary layer thickness in airway, and bloodstream
$t_{\text{circulation}}$	Mean time taken for blood to circulate the body
Z	Airway impedance
ΔHU	Change in Hounsfield units
μ, μ_b	Viscosity of air, blood
ν_b	Dynamic viscosity of blood
ρ, ρ_b	Density of air, blood
σ_b	Solubility of a gas within blood
τ	Time of peak flow over heartbeat

Test indices

AX	Area of low reactance (FOT/IOS)
FEV1	Forced expiratory volume over 1 second (Spirometry)
f_{res}	Resonant frequency (FOT/IOS)
LCI	Lung clearance index (MBW)
R_5	Resistance at 5Hz (FOT/IOS)
R_{20}	Resistance at 20Hz (FOT/IOS)
s_{acin}	Washout acinar zone slope (MBW)
s_{cond}	Washout conducting zone slope (MBW)
X_5	Reactance at 5Hz (FOT/IOS)
σ_{local}	Local ventilation heterogeneity (imaging)
σ_r	Global ventilation heterogeneity (imaging)

No substantial part of the universe is so simple that it can be grasped and controlled without abstraction. Abstraction consists in replacing the part of the universe under consideration by a model of similar but simpler structure. Models, formal or intellectual on the one hand, or material on the other, are thus a central necessity of scientific procedure ...

— Rosenblueth and Wiener (1945)

1 Introduction

The lungs are an incredibly complex pair of organs, whose function is strongly driven by shape and structure. This means that even small changes to the size of airways, or tissue properties can create large changes in overall ventilation patterns. Due to this, one of the most significant challenges within respiratory medicine is the accurate analysis of patient-specific lung structure and ventilation mechanics. This challenge is exacerbated by the fact that many of the most prevalent lung diseases are chronic, with treatment being focused on slowing disease progression as opposed to symptom reversal. This leads to a strong need for sensitive, accurate, and early detection of disease-driven morphological changes in the lungs.

In a clinical setting, lung mechanics are most commonly inferred through a spirometry test, which measures the flow volume and rate associated with a forced maximal exhalation by a patient, following a maximal inhalation. While spirometry is simple to

perform, the reliance on a single maximal exhalation (a move which patients can find hard to consistently replicate) can lead to low sensitivity, particularly in early-stage disease (Johns and Crockett, 2005).

Alongside spirometry, imaging techniques are also commonly used to make inferences about lung structure. These include computed tomography (CT) (Simon, 2005; Tzeng et al., 2009), positron emission tomography (PET) (Gould et al., 2001) and magnetic resonance imaging (MRI) (Tajik et al., 2002). Imaging techniques have the advantage of providing more clearly interpretable information about lung structure than standard pulmonary function tests (PFTs). However, significant cost and time constraints (and for CT and PET scanning, the use of ionising radiation) have limited uptake in clinical settings.

As a way to move beyond the limitations of spirometry and imaging, a variety of more complex PFTs have started to be applied in clinical settings; in particular impedance measurements and the inert-gas washout. Both of these tests have been shown to exhibit higher degrees of sensitivity than standard tests such as spirometry, particularly to changes in the distal airways (Robinson et al., 2013; Smith et al., 2005), while also being significantly less costly than imaging. However, this increased sensitivity acts as a double-edged sword, also increasing the complexity of output interpretation. To improve the clinical utility and viability of these tests, a more detailed understanding of the precise relationship between lung structure and test outputs is needed. One potential avenue towards improving this understanding is through the application of mathematical and computational modelling of the

pulmonary system.

1.1 Aims

Within the literature a substantial body of research has been developed pertaining to the design and computational implementation of mathematical models of airflow, blood flow, tissue mechanics and gas transport throughout the pulmonary system (Kaczka et al., 2007; Lutchen and Gillis, 1997; Tawhai and Hunter, 2001; Tawhai and Burrowes, 2008; Verbanck and Paiva, 1990; Weibel, 1963). Through the application of these models, virtual simulations of pulmonary function tests can be performed. These simulations can be used to probe how changes to lung morphology may affect test responses. While computational models cannot replace clinical data, they can allow for rapid exploration of a wide variety of scenarios, with high precision to minute morphological changes. In this way computational models can underpin and strengthen clinical work by aiding interpretation of why certain physical phenomena occur, and by allowing for more efficient and targeted clinical study design through rapid iterative hypothesis testing.

Considering these advantages in the context of pulmonary medicine, this thesis has been written to explore two primary aims:

- To design and efficiently implement computational models of the human pulmonary system, as a way of investigating the response of various pulmonary function test outputs to morphological changes in lung structure.

- To use these computational models to effectively generate targeted hypotheses pertaining to diagnosis of lung disease, which are suitable for further development within clinical studies.

A more detailed outline of the research aims, associated challenges, and underlying methodology will be presented following a brief review of pulmonary physiology and pathophysiology, and a literature review of pulmonary function testing, and the associated computational modelling of the pulmonary system.

1.2 Physiology of the pulmonary system

To provide context for the thesis proposal, we present a literature review on clinical understanding of pulmonary function tests, and the associated history of computational modelling. As a basis for this, we first give a summary of pulmonary anatomy and physiology at the gross and microscopic levels. Unless otherwise noted, anatomical and physiological information has been taken from the work Saladin and Porth (1998).

1.2.1 Pulmonary system anatomy

Broadly speaking, the human pulmonary system consists of all organs and structures within the body that play a significant role in the process of respiration: the exchange of oxygen (O_2) and carbon dioxide (CO_2) with the environment, to allow for the production of energy. The primary structures for this process are the lungs, which facilitate airflow in and out of the body, and the pulmonary artery, vein and capillary network which transports blood to and from the lungs to allow for gas exchange between blood and air.

Gross anatomy of the lungs

On the macroscale, each lung is visibly separated into lobes by fissures, and partitioned from the other lung by the mediastinum membrane. The right lung consists of three lobes, superior, middle and inferior, while due to the placement of the heart within the thoracic cavity, the left lung only has superior and inferior lobes. The outer surface of each lung and the adjacent internal thoracic wall are lined by the pleural membrane. This membrane protects and suspends the lungs in position, while still allowing for movement, expansion and contraction. The visceral pleura lines the surface of the lungs, while the parietal pleura lines the internal thoracic walls, and surfaces of the mediastinum. The space between the two pleural layers is referred to as the pleural cavity. It contains a serous pleural fluid, which acts as a lubricant for lung expansion and contraction.

Airway and alveoli anatomy

Proximally the lungs start at the trachea, a flexible tubular airway which lies anterior to the oesophagus. The trachea is the largest of all the airways (in both length and diameter), and is lined by smooth muscle tissue, as well as a series of tracheal cartilages which provide rigidity and support, ensuring the trachea always remains open. At its distal end the trachea bifurcates into two separate airways, the left and right primary bronchi, which form the first airways in the left and right lung respectively.

Each bronchi progressively branches into shorter, narrower airways. As the branches become more distal, the amount of cartilage decreases, and the smooth muscle

increases. Eventually, the airways are surrounded only by smooth muscle tissue, and are subsequently referred to as bronchioles. Due to the lack of cartilage, the bronchioles have higher flexibility than the bronchi, allowing for dynamic changes in radii throughout the breathing cycle.

A typical pathway in a lung branches 20-23 times (referred to as generations) before terminating. On average, the first 16 generations participate only in the convection of gas, and are known as the conducting zone of the lungs. Following on from the conducting zone, subsequent branches are lined with elastic cavities called alveoli, which allow for the transfer of gas into and out of the bloodstream. This group of bronchioles and alveoli is collectively known as the respiratory zone of the lungs. Pressure changes in the pleural cavity drive expansion and contraction of alveoli, which in turn account for the majority of change in lung volume throughout the breathing cycle. Each generation of respiratory zone bronchioles is lined with progressively more alveoli, until at approximately generation 23, the bronchioles terminate in bunched collections of alveoli, called the alveolar sacs. A diagram of the entire respiratory system is given in Figure 1.1.

The alveoli form the terminal ends of the respiratory tree, and are the primary sites of gas exchange from the lungs to the bloodstream. Each alveoli has a thin surface interlaced with a bed of capillaries (fine blood vessels connecting arteries and veins), allowing for the diffusion of gases in and out of the lungs. Due to the exponentiating nature of the structure, a normal lung has on the order of 7 million branches and hundreds of millions of alveoli, leading to a surface area of around 50-100

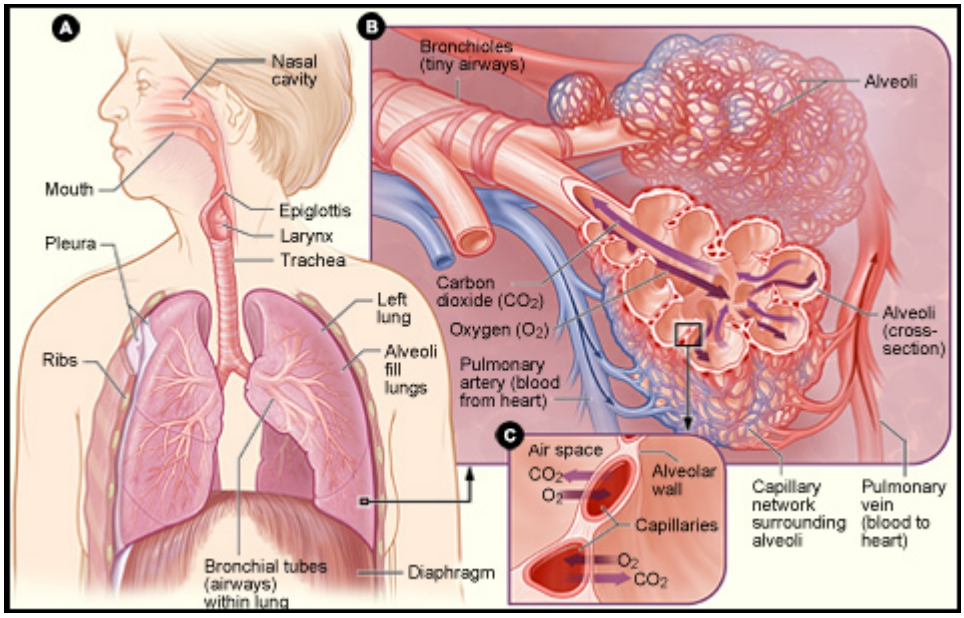

Figure 1.1: Diagram of the human respiratory system. Detail is given of the gross anatomy of the lungs (A), anatomy of the alveoli and respiratory bronchioles (B), and of a capillary (C). Image sourced from Wikimedia Commons.

m^2 (Thurlbeck, 1967).

Arterial network anatomy

The airway structure of the lungs is closely followed by an artery and vein network, whose primary function is to bring blood into contact with the alveoli to facilitate gas exchange. The pulmonary arterial network originates in the pulmonary trunk, a short and wide artery located at the base of the right ventricle of the heart. The pulmonary trunk bifurcates into the left and right pulmonary arteries, which act to deliver de-oxygenated blood from the heart to each respective lung. Each of the pulmonary arteries then bifurcates further into lobar arteries, with subsequent bifurcations approximately following the corresponding airway bifurcation pattern, until the alveolus is reached (Cotes et al., 2009; Saladin and Porth, 1998).

Each alveolus sits in a capillary bed, which allows for the diffusion of CO_2 into the

alveolus, and diffusion of O_2 into the bloodstream. As blood in the capillaries runs over an alveolus, gases diffuse across the membrane, until the partial pressures of gases in the capillaries and alveoli equilibrate. Following passage over the alveolar surface, the capillaries start to reform into a pulmonary vein network. As with the arterial network, the pulmonary vein structure closely follows the airway structure. However, the network does not form back into a left and right main pulmonary vein, instead entering the left atrium of the heart as four major pulmonary veins, corresponding to the four largest lobes of the lungs.

Each individual artery and vein is composed of three tissue layers, an inner endothelial tissue layer, a middle muscular layer, and an external connective tissue layer. Unlike the airways, the arteries and veins are highly elastic, and expand and contract significantly in response to the blood flow originating from the heart. Unlike systemic veins, the pulmonary veins do not have valve structures which enforce unidirectional flow. This is because they still experience significant pressure pulses from the heart, meaning backflow is a much less significant process.

The capillary network in the lungs also differs significantly from capillary networks in other parts of the body. Firstly, the arteries and veins that form the capillary beds have particularly thin walls. This is primarily to aid with diffusion processes, but also helps to keep pulmonary pressure low, minimising the demands placed on the heart. Secondly, most other capillary sets in the body are organised into tubular networks, with few interconnections. The respiratory capillaries instead connect together in a mesh-like fashion (see Figure 1.1), allowing the blood to flow as a thin sheet over the

alveolar wall.

It should be noted that during standard bodily function, not all capillaries are opened. This is part of a mechanism of the respiratory system to decrease resistance as cardiac output increases. This means that some capillary beds are only opened during periods of large cardiac output. To further reduce resistance, the capillaries can also distend, reducing pulmonary pressure, and increasing the surface area that they cover.

Though arteries and veins track the airways closely, due to the lack of alveoli-like structures, the pulmonary blood volume is significantly lower than the corresponding lung volume, typically being 250mL, 60mL of which is located within the capillaries (Saladin and Porth, 1998). A simple diagram of the pulmonary artery and vein network is given in Figure 1.2.

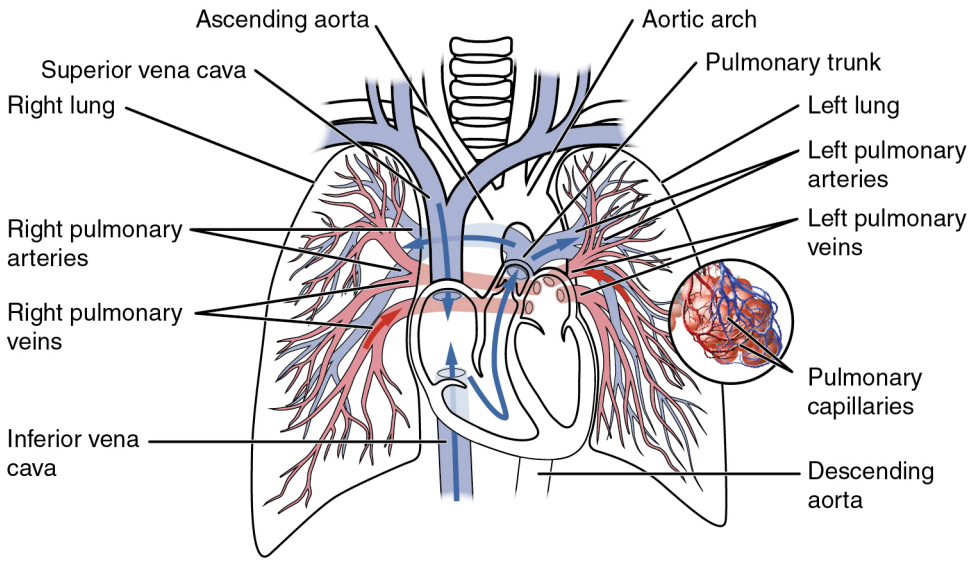

Figure 1.2: Diagram of the human pulmonary system. Detail is given of the pulmonary veins, arteries and capillaries. Image sourced from Wikimedia Commons.

1.2.2 Mechanical processes for breathing

The breathing cycle consists of two separate processes, the inspiration of air to supply the body with oxygen, and the expiration of air to remove carbon dioxide from the body (Cotes et al., 2009; Saladin and Porth, 1998).

Both of these processes are driven by the contraction and relaxation of the diaphragm, and intercostal muscles. During inspiration, the diaphragm and intercostals contract, leading to an expansion of the thoracic cavity and subsequently to a decrease in the pressure within the pleural cavity. This pressure drop drives airflow inwards to the lungs, until the pressure in the alveoli is equal to the pressure at the mouth.

Typically expiration is a passive event (meaning it is not actively controlled by thought), caused by the lungs exhibiting elastic recoil under relaxation of the intercostals. However, forced exhalation can be performed through contraction of these muscles, leading to an accelerated increase in pleural pressure. Similar to inflow, this pressure increase drives air outwards until an equilibrium is reached. It should be noted that under atmospheric pressure equilibration, the lungs have a non-zero volume (referred to as the reserve volume).

1.2.3 Lung compliance

As the pressure in the pleural cavity changes, the system equalises through expansion and contraction of the lungs. The rate of change of volume with respect to pressure is referred to as the lung's compliance. Under tidal (passive) breathing compliance is typically quite stable, being in the range $0.1 - 0.2$ L/cmH_2O for a healthy adult

(Galetke et al., 2007; Mittman et al., 1965). However, outside of this breathing range lung compliance can reduce due to increased stiffness, or increase due to compression. It is also noteworthy that compliance exhibits a hysteresis effect, being different at identical pressures during inspiration and expiration, due to the out of phase relationship between pressure and flow (Lumb, 2016). This hysteresis effect is most pronounced in the tidal breathing range, with inhalation and exhalation compliance converging and stabilising as total lung capacity is approached (as shown in Figure 1.3).

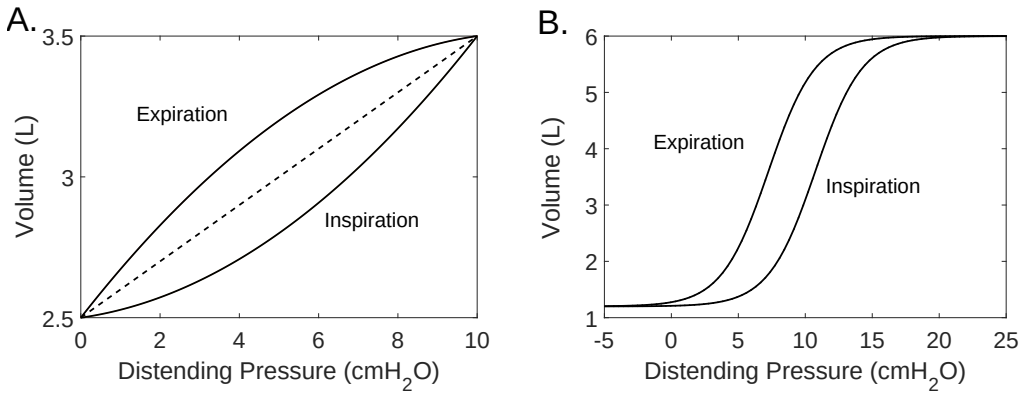

Figure 1.3: Idealised pressure-volume curve of the lungs during tidal breathing (A) and maximal breathing (B). The volume for a given pressure is higher during expiration than inspiration - a hysteresis loop. The compliance of the lung is the gradient of this curve, with the dotted line representing the mean compliance during tidal breathing.

Technically, each alveolar unit expands and contracts independently in response to the pressure gradient at its own spatial location. Thus, total lung compliance is actually a volume weighted aggregation of the compliance of each individual alveolus. Many different factors can affect compliance at this level, including (Lumb, 2016):

- Gravitational effects, causing lower lung regions to expand more easily than higher regions, a phenomenon known as the 'Slinky effect' (Hopkins et al., 2007).

- Breakdown of tissue elasticity at a local level, as is characteristic of diseases such as chronic obstructive pulmonary disease (COPD).

- Interference from other parts of the body, such as the heart, which limit local expansion.

Airway asymmetry, alongside differences in regional compliance means that lung ventilation is not a homogeneous process. Even healthy subjects have these differences, meaning regions of the lungs will ventilate at different rates, to different volumes. However, heterogeneities in ventilation of lung regions are typically exacerbated by the presence of disease (Downie et al., 2007).

Interestingly, differences in pressure and ventilation mean it is possible for the lungs to exhibit reverse-flow, where a small number of airways drive airflow in opposition to the primary flow direction at the trachea. This phenomenon is known as pendelluft, and in particular has been observed in COPD patients (Otis et al., 1956; Vyshedskiy and Murphy, 2012). This is due to COPD patients exhibiting greater regional compliance variation than healthy patients, meaning there can be significant differences in how nearby alveoli ventilate throughout the breathing cycle.

1.2.4 Common lung volume measures

Lung volumes alternate throughout the breathing cycle, as the alveoli expand and contract. Thus, a series of different terms are used to refer to lung volumes at different points in the breathing cycle. These terms are defined relative to passive breathing (inhaling and exhaling without active control) and maximal breathing (inhalation

and exhalation to maximum and minimum possible depths). The most common lung volume terms, illustrated in Figure 1.4, are (Lumb, 2016):

- Total Lung Capacity (TLC): The volume of the lungs after maximal inspiration.
- Residual Volume (RV): The volume remaining in the lungs after maximal exhalation.
- Tidal Volume (V_T): The volume that enters the lungs during passive inhalation.
- Functional Residual Capacity (FRC): The volume remaining in the lungs following passive exhalation.
- Expiratory Reserve Volume (ERV): The maximal volume that can be exhaled at the end of passive exhalation.
- Inspiratory Reserve Volume (IRV): The maximal volume that can be inhaled following passive inhalation.
- Inspiratory Capacity (IC): The maximal volume that can be inhaled following passive exhalation.
- Vital Capacity (VC): The maximal volume that can be inhaled following maximal exhalation.

One other ventilation volume that is commonly referred to is the anatomical dead space. This is the volume of the components of the lung which do not participate in gas exchange (i.e. the volume of the conducting airways and trachea). Due to

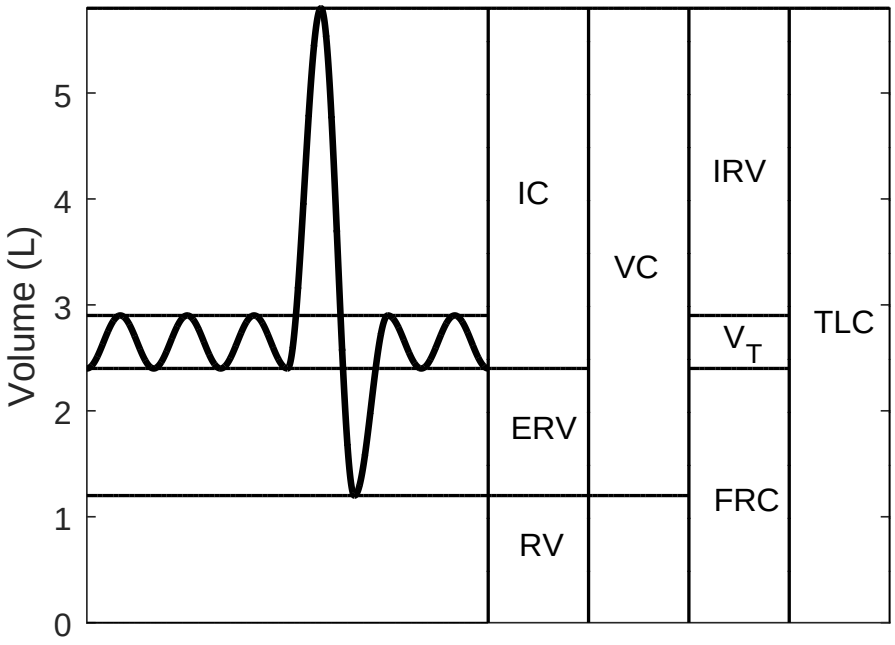

Figure 1.4: Illustration of common lung volumes. The diagram was created using typical values for an adult male.

the elastic nature of the airways, the anatomical dead space changes throughout the breathing cycle. However, due to the tissue properties of the conducting airways (Saladin and Porth, 1998) these changes are quite small. Overall, the volume of the dead space is quite low comparative to the combined volume of the alveoli, typically contributing only 100-300 mL to total lung volume.

1.2.5 Gas exchange between air and blood

The primary purpose of the pulmonary system is to facilitate exchange of gas between the human body (blood) and the external environment (air). This gas exchange process is driven by Fickian diffusion across the alveolar-capillary membrane. The amount of each gas that diffuses across the alveolus surface is directly proportional to the partial pressure gradient of the gas over the boundary, the alveolus surface

area, and the gases' pulmonary permeability. It is also inversely proportional to the wall thickness. The gas diffusion is a completely passive, equilibrating process, being enabled but not driven by the alveoli expansion and contraction (Cotes et al., 2009; Saladin and Porth, 1998).

Since air is comprised of gases, and blood is a liquid, the partial pressures of different gases can differ significantly between both media, even when concentrations are identical. This means that the equilibrium point can occur at largely different concentrations between the two media. In alveolar air, the partial pressure of a gas will be approximately its concentration, multiplied by the gas pressure in the alveolus (total pressure, minus the water vapour pressure). However, the partial pressure of a gas within blood is more complex, being related to solubility of the gas in blood, as well as its binding efficacy with haemoglobin. These factors mean that each gas exists on a saturation behaviour spectrum (Levitzky, 2003). For example, carbon monoxide (CO) exhibits diffusion across the alveolar-capillary membrane. However, upon entering the bloodstream, it forms bonds with haemoglobin (Hb), meaning the blood does not saturate effectively. This type of behaviour means that the amount of carbon monoxide entering the bloodstream is limited by the pulmonary permeability, and not by the blood flow rate, being characterised as diffusion-limited.

However, a gas such as nitrous oxide (N_2O) does not bond with haemoglobin, and as such rapidly saturates the blood. In this case, the amount of N_2O that enters the bloodstream is limited by the amount of blood available, being characterised as perfusion-limited.

Many of the common respiratory gases fall in the middle of this spectrum. Oxygen is perfusion-limited under normal conditions, as while it does bind to haemoglobin, it does not do so with the efficacy of carbon monoxide. However, many pulmonary diseases can alter blood flow significantly enough to create diffusion-limited behaviour instead. An illustration of the perfusion-diffusion spectrum is given in Figure 1.5. A large number of gases have the ability to cross the alveolar-capillary membrane into the bloodstream. However, air is primarily composed of O_2, CO_2 and nitrogen gas (N_2), meaning these are the most commonly referred to. Equally, many gases do not have significant pulmonary permeability, interacting with the airways only.

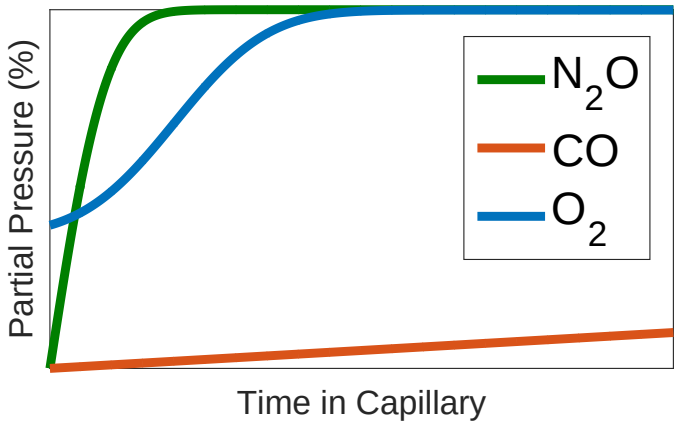

Figure 1.5: Different limiting behaviours of gases in the bloodstream. Carbon monoxide absorption is diffusion-limited, not being strongly affected by the amount of blood present. Nitrous oxide and oxygen gas both behave in perfusion-limited ways, with absorption being driven by the amount of blood available (Levitzky, 2003).

1.2.6 Pathophysiology of lung disease

Within this thesis we are primarily investigating pulmonary function tests. Given that these tests are used clinically to diagnose lung disease, we present a brief overview

of pulmonary pathophysiology. In particular we focus on chronic lung diseases, as the potential heightened sensitivity of complex PFTs is of particular benefit when considering early diagnosis of chronic disease.

Asthma

The most commonly occurring lung disease by far is asthma, affecting approximately 10% of the population (British Lung Foundation, 2016). Asthma is an inflammatory disease that predominantly affects the distal airways in the conducting zone of the lungs (Holgate, 2008). Occurrence of asthma is chronic and driven by increased airway hyper-responsiveness. During an asthma 'attack', the afflicted airways inflame in response to the presence of an allergen. The inflammation occurs in the smooth muscle tissue, and is often accompanied by mucous secretion within the airway. These two factors lead to narrowing or sometimes full closure of the affected airway. This in turn leads to reduced airflow, and coughing or wheezing, as the lungs try to expel the allergen.

The narrowing that occurs during an attack is typically reversible, with or without treatment. However, due to the chronic nature of the disease, subjects with asthma may experience constant mild bronchoconstriction, alongside the more severe constriction associated with attacks.

While there is no direct cure for asthma, a series of steps can be taken for symptom management. Primarily this is done through reduction of exposure to allergens. This can be problematic though, as allergens can be quite different for each patient, making

precise identification difficult. Treatment of attack symptoms is often achieved through the inhalation of bronchodilators, or corticosteroids (British Lung Foundation, 2016).

Chronic obstructive pulmonary disease

COPD is a disease that causes airflow limitation and air trapping. Physiologically, COPD is driven by a breakdown in the elasticity, recoil, and structure of lung tissue, and obstruction of airways in the respiratory zone of the lungs. However, the relative magnitude of these two factors can differ greatly between patients (MacNee, 2005).

COPD typically develops as a chronic inflammatory response to repeatedly inhaled irritants and allergens, particularly from behaviours such as smoking. The stresses that these irritants place on the lungs eventually lead to breakdowns in the connective tissues surrounding the alveoli. The tissue breakdown of neighbouring alveoli can lead to the formation of large air pockets, known as bullae, which function as extremely large alveoli. The presence of bullae, alongside a decrease in the elastic recoil of lung tissue, leads to the lungs becoming overly compliant during inspiration, causing hyperinflation (Murphy and Sethi, 2002).

The tissue breakdown also causes a decrease in compliance during expiration. Alongside this, scarring and inflammation of the distal airways may occur, reducing airflow. The combination of these two factors can lead to air trapping, meaning the expired volume in a breath cycle is repeatedly less than the inspired volume. This in turn can lead to insufficient ventilation and low blood oxygen levels (MacNee, 2005).

Similarly to asthma, there is no known cure for COPD, and most treatment focuses around symptom management. Primary management is first achieved through removal

of irritants and allergens from the air supply, such as through smoking cessation. Alongside this, exercises to increase lung strength are performed to improve a patient's ability to breathe with minimal effort. Bronchodilators and inhaled corticosteroids have been shown to have mild benefits to COPD patients, through widening of the inflamed airways. However, typical COPD patient responses are much smaller than those seen in asthma patients undergoing similar treatments.

Cystic fibrosis

Cystic fibrosis (CF) is a disease that affects the function of multiple organs, primarily the lungs. CF is inherited as an autosomal recessive gene, with the most common carriers being of Northern European Ancestry. The most common pathophysiological change caused by the disease is constriction of airways due to the build-up of mucous. This build-up occurs due to excessive secretion of mucous, decreased mucociliary clearance, and inflammation of the airways, leading to decreases in internal surface area (Gibson et al., 2003).

This airway constriction and narrowing can lead to reductions in airflow, excessive coughing, and lowered blood oxygen levels. Many different types of bacteria are also known to colonise within the mucous, which can lead to further infections in later stages of the disease. As with many other major lung diseases, cystic fibrosis is chronic, with no direct cure. Instead, symptom management is performed to maximise patient lifespan and quality of life (Gibson et al., 2003).

Typically, CF patients use antibiotics to prophylactically suppress infection. These are usually taken even by healthy CF patients, to prevent the build up of infection from

bacteria colonies in the mucous. Other management techniques include chest physiotherapy and regular exercise to help dislodge built-up mucous, and medications that help loosen secretions. In severe cases of bacterial infection, full lung transplantation can be performed.

Bronchiectasis

Bronchiectasis is a lung disease which is characterised by permanent widening of the central airways in the lung. Due to a lack of animal studies, the pathogenesis of bronchiectasis is still not well defined. However, current evidence (King, 2011) suggests that the causes of the disease can be quite varied, with both congenital and acquired causes. Congenitally, bronchiecstasis can develop from cystic fibrosis, or infections that damage cilia motility. Acquired causes are more varied, but include lung infections such as tuberculosis and pneumonia, as well as repeated exposure to allergens, and bronchial tumours.

Interestingly, while one of the primary physiological changes driven by bronchiecstasis is widening of central airways, the disease typically leads to airflow obstruction. This is due to a simultaneous narrowing of distal airways and bronchioles, caused by mucous build up, and inflammation. As the majority of lung volume is driven by the small airways, the net effect is airflow obstruction, even though airflow in the central airways increases (King, 2011).

Treatments for bronchiectasis are centred around control of infection. Immunisation against lung infections (such as measles, pneumonia, and influenza) are performed as preventative measures, and to limit progression of the disease. Beyond this, antibiotics

are typically used to attempt to reduce and control infection. In severe cases, surgical removal of affected portions of the lung may be performed.

Pulmonary Fibrosis

Pulmonary fibrosis is a respiratory disease which results in the scarring of lung tissue. This is driven by fibrosis, an accumulation of excessive fibrous connective tissue, leading to thickening of airway walls, and subsequent airway obstruction. The stiffening of tissues also reduces the diffusing capacity of oxygen, and leads to a decrease in lung compliance, restricting lung volume (Katzenstein and Myers, 1998; Mallory, 1948).

Pulmonary fibrosis may occur as a response to other diseases, including autoimmune disorders, as well as viral and bacterial infections. However, many cases of pulmonary fibrosis develop idiopathically, with no known cause. Evidence in the literature suggests that a subset of the population may have a genetic predisposition to the development of fibrosis (Fingerlin et al., 2013).

The creation of scar tissue within the lungs is a permanent process, and as such, no cure exists for pulmonary fibrosis. Treatments instead involve slowing the progression of the scar tissue. Some pharmacological and anti-inflammatory agents have been shown to reduce the predicted rate of progression, however, these effects can often by minimal (Mallory, 1948). In severe cases, transplantation of the lungs is considered the only viable treatment option.

1.3 Literature review

In the previous section we have provided a brief review of physiology and pathophysiology of the pulmonary system. Here we build upon this by presenting a literature review on pulmonary function testing. Given that the focus of this thesis is on the investigation of alternative PFTs to spirometry, the literature review will only briefly touch upon this test. Instead, we will take an in-depth look at other more complex PFTs, including clinical studies, and computational studies to improve output interpretation.

1.3.1 Spirometry

The most common pulmonary function test is spirometry. It is typically used as a tool for diagnosis of asthma, pulmonary fibrosis, cystic fibrosis and COPD (Miller et al., 2005). Spirometry is performed using a flow-measurement device called a spirometer, which produces volume-flow and volume-time curves based on a patients exhalation (typical volume-flow and volume-time curves are given in Figure 1.6). The test is performed by having the patient undergo a maximal inhalation, followed by as rapid a maximal exhalation as they can manage.

As the manoeuvre requires active patient participation, it is usually performed at least three times, to help improve stability and reproducibility. It also cannot be performed with patients who cannot comprehend the instruction (i.e. young children), or those unable to make a vigorous respiratory effort.

Three major values are typically taken from a spirometry test:

- Forced vital capacity (FVC): The volume of air that can be forcibly blown out after full inspiration.

- Forced expiratory volume in 1 second (FEV1): The volume of air that can be forcibly blown out during the first second following full inspiration. This is often presented as a volume, or as a percentage of FVC.

- Forced expiratory flow (FEF): The airflow rate at discrete times during the exhalation. Typically the mean flow rate over the middle half of the procedure (FEF25-75%) is taken.

- Peak expiratory flow (PEF): The maximal flow rate achieved during the manoeuvre.

These values are then interpreted in reference to standard values for a patient's age, gender, race and weight (Quanjer et al., 2012). As an example, the level of lung damage is often inferred through seeing whether a patient's FEV1 is significantly lower than the standard FEV1 for their demographic.

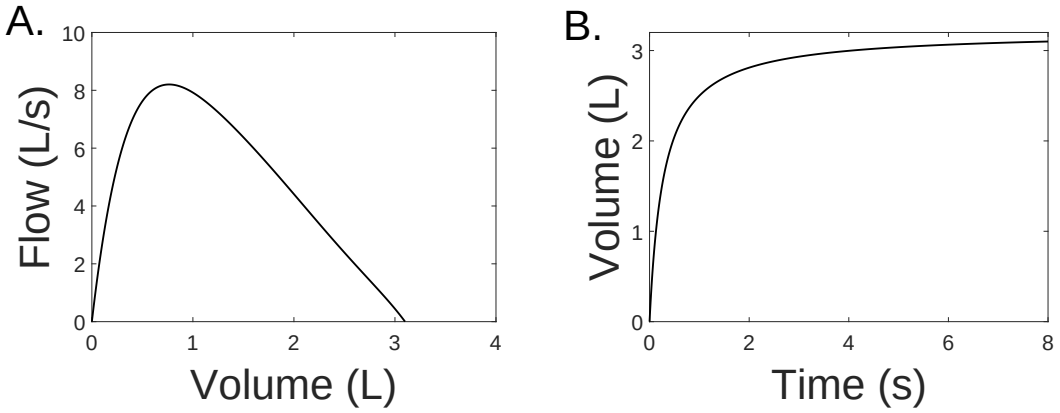

Figure 1.6: Typical volume-flow (A) and volume-time (B) spirometry curves for a healthy patient.

1.3.2 Magnetic resonance imaging

Alongside spirometry, a range of different imaging techniques have also been shown to successfully resolve ventilation heterogeneity (VH), one of the primary outcomes of many lung diseases. These techniques include scintigraphy, CT, and PET (Gould et al., 2001; Simon, 2005; Tzeng et al., 2009). However, while these techniques can produce high resolution images, the use of ionizing radiation limits application in many clinical settings, particularly paediatric, and longitudinal studies.

Due to the inherent dangers of imaging using ionising radiation, alternative VH imaging techniques such as MRI have gained traction in recent years. In particular, proton MRI (Bauman et al., 2009; Biederer et al., 2012; Sá et al., 2010) and hyperpolarised gas MRI (Fain et al., 2007; Möller et al., 2002; van Beek et al., 2004) have exhibited increased uptake, and strong improvements in resolution and cost.

One of the simplest measures for quantifying VH from an image is the calculation of the number of ventilation defects, a defect being defined as a region (image voxel) with measured ventilation below a chosen threshold (Altes et al., 2001). Other studies have instead processed multiple images to approximate the residual gas within, and amount of gas entering a voxel over each inhalation cycle. Typically, this result is used to calculate measures for how well ventilated each voxel is. From estimates of voxel ventilation, a series of different measures of ventilation heterogeneity can be calculated. Within the literature, there does not appear to be a single standard index used to quantify VH from imaging data, however, most indices can be loosely categorised as quantifying heterogeneity at a global (Biederer et al., 2012; Horn et al., 2014), or local

(Tzeng et al., 2009) level.

MRI techniques have become more viable due to reductions in time, alongside improvements in image resolution. However, the relative cost, and lack of standardised imaging protocols have limited large scale uptake (Biederer et al., 2012). Equally, there are fewer studies (relative to many PFTs) investigating the relationship of MRI outputs to disease classification, particularly beyond cancer.

1.3.3 Inert-gas washout

A clinical test for VH that is becoming increasingly common is the inert gas washout (Macleod et al., 2009; Robinson et al., 2013; Verbanck et al., 2003). In this test, information about lung function is ascertained by measuring the exhalation of a previously inhaled gas over either a single or multiple breaths. The multiple-breath washout (MBW) is performed in one of two ways; either air mixed with an inert-gas (such as sulfur-hexaflouride (SF_6) or hyper-polarised helium (^3He)) is washed-in (breathed in until it is assumed to have equilibrated in the lungs) by the patient and then washout of the gas is performed by switching the patient back to an air mixture without the gas; or in the case of nitrogen washouts, since N_2 is already present in air, no wash-in is performed, and instead a washout is performed using pure oxygen. By monitoring the exhaled gas concentrations during the washout process, a number of VH indices can be derived. These include the Lung Clearance Index (LCI), s_{cond}, and s_{acin} (Verbanck et al., 1998). The LCI is the amount of time taken from the start of the washout phase until mean exhaled concentration over an exhalation drops below

1/40th of the initial exhaled concentration. To normalise between patients, this time is expressed as the number of lung turnovers performed, turnover being the cumulative expired volume divided by the individual's FRC.

The other two measures typically derived from the MBW, s_{cond} and s_{acin}, are more complex in definition. For each exhalation, a plot of exhaled gas concentration over cumulative expired volume can be generated. Typically this plot undergoes four distinct phases; an initial plateau, a steep rise, a second plateau, and a final rise (Verbanck et al., 1998). An s_{III} value is defined as the slope of the third phase of each curve, divided by the mean exhaled concentration over the third phase. The index s_{cond} is defined as the mean gradient of the s_{III} values between turnovers 1.5-6, and s_{acin} as the s_{III} value from the first exhalation, minus the contribution from the s_{cond} slope. An example of this is given in Figure 1.7.

A single-breath washout (SBW) is performed in a similar way to the MBW, except that the wash-in and washout phases last for a single breath each. This leads to a reduction in sensitivity, but means the test can be performed much more easily, and with higher reproducibility (Van Muyleim et al., 1992).

The uptake of the inert-gas washout as a clinical test of VH has in large part been driven by the correlation of MBW and SBW indices with clinical classifications of many lung diseases, including cystic fibrosis (CF) (Aurora et al., 2004, 2005a; Horsley et al., 2008) and asthma (Gustafsson, 2007; Verbanck et al., 1999). However, these indices are only indirect measures of VH, whose exact relationship to lung structure is not yet fully understood (Robinson et al., 2013).

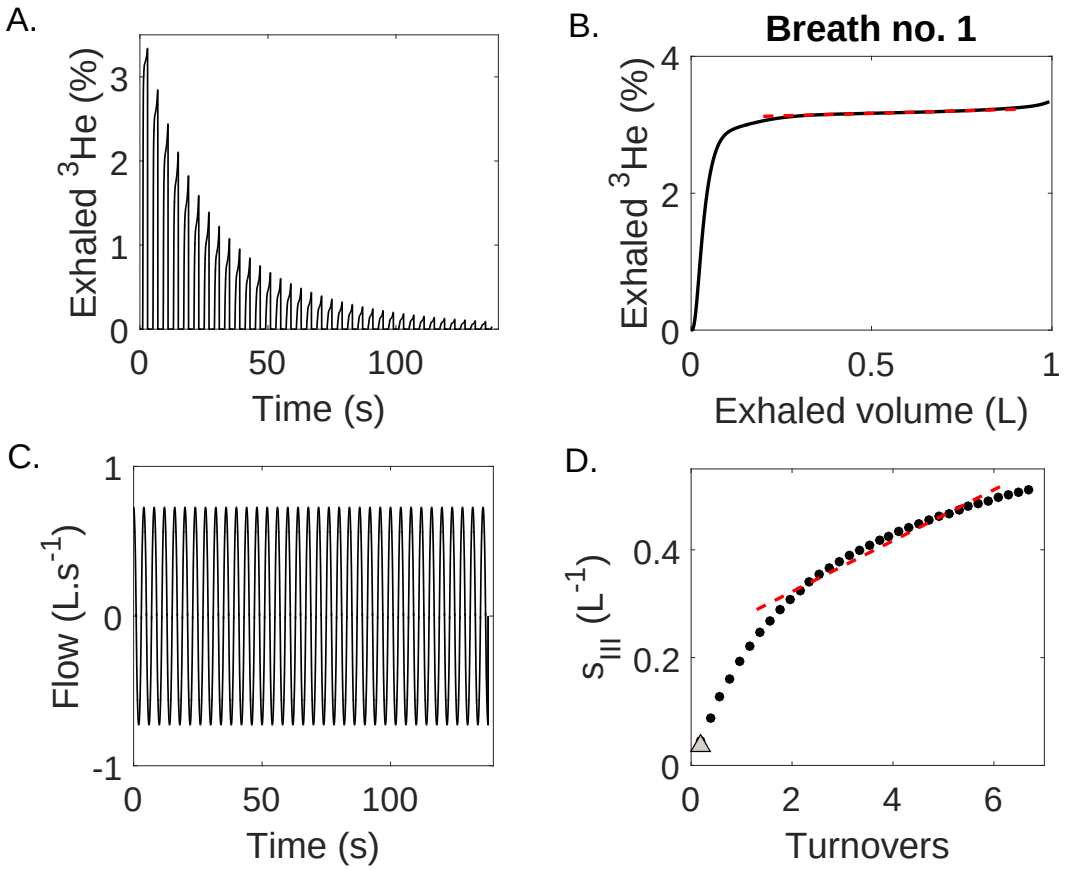

Figure 1.7: Simulated ^{3}He multiple breath washout curve. The actual curve is given (A), alongside the profile (B) for the 1st breath (black line), with the s_{III} slope before normalisation overlaid (red dashed line). The flow rate out of the mouth throughout the washout is also given (C), as well as the total set of s-values (D), with the slope s_{cond} overlaid (red dashed line), and the index s_{acin} plotted (grey triangle).

A variety of different clinical studies have helped improve understanding of washout indices, by investigating the MBW and SBW in a variety of different scenarios. Prisk et al. (1998) performed many investigations of the inert-gas washout in micro-gravity, leading to conclusions that test indices partially respond to the heterogeneity caused by the gravitational ventilation gradient, even in healthy subjects. Many studies in the literature have further investigated the effects of gravity through comparing MBW and SBW (and related PFT) indices in different body positions (orthostatic,

supine, left/right-lateral). However, while some of these studies have shown little or no changes in indices when moving from supine to standing (Grönkvist et al., 2002), or supine to prone (Peces-Barba et al., 2004; Rodríguez-Nieto et al., 2002), other studies have shown drastic but inconsistent changes, particularly in unhealthy or elderly population groups (Attinger et al., 1956; Badr et al., 2002; Manning et al., 1999; Petersson et al., 2007).

While clinical tests have helped improve understanding of inert-gas washout indices, they are often limited in their ability to create function-form links between structural changes and index changes. For this reason, computational and theoretical modelling has been used alongside clinical experimentation to improve understanding. Early work by Otis et al. (1956) advanced this understanding through the concept of time constants, a measure of how effectively different pulmonary regions of the lung ventilate. A time constant is defined as the average resistance of a region multiplied by the average compliance, with larger time constants corresponding to a smaller phase shift between pressure and flow. Through experimental results and theoretical calculations, Otis et al. (1956) showed that regional differences in time constants could significantly change flow behaviour at the mouth, suggesting the potential to identify regional mechanics through analysis of tracheal flow.

The desire to understand the effect of structural changes more precisely led to the development of a wide array of computational modelling approaches. In early work, Verbanck and Paiva (1990) applied a gas transport model, performed on an idealised lung structure based on the work of Weibel (1963), to investigate the effect

flow rates had on concentration profiles during the washout phase. The study showed that concentrations gradients over each exhalation became increasingly sensitive to flow rates as the washout progressed, meaning that the MBW could be quite sensitive to changes in lung structure.

Understanding was further advanced by the computational modelling work of Cruz et al. (1997). Through the simulation of a washout process on a single region lung model, and a 7 region lung model, they investigated the effect that serial and parallel heterogeneities had on washout curves. They showed that the incorporation of parallel heterogeneities produced results that more closely resembled clinical data than simulations involving only serial heterogeneities. Shortly after, they expanded upon this work to more accurately incorporate bloodstream gas transfer of N_2, showing that this led to more physiologically meaningful results (Han et al., 2001).

The investigation of the MBW through simulation of convection-diffusion transport models was further developed by Tawhai and Hunter (2001). In their work, a transport model was simulated on a geometrically realistic conducting airway zone structure, and coupled to a lumped parameter model of the acinar regions (a collective term for a grouped region of alveoli and respiratory bronchioles). Through this coupling, they showed that computational simulations could reproduce clinically realistic values of s_{cond} and s_{acin}. More recently, Mitchell et al. (2012) adapted the work of Tawhai and Hunter to develop an MBW model that calculated flow rates based on the pleural-pressure gradient, and simulated the test on geometries drawn from imaging data. Within this study they performed an investigation of how different types of constriction

could affect LCI and s_{cond}. Their analysis suggested that s_{cond} and LCI may fail as predictors of VH under severe airway constriction. However, computational constraints strongly limited the number of simulations that were performed, and thus only limited insight could be gained. It should be noted that, while advanced, the mathematical model still relied on parameter fitting to produce physically realistic MBW indices.

Significant progress has been made in the field since the initial work of Verbanck and Paiva. While there is now strong evidence to suggest that MBW indices directly relate to VH in both the conducting and respiratory zones, the exact nature of these relationships is still unknown (Robinson et al., 2013). The clinical and computational work in the literature suggests sensitivity of the test to early-stage disease and bronchoconstriction. However, more clarity is needed as to whether this sensitivity can be more precisely quantified, and subsequently utilised clinically.

1.3.4 Lung impedance

Two other PFTs that are increasing in clinical uptake are the forced oscillation technique (FOT) and impulse oscillometry (IOS) (DuBois et al., 1956; Marchal and Hall, 2010; Smith et al., 2005). In short, these techniques are performed by applying oscillations of varying frequencies at the mouth, either as controlled pressure pulses (FOT), or as pseudo-random noise (IOS). By measuring central airflow and pressure at the mouth, estimates can be made of the resistance (R), and reactance (X) of the lungs; the in and out of phase relationships between pressure and airflow, known collectively as impedance. Resistance details the lung's mechanical dissipation properties, whereas

reactance details the tissue's capacity for energy storage. Both of these properties have been shown to exhibit strong frequency dependence (Oostveen et al., 2003), with typical curves given in Figure 1.8.

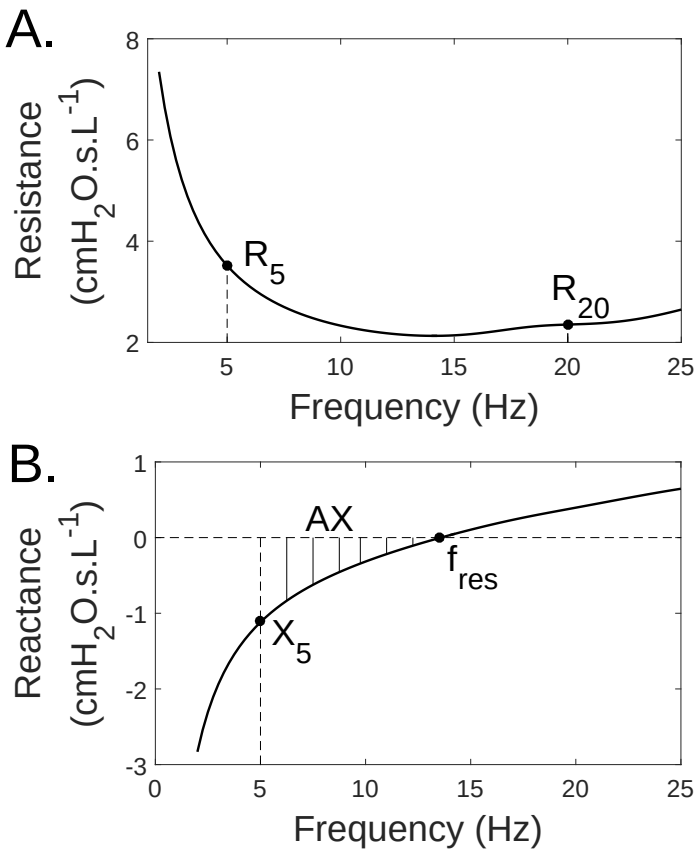

Figure 1.8: Simulated resistance (A) and reactance (B) curves. The key FOT/IOS parameters R_5, R_{20}, X_5, f_{res}, and AX are marked.

Application of the FOT and IOS to the detection of lung disease has been driven by the passive nature of the test. It requires no forced manoeuvres from the patient, as measurements are made in much higher frequency ranges than standard breathing (Smith et al., 2005). This has led to a variety of different applications of lung impedance measures to the detection of asthma and cystic fibrosis, particularly in pediatric settings (Marchal and Hall, 2010). Due to the test's potential sensitivity

to peripheral airway function, it is also experiencing increased application to the detection of small airway disease in adults.

In the literature, many different studies have investigated changes in reactance across differing patient groups. Diseases such as asthma and COPD have been shown on average to lead to an increase in magnitude in both resistance and reactance measures (Smith et al., 2005; Crim et al., 2011), often with higher sensitivity than spirometry. FOT and IOS indices have also shown high sensitivity when measuring airway constriction in bronchodilator studies. Results such as these suggest a strong sensitivity to small airway constriction, however, similarly to the MBW, the complex nature of the test has limited precise interpretation of the indices.

Since initial development of the FOT and IOS, improvements in output interpretation have occurred through a combination of modelling, clinical and animal studies. A variety of clinical studies have shown that resistance appears to be significantly raised in unhealthy patient groups (Crim et al., 2011; Grimby et al., 1968). Morphometric models of animal lungs have also suggested that both resistance and reactance show sensitivity to heterogeneous airway constriction, particularly in the distal airways (Lutchen and Gillis, 1997; Thorpe and Bates, 1997).

These combinations of clinical, animal and computational modelling studies have led to the interpretation of low frequency resistance as a measure of total ventilation heterogeneity, and high frequency resistance as a measure of central airway constriction. Considering this, the difference between low frequency and high frequency resistance (e.g. R at 5Hz minus R at 20Hz, $R_5 - R_{20}$) is often taken as a marker of distal airway

constriction (Goldman et al., 2005; Smith et al., 2005). While resistance indices are often interpreted as markers of bronchoconstriction, the exact relationship to this type of lung disease is not yet fully understood. Furthermore, recent studies have highlighted potential issues with measurements of lung resistance through the FOT, including interference from shunting in the cheeks and soft palate (Bhatawadekar et al., 2015).

Clinical and modelling studies have also shown that low frequency reactance decreases in magnitude in asthmatic patients, comparative to healthy control groups, and that low frequency reactance can be increased with the use of bronchodilators (Cavalcanti et al., 2006; Kaczka et al., 1999; Smith et al., 2005). Since asthma is understood to be driven by behaviour in the distal airways (Kraft, 1999), this suggests that low frequency reactance may be sensitive to constriction at this depth. This assertion has been shown to hold in morphometric modelling studies (Bhatawadekar et al., 2015; Kaczka et al., 2007; Lutchen and Gillis, 1997). However, similarly to resistance indices, the exact nature of this response in relation to lung disease such as bronchoconstriction is not yet fully understood.

Similar to the inert-gas washout, the developed literature on lung impedance measures shows they may have higher sensitivity to early stage lung disease (particularly in the small airways), than spirometry. However, for this sensitivity to be utilised clinically, it must be precisely quantified and understood - a process which may be aided by continued improvements in computational modelling.

1.3.5 Virtual lung structures

As detailed in sections 1.3.1-1.3.4, improved understanding of many PFTs has been driven by the use of computational modelling. However, computational modelling of the lungs is significantly underpinned by the ability to create meaningful virtual representations of the organ. These virtual structural representations form a key component of all computational lung models, providing a domain on which mathematical models can be simulated. Early mathematical modelling (Bates et al., 1985; Hahn et al., 1993; Otis et al., 1956), often used highly simplified representations, consisting of a few elastic chambers, characterised by key parameters such as resistance and compliance. The simplicity of these models was in many ways driven by computational constraints and a lack of detailed physiological information.

Significant advancement in this field was driven by the work of Weibel (1963). In what is considered a foundational piece in the field, Weibel presented detailed structural information of the lungs, gathered from statistical sampling of healthy adult lung tissues. This was the first truly detailed set of baseline values for properties such as airway radii, and tissue density, at each generation of the lungs. The provision of this information meant that models of the lung that incorporated information at each airway generation could effectively be designed and simulated on. Weibel's data was used to design symmetric structural representations, with the number of generations incorporated typically being limited by availability of computational power (Lutchen and Gillis, 1997; Verbanck and Paiva, 1990).

More recently, advances in imaging technology have allowed for detailed, patient

specific structural models to be built. Research by Fetita et al. (2004) and Tawhai et al. (2004) showed how detailed structural representations of the central airways (generations up to 6-10) could be obtained through image processing of CT scan data. They coupled this with algorithmic procedures, to generate full airway models of the conducting zone of the lungs. A visualisation of a structural lung representation, from a set produced using these techniques, and presented by Bordas et al. (2015) is given in Figure 1.9.

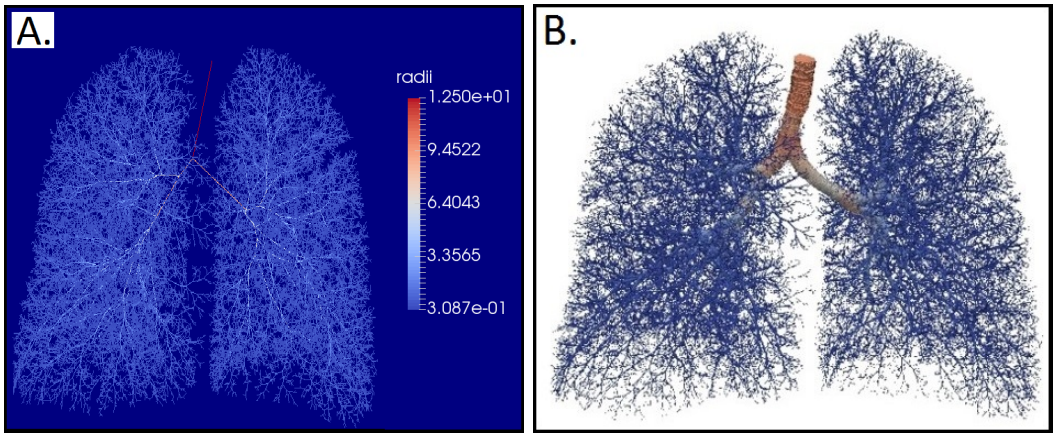

Figure 1.9: Visualisation of a structural lung representation. The model is visualised as a centreline wireframe (A), and as a surface (B). This model was taken from a set originally presented by Bordas et al. (2015), and visualised using ParaView.

While significant improvements have been made since the early single compartment model lung representations, structural representations that account for the true complexity of the lung are not yet in use. The detail of current representations is still primarily limited by achievable resolutions with imaging techniques such as CT scanning and MRI. Further to this, full structural representations which incorporate individual alveoli would be computationally intractable for most types of models, due to the sheer number of alveoli.

1.4 Thesis proposal

Given the context of the literature review, a clear gap in current research can be identified. Within clinical practice, spirometry is by far the most commonly used method for diagnosis of lung disease. However, spirometry often lacks the sensitivity to detect early-stage disease, or to distinguish between different types of disease. More complex PFTs, such as the inert-gas washout, FOT and IOS may offer increases in sensitivity which can be utilised for improvements in clinical diagnosis. However, for this to be viable more precise frameworks for output interpretation must be developed. Given the significant improvements in computational power, and imaging resolutions in recent years, we believe that computational modelling may help address this gap. In particular, we believe that computational models of the pulmonary system may allow for improvements in interpretation of test outputs, as well as help generate more targeted clinical hypotheses pertaining to the tests.

The primary aim of this thesis is to apply computational modelling techniques towards these two goals. In particular, the work will focus on the MBW, FOT and IOS. These tests have been chosen as they are experiencing increased clinical uptake, due to potentially higher sensitivity, but are also limited by a lack of precision in output interpretation.

Currently in the literature, there already exist mathematical and computational models of both the MBW (Mitchell et al., 2012; Verbanck and Paiva, 1990) and FOT/IOS (Kaczka et al., 2007; Lutchen and Gillis, 1997). However, to the best of our

knowledge these models lack large-scale benchmarking against clinical measurements, and often rely on significant data fitting. Equally, the majority of studies do not make effective use of more recent advancements in computing power, either using quite restrictive structural approximations, or relying on small numbers of simulations to drive conclusions. We believe that these two factors represent a significant gap in the literature which we will address.

Given these gaps, work within this thesis has focused on four main points. Firstly, we have developed and implemented more detailed and accurate mathematical models of the human pulmonary system. These models have been designed with a preference towards capturing the major underlying physical mechanisms of the pulmonary system, with a desire to reduce the number of parameters in each model, so as not to introduce fitting bias. These models have been efficiently implemented to allow for rapid simulation of PFTs, making clinical hypothesis generation feasible.

Following design and implementation, the models were used to specifically simulate the MBW and FOT/IOS under a variety of different lung disease scenarios. This was treated as a large scale exploratory analysis. In doing this, we provide a more detailed map of how outputs from each test responds to different types of lung disease, highlighting sensitivities, and improving interpretability.

Alongside this, we have worked closely with engineers, imaging specialists, and clinical researchers to effectively validate the computational models. To provide a strong and necessary link between computational models, and clinical practice, we have collected clinical and experimental data which was then used to directly assess

the accuracy of each model.

Finally, following clinical and experimental validation, we applied the models to a series of more targeted clinical questions. By doing this, we illustrated how the models can aid in the design of clinical studies, allowing for efficient and effective generation of meaningful clinical hypotheses.

The work within this thesis has been built upon prior work both in the literature, and within the University of Oxford's Department of Computer Science. In particular, this work does not focus on the development of realistic virtual representations of the lungs. Instead, all of our models have been implemented on patient-specific virtual lung structures that have been previously developed by researchers within the University of Oxford (Bordas et al., 2015). These structures have associated clinical and experimental measurements for both the MBW and FOT/IOS, which have been used for direct validation of the mathematical models. The clinical and experimental data used for validation has been collected by research partners at the University of Leicester, and the University of Nottingham (with details presented in the relevant chapters).

1.5 Chapter outline

This thesis is comprised of 9 chapters, detailing the results from a variety of different studies involving simulation of pulmonary function tests. The thesis is structured as follows:

- **Chapter 2:** A series of different computational models for ventilation, gas transport and lung impedance are detailed, including information on numerical implementation and error convergence.

- **Chapter 3:** A model of ventilation and the MBW is applied to a joint exploratory analysis of MBW and MRI outputs, under a variety of bronchoconstriction scenarios.

- **Chapter 4:** Following on from Chapter 3, the MBW and lung impedance models are applied to the joint investigation of test outputs under a variety of bronchoconstriction scenarios.

- **Chapter 5:** A large scale validation of the lung impedance model is presented using a combination of clinical data, and a 3D printed airway structure. Following this, the model is used to analyse the suitability of $R_5 - R_{20}$ as a measure of small airways disease.

- **Chapter 6:** Similar to in Chapter 5, clinical data is used to perform a detailed validation of the MBW model. Following this, the model is used to investigate the sensitivity of test outputs to changes in body position.

- **Chapter 7:** Building upon the previous chapters, the MBW model is extended to incorporate effects of the bloodstream, leading to a more generalisable model. This model is implemented in a high-performance computing environment, to allow for clinical research utility.

- **Chapter 8:** As a final study, the model developed in Chapter 7 is applied to the analysis of how different gas choices may affect MBW outputs.

- **Chapter 9:** Finally, we close the thesis with a detailed discussion of the ramifications of this work, and of potential future research directions.

1.6 Publication list

The work within this thesis has formed the basis of 7 academic journal articles, and 4 conference presentations. The following is a list of the academic journal articles connected to this body of work (ordered by relevance to thesis chapters):

- *Modelling responses of the inert-gas washout and MRI to bronchoconstriction* published in *Respiratory Physiology & Neurobiology* (Foy et al., 2017). Connected to Chapter 3.

- *A computational comparison of the multiple-breath washout and forced oscillation technique as markers of bronchoconstriction* published in *Respiratory Physiology & Neurobiology* (Foy and Kay, 2017). Connected to Chapter 4.

- *Lung computational models provide unique insights into the clinical role of the small airways in asthma*, under review. Connected to Chapter 5.

- *Characterising the role of the small airways in severe asthma using tidal breathing low frequency forced oscillations: A combined computational models and clinical approach*, under review. Connected to Chapter 5.

- *Functional CT imaging for identification of the spatial determinants of small airways disease in adult asthma*, under review. Connected to Chapter 5.

- *Modelling the effect of gravity on inert-gas washout outputs*, published in *Physiological Reports* (Foy et al., 2018). Connected to Chapter 6.

- *A computationally tractable scheme for simulation of the human pulmonary system*, under review. Connected to Chapters 7 and 8.

The following is a list of conference publications and presentations connected to this body of work (ordered by relevance to the thesis chapters):

- *The evaluation of frequency dependence of resistance using a patient-specific 3D printed airway model and computational simulation*, presented at *2017 Meeting of the European Respiratory Society*. Connected to Chapter 5.

- *Inert-gas washout and forced oscillation technique show sensitivity to the degree of regionalisation of bronchoconstriction*, presented at *2017 American Thoracic Society Congress*. Connected to Chapters 5 and 6.

- *Sacin responds to total compliance heterogeneity, and is less sensitive to regionalisation than scond*, presented at *2018 American Thoracic Society Congress*. Connected to Chapter 6.

- *Low frequency lung resistance is a global bronchoconstriction detection measure, but is still sensitive to small airways disease*, presented at *2018 American Thoracic Society Congress*. Connected to Appendix B.

2

Designing computational models of the lungs

To address the literature gap identified in Chapter 1, we aim to use computational models to analyse various pulmonary function tests. Within this chapter we present these models, alongside their implementation, limitations and error convergence. In particular, models for simulating ventilation and mimicking MR images, and simulating the multiple-breath washout and lung impedance are presented.

2.1 Virtual lung structures

To effectively simulate processes within the lungs, we first require a physically realistic virtual representation of the lungs. The structural models used in this body of work

were taken from a set of structures originally presented by Bordas et al. (2015). The creation of this set was performed through a combination of CT segmentation to obtain the central airways (to generation 6-10) and algorithmic airway generation for the remainder of the conducting airways (to an average generation of 16), using processes originally described by Fetita et al. (2004); Tawhai et al. (2004). While this work was performed prior to the studies in this thesis, for completeness we briefly present details of the segmentation and algorithmic generation process.

Segmentation of the central airways primarily involved detection of the bronchial walls, based on their high-density of vascularized tissue, comparative to the surrounding parenchyma. Due to limitations in imaging resolutions, this process could only provide clarity to the reconstructions of airway diameters approximately 1mm or larger, making the process typically appropriate for airway generations 1-10. In the initial work of Fetita et al. (2004), results for the CT segmentation were compared to manual detection performed by a radiologist, showing an accuracy of approximately 91%.

The remaining conducting zone airways were generated using a space filling algorithm, based on local energy minimisation. Full details of the algorithm are presented by Bordas et al. (2015), but in brief, a uniform array of seed points was first created within each lobe, with each point being assigned a volume of $187mm^3$ (an approximation of mean acinar volume in humans). Each seed point was then uniquely assigned to the closest terminal segmented airway within its lobe. The cloud of seed points associated with a given terminal airway was then split into two clouds, based on a plane extended from its centroid to the parent airway. Following this, two new

daughter airways were grown 40% of the length to the two new seed cloud centroids, with radii based off of histological branching factors. This process was continued iteratively until each new daughter branch was either below a set branch length (2mm), or had only one seed point associated with it.

The set of structures presented by Bordas et al. (2015) consists of 35 patient-specific structures, with each patient being classified as either healthy (n = 11), or asthmatic (n = 24). Asthma classifications were made using a GINA score, as outlined by the Global Initiative for Asthma (Global Initiative for Asthma, 2017). A GINA score of 0 corresponds to healthy, 1-3 as mildly asthmatic, and 4-5 as severely asthmatic.

Throughout this thesis, we will repeatedly use this entire set (and specific subsets) to perform simulations, referring to it as the *Bordas set*. However, each of the lung structures is patient-specific, and thus even the healthy structures may contain bias, and not be truly representative of a perfectly healthy state. To account for this, a lung structure was built using mean-field airway data. To create this structure, airway radii in one of the healthy patient structures in the Bordas set was discarded, and regenerated using the idealised mean-field model (Horsfield et al., 1976)

$$\log d(x) = (x - N)\log(R_d S) + \log(d_n), \tag{2.1}$$

where d is the airway diameter, x is the Strahler order (Strahler, 1957) of the branch, N is the maximum Strahler order of the tree, d_n is the maximum diameter, and $R_d S$ is the anti-log of the slope of the airway diameter plotted against Strahler order, taken as 1.4. Equation (2.1) represents a relationship that recreates typical decrease rates in

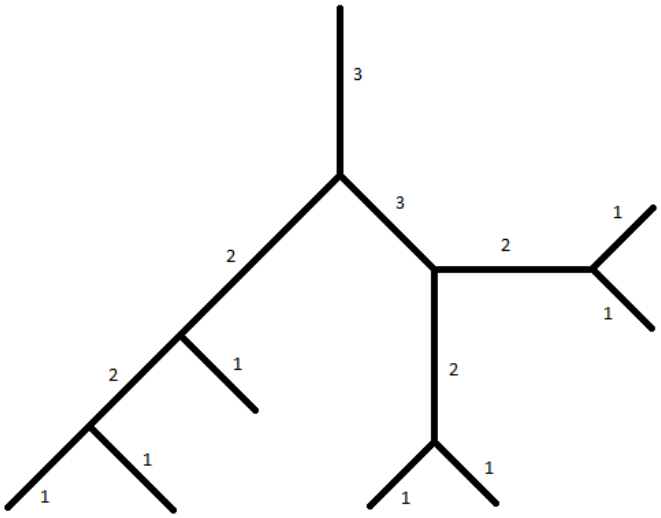

Figure 2.1: Illustration of Strahler order in a simple asymmetric tree

airway diameters, as seen in population studies performed by Horsfield et al. (1976) and Weibel (1963), taking the tracheal diameter as an initial input. This structure is used to represent an idealised healthy patient, and throughout the thesis is referred to as the *baseline* structure of the Bordas set.

This relationship (Equation (2.1)) uses Strahler order instead of branch generations, to create symmetry. The Strahler order of a branch is defined as the minimum number of branches between a given branch (including itself) and the nearest distal terminal branch (see Figure 2.1). Thus, comparative to branch generation, Strahler order creates symmetry relative to the terminal bronchioles, rather than the trachea. This is particularly useful when investigating models that are primarily driven by behaviour in the respiratory zone, and small conducting airways.

Alongside the Bordas set, another set of 31 patient-specific structures (7 healthy, 24 asthmatic) was gathered from the control group of a randomised clinical trial for

Fevipiprant (Gonem et al., 2016). This set is referred to as the *Novartis set*, as the associated clinical trial was partially funded by Novartis. The Bordas set is primarily used throughout the thesis, however, the Novartis set is used in Chapter 6, as it has paired clinical MBW measurements. Basic statistics of each clinical group are summarised in Appendix A.

2.2 Ventilation model

Given a set of virtual lung structures to simulate upon, we now present the design and implementation of a series of models for simulating various physical processes within the lungs, with the primary goal being to simulate pulmonary function tests. As a first step, the most natural model to build is one for calculating ventilation and volume changes throughout the breathing cycle. This is done by adapting and building upon prior models of ventilation (Mitchell et al., 2012), and airway resistance (Bordas et al., 2015) in the literature.

To start, we first define the domain of the model as the total set of 1D branches in a given virtual lung structure from the Bordas or Novartis set. To account for the respiratory zone of the lungs, we assume each terminal conducting zone branch is subtended by a simple spherical acinar unit, with associated volume V_{acin}. Since airflow in the lungs is primarily driven by pressure, we assume that each branch has an associated flow rate Q, and each bifurcation point an associated pressure P. A simple schematic of the ventilation model domain is given in Figure 2.2.

We first assume that flow is 1D in nature, and primarily driven by the pressure

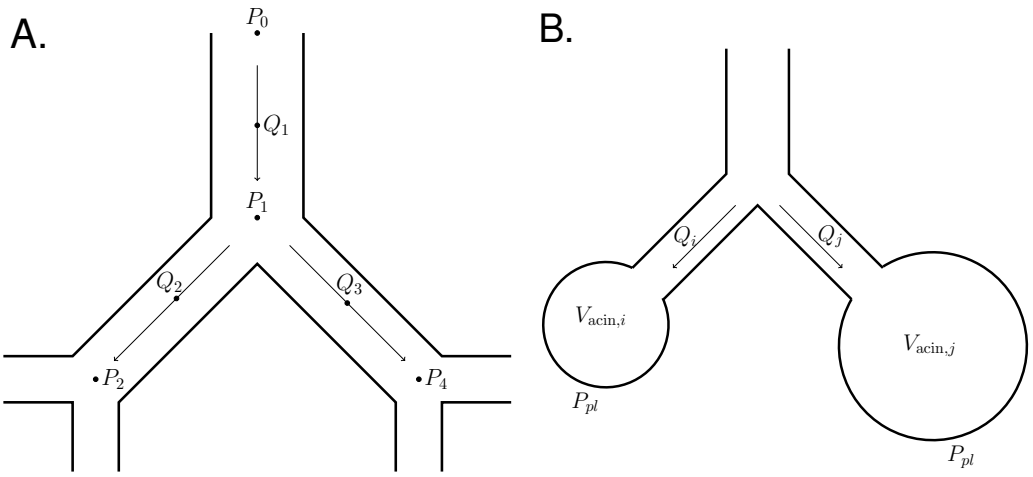

Figure 2.2: Diagram of the ventilation model domain. An idealised 2D cross-section of the problem domain, showing branch bifurcations, flow rates and pressures (A), and the connection of terminal conducting zone branches to acinar regions (B).

gradient from the pleural cavity to the trachea. Given the assumption of pressure-driven flow, the flow rate in each branch can be related to the pressure gradient over the branch, such that

$$\Delta P = R(Q)Q,$$

where P is pressure, $Q = Au$ is the flow rate, A is the cross-sectional area of the branch, u is the airflow velocity and $R(Q)$ is the flow resistance of the branch. For flow resistance, we use the model first presented by Pedley et al. (1970), an adaptation of Poiseuille flow, given as

$$R(Q) = \frac{32\mu Lc}{\pi d^4}\left(\text{Re}(Q)\frac{d}{L}\right)^{1/2}, \tag{2.2}$$

where d and L are branch diameter and length respectively, μ is the viscosity of air, $c = 1.85$ is a correction constant, and $\text{Re}(Q)$ is the Reynold's number of the flow:

$$Re(Q) = \frac{4\rho|Q|}{\mu\pi d},$$

where ρ is the density of air.

The pressure-driven flow model is coupled with the physical condition of flow conservation at each bifurcation, meaning

$$Q_{\text{parent}} = \sum Q_{\text{daughter}},$$

where Q_{parent} is the flow rate proximal branch in the bifurcation, and the sum is over the set of all distal branches in the bifurcation.

Distal to each terminal conducting bronchiole, we assume the expansion and contraction of the associated acinar region is driven by flow within the terminal bronchiole and pressure from the pleural cavity, such that

$$\frac{dV_{\text{acin},i}}{dt} = Q_i,$$

$$P_{T,i} - P_{pl,i} = \frac{1}{\mathbb{C}_i} V_{\text{acin},i},$$

where Q_i is the flow rate within the terminal bronchiole, $P_{T,i}$ is the pressure at its distal end, $P_{pl,i}$ is the pleural pressure surrounding acinar unit i, and $\mathbb{C}_i$ is the compliance of the acinar region (with total lung compliance set as 0.2 L/cmH_2O throughout this thesis). This is a simple constant compliance model of acinar mechanics, adapted from the work of Ben-Tal (2006).

To close this system, we need to define the pressure values at the proximal and distal ends of the branch network. At the tracheal boundary we enforce atmospheric pressure, while distally we specify the pleural pressure P_{pl} to ensure the desired FRC, breath frequency and depth. The pleural pressure surrounding each acinar unit i is

taken as sinusoidal, of the form

$$P_{pl,i}(t) = A_{pl} + R_{pl}\sin(\frac{2\pi t}{T}),$$

where A_{pl}, and R_{pl} are the mean pleural pressure, and pleural pressure range respectively, and T is the breathing period (typically 4 seconds).

2.2.1 Gravitational ventilation gradient

Many studies within the literature have detailed the effects that gravity has on ventilation of different units within the lungs (Kaneko et al., 1966; Musch et al., 2002). Gravity is seen to have a deforming effect, with spatially lower units ventilating to higher degrees, a phenomenon known as the 'Slinky effect' (Hopkins et al., 2007).

Within our ventilation model, FRC and breathing depth are enforced through modification of the pleural pressure range R_{pl}, by a linear gradient. Other modelling studies such as Swan et al. (2012) have presented detailed models of compliance and pressure heterogeneity, based on complex solid mechanics calculations. Due to computational constraints, a model of this complexity was deemed infeasible.

Considering a unidirectional gravitational field, in one of the the three primary axes, we define a linear gradient factor f, as

$$f(z) = 1 - \frac{z - \bar{z}}{z_{\max} - z_{\min}} g_{\text{strength}},$$

where g_{strength} is the gradient strength, z is the vertical height in the gravitational axis, and $\bar{z}, z_{\max}$ and $z_{\min}$ are the average, maximum and minimum heights of the terminal bronchiole distal ends. This factor is used to disperse values of R_{pl} linearly, while

maintaining the desired centre point. For an acinar unit i, at height z (relative to the axis gravity is acting in), the pleural pressure at time t is given by

$$P_{pl,i} = A_{pl} + R_{pl} \sin\left(\frac{2\pi t}{T}\right) f(z).$$

By changing which axis this gradient is enforced in, and which direction is positive, ventilation can be simulated in all of the primary body positions (orthostatic, supine, prone, left-lateral and right-lateral). Consistent with studies in the literature (Kaneko et al., 1966; Musch et al., 2002), a gravitational gradient strength of 1.5%/cm was chosen.

2.2.2 Numerical implementation

The total ventilation model forms a non-linear differential algebraic equation (DAE) system, comprised of

$$\Delta P = R(Q)Q, \qquad \text{for each branch,} \tag{2.3}$$

$$Q_{\text{upper}} = \sum Q_{\text{lower}}, \qquad \text{for each bifurcation,} \tag{2.4}$$

$$\frac{d}{dt}V_{\text{acin},i} = Q_i, \qquad \text{for each terminal branch,} \tag{2.5}$$

$$P_{T,i} - P_{pl}(t) = \frac{1}{\mathbb{C}_i}V_{\text{acin},i}, \qquad \text{for each terminal branch.} \tag{2.6}$$

To implement this system numerically, a backward Euler discretisation (Smith, 1985) was applied to Equation (2.5), such that

$$V_{\text{acin},i}^{n+1} - dtQ_i^{n+1} = V_{\text{acin},i}^{n},$$

where the notation Q^n is used to denote the value of variable Q at timestep n, dt is the time step size, and all other variables in Equations (2.3)-(2.6) were taken at timestep $n+1$.

Applying this discretisation to Equations (2.3)-(2.6), the resulting system can be written in vector notation as

$$\mathbf{F}(\mathbf{x}) = \mathbf{0} \tag{2.7}$$

where $\mathbf{x} = (\mathbf{P}^{n+1}, \mathbf{Q}^{n+1}, \mathbf{V}_{\text{acin}}^{n+1})^T$, and $\mathbf{P}^{n+1}, \mathbf{Q}^{n+1}$, and $\mathbf{V}_{\text{acin}}^{n+1}$ are vectors comprising all the P, Q and V_{acin} variables respectively. We solve this system using a standard vector Newton Method (Kelley, 2003), of the form

$$\mathbf{dx} = -\mathcal{J}^{-1}\mathbf{F}(\mathbf{x}), \tag{2.8}$$

$$\mathbf{x} = \mathbf{x} + \mathbf{dx}, \tag{2.9}$$

where $\mathcal{J}$ is the Jacobian of $\mathbf{F}$. To solve Equation (2.7), we iteratively update $\mathbf{x}$ using Equation (2.9) until $||\mathbf{F}(\mathbf{x})||_2$ and $||\mathbf{dx}||_2$ both fall below the desired tolerance *tol* (set as 10^{-6} unless otherwise noted). The matrix system in Equation (2.8) was solved using LU factorisation with approximate minimum degree reordering applied to the columns (see Figure 2.3). Iterative solution algorithms such as *BiCGStab* and *GMRES* were investigated (with reordering, and preconditioning), however were seen to be less efficient than reordered LU factorisation.

Noting the form of Equations (2.3)-(2.6), we can see that the majority of terms in the Jacobian are constant. The only temporally changing component of the Jacobian

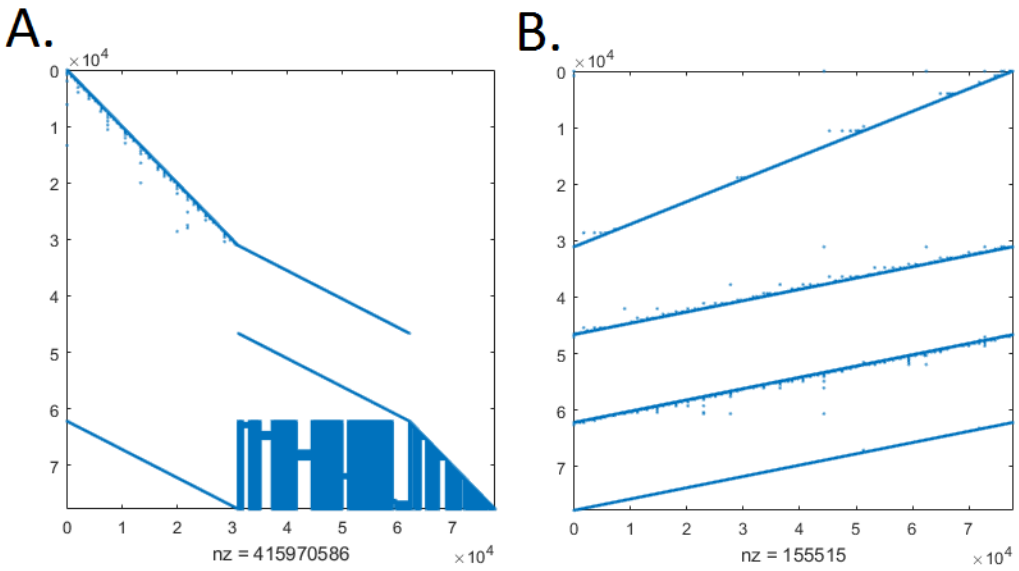

Figure 2.3: Spy plots of Jacobian LU factors with and without AMD reordering. The original factorisation (A) produces 2500 times more nonzeros than the reordered factorisation (B). This was created through simulation of ventilation in one of the healthy structures from the Bordas set.

derives from the flow resistance, and (specifically for the chosen resistance function given in Equation (2.2)) this contribution is given as

$$\frac{d}{d\mathbf{Q}}(-R(\mathbf{Q})\mathbf{Q}) = \text{diag}\left(-\frac{3}{2}R(\mathbf{Q})\right).$$

Thus updating the Jacobian throughout the iterative process is efficient, requiring only the calculation of $R(\mathbf{Q})$ once per iteration. Solutions were attempted with infrequent Jacobian updating, but this was seen to increase runtime, suggesting that the convergence improvements gained by regular update of the Jacobian offset the inefficiency of the update procedure.

It should be noted that in the numerical scheme, pleural pressure parameters A_{pl} and R_{pl} must be calculated iteratively. Initially A_{pl} and R_{pl} are set as -1500 Pa and 500 Pa respectively (typical values for a healthy male). However, to enforce

the desired FRC and breathing depth V_{depth}, they are adaptively chosen for each simulation. Initially, total lung volume (V) is calculated over an entire breathing cycle using the initial A_{pl} and R_{pl}. A_{pl} is then updated according to the ratio between the desired mean lung volume (FRC + $\frac{1}{2}V_{\text{depth}}$) and calculated mean lung volume. Similarly, R_{pl} is updated according to the ratio between desired breathing depth and actual breathing depth. This leads to the update formulae:

$$A_{pl} = \frac{\text{FRC} + \frac{1}{2}V_{\text{depth}}}{\frac{1}{2}(V_{\min} + V_{\max})} A_{pl},$$
$$R_{pl} = \frac{V_{\text{depth}}}{V_{\max} - V_{\min}} R_{pl},$$

where $V_{\min}$ and $V_{\max}$ are the minimum and maximum values of V in the calculated breathing cycle. A_{pl} and R_{pl} are updated until the difference between desired and actual breathing depth, and desired and actual mean lung volume are both below a given tolerance. Within this thesis, the tolerance is set as 5% unless otherwise noted.

A typical flow and volume profile, simulated on a healthy subject from the Bordas set, is given in Figure 2.4.

2.2.3 Error convergence

Due to the complexity of the ventilation model and its domain, performing error analysis against an analytical solution is infeasible. Instead, relative error of a solution profile $\mathbf{x}$ is calculated relative to a fine mesh solution ($\mathbf{x}_{\text{fine}}$) such that

$$\text{err} = \max \left| \frac{\mathbf{x} - \mathbf{x}_{\text{fine}}}{\mathbf{x}_{\text{fine}}} \right|. \tag{2.10}$$

Note that to avoid catastrophic cancellation, solution error is only calculated at points where the elements of $\mathbf{x}_{\text{fine}}$ are sufficiently different from 0. For the ventilation model,

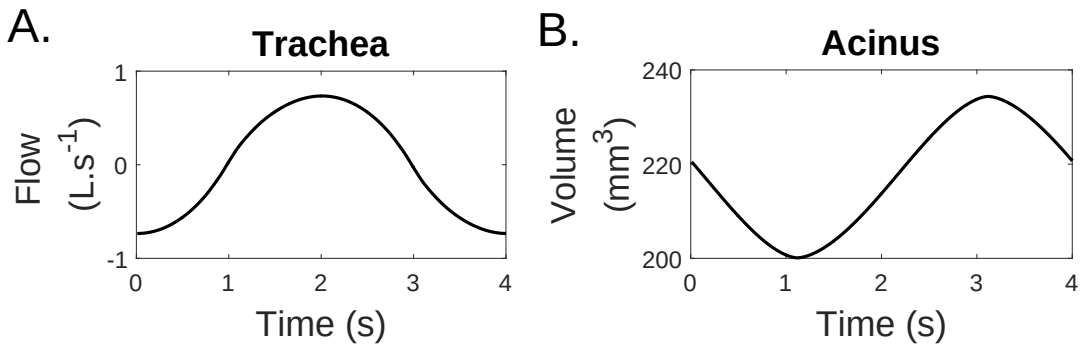

Figure 2.4: Typical ventilation model profiles. A profile of flow rate in the trachea (A) and volume of a single acinar region (B) over one breathing cycle are given. Note that volume changes are offset from flow rates, though not necessarily by exactly 1 second. Values were simulated on a healthy subject from the Bordas set.

we calculate the fine mesh solution using a step size of $dt = 0.001$ and measure the error against this solution, using $dt = 0.5$, 0.1, 0.02, 0.01, 0.008, 0.005, and 0.002. Convergence of ventilation over 12 seconds of breathing, in both a healthy and an asthmatic structure (from the Bordas set) can be seen in Figure 2.5. For these simulations, the gravitational gradient was applied to the pleural pressure range in the dorso-ventral axis (saggital plane), corresponding to the supine position. As the figure shows, error converges smoothly as dt is decreased. Based on the results in this figure, an optimal step size of 0.01 was chosen, which was seen to produce less than 1% error comparative to the fine mesh solution.

2.3 MRI model

The ventilation model described in Section 2.2 allows for the calculation of acinar region volumes throughout the breathing cycle, for a given breathing depth, and FRC. This information can then be used to approximate clinical indices derived from a lung MRI.

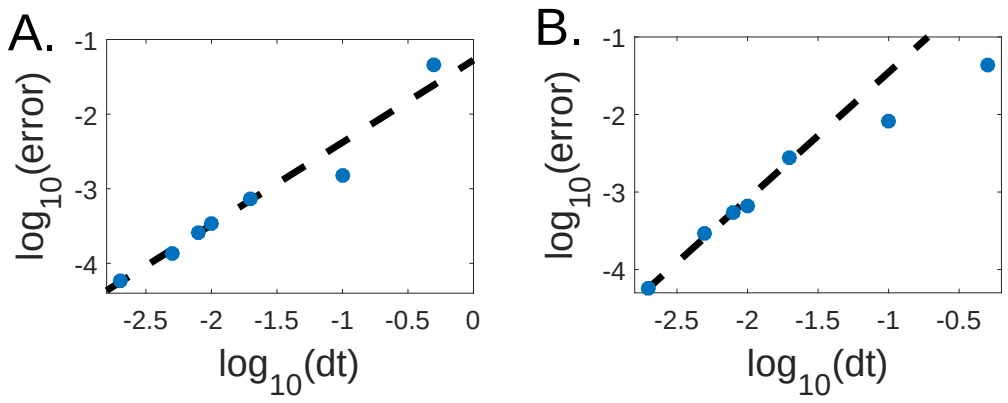

Figure 2.5: Error convergence of the ventilation model. Convergence is shown for a healthy structure (A) and an asthmatic structure (B) from the Bordas set.

Alongside visual analysis and classification of images, information is gained from MR images through the calculation of ventilation indices. Within the literature there are many competing standards for indices. However, they can broadly be classified as either global or local. To approximate these two classes of indices, we first define the ventilation ratio (Horn et al., 2014) of a region as

$$r = \frac{V_f}{V_f + V_r},$$

where V_f is the fresh gas entering a region over an inhalation, and V_r is the residual gas at the end of exhalation. Within our model, we can directly calculate an r value for each acinar region, based on volume changes over the breathing cycle. We can also do this for larger regions, by summation of acinar regions, or measurement of flow through branches at higher Strahler orders.

To approximate an MR image, we overlay a 3D grid onto the lung structure, and take the mean r value of all acinar regions within each voxel (grid rectangular prism). The global ventilation heterogeneity measure (σ_r^2) is defined as the variance of the

total set of r voxel values. The local ventilation heterogeneity measure (σ^2_{local}) is defined as the variance relative to a local mean, such that

$$\sigma^2_{\text{local}} = \frac{1}{N}\sum_{i=1}^{N}(r_i - r_{i,\text{local}})^2, \tag{2.11}$$

where $r_{i,\text{local}}$ is the mean r value of all voxels sharing an edge with voxel i, and N is the total number of voxels.

For results within this thesis, we have applied a grid mesh consisting of $80 \times 80 \times 80$ rectangular prisms leading to an average voxel resolution of 4 x 2.5 x 3.5 mm, consistent with clinical MRI studies in the literature (Horn et al., 2014; Qing et al., 2014; Stavngaard et al., 2005). In Chapter 3 we present a brief analysis of how grid size may influence σ_r and σ_{local}. Analysis of solutions of the MRI model are presented in later chapters. However, in Figure 2.6 we visualise a 2D slice of r values, created from simulation of ventilation in the baseline structure (without a gravitational gradient).

2.4 Gas convection model

The design and implementation of a ventilation model allows for the analysis of flow profiles in the lungs, under a variety of different conditions. However, to simulate pulmonary function tests such as the inert-gas washout, a model for gas transport throughout the airways is also needed. In this section we detail a model for simulating convective transport of gas throughout the lungs.

Similar to the ventilation model, we first define the domain of the convective gas transport model as the set of all 1D branches in the lung, and the associated spherical acinar regions. To model the concentration distribution $C(x,t)$, throughout the lungs,

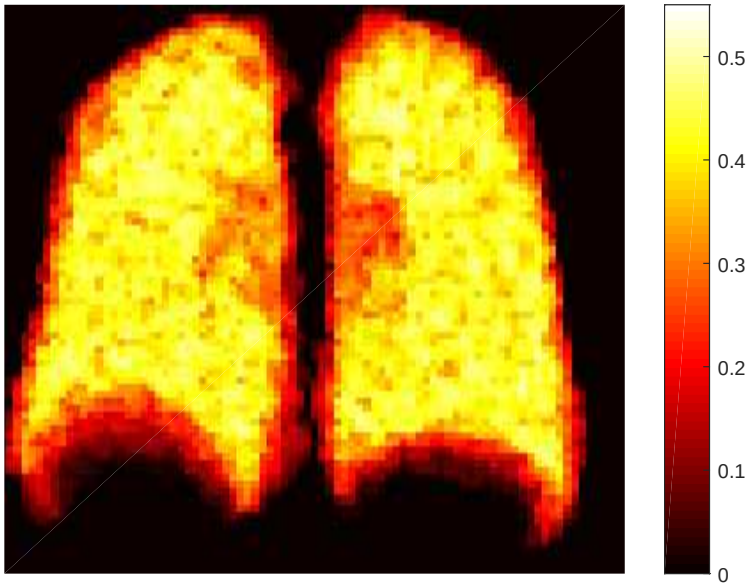

Figure 2.6: 2D slice of a simulated set of ventilation ratios. This slice was taken through the centre of the lung, in the coronal plane. Brighter colours indicate higher ventilation. This simulation was generated from the baseline structure of the Bordas set.

we first discretise each branch into a series of nodes, each with a corresponding concentration C_i, and place a node at the centre of each acinus, with concentration C_{acin}. A 2D schematic of this domain is given in Figure 2.7.

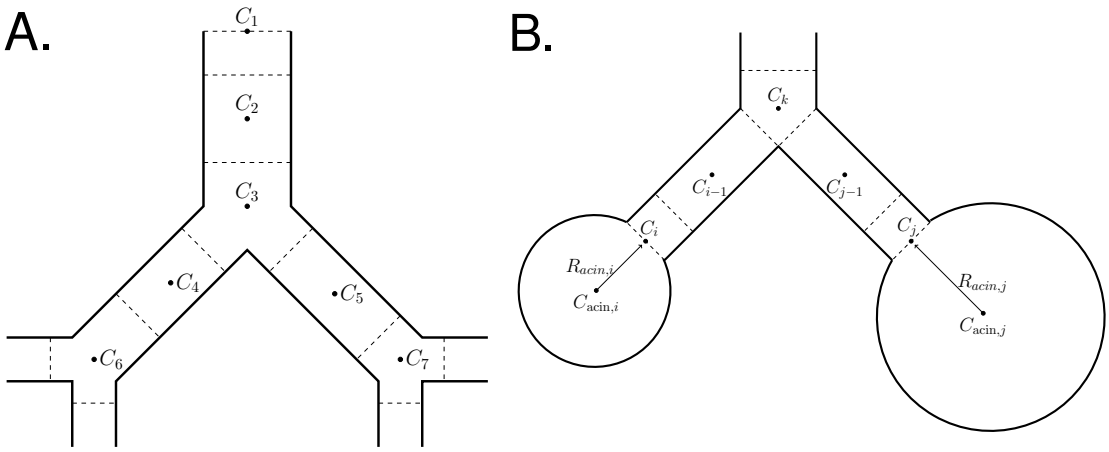

Figure 2.7: Diagram of convection model domain. An idealised 2D cross-section of the problem domain, showing concentration nodes and finite volume boundaries in the branches (A), and the acinar regions (B).

Considering this domain, we model gas transport using a 1D convection partial differential equation (PDE):

$$\frac{\partial C}{\partial t} = -u\frac{\partial C}{\partial x}, \tag{2.12}$$

where u the air velocity, x is the spatial location, and t is time.

To apply this model to the entire airway structure, we treat each branch as a 1D pipe, with connections at each bifurcation. Due to the fact that the ventilation model maintains conservation of flow at bifurcations, no implicit conservation constraints are needed at each bifurcation.

2.4.1 Numerical implementation

To implement the convection model numerically we use a finite difference method. Over each branch, spatial derivatives are approximated by an upwinding and downwinding scheme, meaning for a node i

$$\frac{\partial C_i}{\partial x} \approx -\frac{1}{\Delta x}(u_i C_i - u_{i-1} C_{i-1}),$$

when flow is positive (from the trachea towards the alveoli), and

$$\frac{\partial C_i}{\partial x} \approx \frac{1}{\Delta x}(u_i C_i - \sum_{j \in \text{dist}_i} u_j C_j),$$

when flow is negative, where dist_i is the set of all nodes immediately distal to node i, and Δx is the distance between the two relevant nodes.

For the temporal derivative, we use a Backward Euler discretisation, with timestep size dt, such that during positive flow at node i, Equation (2.12) becomes:

$$C_i^{n+1} - C_i^n = -\frac{dt}{\Delta x}(u_i^{n+1} C_i^{n+1} - u_{i-1}^{n+1} C_{i-1}^{n+1}),$$

where C_i^n denotes the value of C_i at timestep n, and dt is the time step size.

Applying the appropriate up and downwinding schemes, alongside the backward Euler discretisation to all nodes in the domain, leads to an equation system (in matrix form)

$$\mathbf{A}\mathbf{C}^{n+1} = \mathbf{C}^n, \tag{2.13}$$

where $\mathbf{C}$ is the collection of C_i values, $\mathbf{A}$ is the coefficient matrix, and the notation $\mathbf{C}^n$ denotes the value of $\mathbf{C}$ at time t_n ($t = 0, t_1, \ldots, t_{\text{end}}$).

2.4.2 Boundary conditions

To close the model, we must specify boundary conditions for C at the trachea and at the distal end of each terminal bronchiole. Considering that we wish to simulate the multiple-breath washout, we design our boundary conditions specifically for this case. This test involves the wash-in and washout of a tracer gas (e.g. sulfur hexaflouride: SF_6), carried in air.

To simulate the wash-in and washout phases of the PFT, we have two separate boundary conditions at the trachea. At the start of the wash-in phase we apply an initial condition of no gas concentration $C(x, 0) = 0$. During inhalation in this phase, a tracer gas of a constant concentration C_0 enters the trachea proportional to the flow rate, meaning

$$\frac{\partial C}{\partial \mathbf{n}} = -u_1 C_0, \tag{2.14}$$

where u_1 is the flow rate in the tracheal branch, and $\mathbf{n}$ is an outward normal vector.

During exhalation, gas leaves the trachea proportional to the tracheal velocity, meaning

$$\frac{\partial C}{\partial \mathbf{n}} = -u_1 C_1, \tag{2.15}$$

where C_1 is the gas concentration at the most proximal tracheal node.

During the washout phase we have the same tracheal boundary condition during exhalation, but during inhalation, we have the Neumann condition

$$\frac{\partial C}{\partial \mathbf{n}} = 0. \tag{2.16}$$

Within the model, each terminal bronchiole is connected at an acinar region i, with corresponding volume $V_{\text{acin},i}$, and concentration $C_{\text{acin},i}$. For each terminal bronchiole node i, with associated acinar region j, we have the boundary condition

$$\frac{\partial C}{\partial \mathbf{n}} = u_i C_i,$$

when flow is positive, and the condition

$$\frac{\partial C}{\partial \mathbf{n}} = u_i C_{\text{acin},j},$$

when flow is negative.

To close the system, acinar concentration changes are driven by the equation

$$\frac{dV_{\text{acin},j} C_{\text{acin},j}}{dt} = Q_i C_i,$$

when Q_i is positive, and

$$\frac{dC_{\text{acin},j}}{dt} = 0,$$

when Q_i is negative.

To maintain linearity of the overall equation system, boundary conditions are first applied using $\mathbf{C}^n_{\text{acin}}$, with $\mathbf{C}^n_{\text{acin}}$ then updated using the forward Euler discretisation:

$$C^{n+1}_{\text{acin},j} = \frac{V^n_{\text{acin},j} C^n_{\text{acin,j}} + dt Q^n_i C^n_i}{V^{n+1}_{\text{acin},i}},$$

when Q^n_i is positive, and

$$C^{n+1}_{\text{acin},j} = C^n_{\text{acin},i},$$

when Q^n_i is negative.

Similarly to the ventilation model, the matrix system in Equation (2.13) is solved using LU factorisation with approximate minimum degree reordering applied to the columns. Iterative solution algorithms such as *BiCGStab* and *GMRES* were investigated (with reordering, and preconditioning), however were seen to be less efficient than reordered LU factorisation.

An example solution profile from the convection model (at the trachea) is given in Figure 2.8. This profile was generated through simulating an 4% SF_6 washout on a healthy subject from the Bordas set, in an orthostatic position.

2.4.3 Error convergence

Similar to the ventilation model, error convergence of the convection model is performed through comparison to a fine mesh solution, using the formula in Equation 2.10. A series of solutions were calculated with increasing numbers of nodes along each branch, starting with 1 node (excluding bifurcations), then 3, 5, 7, 9, 13, and 15, with corresponding dt values $0.5, 0.1, 0.02, 0.01, 0.008, 0.005$, and 0.002 (note that the same dt value was first used to calculate ventilation). The fine mesh solution was taken as

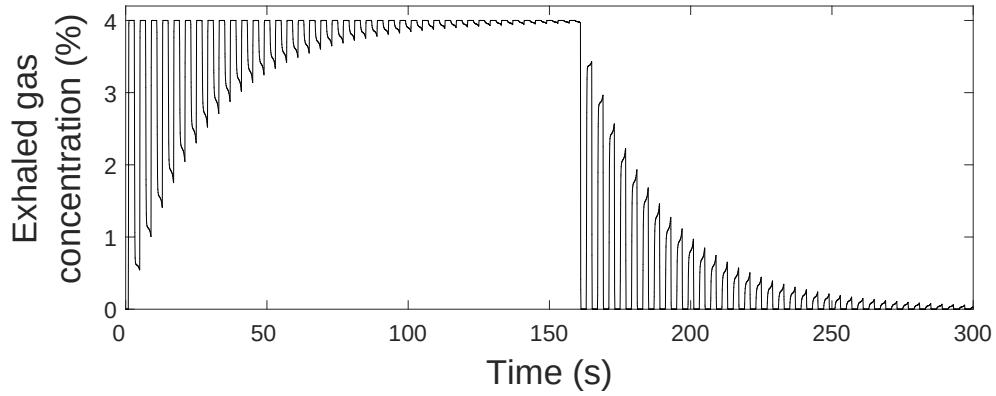

Figure 2.8: Example washout profile using the convection model. The exhaled gas concentration at the trachea is given over the wash-in phase (up to 160s) and washout phase (160-300s). The profile was generated through simulating a 4% SF_6 washout on a healthy subject from the Bordas set, in an orthostatic position.

the exhaled gas concentration curve over first and tenth washout breaths, calculated using 17 branch nodes, and $dt = 0.001$. The error of the washout curve was measured instead of the error of the actual concentration distribution, as test indices are directly calculated from this curve. In Figure 2.9, we show the convergence of the convection model in a healthy and asthmatic structure (from the Bordas set), in the orthostatic position. In each case error was calculated following the simulation of an SF_6 washout over 160 seconds (following a 120s wash-in). As the figure shows, error converges smoothly under spatial and temporal refinement. Based on these results, we perform simulations in this thesis using $dt = 0.01$ which produced less than a 1% error, comparative to the fine mesh solution.

2.4.4 Limitations of the convection model

This convection model allows for the simulation of gas transport throughout the conducting zone of the lungs. However, it does not account for the diffusion of a tracer

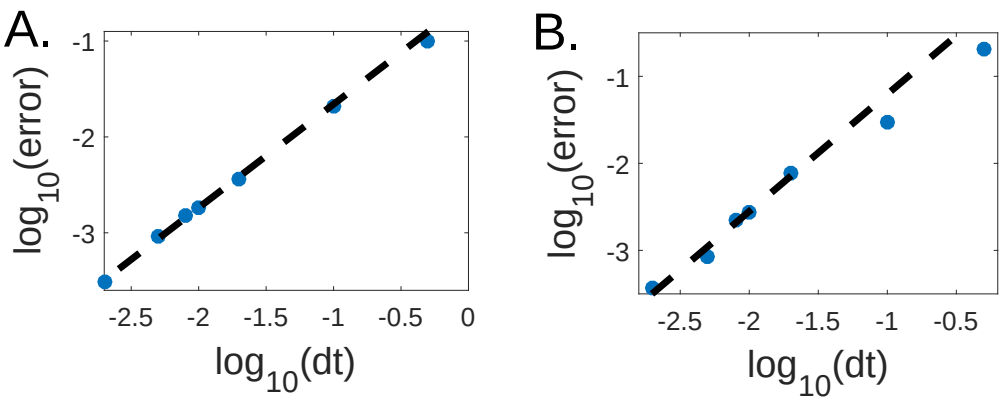

Figure 2.9: Error convergence of the convection model. Error convergence is shown for a healthy structure (A) and an asthmatic structure (B) from the Bordas set.

gas throughout the lungs. This has the advantage of making implementation and numerical simulation of the model much simpler.

Initial work within this thesis (Chapters 3 and 4) was performed using the simpler convection model. However, to allow for more clear comparison to clinical data, in later work (Chapter 6 onwards) the model was updated to incorporate the effects of diffusion. In the next section we outline the convection-diffusion model, while in Chapter 6 we give a brief comparison of MBW simulations with and without diffusion.

2.5 Gas convection-diffusion model

Due to the limitations of a convection only model, later results in the thesis (Chapter 6 onwards) are generated using a convection-diffusion model. Within this section we outline the updated model.

The incorporation of diffusive effects into the transport model was performed using a model first proposed by Paiva (1973), which is a convection-diffusion PDE, adapted

to account for diffusion in a bifurcating domain. This model is given as

$$\frac{\partial C}{\partial t} = D\frac{\partial^2 C}{\partial x^2} + \frac{D}{A}\frac{\partial A}{\partial x}\frac{\partial C}{\partial x} - u\frac{\partial C}{\partial x},$$

where D is the diffusion coefficient of the tracer gas in air, and A is the cross-sectional area of the branch.

Similarly to the convection model, we discretise the domain into a series of nodes, with corresponding concentration values C_i. Again, multiple nodes are placed on each branch, and a single node at the proximal end of the trachea, and at the distal end of each terminal bronchiole. However, instead of placing a node at each bifurcation point, the bifurcation nodes are placed slightly proximal to the bifurcation, with a schematic of the domain given in Figure 2.10.

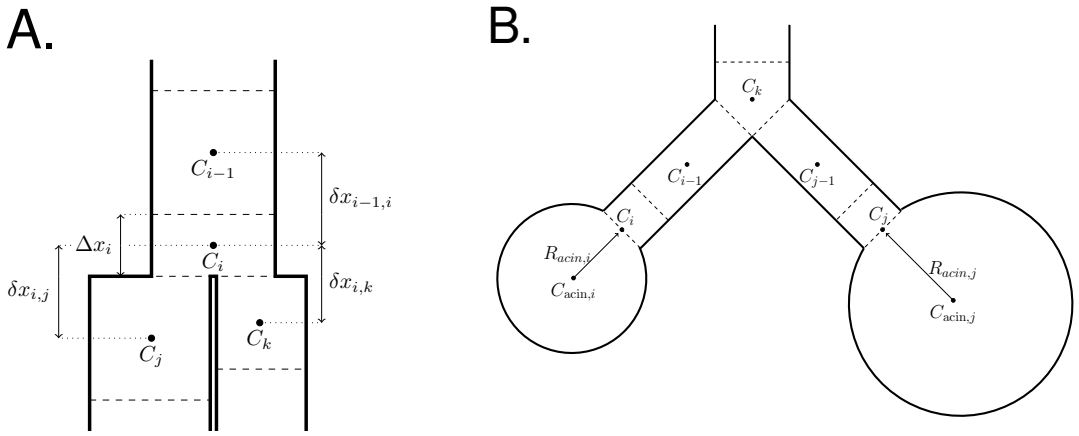

Figure 2.10: Diagram of convection-diffusion model domain. An idealised 2D cross-section of the problem domain for the convection-diffusion model, showing concentration nodes and finite difference boundaries in the branches (A), and the acinar regions (B).

2.5.1 Numerical implementation

To implement the convection-diffusion model numerically, we use a finite difference discretisation. Considering the notation marked in Figure 2.10, for nodes centred at a

bifurcation, as outlined by Dutrieue et al. (2000), the finite difference scheme is

$$\frac{dC_i}{dt} = \frac{D}{\Delta x_i}\left(\frac{1}{A_j + A_k}\left\{\frac{[C_j - C_i]A_j}{\delta x_{i,j}} + \frac{[C_k - C_i]A_k}{\delta x_{i,k}}\right\} - \frac{C_i - C_{i-1}}{\delta x_{i-1,i}}\right) + \frac{D}{2A_i}\left(\frac{\left\{A_j - A_i\frac{A_j}{A_j+A_k}\right\}[C_j - C_i]}{\delta x_{i,j}^2} + \frac{\left\{A_k - A_i\frac{A_k}{A_j+A_k}\right\}[C_k - C_i]}{\delta x_{i,k}^2}\right) + \begin{cases} \dfrac{u_i C_i - u_{i-1}C_{i-1}}{\Delta x_i}, & \text{during positive flow} \\ \dfrac{u_j C_j + u_k C_k - u_i C_i}{\Delta x_i}, & \text{during negative flow.} \end{cases}$$

For nodes not at a bifurcation, we note that $\partial A/\partial x = 0$, as the radius of each branch is assumed constant. For these nodes, we use an averaging approximation for the diffusive term, meaning during positive flow

$$\frac{dC_i}{dt} = \frac{D}{\Delta x^2}(C_{i+1} + C_{i-1} - 2C_i) - \frac{u}{\Delta x}(C_i - C_{i-1}),$$

and during negative flow

$$\frac{dC_i}{dt} = \frac{D}{\Delta x^2}(C_{i+1} + C_{i-1} - 2C_i) - \frac{u}{\Delta x}(C_{i+1} - C_i),$$

where Δx is the spacing between adjacent nodes on the branch.

Similar to the convection model, a backward Euler discretisation with time step size dt is applied, leading to a system of equivalent form to that in Equation (2.13).

2.5.2 Boundary conditions

The boundary conditions for the convection-diffusion model are similar to those outlined previously for the convection model. Since at the trachea, the system is convection dominated, the effects of diffusion are ignored, and the same flow conditions are applied as in Equations (2.14)-(2.16).

However, at the terminal bronchioles, the system behaviour is no longer dominated by convection, and thus the effects of diffusion must be accounted for. To account for the diffusion between a terminal bronchiole node i, and associated acinar region j, we first define the radial distance $R_{\text{acin},j}$ from node i to the centre of region j as the radius of the corresponding spherical volume, such that

$$R_{\text{acin},j} = \left(\frac{3}{4\pi} V_{\text{acin},j}\right)^{1/3}.$$

The boundary condition at the terminal bronchiole is then

$$\frac{\partial C}{\partial \mathbf{n}} = -u_i C_i + D\frac{C_{\text{acin},j} - C_i}{R_{\text{acin},j}},$$

when u_i is positive, and

$$\frac{\partial C}{\partial \mathbf{n}} = -u_i C_{\text{acin},j} + D\frac{C_{\text{acin},j} - C_i}{R_{\text{acin},j}},$$

when u_i is negative.

Gas concentrations in the acinar regions are driven by the equation

$$\frac{dV_{\text{acin},j}C_{\text{acin},j}}{dt} = Q_i C_i - DA_i\frac{C_{\text{acin},j} - C_i}{R_{\text{acin},j}},$$

when Q_i is positive and

$$\frac{dV_{\text{acin},j}C_{\text{acin},j}}{dt} = -DA_i\frac{C_{\text{acin},j} - C_i}{R_{\text{acin},j}},$$

when Q_i is negative.

Similar to the convection model, boundary conditions at each step are first calculated using $\mathbf{C}^n_{\text{acin}}$, and then $\mathbf{C}_{\text{acin}}$ is updated using a forward Euler discretisation.

The resulting matrix system for this model was solved using LU factorisation with approximate minimum degree reordering applied to the columns.

An example solution profile from the convection-diffusion model (at the trachea) is given in Figure 2.11. This profile was generated by simulation of a 4% SF_6 washout on a healthy subject from the Bordas set, in an orthostatic position. It can be noted that this washout profile looks incredibly similar to the convection model profile in Figure 2.8. This is to be expected in a healthy subject, where convection is a much more dominant process. A detailed comparison of results from the convection and convection-diffusion washout models is given in Chapter 6.

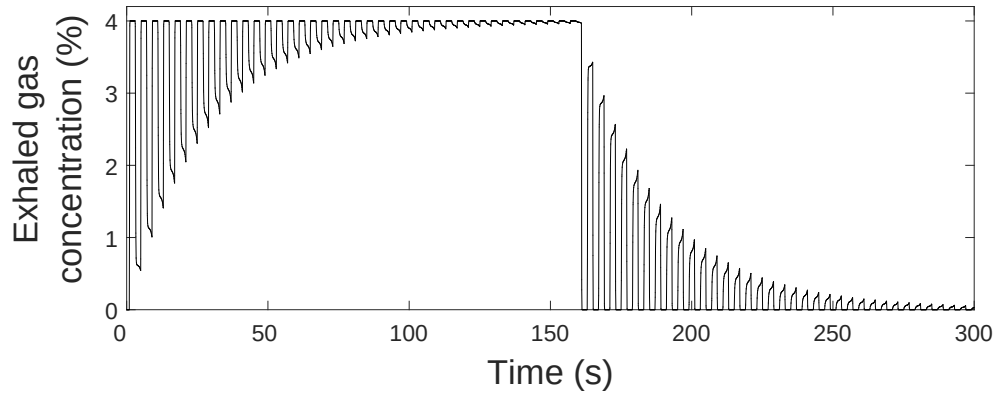

Figure 2.11: Example washout profile using the convection-diffusion model. The exhaled concentration at the trachea is given over the wash-in phase (up to 160s) and washout phase (160-300s). The profile was generated by simulation a 4% SF_6 washout on a healthy subject from the Bordas set.

2.5.3 Error convergence

As with the convection and ventilation models, error convergence of the convection-diffusion model is calculated relative to a fine mesh solution, using Equation (2.10). Solutions were calculated with (excluding bifurcations) 1, 3, 5, 7, 9, 13 and 15 nodes on

each branch, with corresponding dt values $0.1, 0.05, 0.02, 0.01, 0.008, 0.005$, and 0.002. Similar to the convection model, the fine mesh solution was taken as the exhaled gas concentration curve over the first and tenth washout breaths, using 17 branch nodes, and $dt = 0.001$. In Figure 2.12, we show the convergence of the convection-diffusion model in the baseline structure and in an asthmatic structure, in the orthostatic position. Similar to the convection model, error was calculated after simulation of a 160s SF_6 washout, following a 120s wash-in. Based on the results in Figures 2.9 and 2.12, we perform simulations of the convection-diffusion model in this thesis using $dt = 0.01$ which produced less than a 1% error, comparative to the fine mesh solution.

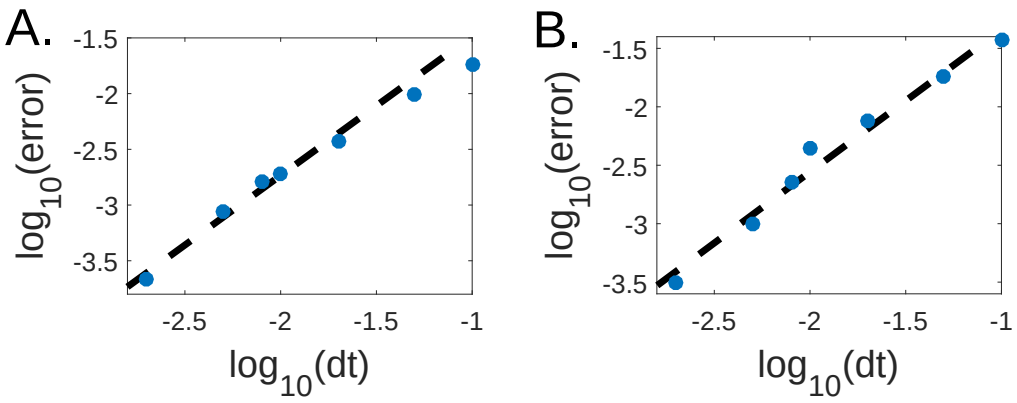

Figure 2.12: Error convergence of the convection-diffusion model. Error convergence is given for a healthy structure (A) and an asthmatic structure (B) from the Bordas set.

2.6 Lung impedance model

The final model presented within this chapter is one for calculation of lung impedance under oscillations applied at different frequencies, analogous to the FOT and IOS. Unlike the ventilation and gas transport models, lung impedance is calculated within frequency space, not temporal space. These calculations are performed by assuming an

electrical circuit analagous structure, with each branch having an associated impedance, due to oscillatory flow, and airway branches being connected in series and parallel.

Calculations of the flow-driven impedance in each airway branch are based on approximations from the work of Benade (1968) and Thurston (1952). By solving the 1D wave equation in its associated Fourier space, the impedance Z_j, experienced by a branch j, caused by the propagation of a frequency f, can be approximated as

$$Z_j = R_j + iX_j = \left(i\frac{\omega\rho_a l}{\pi r_j^2}\right)(1 - F_v e^{i\phi r_j})^{-1}, \tag{2.17}$$

where R_j and X_j are the branch resistance and reactance, ρ_a is the air density, $\omega = 2\pi f$, l and r are the branch length and radius respectively, and $i = \sqrt{-1}$. The exponential contribution is defined as

$$F_v e^{i\phi r} = \frac{2}{r_v\sqrt{-i}}\frac{J_1(r_v\sqrt{-i})}{J_0(r_v\sqrt{-i})}, \qquad r_v = \left(\frac{\omega\rho_a}{\mu_a}\right)^{\frac{1}{2}} r$$

where J_0 and J_1 are the zeroth and first bessel functions, μ_a is the air viscosity, and r_v is the boundary layer thickness.

To simulate impedance of the lung, Equation (2.17) is first used to calculate impedance of each individual branch in the network. Total lung impedance can then be calculated by adding impedances in series and parallel, analogous to calculations in an electrical circuit, as illustrated in Figure 2.13. As an example, for a parent branch i, with two daughter branches j and k, the effective impedance ($Z_{i,\text{effective}}$) is calculated as

$$Z_{i,\text{effective}} = Z_i + \left(\frac{1}{Z_{j,\text{effective}}} + \frac{1}{Z_{k,\text{effective}}}\right)^{-1},$$

where $Z_{j,\text{effective}}$ and $Z_{k,\text{effective}}$ are the effective impedances of branches j and k.

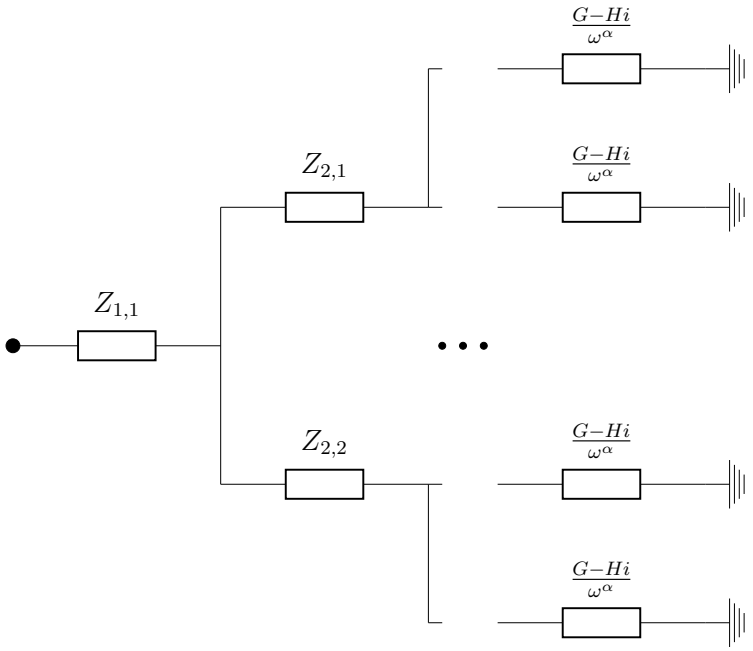

Figure 2.13: Diagram of lung impedance circuit. Each branch is treated as a component in an electrical circuit, with an acinar impedance unit connected to each terminal bronchiole.

2.6.1 Boundary conditions

At the end of each terminal bronchiole, a constant-phase viscoelastic model (Kaczka et al., 2007; Lutchen and Gillis, 1997) is used to account for acinar contributions to impedance (as illustrated in Figure 2.13) such that

$$Z_{\text{acin}} = \frac{G - iH}{N\omega^\alpha},$$

where G and H are coefficients for tissue damping and elastance respectively, N is the number of terminal bronchioles and

$$\alpha = \frac{2}{\pi}\tan^{-1}(H/G).$$

Typically, in modelling studies the values of G and H are inferred from statistical fitting to clinical data. To reduce reliance on statistical fitting, for our model we have

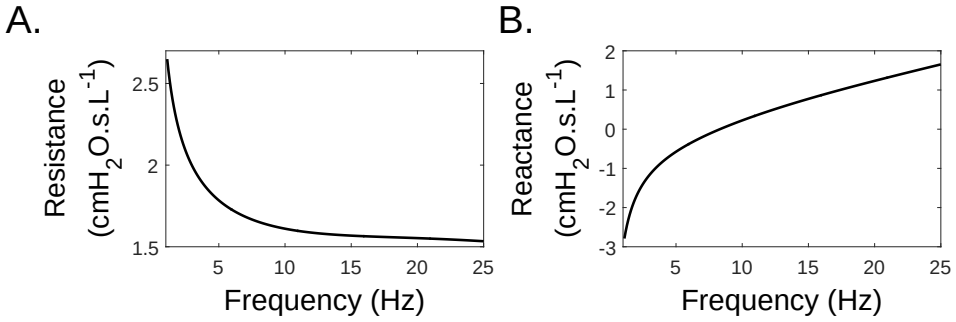

Figure 2.14: Example impedance profile for a healthy subject. The resistance (A) and reactance (B) profiles were simulated on a healthy subject from the Bordas set.

instead taken standard values of G and H from the literature (Kaczka et al., 1997) as 3.75 and 12.5 $\mathrm{cmH_2O.L^{-1}}$ respectively.

The inclusion of the constant-phase boundary conditions allows for closure of the model. An example impedance solution profile, simulated from a healthy subject in the Bordas set, is given in Figure 2.14.

2.7 Summary

Within this chapter we have presented the development and numerical implementation of a variety of different models for simulating physical processes within the lungs. In particular, these models allow for simulation of ventilation, MR imaging, the multiple-breath washout and the FOT and IOS. These models underpin the entirety of this thesis, and will be used to simulate and analyse PFTs throughout the remaining chapters.

3

Exploratory analysis of the washout and imaging models

In the previous chapter, a series of models for simulating ventilation, and the inert-gas washout were developed and implemented. Within this chapter, we use these models to perform an exploratory analysis of the response of multiple-breath washout and imaging derived indices to bronchoconstriction in the conducting zone.

Work within this chapter is based on the study *Modelling responses of the inert-gas washout and MRI to bronchoconstriction*, published in *Respiratory Physiology & Neurobiology*.

3.1 Rationale

As explored in the literature review (see Chapter 1), the MBW is becoming increasingly common in clinical scenarios as a test for VH (Robinson et al., 2013). MBW indices such as s_{cond} and LCI have been repeatedly shown to correlate with clinician classifications of lung diseases such as cystic fibrosis (Aurora et al., 2004, 2005b; Horsley et al., 2008) and asthma (Gustafsson, 2007; Verbanck et al., 1999). However, the complexity of the indices, in particular of s_{cond}, has led to a lack of precision in understanding this response and exactly what drives it.

In the literature, attempts to improve this precision have been made by using computational modelling to understand test output sensitivities. This includes early modelling on idealised structures (Cruz et al., 1997; Verbanck and Paiva, 1990), and more recent studies involving patient-specific structures (Mitchell et al., 2012; Tawhai and Hunter, 2001). These studies have suggested sensitivity of MBW indices to bronchoconstriction, particularly in the small airways. However, there is still utility to more precise quantification of this relationship.

Alongside this, another approach that has been used recently to improve understanding of the MBW is comparison to imaging measurements. Some recent preliminary studies have investigated the relationship between MBW and MRI indices within the same patient groups (Capaldi et al., 2015; Horn et al., 2015; Horsley et al., 2014). Initial studies show promise, with correlations seen between certain MBW indices, and MRI indices. However, these correlations breakdown in certain regions,

with no justification given for significant outliers. Furthermore, to our knowledge no full studies in the literature have analysed this relationship in significant detail, or confirmed any preliminary results.

These recent results in the literature inspired the exploratory study outlined in this chapter. Within the chapter, we use computational modelling of the MBW and MRI to probe the response of indices from both tests to bronchoconstriction in the conducting zone. By analysing these responses both separately and comparatively, we provide more clarity of the nature of the response, and illustrate key differences between them. In particular, comparison of the MBW and MRI indices show that s_{cond} and LCI respond similarly to global MR indices, being particularly sensitive to disease severity. In contrast, the local MR indices appear to respond most sensitively to the degree of regionalisation, and depth of constriction. Alongside these results, we also give insights to the sensitivity of MRI indices to voxel size and imaging resolution.

3.2 Simulation protocol

Simulations of the MBW and MRI were performed on the baseline lung structure from the Bordas set under a variety of bronchoconstriction scenarios. The MBW was simulated using the convection model (outlined in Section 2.4) and the MRI was simulated using the ventilation model (outlined in Sections 2.2 and 2.3). SF_6 was chosen as the tracer gas for the washout, and all simulations were performed in an orthostatic position.

A Monte Carlo random sampling approach was used to select bronchoconstriction

scenarios for each simulation. Each scenario was characterised by a constriction severity, and a constriction depth. Constriction severity was the percentage that a chosen branch was constricted (had its radius reduced by). Strahler order was used as the marker of depth, with Strahler order 1 corresponding to terminal bronchioles, and 10 corresponding to primary lobar bronchi. Strahler order was used as the main depth marker instead of branch generation, as the mechanics of the washout model are more strongly driven by behaviour at the terminal bronchioles (and in the respiratory zone) than at the trachea. However, for comparison, some results were also generated using branch generation as the depth marker.

For each simulation, a constriction severity (0-99%) and constriction depth (Strahler order, 1-10) were uniformly randomly chosen, and a uniformly random 20% of branches at that depth were constricted to the chosen severity. Airway constriction was applied in a spatially coherent manner through adaptation of work by Leary et al. (2012), meaning constricted branches passed on some of their constriction to lower generations. The diameter of a branch j, with a parent branch i, that has undergone constriction, inherited part of this constriction, such that

$$d_j = \phi d_i \left(\frac{d_{\text{base},j}}{d_{\text{base},i}} \right) + (1 - \phi) d_{\text{base},j}, \tag{3.1}$$

where d_{base} denotes the diameter of the airway before constriction, and ϕ is known as the coherence parameter.

Simulations were applied using a coherence of 60%, meaning each child branch inherited 60% of the parent's constriction, each grandchild inherited 36% and so

on. The value $\phi = 0.6$ was chosen as it provided significant spatial coherence and smoothness of constriction, but has been shown to not significantly affect the variance of airway resistances (Leary et al., 2012).

Each simulation was performed until the mean exhaled gas concentration fell below 1/40th of the mean exhaled concentration of the first breath for three consecutive exhalations, and at least six turnovers had occurred. Following this, LCI, s_{cond}, σ_r and σ_{local} (for definitions see Sections 1.3.3 and 2.3) were calculated and a voxel map was generated.

In total 2000 simulations were performed, a much higher number than in similar studies in the literature (Mitchell et al., 2012).

3.3 Results

As a reference, we give the initial values for LCI, s_{cond}, σ_r and σ_{local} produced with the baseline structure under no constriction as 4.948 turnovers, 0.0012 L^{-1}, 0.00016, and 2.19×10^{-5} respectively.

For readability, units have been omitted from some figures, with s_{cond} always being presented in L^{-1}, LCI in turnovers, and σ_r and σ_{local} being dimensionless.

3.3.1 Responses to constriction severity

Within Figure 3.1 we see the response of the MBW and MRI indices to increasing constriction severity. Initially we see all four indices exhibit a positive response, however, as severity approaches 100% the MBW indices monotonically decrease back towards baseline. This is representative of the inability of the MBW to detect airway

closure, as seen previously in the literature (Mitchell et al., 2012). Considering the response of σ_{local}, we also see the index rise as constriction severity increases. However, the strength of this response is weaker and more variable than that of the other indices.

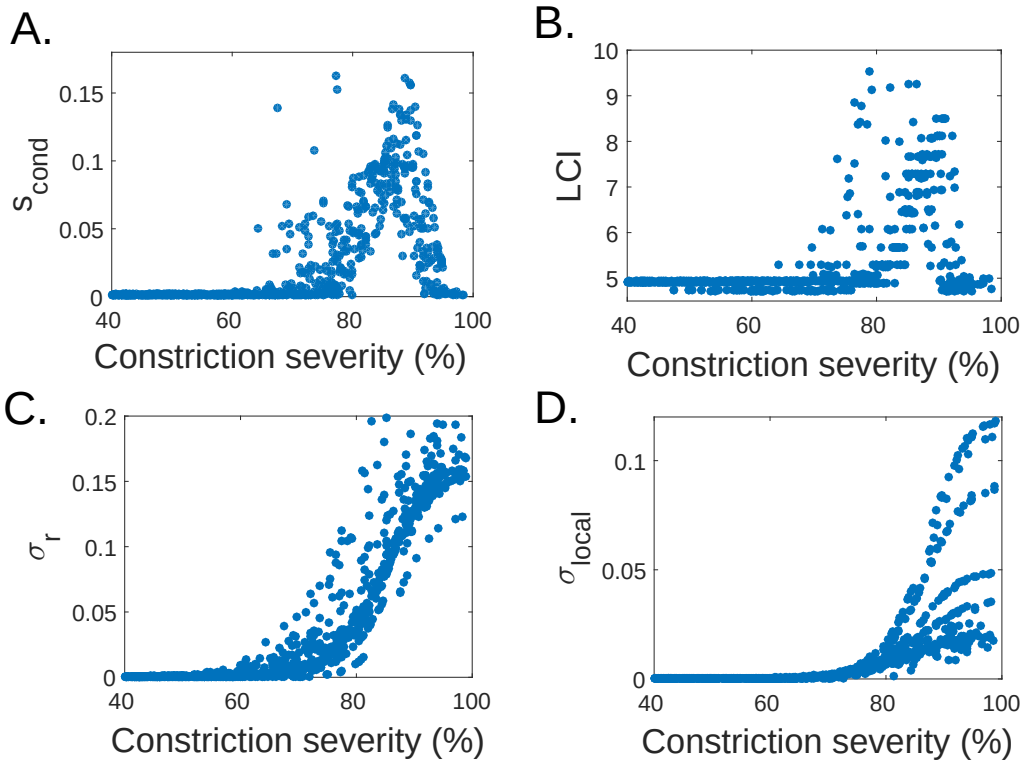

Figure 3.1: Variation of s_{cond} (A), LCI (B), σ_r (C), and σ_{local} (D) against constriction severity at various Strahler orders. Positive responses are initially seen from all four indices, followed by a decrease towards initial values in the MBW indices as the applied constriction severity approaches 100% (airway closure). The variance of σ_{local} is also seen to be significantly larger than that of the other indices, with distinct response bands.

Given the response of LCI, s_{cond}, and σ_r, we would expect all three indices to correlate strongly, until airway closure is approached. At this point, σ_r should continue to respond, while the MBW indices decrease back towards their initial values. This is illustrated in Figure 3.2, with results separated into three bands, corresponding to constriction severities: $< 80\%$, $80 - 90\%$, and $> 90\%$

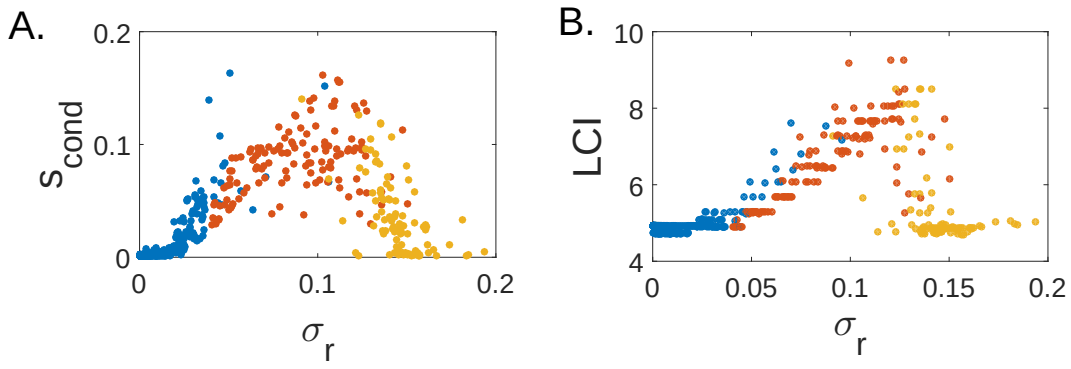

Figure 3.2: Correlation of σ_r with s_{cond} (A) and LCI (B) Data has been split into three groups based on constriction severity: less than 80% (blue), 80-90% (red) and greater than 90% (yellow). A strong positive correlation can be seen until constriction levels pass 80%, indicating different sensitivities to airway closure.

3.3.2 Responses to constriction depth

Figure 3.3 shows the change in the four indices as constriction depth becomes more proximal (Strahler order increases). To separate out the response from constriction severity, results have been grouped into six different severity bands: $< 50\%$, 50-75%, 75-85%, 85-90% 90-95%, 95-100%. Considering the MBW indices, no consistent response to constriction depth is noted, with the nature of the dependence changing across each severity band. As depth becomes more proximal, a small rise in variance of both indices is seen, however, there is no clear trend in mean values.

The MRI indices appear to respond to changes in depth in more consistent ways. The global index shows a consistent increase as depth becomes more proximal. The response is much weaker than the index's response to constriction severity, but is clearly present. As severity increases though, the response appears to become weaker, disappearing as closure is approached.

The local MRI index σ_{local}, appears to show the most consistent dependence on

constriction depth. For each severity band, σ_{local} peaks at Strahler order 2, then monotonically decreases as depth becomes proximal. The variance of this response decreases significantly as severity increases, forming very tight bands as airway closure is approached. This, alongside the results in Figure 3.1 suggests that local VH indices such as σ_{local} may more easily detect constriction depth than global indices. This is further illustrated in Figure 3.4 which gives a series of ventilation maps corresponding to high constriction severity at varying depths, with each producing similar σ_r values, but strongly different σ_{local} values.

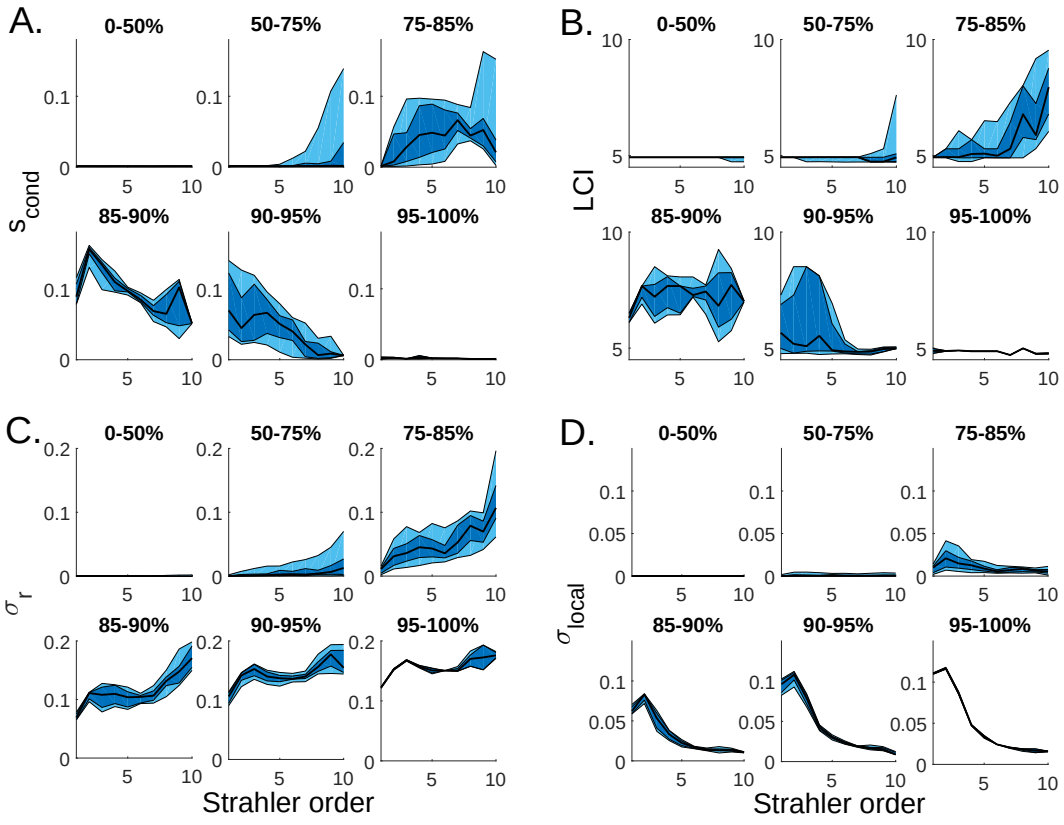

Figure 3.3: Variation of s_{cond} (A), LCI (B), σ_r (C), and σ_{local} (D) against constriction depth (Strahler order). Results have been separated into six different constriction severity bands. For each band, the median output (line) is presented alongside a band for the interquartile range (dark blue), and a band to the min and max values (light blue).

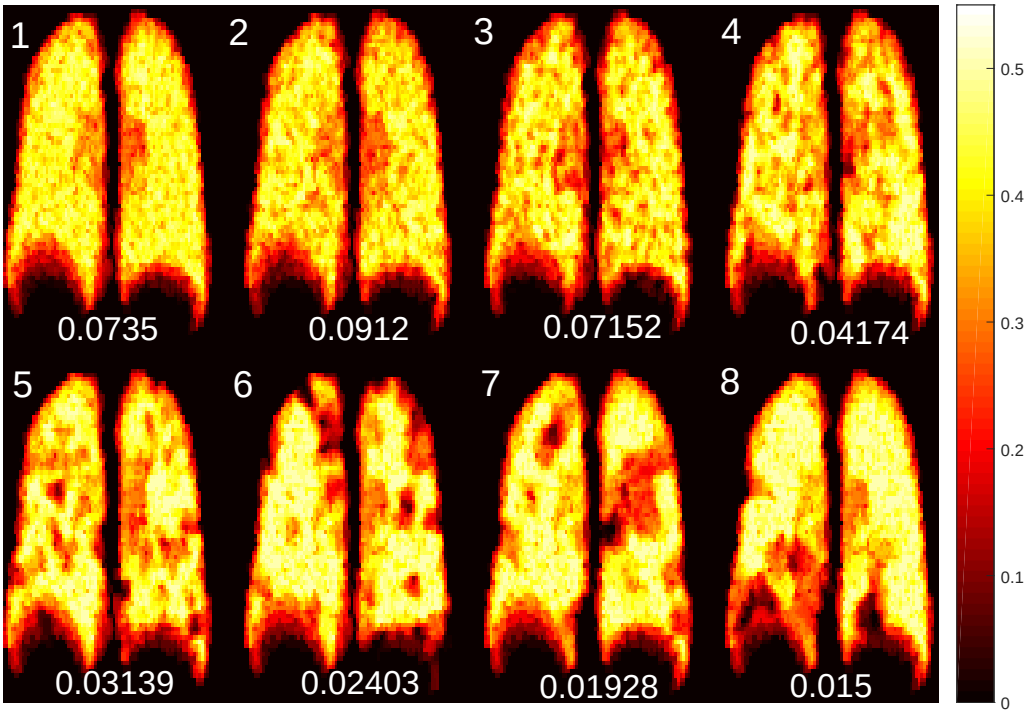

Figure 3.4: Ventilation maps. A series of 8 ventilation maps, corresponding to severe constriction (80%) of 20% of airways at Strahler Orders 1-8 (denoted). Each map has a similar σ_r value (0.08-0.11), but significantly different σ_{local} values (annotated). Brighter colours indicate higher ventilation.

3.3.3 Sensitivity of σ_{local} to grid resolution

The calculation of σ_{local} is performed in reference to a local neighbourhood (see Equation (2.11)). Thus, the index is dependent on the size of the neighbourhood. To analyse this dependence we simulate the response of σ_{local} to changes in constriction depth, under different grid resolutions. For comparison to the grid resolution used in this study ($80 \times 80 \times 80$), three different resolutions were used: medium ($40 \times 40 \times 40$); coarse ($20 \times 20 \times 20$); and very coarse ($10 \times 10 \times 10$). Note that we present no results for finer resolutions than $80 \times 80 \times 80$, due to the number of acinar regions present in the model, meaning higher resolutions resulted in too many empty voxels to give accurate representations of ventilation.

In Figure 3.5 we give the results of this analysis. As the figure shows, σ_{local} is strongly affected by image resolution. As resolution decreases, the depth at which σ_{local} maximises becomes more proximal, peaking at Strahler orders 3, 4-5 and 7 for the medium, coarse and very coarse resolutions respectively. This suggests that while a local VH parameter may help to identify constriction depth, interpretation must be made with careful reference to the imaging resolution.

3.3.4 Comparison of Strahler order and branch generation

The results presented in the previous section were created through applying airway constrictions to the lungs at various branch depths, as designated by Strahler order. For completeness, below we present results generated using airway generation as the marker of branch depth instead. These results were generated using the same constriction protocol as outlined in Section 3.2, except instead of randomly selecting a Strahler order, a branch generation (1-16) was randomly selected.

In Figure 3.6, we give plots of s_{cond}, LCI, σ_r and σ_{local} against constriction severity. Within this figure we see the same trends as exhibited in Figure 2.2. The only significant difference is that σ_{local} has a smaller peak value when constricting by branch generation than when constricting by Strahler order. This is most likely due to less branches being constricted overall. Since there are 16 branch generations but only 12 Strahler orders, 20% of branches of a given generation represents a smaller overall share of the airway tree, than 20% of branches in the corresponding Strahler order.

Within Figure 3.7 we give plots of s_{cond}, LCI, σ_r and σ_{local} against branch generation.

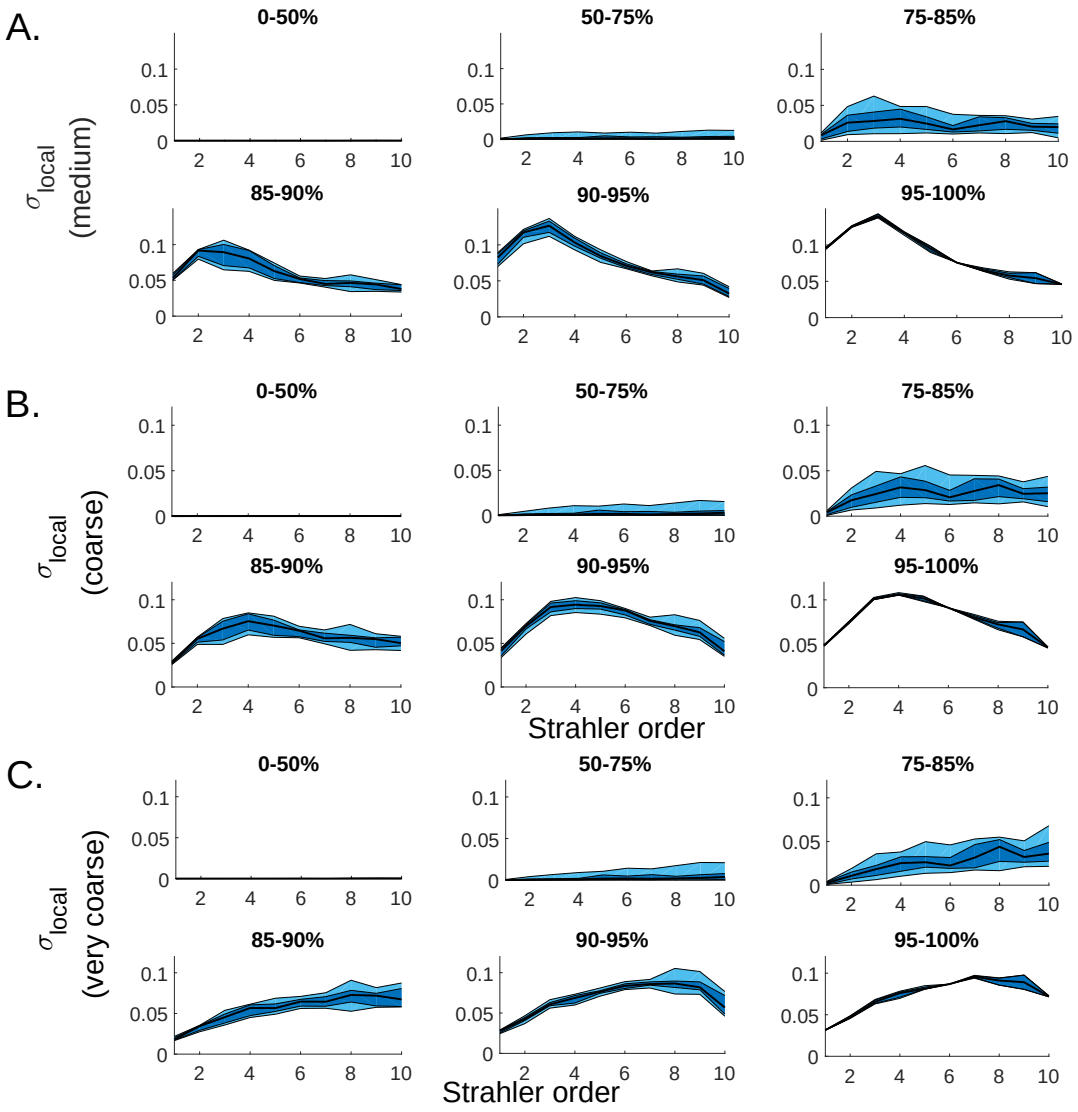

Figure 3.5: Variation of σ_{local} against constriction depth under various grid resolutions. Three different grid resolutions have been used: very coarse (A), coarse (B), medium (C). For each grid resolution, results have been separated into six constriction severity bands. For each severity band the median output (line) is presented alongside an inner band to the interquartile range (dark blue), and an outer band to the minimum and maximum values (light blue). Changes in grid resolution strongly affect σ_{local} changing the depth at which the index maximises.

Results have been separated into six bands of constriction severity: $< 50\%$, 50-75%, 75-85%, 85-90% 90-95%, 95-100%. Comparative to Figure 3.2, the overarching trends are the same, with the direction reversed, due to the fact that high Strahler order and low generation both represent proximal depth. The response when marking depth

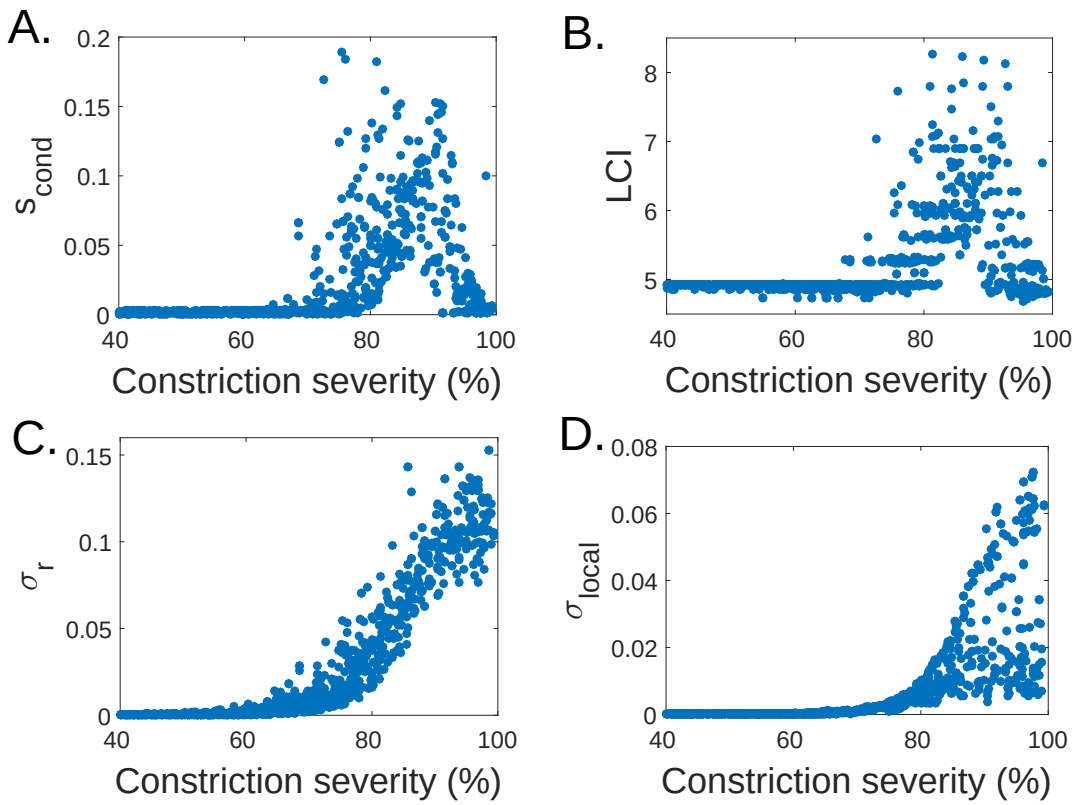

Figure 3.6: Variation of s_{cond} (A), LCI (B), σ_r (C), and σ_{local} (D) against constriction severity, at various branch generations. Positive responses are initially seen from all four indices, followed by a decrease to baseline in the MBW indices as severity approaches airway closure. The variance of σ_{local} is seen to be significantly larger than that of the other indices.

with Strahler order appears to be slightly less noisy, however this effect is quite mild. As can be seen, Figure 3.7 still clearly illustrates that σ_{local} has the strongest and most consistent response to constriction depth of the four indices.

3.4 Discussion

In this chapter we have presented a comparative exploratory analysis of the multiple-breath washout and MR imaging to conducting zone bronchoconstriction. Using the models outlined in Chapter 2, simulations of indices derived from both tests were performed in the baseline structure of the Bordas set, after application of artificial

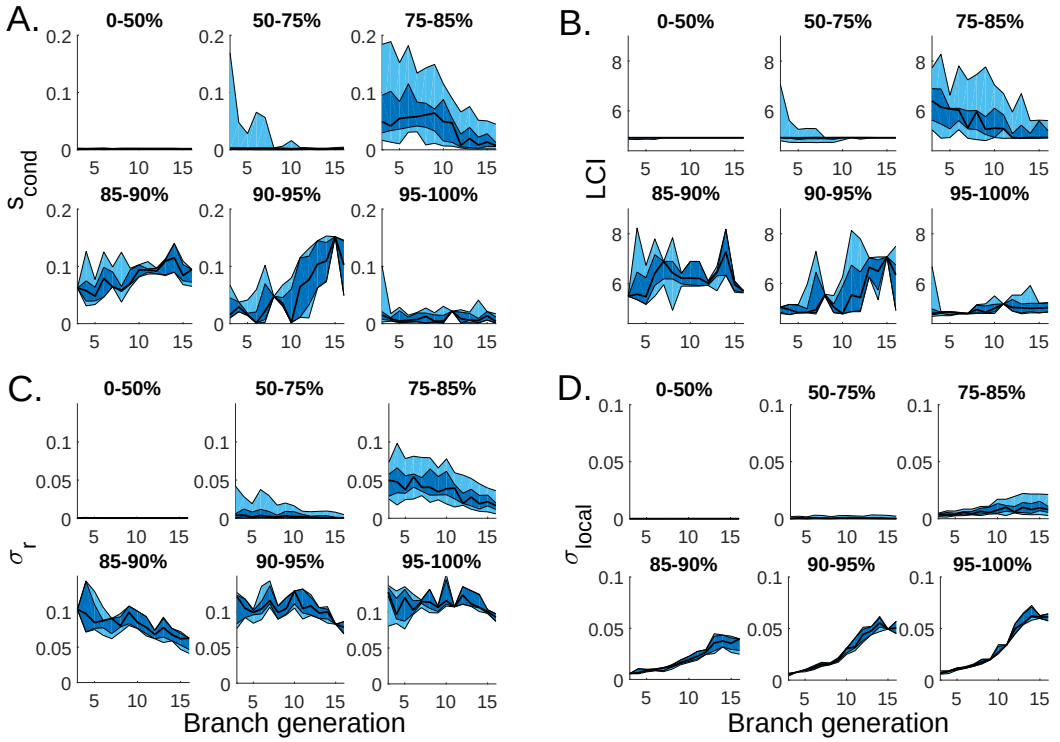

Figure 3.7: Variation of s_{cond} (A), LCI (B), σ_r (C), and σ_{local} (D) against constriction depth (branch generation). Results have been separated into six different constriction severity bands. For each band, the median output (line) is presented alongside an inner band representing the interquartile range (dark blue), and an outer band to the minimum and maximum values (light blue).

airway constrictions. These constrictions were applied at a variety of different depths, with differing constriction severities.

3.4.1 Comparison of MBW and MRI indices

Comparative analysis of MBW and MRI indices produced interesting insights. As seen in Figure 3.1, LCI, s_{cond}, and σ_r all responded positively to increases in constriction severity. Unlike the MBW indices though, σ_r remained unaffected by the development of airway closure. This is logical, considering closed airways do not participate in the distribution of ventilation at the mouth, but will still be resolved as unventilated by an MRI. The ability of MRI indices to detect airway closure may offer explanation

to outliers in correlations of the two measures, as seen in recent preliminary clinical studies (Capaldi et al., 2015; Horn et al., 2015; Horsley et al., 2014).

3.4.2 Local MRI indices

The local imaging index σ_{local} exhibits different sensitivites to the other three indices. As shown in Figures 3.1, 3.3 and 3.4 the index shows strong and consistent responses to changes in constriction depth, despite only showing a weak correlation to severity. However, the results in Figure 3.5 suggest a high sensitivity of the index to voxel size, meaning interpretation must be made with reference to the imaging resolution. As noted in the literature review, there are many competing standards for MRI indices within the literature. Other strategies, such as scaling, or the use of covariance have been employed in the literature to help normalise the effect of neighbourhood size on σ_{local} (Tzeng et al., 2009). Within this work we have demonstrated the importance and utility of local MRI indices, however, the comparative evaluation of local MRI indices is a clear area for future research.

3.4.3 Positivity of s_{cond}

Interestingly, our model of the MBW achieved a positive initial value for s_{cond} without the use of parameter fitting. This is in direct contrast to what has been seen in previous studies in the literature (Mitchell et al., 2012). To investigate the cause of this, we performed simulations at baseline removing different components of our model. The removal of the gravitational gradient, and the Pedley resistance caused decreases in the baseline s_{cond} of 12%, and 64% respectively. This appears logical,

as when considering the asymmetry of the airway tree, each of these factors should add to heterogeneity of tracheal airflow, thus increasing s_{cond}. We also simulated the model at baseline, with no gravitational gradient, using a symmetric branch structure (to generation 16) based off of the mean-field data of Weibel (1963). This produced an s_{cond} of approximately 0, suggesting that the asymmetry of the branch structure significantly drives positivity of the index. Finally, we believe the incorporation of independently ventilating acinar regions (as opposed to a global ventilation model), allowed for strong intra-regional variations in ventilation and flow, contributing to the positivity of s_{cond}.

3.4.4 Clinical significance

The results within this chapter suggest that both LCI and s_{cond} are most dominantly sensitive to the severity of airway constriction, being less significantly affected by changes in dominant constriction depth. Prior results in the literature (Robinson et al., 2010; Verbanck et al., 1998, 2003) have suggested that MBW indices may be quite sensitive to small airways constriction. However, the results in this chapter suggest that this apparent sensitivity may actually be due to other factors (such as the larger number of distal airways). Further to this, the fact that response to constriction severity appears clean and consistent suggests more clarity in interpretation of the indices as measurements of global VH. Clearly, further investigation would be needed to confirm this interpretation.

Interestingly, the response of the MBW indices in Figure 3.1 suggest that these

indices have similar levels of sensitivity to the MRI indices (with increases in all cases starting around 60% constriction). Again, further investigation would be needed to confirm this interpretation. However, this is an important factor to understand, as it provides justification for the use of the test as an alternative to more costly imaging methods.

Finally, the results in this chapter highlight some potentially valuable information about the MRI indices. Logically, the local heterogeneity was shown to be much more sensitive to constriction depth, than the global measure. However, this sensitivity was shown to depend strongly on the imaging resolution. This suggests that clinical interpretation of indices such as σ_{local} should be done with direct reference to the resolution that it was calculated under.

Overall, the results show clear distinctions between how MBW and imaging indices respond to bronchoconstriction. Some of the trends, such as the failure of the MBW under airway closure, have been exhibited in previous studies (Mitchell et al., 2012). However, to our knowledge, this is the first study that has investigated the relationship between MBW and MRI derived indices in such detail.

3.4.5 Limitations

In considering the limitations of the study, it should be noted that the initial values of s_{cond} and LCI produced by the model before constriction were lower than standard healthy values reported in the literature (Verbanck et al., 1997). This can be partially explained as resulting from the simplifying assumptions made in the model (such as

the assumption of unidirectional flow, lack of airway dynamism, and simplistic respiratory zone approximations), which would lead to an underestimation of ventilation heterogeneity. Equally, the reduced baseline responses may partially result from the fact that the baseline structure is less heterogeneous than a standard healthy structure would be.

The simulated maximum values of s_{cond} were also higher than values seen in the literature for patients exhibiting bronchoconstriction (Verbanck et al., 1997). The constriction of a small number of airways at a specific depth, by identical amounts, will naturally lead to sharp distinctions between the time constants of healthy and unhealthy regions. These distinctions would be sharper than what would be seen clinically, where the transition between healthy and unhealthy regions occurs as a spectrum. This difference explains the higher index values exhibited in severe VH regimes, as well as the observation that most significant index changes occurred once constriction severity exceeded 50%. We do not believe that these differences significantly detriment the results in this chapter though, as the primary aim was to investigate how test indices respond to structural changes in the lung, not to specifically recreate patient scenarios.

Finally, the results in this chapter focused on the investigation of bronchoconstriction within the conducting zone of the lungs. This is most typical of lung diseases such as asthma. However, other common lung diseases such as emphysema and COPD are more strongly characterised by regional compliance heterogeneity. While other studies in the literature have incorporated disease-driven heterogeneity in respiratory zone

compliance (Henry et al., 2012; Milic-Emili et al., 2007; Tawhai and Hunter, 2001), there are still large questions surrounding the use of the MBW in detection of this type of respiratory zone heterogeneity. Clearly, this is a potential avenue for future research.

3.5 Summary

The simulations performed within this chapter suggest that LCI, s_{cond}, and σ_r are all sensitive to increases in constriction severity. Under severe constriction, σ_r appears to remain a strong predictor of disease, while the MBW indices decrease back towards baseline, as expected. This leads to a strong correlation between the MBW indices and σ_r until airway closure is approached. Despite strong dependence on constriction severity, all three indices exhibit only weak dependence on constriction depth. Local VH imaging indices such as σ_{local}, appear to relate more strongly to constriction depth. However, the nature of this relationship is dependent on voxel neighbourhood sizes, meaning interpretation should be made in reference to the imaging resolution.

4

Exploratory analysis of the impedance and washout models

Exploratory analysis of the washout model in Chapter 3 showed that MBW indices have differing sensitivities to bronchoconstriction than imaging derived indices. Within this chapter we expand upon this finding by exploring the joint response of the MBW and FOT/IOS model to bronchoconstriction. Through this, we highlight the potential clinical utility in joint interpretation of outputs from the two tests.

Work within this chapter is based on the study *A computational comparison of the multiple-breath washout and forced oscillation technique as markers of bronchoconstriction*, published in *Respiratory Physiology & Neurobiology*.

4.1 Rationale

As examined in the previous chapter, indices derived from the MBW have demonstrated sensitivity to small airways disease and bronchoconstriction. Gaining an improved understanding of this test and its sensitivities could be of great clinical value, potentially allowing for more specific disease diagnosis. However, the MBW is by no means the only pulmonary function test used as an alternative to spirometry.

Alongside the MBW, the FOT and IOS are also experiencing increased clinical uptake (Smith et al., 2005). The two techniques are performed slightly differently (see Chapter 1 for details), but are both used to provide measurement of lung resistance and reactance in response to varying oscillation frequencies. It has been repeatedly shown in the literature that impedance exhibits frequency dependence, the nature of which can be strongly affected by bronchoconstriction (Grimby et al., 1968; Lutchen and Gillis, 1997; Oostveen et al., 2003). Due to this dependency, many different impedance derived indices are taken as markers of airway constriction. The accumulation of both clinical and morphometric modelling studies has led to the interpretation of low frequency resistance as a measure of total airway constriction, high frequency resistance as a measure of central airway constriction (Goldman et al., 2005; Smith et al., 2005), and reactance indices as markers of distal airway constriction (Cavalcanti et al., 2006; Kaczka et al., 1999, 2007). However, there is a lack of precision in these interpretations, and while it is clear that FOT/IOS indices respond to bronchoconstriction, for more widespread clinical uptake to be viable more information is needed.

The rationale of the work detailed in this chapter is to improve understanding of FOT and IOS indices, while extending upon the insights about MBW index sensitivities gained in the previous chapter. In Chapter 3, clear and consistent responses of LCI and s_{cond} to constriction severity and depth were illustrated. Given this, it is a natural step to question whether these responses also occur within other PFTs. To explore this question, we aim to jointly investigate the response of lung impedance measures, and MBW outputs to bronchoconstriction. We hypothesise that some of the responses may be different, yet still clear and consistent, allowing for potential value in joint interpretation of test outputs.

Within this chapter we apply computational modelling to simulate both the MBW and lung impedance under various types of conducting zone bronchoconstriction. By simulating the test outputs over a range of scenarios, we show that lung resistance and reactance measures respond clearly and consistently to constriction depth and severity. In particular, we show that the reactance indices, and the low-frequency to high-frequency resistance difference $R_5 - R_{20}$, give significantly different responses to constrictions applied proximally and distally. Following on from Chapter 3, the MBW indices are again shown to predominantly respond to constriction severity, with only small differences in response as constriction depth is changed. By considering the different sensitivities of outputs from the two tests, we highlight the value of joint interpretation, showing it leads to distinct groupings of different lung disease scenarios. We close the chapter with a discussion of the clinical relevance of the results, and limitations of the model.

4.2 Simulation protocol

The joint exploratory analysis of the MBW and FOT/IOS in this chapter is performed using a similar protocol as in Chapter 3. Simulations of both the MBW and lung impedance were performed on the baseline structure from the Bordas set, under a variety of different bronchoconstriction scenarios. Simulations of the MBW were performed using the convection-only model, with SF_6 as the tracer gas, and an orthostatic gravitational gradient.

Results were gathered from two separate batches. Within the first batch we performed an exploratory analysis of the impedance indices alone, using the same procedure as in Chapter 3. A Monte Carlo approach was used to randomly sample bronchoconstriction depth and severity. Constrictions were applied by reducing radii of a uniformly random 20% of branches at a given Strahler order (1-10) by a given percentage (0-80%). As in Chapter 3, airway constrictions were applied in a spatially coherent manner (see Equation (3.1)), with a coherence of 60%. For each simulation, resistance and reactance at 5 Hz (R_5, X_5), resistance at 20 Hz (R_{20}), low reactance area (AX) and resonant frequency f_{res} were all calculated (each of these indices is denoted in Figure 1.8).

Within the second simulation batch, lung impedance indices and inert-gas washout indices were jointly simulated under a series of different constriction scenarios. To expand upon the scenarios explored in Chapter 3, a more detailed constriction protocol was used. Strahler order was still used as the primary marker of depth, but branches

were instead classified into three groups: distal (orders 1-3), medial (orders 4-7), and central (orders 8-10). These groupings roughly approximated the small conducting bronchioles (diameter $<$ 1mm), the large conducting bronchioles (1mm $<$ diameter $<$ 2mm) and the secondary and tertiary bronchi (though exclude the trachea and left/right primary bronchi, orders 11-12).

For each simulation, a depth (distal, medial, central) and mean constriction severity μ_{cond} (0-60%) were uniformly randomly chosen. Each branch in the chosen depth group was then constricted, with severities (c) drawn from the normal distribution

$$c \sim N(\mu_{\text{con}}, 0.2\mu_{\text{con}}).$$

The constrictions were applied to every branch in the chosen depth group, with no preference given to branch sizes or locations. If any constriction rate exceeded 95% it was floored to this value to prevent the numerical error associated with near-infinite resistance pathways (which occur under full closure of an airway). The value of $0.2\mu_{\text{con}}$ was chosen as the standard deviation to provide a high degree of variability and noise to the constriction protocol. This simulation protocol was designed as an adaptation of the protocol used in Chapter 3, with a higher degree of heterogeneity, as would be seen clinically. In practice, disease does not act homogeneously across the entire lung, and can often be most dominant at a particular depth (e.g. asthma is known to strongly affect the small airways (Usmani et al., 2016)).

For each simulation in the second batch, the 5 lung impedance indices were calculated. Alongside this, under the same constriction pattern, a multiple-breath washout

was simulated (with 4% SF_6, in an orthostatic position), with the corresponding LCI and s_{cond} values calculated.

In total 2000 simulations were performed in batch 1, and 600 in batch 2.

4.3 Results

For reference, we give the baseline values of the model (produced under no constriction) as 0.3478, 0.3154, and 0.4779 $\text{cmH}_2\text{O.s.L}^{-1}$ for R_5, R_{20} and $|X_5|$ respectively, 8.79Hz for f_{res}, 0.816 $\text{Hz.cmH}_2\text{O.s.L}^{-1}$ for AX, 0.0012 L^{-1} for s_{cond} and 4.948 turnovers for LCI.

For readability, units have been omitted from some of the figures within this chapter. All resistance and reactance measures are given in $\text{cmH}_2\text{O.s.L}^{-1}$, frequencies are given in Hz, reactance area in $\text{cmH}_2\text{O.s.L}^{-1}$.Hz, LCI in turnovers, and s_{cond} in L^{-1}.

4.3.1 Response of impedance to bronchoconstriction

In Figure 4.1 we give the response of the impedance measures to homogeneous airway constriction at varying depths (simulation batch 1). As the figure shows, all of the indices exhibit an increase in magnitude as constriction severity is increased. R_5 shows the cleanest response, changing with a much lower degree of noise than all other indices. Interestingly, we note that the resistance measures appear to stabilise as airway closure is approached, while the reactance measures continue to increase. Finally, we note that the reactance measures all experience a decrease (as constriction severity is increased) for a small set of values.

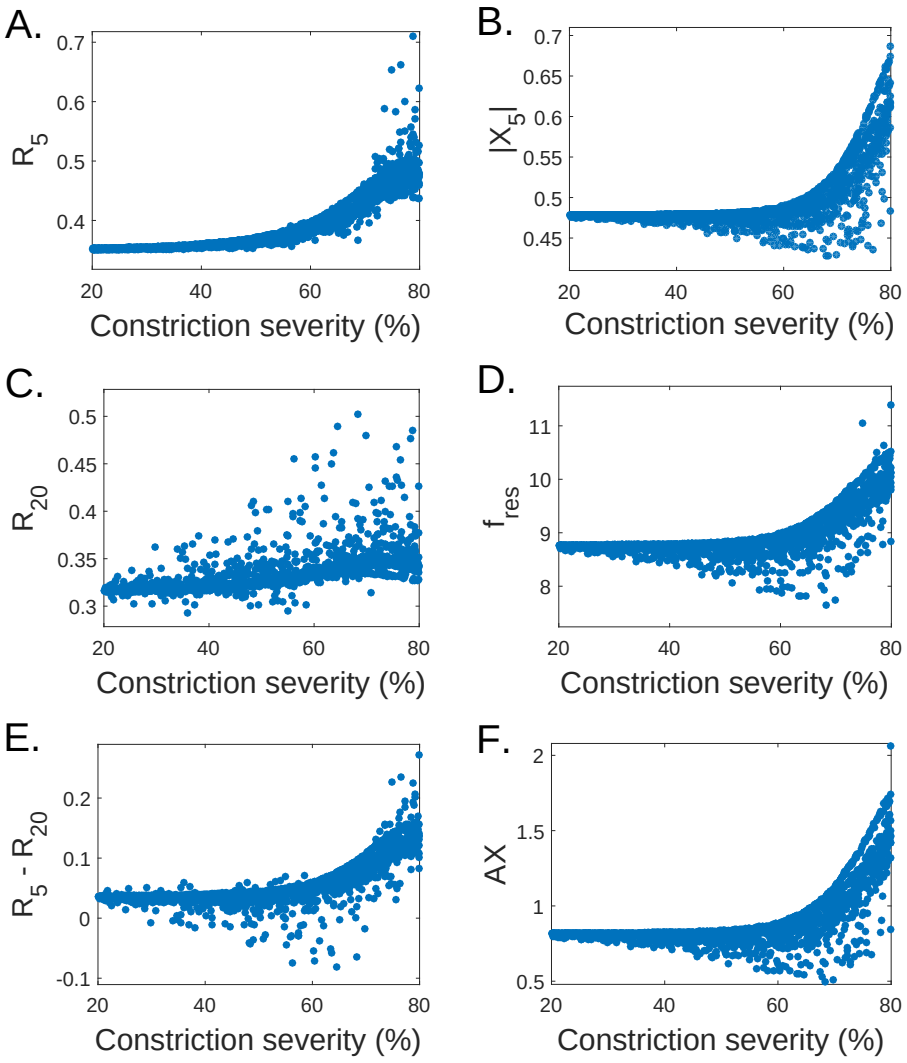

Figure 4.1: Response of resistance (A,C,E) and reactance (B,D,F) measures to constriction severity. Constrictions were applied homogeneously to 20% of airways at a given Strahler order (1-10).

This small set of decreases can be better understood by considering the response of the indices to constriction depth, shown in Figure 4.2. As in Chapter 3, these responses have been separated into different constriction severity bands, to allow for more clear interpretation. Considering both Figure 4.1 and 4.2, R_5 appears to show no significant response to depth, despite responding consistently to severity. Distally, R_{20} responds similarly to R_5, however, at proximal depths (orders 7-10) the index

consistently increases. It follows from this that $R_5 - R_{20}$ should respond most strongly to small airways constriction, which is clearly seen in the figures (though there is higher variability). This is a standard interpretation of $R_5 - R_{20}$ from the literature, and one which we explore further in Chapter 5.

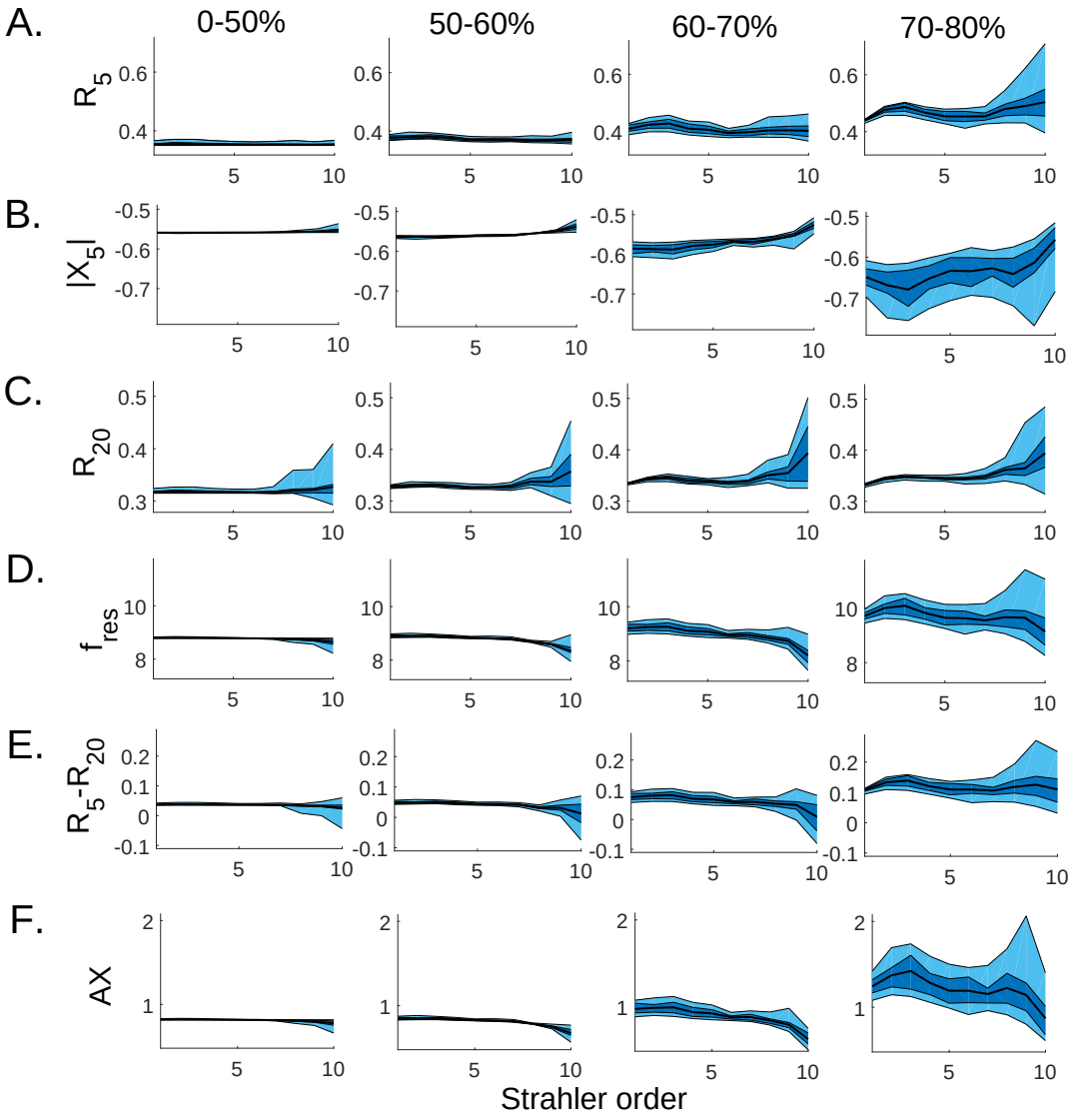

Figure 4.2: Response of resistance (A,C,E) and reactance (B,D,F) measures to constriction depth. Results are separated into bands of different constriction severities (0-50%, 50-60%, 60-70%, 70-80%). The median response is given (line) alongside an inner band to the interquartile range (dark blue), and outer band to the minimum and maximum values (light blue).

The reactance indices all illustrate consistent responses to depth. All three indices decrease in magnitude as depth becomes more proximal. However, similarly to $R_5 - R_{20}$, we see an increase in variability both as Strahler order becomes more proximal, and as constriction levels become more severe.

Correlations of the resistance and reactance indices against each other can be seen in Figures 4.3 and 4.4. From these plots, it can be seen that all three reactance measures appear to correlate strongly with each other, with slight curvatures. The resistance measures show significantly less correlation with each other, though the results in Figure 4.3 highlight that the response of $R_5 - R_{20}$ is most dominated by R_5. Only weak correlations appear between R_5, R_{20} and the reactance measures, while $R_5 - R_{20}$ correlates much more clearly with all three. This follows from the fact that $R_5 - R_{20}$, X_5, f_{res}, and AX can all be seen to respond strongly to variations in constriction depth. It should be noted that the correlations exhibited here are in line with prior results in the literature (Johnson et al., 2005; Oppenheimer et al., 2009).

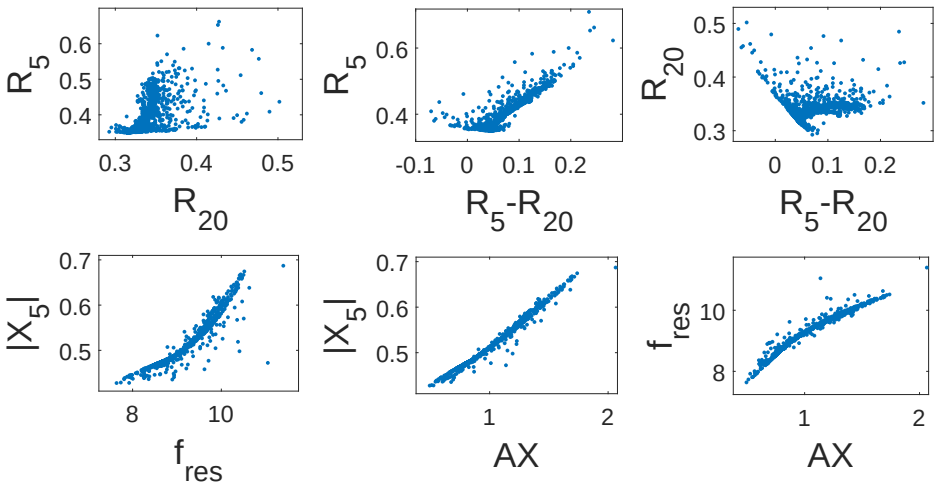

Figure 4.3: Correlation between resistance measures and between reactance measures. These results were generated from simulation batch 1.

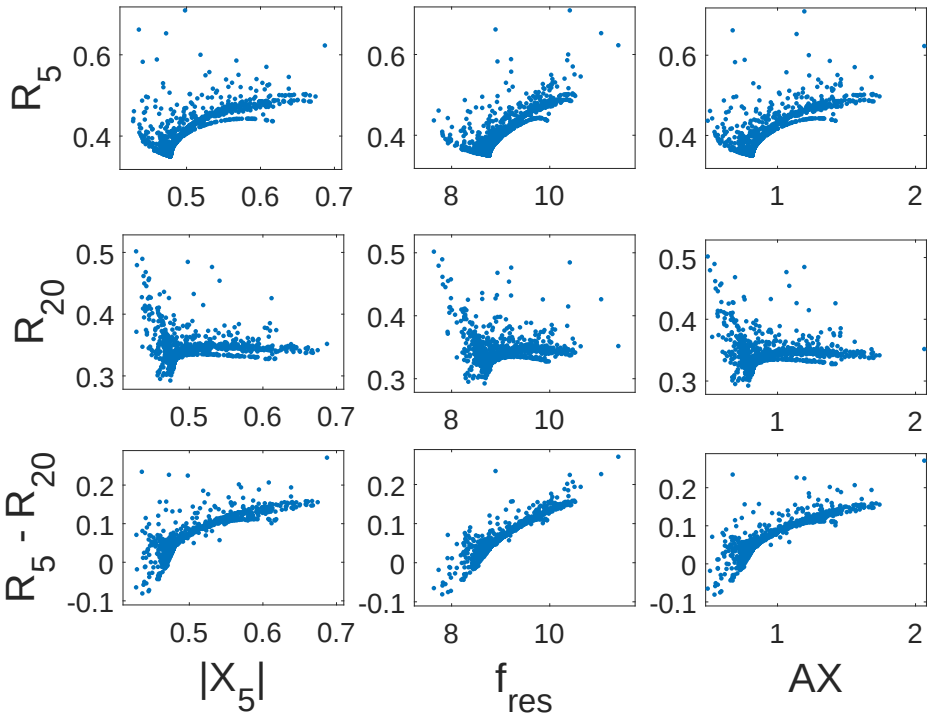

Figure 4.4: Correlation between resistance and reactance measures. These results were generated from simulation batch 1.

4.3.2 Joint response of impedance and MBW indices to constriction

Following the initial exploratory analysis of the impedance indices, we now present results from simulation batch 2. In Figure 4.5, we give the responses of the impedance indices to increases in mean constriction severity. Results have been separated into the three depth groups: distal, medial and central. Considering the resistance indices, both R_5 and R_{20} show clear positive responses to increasing constriction severity. However, neither R_5 nor R_{20} show clear distinctions between the three depth groups. $R_5 - R_{20}$ appears to distinguish more between constriction depths, with the distal group having a significantly lowered response. Similarly to the resistance indices, each reactance index responds strongly to increases in constriction severity; however, the

nature of this response differs between each depth group. For all three indices, the distal and medial groups experience monotonic increases, while the central group decreases, before eventually increasing as the constriction rate becomes severe. Unlike the resistance indices, the reactance indices show distinct separations between the medial and distal groups.

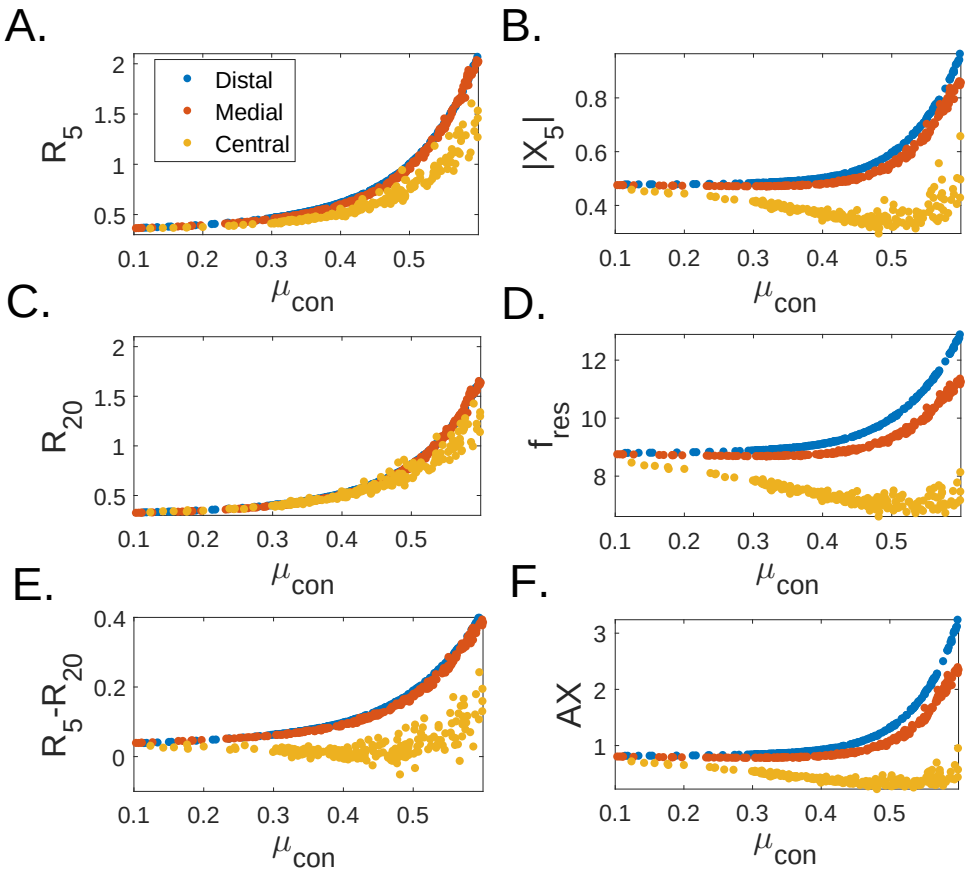

Figure 4.5: Response of the resistance (A,C,E) and reactance (B,D,F) indices to increases in mean constriction severity. Results have been separated by the three constriction groups: distal (blue), medial (red) and central (yellow).

These results correspond clearly to those illustrated within Figure 4.1. This comparison highlights that much of the noise in Figure 4.1 is directly due to constriction depth. We note that the new constriction scheme produces overall higher index values

than those seen in Figure 4.1. This is due to the significantly higher number of airways that are constricted within the scheme.

In Figure 4.6, we give the response of s_{cond}, and LCI, to increases in mean constriction severity. As the figure shows, both indices exhibit a clear positive response to increasing severity. The index s_{cond} appears to show some ability to distinguish between the three depth groups (in particular the distal group). However, similarly to the resistance indices, there is a high degree of variability to the responses, meaning there is significant overlap between the three groups. Considering the responses of LCI, we see the formation of distinct bands. This is due to the discrete threshold used in the calculation of LCI, meaning small changes in VH can cause step-wise changes in the index. Due to this phenomenon, LCI appears to separate depth groups less clearly than s_{cond}. These results align closely to previous results within the thesis. As illustrated in Chapter 3, the MBW indices appear to show a strong response to constriction severity, but little ability to separate out constriction depth.

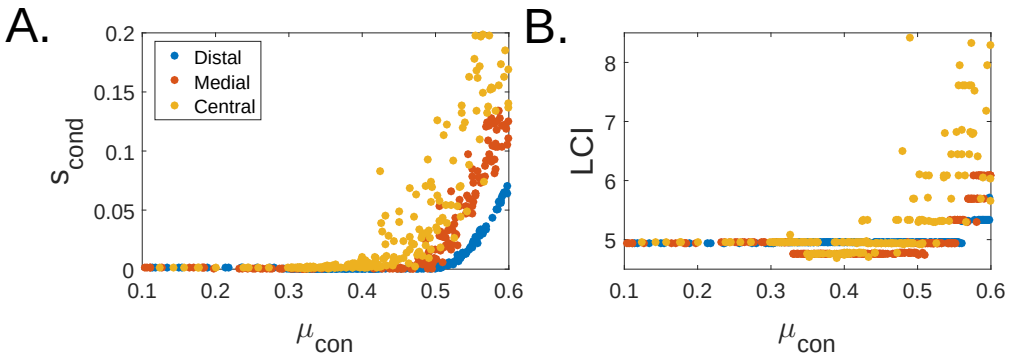

Figure 4.6: Response of s_{cond} (A) and LCI (B) to increases in mean constriction severity. Results have been separated by the three constriction groups: distal (blue), medial (red) and central (yellow).

Given that $R_5 - R_{20}$, f_{res}, X_5 and AX all strongly distinguish between variations

in constriction depth, while LCI and s_{cond} respond most significantly to constriction severity, it follows that joint interpretation may help separate out both factors. To illustrate this, we show the joint response of impedance indices and s_{cond} in Figure 4.7. For each of the subplots the three depth groups are distinctly separated. Equally, as shown by the arrows, there is clear separation based on mean constriction severity. The distinction between groups is the most significant with the reactance indices. This is logical, as the results from Figure 4.2 and 4.5 both illustrate that reactance appears to more cleanly distinguish depth groups than $R_5 - R_{20}$.

4.4 Discussion

In this chapter we have detailed a comparative exploratory study of the MBW and lung impedance measures. Using the baseline structure from the Bordas set, the multiple-breath washout, and lung impedance, were simulated under a range of different bronchoconstriction scenarios. Initial simulations were used to explore the response of impedance indices in isolation, before a more complete comparative analysis alongside LCI and s_{cond}.

4.4.1 Sensitivity of impedance measures

In the initial exploratory analysis of the impedance indices (Figures 4.1-4.4), a range of different behaviours were seen. R_5 was seen to respond most strongly to constriction severity, being fairly invariant as the depth of the applied constriction was altered. R_{20} appeared to be more sensitive to depth, peaking under proximal constriction. This suggests that the 5 Hz signal may probe the lung more deeply than the 20 Hz signal,

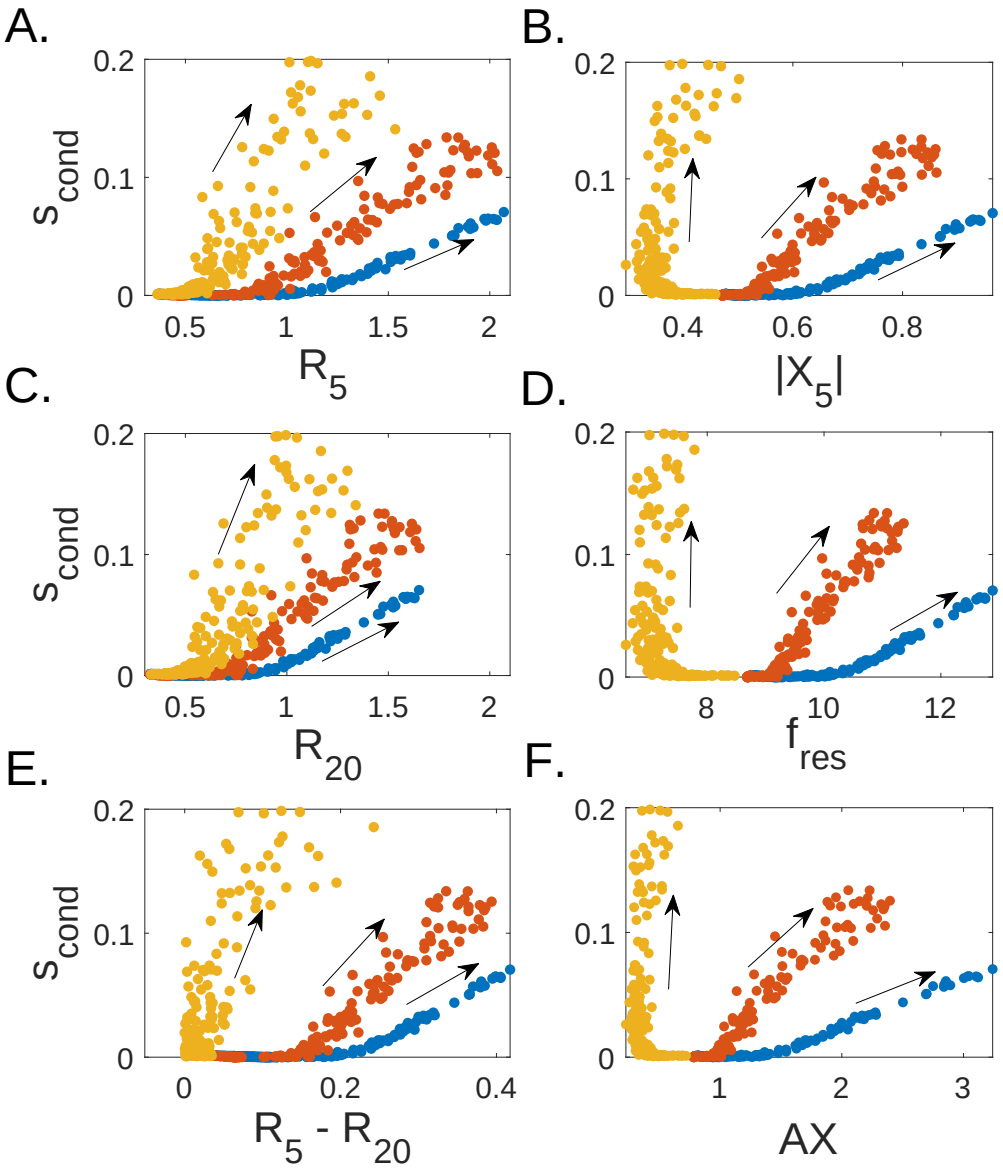

Figure 4.7: Comparative responses of the resistance (A,C,E) and reactance (B,D,F) indices against s_{cond}. Results have been separated by the three constriction groups: distal (blue), medial (red) and central (yellow). Directions of increasing constriction severity for each depth group are marked by arrows.

a result also seen in other studies in the literature (Bhatawadekar et al., 2015), which underpins the use of $R_5 - R_{20}$ is an indicator of small airways disease.

The reactance measures were seen to respond much more clearly to constriction depth than any of the resistance measures, with an overall lower degree of noise.

This separation was seen even more clearly when applying heterogeneous airway constrictions (Figure 4.5). It should also be noted that the reactance indices all occurred within ranges seen in clinical studies (Crim et al., 2011), while the baseline resistance values were all lower than standard clinical values. This may partially be due to the lack of upper airway/chest wall contributions and cheek shunting within the model; an idea which is investigated in more detail within Chapter 5.

4.4.2 Comparison of MBW and impedance measures

Unlike the impedance indices, the MBW indices showed only small responses to changes in constriction depth (Figure 4.6). Instead, the response in both LCI and s_{cond} was dominated by the constriction severity, in line with the results in Chapter 3. Considering that many of the impedance measures respond quite strongly to constriction depth, while neither of the MBW indices do, the separation seen when jointly comparing indices (figure 4.7) is not surprising. However, to the best of our knowledge, no prior study has investigated this connection. As the figure shows, the joint interpretation of MBW and FOT/IOS indices provides separation of the simulations based on both constriction depth and constriction severity, with an example diagram given in Figure 4.8.

It is noteworthy that the MBW and impedance models operate completely independently of each other. The only shared information between the two tests is the branch structure, and airway constriction pattern. No parameters are shared between the two models, and the underlying model assumptions and mechanics are quite different,

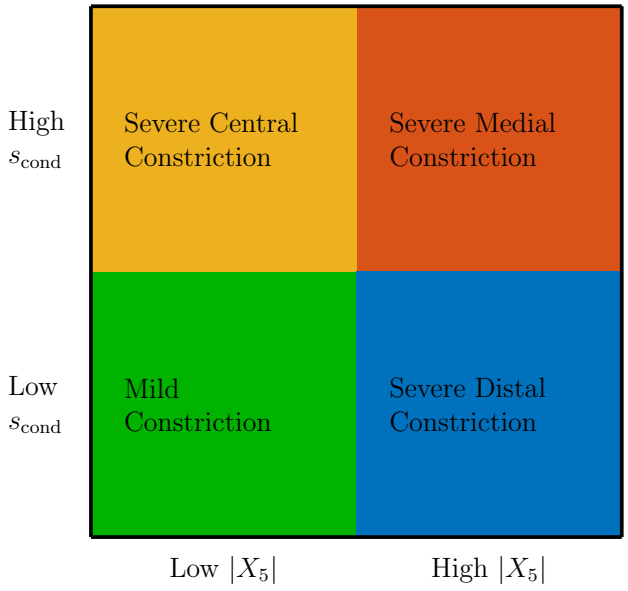

Figure 4.8: An illustration of the combined interpretation of the indices derived from the two computational models, separating out constriction severity and depth.

with the MBW model simulating ventilation and gas transfer over the course of a few minutes, while the impedance model simulates frequency propagation (and has no temporal component). This makes the clear and distinct separation of groups, and the low level of variance within each group quite impressive.

These results also raise the question of why, mechanistically, lung impedance exhibits more sensitivity to depth than actual ventilation (which directly influences the MBW). One potential reason for this may be an underlying sensitivity to the number of branches undergoing constriction. The MBW is primarily used as a measure of ventilation heterogeneity (Robinson et al., 2013), meaning parameters such as s_{cond} may naturally respond more sensitively to the magnitude of difference in time constants between different regions (Otis et al., 1956), than to the relative size of these regions. Conversely, due to the parallel nature of calculations in the impedance model, its

outputs will naturally show significant sensitivity to the total number of constricted branches. If this is one of the driving mechanistic differences between the two tests, understanding it could be quite valuable. However, clinical evidence would be needed to fully test this hypothesis.

4.4.3 Comparisons to the literature

The constriction distributions used in this study were not intended to be true representations of asthmatic bronchoconstriction, but rather to explore in a broad sense the responses of the two tests to bronchoconstriction depth and severity. Clearly, experimental measurements would be needed to be certain of the physiological interpretation of the observed relationships within this study. However, it should be noted that the interpretation of $R_5 - R_{20}$ and reactance measures as indicators of small airways constriction is held within the literature (Bhatawadekar et al., 2015). Equally, that LCI and s_{cond} exhibit increases in response to airways constriction (as is seen in asthma) has been illustrated both in prior modelling studies (Mitchell et al., 2012), and clinical studies (Downie et al., 2007). Given this, the results in this study can be taken as providing further evidence to these prior existing conclusions. Furthermore, the results can be taken as hypothesis-generating, suggesting the potential ways the lungs might respond to bronchoconstriction. We believe that the hypothesised relationship of the MBW and FOT/IOS to conducting zone bronchoconstriction (presented in Figure 4.8) is one that warrants further investigation in a clinical setting.

Comparative to other studies in the literature (Mitchell et al., 2012; Lutchen

and Gillis, 1997), constrictions within simulation batch 2 were drawn from a normal distribution, $\mathcal{N}(\mu_{\text{cond}}, 0.2\mu_{\text{con}})$, as opposed to being uniformly distributed. Increases in constriction heterogeneity may create a greater spectrum of time constants (Otis et al., 1956) in the lung, and as such should lead to higher s_{cond} values. Comparing the washout indices in this study to the results in Chapter 2 and those of Mitchell et al. (2012) we see that this occurs. Equally, comparing the results within this study to prior results in the literature (Lutchen and Gillis, 1997), similar behaviours can be seen for lung impedance, with the degree of heterogeneity of the applied constriction affecting index magnitudes. Since increased heterogeneity appears to cause increases in both impedance and MBW indices, the conclusions seen in this study should remain consistent if constriction heterogeneity is changed. This is clearly a question for future investigation though.

4.4.4 Clinical significance

The results illustrated in Figures 4.1-4.8 strongly highlight the potential clinical utility of both MBW and impedance measures. Consistent with the results in Chapter 3, the MBW indices are shown to most dominantly respond to constriction severity, behaving fairly independently of depth. The impedance indices however, are shown to have a much greater sensitivity to depth, with distinct differences between central and distal airways constriction. This suggests that impedance indices may have potential use in separating patient groups in clinical trials where treatments can target different depths (e.g. using corticosteroid inhalers with different particle sizes).

Further to this, the results suggest strong potential utility in joint interpretation of LCI or s_{cond} with reactance indices, or $R_5 - R_{20}$. Since the sensitivities of these measures are quite different, comparative analysis appears to separate constriction types, allowing for simultaneous classification of depth and severity. While this result would need to be confirmed with clinical research, it may allow for more targeted treatment of patients in clinical practice, or the design of more precise clinical trials.

More broadly, increased precision in the interpretation of MBW and lung impedance measures may help improve clinical uptake of the two techniques, allowing for more sensitive detection of early-stage lung disease. The results in this chapter add to the body of work within the literature, and help to improve this precision.

4.4.5 Limitations

While we believe that the results in this chapter are quite novel, there are some key limitations to the two models. As discussed in Chapter 3, the MBW model does not incorporate airway dynamism, and applies a quite simplistic approximation for the respiratory zone. It would be expected that dynamic airways would lead to an increase in total lung resistance, leading to slower washout times, and increasing LCI. Equally, a more detailed respiratory zone model would likely increase resistance as well, again increasing LCI. However, it would not be expected that either of these factors would significantly change the nature of the model's response to changes in constriction depth or severity.

The lung impedance is also limited by the same lack of dynamic airway behaviours.

Original designs of the impedance model incorporated the effects of airway compliance, using techniques described by Kaczka et al. (2007). However, contributions from airway compliance were seen to be minimal, and thus for simplicity were removed. Further to this, the model did not incorporate contributions to impedance from shunting in the cheeks and upper airways. In clinical applications, cheek shunting effects are minimised by having the patient hold their cheeks throughout the procedure. While useful, this action has been shown to not completely remove potential contributions (Cauberghs and Van de Woestijne, 1983; Oostveen et al., 2003; Peslin et al., 1985). Shunting is known to influence frequency dependence, particularly for resistance measures, due to increased shunting at higher frequencies. Within Chapter 5, we adapt the impedance model to incorporate shunting effects. Notably, this increases the baseline resistance values (raising them to within standard clinical ranges), and allows for direct comparison of the model to clinical data. While shunting does have a significant effect on resistance (and reactance to a lesser degree), it is considered a fairly random contribution, not being significantly related to the subject's state of disease (Oostveen et al., 2003). Thus, we do not believe that this lack of incorporation significantly affects the key results in this chapter.

Finally, similar to the MBW model, the impedance model applied a simplistic approximation (the constant-phase model) to account for respiratory zone mechanics, parameterised using constant mean-population values (see Chapter 2 for more details). In practice it would be expected that parameters of this model would be patient-specific, being related to morphological properties of the subject's acinar regions.

However, due to imaging resolution limitations, there is a lack of available information to give more detail to the respiratory zone parameters. The development of more detailed respiratory zone models capable of replicating behaviour in sufficient detail to investigate disease at this level, is a clear direction for future research.

4.5 Summary

Within this chapter, computational models were used to investigate the response of MBW and impedance indices to bronchoconstriction in the conducting zone. Building upon the results of Chapter 3, the MBW indices were again seen to respond most dominantly to constriction severity. However, the reactance indices, and $R_5 - R_{20}$ were seen to respond quite cleanly to changes in constriction depth. This suggests that joint interpretation of outputs from the two tests may allow for clearer classification of different types of lung disease, generating a clear hypothesis for future clinical investigation.

5

Clinical validation and application of the impedance model

Within Chapter 4 we detailed an exploratory analysis of the lung impedance model, showing potential clinical utility of impedance measures as sensitive detectors of airways constriction. However, for these results to be meaningful there is a clear need for validation of the impedance model. In this chapter we provide this validation, showing strong concordance with experimental and clinical data. We then show how the model can be used to more precisely analyse the clinical utility of the impedance measure $R_5 - R_{20}$.

Work within this chapter is connected to a series of different journal articles:

- *Lung computational models provide unique insights into the clinical role of the small airways in asthma*, under review;

- *Characterising the role of the small airways in severe asthma using tidal breathing low frequency forced oscillations: A combined computational models and clinical approach*, under review;

- *Functional CT imaging for identification of the spatial determinants of small airways disease in adult asthma*, under review;

and conference papers:

- *The evaluation of frequency dependence of resistance using a patient-specific 3D printed airway model and computational simulation*, presented at the *2017 Meeting of the European Respiratory Society*;

- *Inert-gas washout and forced oscillation technique show sensitivity to the degree of regionalisation of bronchoconstriction*, presented at the *2017 American Thoracic Society Congress*.

This work relied heavily on experimental and clinical data collected by our collaborators. In particular, the parts of the study in this chapter were designed by Professor Siddiqui (University of Leicester); the clinical data was collected and analysed by Dr Soares (University of Leicester) and Professor Siddiqui; the 3D-printed airway structure was created by Dr Timmerman (University of Warwick) in collaboration

with Professor Owers-Bradley (University of Nottingham); and the 3D-printed airway experiments were performed by Dr Soares and Professor Owers-Bradley's group. Where noted, the computational results in this chapter build upon prior work by Dr Bordas (University of Oxford).

5.1 Rationale

As discussed previously, asthma is a complex and chronic inflammatory disease, involving both central and small ($\leq$ 2mm in diameter) airways. While there is strong evidence to suggest small airways are dysfunctional, and inflamed in asthma (Hamid et al., 1997; Usmani et al., 2016), there is a lack of validated tools to identify disease in the small airways, rendering standardised assessment difficult in large clinical studies.

The use of PFTs that have higher sensitivity to morphological changes than spirometry may help overcome this difficulty. However, tests such as the FOT/IOS are still strongly limited by lack of precision in interpretation of test outputs. The frequency dependence of lung resistance has been shown to change with disease, in both computational and clinical studies (Smith et al., 2005). These studies have led to the interpretation of low frequency resistance as evolving from contributions over the entire conducting zone, and high frequency resistance as evolving from central airway contributions. Thus, the low-high frequency resistance difference (e.g. resistance at 5Hz - resistance at 20Hz, $R_5 - R_{20}$) is taken as a marker of small airways dysfunction (Bhatawadekar et al., 2015; Smith et al., 2005; Yamaguchi et al., 2009). However, this interpretation is by no means conclusive, and may be confounded by factors such

as upper airway shunting. Equally, it is still not yet known whether the response is consistent and sensitive enough for truly widespread clinical application.

As explored in the previous chapters, computational modelling may allow for more precision in interpretation of lung impedance indices. However, for this to be a valid approach, there needs to be confidence that the computational models are accurately capturing the mechanisms underpinning the test which they are simulating. The models need validation both of their ability to recreate patient-specific data, and of their ability to capture physical mechanisms accurately enough to respond to non patient-specific morphological property changes.

In this chapter, we apply the above rationale to the impedance model developed within Chapter 2, and to specific analysis of $R_5 - R_{20}$ as a small airways dysfunction marker. We first perform a detailed validation of the impedance model, using a combination of clinical data and experimental measurements taken from a 3D-printed airway. Following this validation, we apply the model to a more in-depth analysis of $R_5 - R_{20}$, with particular focus on its response to small airways disease. Through this, we provide evidence of the utility of the index as a useful marker of small airways dysfunction in clinical settings.

5.2 Validation of the impedance model

Considering the impedance model outlined in Chapter 2, there are two major components it consists of: the patient-specific conducting zone model, and the constant-phase respiratory zone model. However, to validate these models we first consider the two

components separately, before validating their combined effects against clinical data. To properly validate against clinical data, the effects of upper airway and cheek shunting cannot be ignored, as was done in Chapter 4. With this in mind, the model outlined in Chapter 2 is also updated to include these effects.

As a note, similar to other chapters within this thesis, for readability units have been omitted from some figures. All resistances and reactances are given in $cmH_2O.s.L^{-1}$, frequencies in Hz, and reactance area in $cmH_2O.s.L^{-1}.Hz$.

5.2.1 Experimental validation

To validate the conducting zone component of the lung impedance model, a 3D-printed airway structure was created by Dr Timmerman, at the University of Warwick (Timmerman et al., 2013). This was done to allow for direct comparison of contributions to branch resistances without interactive effects from the elasticity of the respiratory zone. Firstly, a virtual model structure was derived from central airway segmentation of inspiratory-expiratory CT scans of a single asthmatic patient from the Bordas group. Due to size-complexity constraints of the 3D-printing, only generations 1-6 were segmented. This led to a virtual structure with 61 terminal branches, and 120 overall branches, with radii in the range 0.6-7 mm. A replica of this virtual structure was 3D-printed by casting an optically clear elastomer around a CT-based additive layer manufactured core, which was subsequently removed. The elastomer used in the model possessed a level of elasticity similar to that of cartilage in the trachea, allowing for flow study at near-realistic airway compliance (Lambert et al., 1991). The virtual

structure, and corresponding 3D-printed structure can be seen in Figure 5.1.

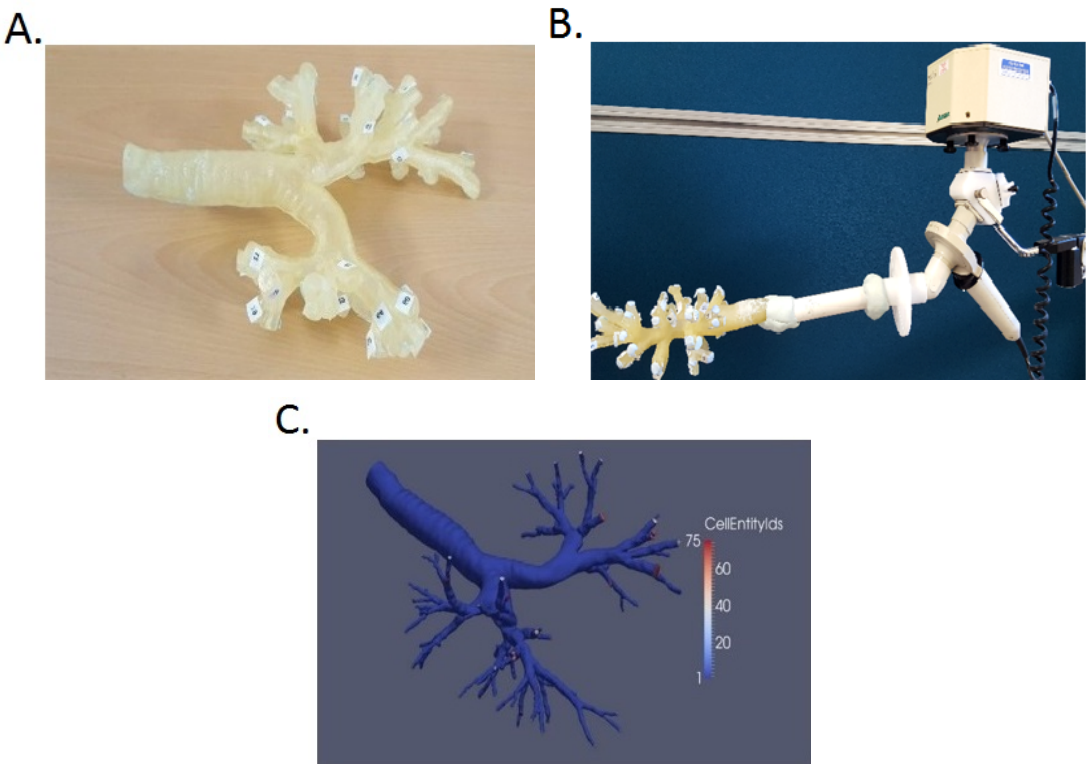

Figure 5.1: Physical and virtual models. The 3D-printed structure can be seen on its own (A), connected to the FOT device (B), and as a virtual representation (C). Physical images were originally taken by Professor Owers-Bradley's group, and Dr Timmerman. The virtual image is a recreation of an image originally created by Dr Bordas.

To validate the computational model, impedance measurements were taken in the 3D-printed structure with increasing numbers of occlusions at the terminal branches (created using blue-tack), by Professor Owers-Bradley's group (University of Nottingham) and Dr Soares (University of Leicester). Terminal branches were chosen randomly for occlusion with random alternation between the right and left lungs. Simulations of lung impedance were also performed using the virtual structure, with the same occlusion pattern. Originally this work was performed by Dr Bordas, however, simulations were recomputed for this thesis, through recreation of Dr Bordas' work.

The correlations between resistance and reactance at 5 Hz and 20 Hz are shown in Figure 5.2. As can be seen, the correlation between the model and physical structure is remarkably strong for all four outputs, with $R^2 = 0.975, 0.972, 0.955$, and 0.969 for R_5, R_{20}, X_5, and X_{20}. However, while the response to occlusion is captured, the simulated values are roughly an order of magnitude lower than the physical values. This may be partially due to the simplified 1D nature of the model, meaning it ignores turbulent effects, as well as to physical factors such as the potential shunting at the connection point of the device to the 3D-printed lung.

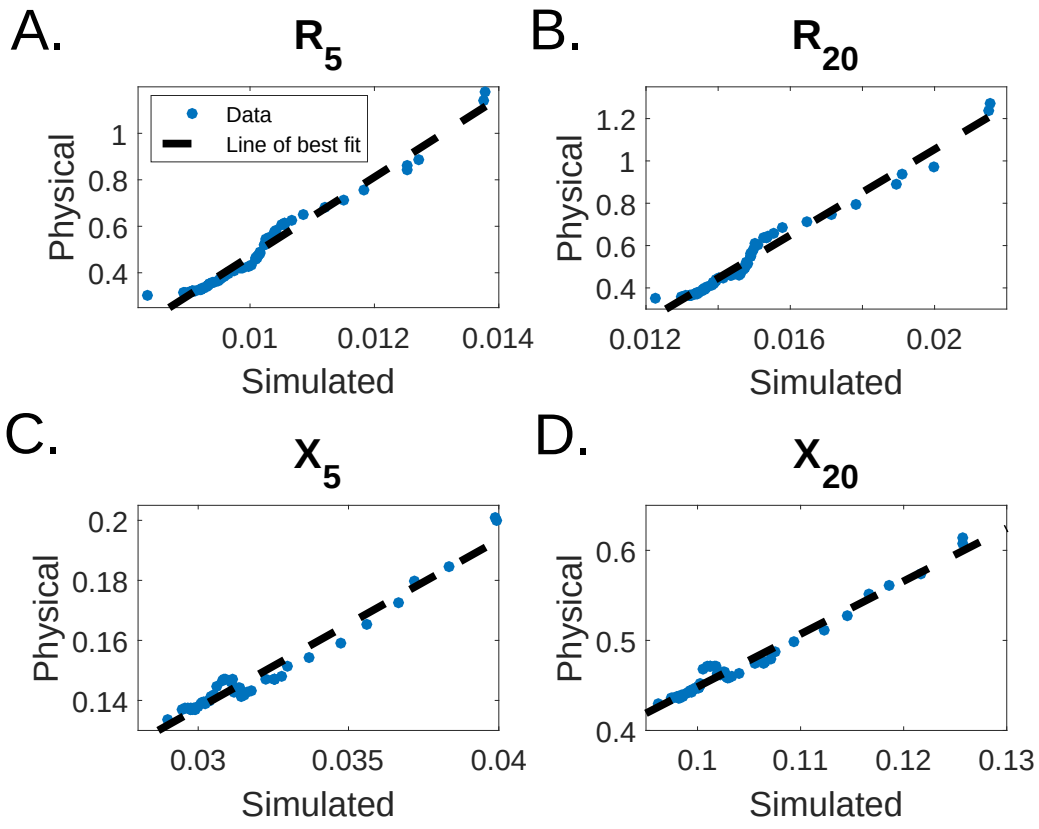

Figure 5.2: Correlation of physical and simulated resistance and reactance. Correlations of R_5 (A, $R^2 = 0.975$), R_{20} (B, $R^2 = 0.972$), X_5 (C, $R^2 = 0.955$), and X_{20} (D, $R^2 = 0.969$) are given. This figure is a recreation of a figure originally created by Dr Bordas.

5.2.2 Incorporation of shunting

Unlike the results in the previous chapters, within this chapter we aim to compare the model directly to clinical data. To do this, we extend upon the original model outlined in Chapter 2 by adding components to account for upper airway and cheek shunting, as well as overall chest wall elastance. In standard practice, when taking FOT/IOS measurements subjects are instructed to hold their cheeks, to minimise shunting effects. However, this action does not entirely negate the effects of shunting, and so to effectively validate the model against clinical data, these effects must be incorporated. This was performed using a technique outlined by Bhatawadekar et al. (2015). Firstly, tracheal, glottis and chest wall resistances were assigned constant values of 0.5 $\mathrm{cmH_2O.s.L^{-1}}$ each (Nagels et al., 1980), and chest wall elastance a value of 10.6 $\mathrm{cmH_2O.s.L^{-1}}$ (Barnas et al., 1990). These terms were added in series to the total airway impedance. Following this, cheek shunting impedances were added in parallel to the total model impedance, parameterised using the experimental data presented by Cauberghs and Van de Woestijne (1983) (for an illustrative diagram, see Figure 5.3). Cauberghs and Van de Woestijne (1983) collected this data with subjects supporting their cheeks during testing, and so the values represent the effect of shunting under normal FOT/IOS practice. To allow for use of values outside the initially presented set, we interpolated the data using the model $a/(b+f)$ for resistance, and $c\log(f)+d$ for reactance, where f is frequency, and a, b, c and d are data-fitting parameters. These shape functions were chosen due to their similarity to standard resistance and reactance curves (see Figure 1.8).

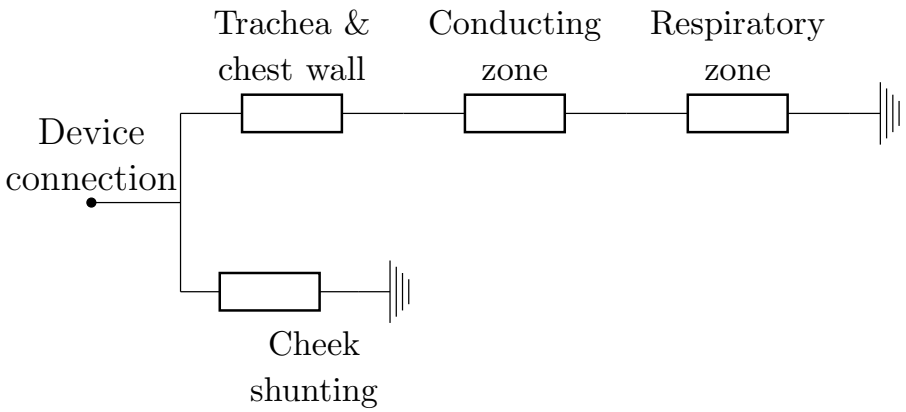

Figure 5.3: Diagram of the shunting model. Diagram illustrating the series and parallel interactions of cheek shunting impedance, tracheal and glottal resistance, and chest wall impedance with the conducting and respiratory zone models.

5.2.3 Clinical validation

The total impedance model was validated using patient-specific clinical data, collected by Professor Siddiqui's research group (in particular Professor Siddiqui, and Dr Soares). 129 asthmatic adults, and 11 healthy volunteers were recruited for the clinical study. Asthma was diagnosed by a secondary care physician, according to the current British Thoracic Society guidelines (British Thoracic Society, 2016), with severity defined according to the Global Initiative for Asthma (GINA) treatment intensity steps (Global Initiative for Asthma, 2017). Impulse oscillometry was performed three times for each patient, under standard procedure (Oostveen et al., 2003). Participants wore a nose clip and supported their cheeks (to minimise shunting), while an impulse wave was delivered to their lungs via a loudspeaker connected to the mouthpiece. Each test lasted for a period of 60 seconds, during which the patient breathed tidally. From the pressure and flow measurements resistance at 5Hz (R_5), and 20 Hz (R_{20}) as well as reactance at 5 Hz (X_5), were all calculated. 20 of the asthmatic patients, and

10 of the healthy volunteers were part of the Bordas et al. (2015) virtual airway generation study, meaning 30 of the 35 patient-specific structures in the Bordas set have corresponding clinical impedance measurements.

For each of these structures, total lung resistance and reactance at 5 Hz and 20 Hz were simulated. Comparisons of simulated and physically measured R_5, R_{20}, X_5 and f_{res} values can be seen in Figure 5.4, with corresponding R^2 values of 0.35, 0.28, 0.22, and 0.25 respectively. As the figure shows, the simulated resistance values clearly correlate with the physical resistance measurements, with relatively little scaling between the two. Two significant outliers can be noted, both corresponding to severely asthmatic patients. This is to be expected, given that the segmentation of the virtual structures is only accurate to approximately generation 10. Thus, the differences between virtual and physical structures (and corresponding breakdown of correlation) is expected to be most strong in severely asthmatic patients whose disease originates at a depth lower than generation 10. The reactance measures also appear to be correlated, however, this correlation is noticeably more noisy than that of the resistance measures. This is most likely due to the constant-phase model not incorporating patient-specific values of G and H, as in clinical studies, respiratory zone elasticity changes (as occur in many lung diseases) appear to affect reactance more strongly than resistance (Crim et al., 2011).

Overall, the results in Figure 5.2 and 5.4 suggest that the model is capable of capturing physical values with enough accuracy to distinguish between the effects of different disease states, particularly in regards to resistance measures. This provides a

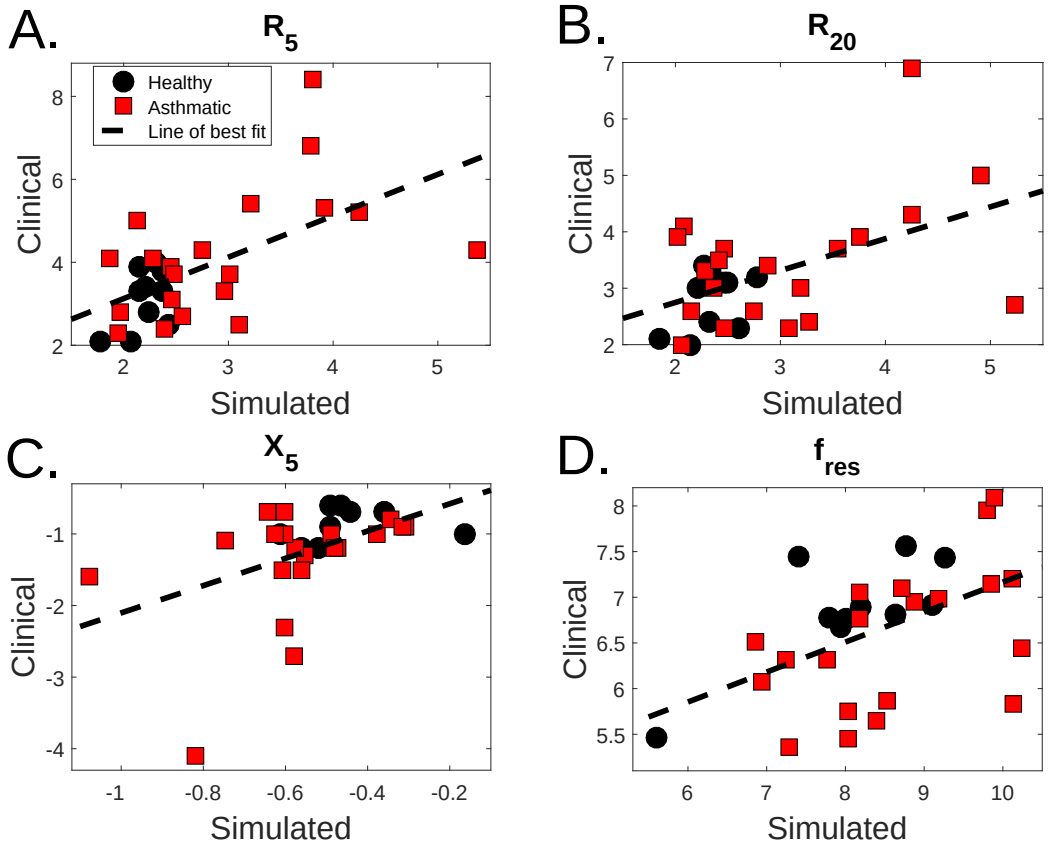

Figure 5.4: Correlation of clinical and simulated resistance and reactance. A comparison of clinical and simulated resistance at 5Hz (A), 20Hz (B), reactance at 5Hz (C), and resonant frequency (D). The line of best fit is given for each comparison. The fits have R^2 values of 0.35 (R_5), 0.28 (R_{20}), 0.22 (X_5), and 0.25 (f_{res}) respectively, with all fits having strong statistically significant ($p \ll 0.05$). The correlation of resistance measures is noticeably less noisy than that of the reactance measures.

foundation for the application of the model to investigate the utility of $R_5 - R_{20}$, as a detector of small airways dysfunction.

5.3 Analysis of R5-R20 as a small airways dysfunction measure

Following validation of the computational model, we aim to apply it to a more targeted question than the exploratory analyses detailed in Chapters 3 and 4. As explored in the literature review, one of the clinical challenges facing the FOT and IOS is the lack

of simple frameworks to precisely interpret test outputs. Given the results in Chapter 4, it appears sensible that the reactance indices and $R_5 - R_{20}$, may be interpreted primarily as indicators of small airways dysfunction. Using the updated impedance model (outlined in Section 5.2.2), we aim to probe this question more deeply, in particular focusing on $R_5 - R_{20}$, due to the physical interpretation of resistance being simpler than that of reactance.

To more clearly investigate the response of the index to small airways dysfunction, we perform two batches of simulations on the baseline structure from the Bordas set, with constrictions artificially applied at various depths. Within the first batch, constrictions were applied to all branches of a chosen Strahler order (1-12). These constrictions were either applied homogeneously, with a constant constriction factor c, or heterogeneously, drawing constrictions from the normal distribution $\mathcal{N}(c, 0.2c)$. Similar to in Chapter 4, any constriction factors which exceeded 95% were floored to this value. Since constrictions were applied to a whole Strahler order at a time, a maximum mean factor of 0.7 (representing a 70% reduction in radii) was chosen, to avoid non-physical closure of the entire airway tree. With this in mind, simulations were performed using $c = 0, 0.1, 0.2, \ldots, 0.7$. For each simulation, the output $R_5 - R_{20}$ was calculated, with results shown in Figure 5.5. As the figure shows, the response of $R_5 - R_{20}$ is greatest within the lower Strahler orders, peaking at order 6. This result could be seen in both the homogeneous and heterogeneous constriction scheme. Interestingly, the index showed a negative response under severe constriction of the central airways (orders 11-12). As expected, heterogeneous constriction also increases

the noise of the response, leading to less smooth transitions as severity and depth are increased.

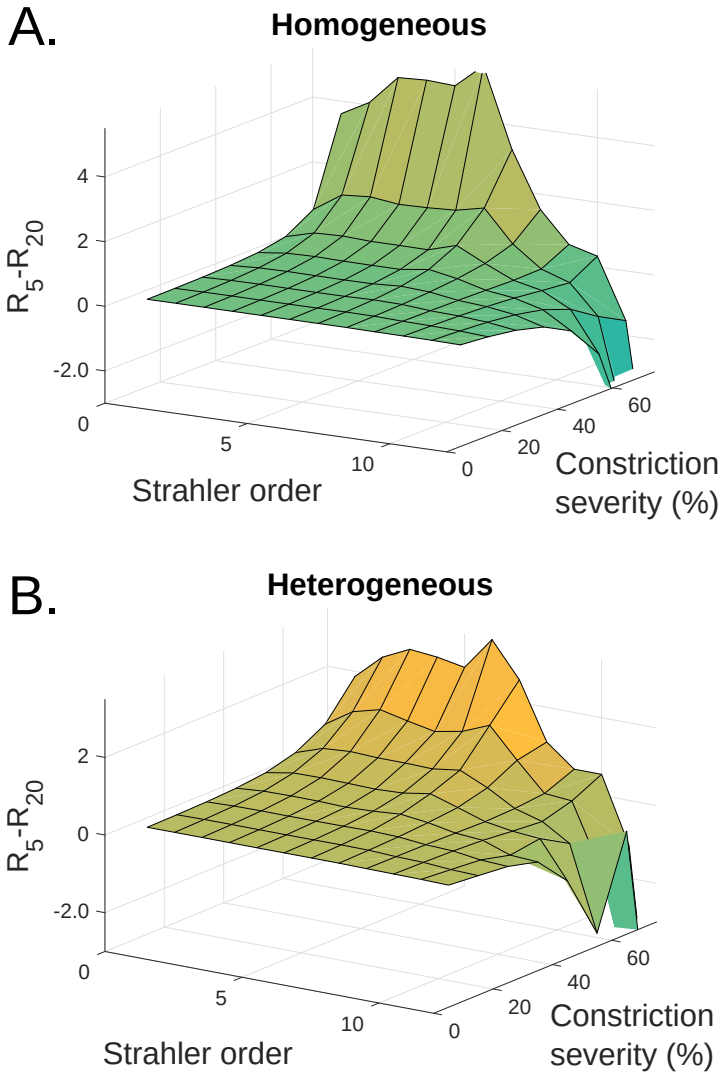

Figure 5.5: Simulated response of R_5-R_{20} to bronchoconstriction of a Strahler order. The response to homogeneous (A) and heterogeneous (B) constriction can be seen for various constriction severities. In both cases output values are highest when constricting the small airways (orders 1-6), and a negative response is generated when severely constricting the upper airways (orders 11-12)

Within the second simulation batch, constrictions were instead applied to the lower half of airways (Strahler orders 1-6), or all of the larger airways (Strahler orders 7-12). Similar to the first simulation batch, constrictions were either applied homogeneously,

or heterogeneously, but using the constriction factors $c = 0, 0.01, 0.02, \ldots, 0.7$. Results from this batch of simulations can be seen in Figure 5.6. Similar to the results of Figure 5.5, this figure shows a strong positive response of $R_5 - R_{20}$ to small airways constriction, while central airways constriction creates a negative response (though this response becomes positive again under severe constriction). We note that the response in Figure 5.6 is of a much greater magnitude than in Figure 5.5, due to the significantly larger number of airways being constricted.

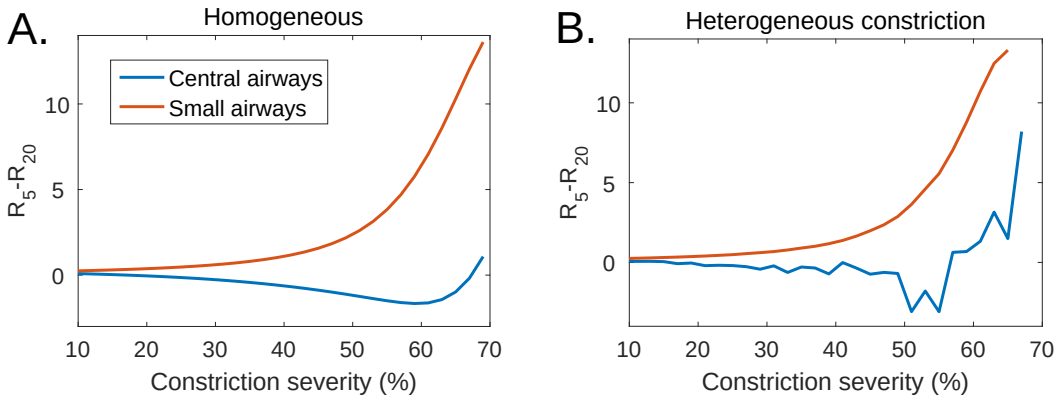

Figure 5.6: Simulated response of $R_5 - R_{20}$ to bronchoconstriction of the small and central airways. The response to homogeneous (A) and heterogeneous (B) constriction can be seen for various constriction severities. In both cases, output values are highest when constricting the small airways, and a negative response is generated when constricting the central airways.

To provide a final point of clarity to the results, further analysis was performed for three distinct cases: healthy, mild bronchoconstriction, and severe bronchoconstriction of the small airways. The healthy state was analysed using the baseline state of the airway structure, while the bronchoconstriction states were analysed by homogeneously constricting all small airways in the structure by 20% and 50% respectively. For each of the cases, the relative contribution of small airways resistance, central airways resistance, and of shunting to overall R_5 and R_{20} values, was calculated. These can be

seen in Figure 5.7, which shows that the small airways contribute more heavily to R_5 than R_{20}, regardless of the disease state. This, alongside the fact that small airways constriction drastically increases the relative contribution of small airways resistance, suggests that $R_5 - R_{20}$ will respond strongly to small airways bronchoconstriction.

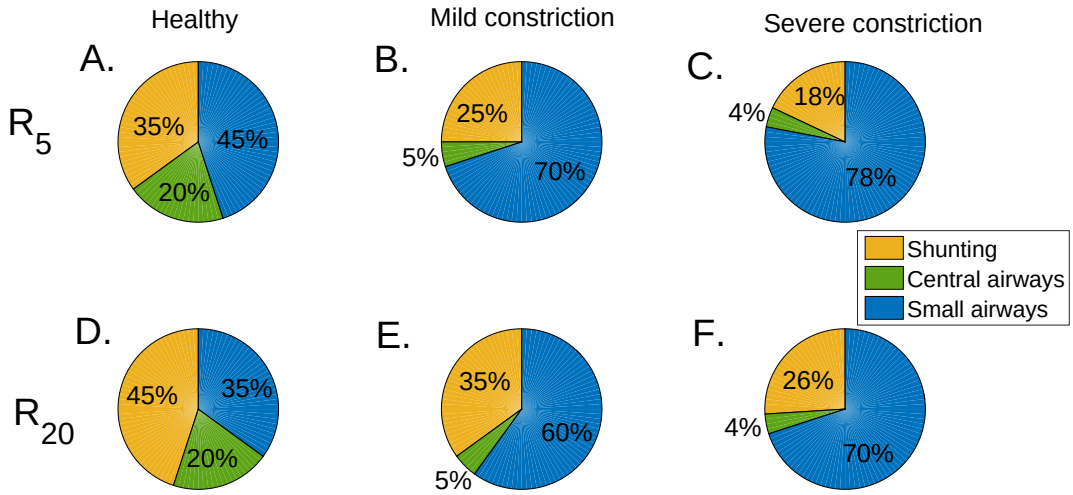

Figure 5.7: Relative contributions of small airway resistance, central airway resistance and shunting to R_5 (A-C) and R_{20} (D-F). The response can be seen in a healthy state (A,D), mild constrictive state (B,E), and severe constrictive state (C,F). In all cases, small airway resistance contributes more heavily to R_5 than to R_{20}, and is magnified in the presence of small airways constriction. The corresponding $R_5 - R_{20}$ values are 0.126, 0.222, and 0.8412 $cmH_2O.s.L^{-1}$ for healthy, mild and severe respectively.

5.4 Discussion

The integration of the FOT and IOS into clinical practice can only be done if there are straightforward and effective ways to interpret test outputs. In this study, we aimed to strengthen the interpretation of $R_5 - R_{20}$ as a detection tool for small airways bronchoconstriction, through the use of computational simulations performed on a clinically and experimentally validated model.

5.4.1 Validation of the model

Model validation was first performed using a 3D-printed airway, to analyse the ability of the model to capture airway impedance, without accounting for shunting or respiratory zone contributions. The correlations between the physical and simulated model are incredibly strong, for both resistance and reactance. However, it can be noted that while the model recreates the response of the physical structure to obstruction and airway closure, the simulated values are significantly lower than the physical resistance. This may in part be due to the 1D nature of the virtual approximation, meaning it cannot account for ridging along the airways, and similar phenomena which may cause turbulent effects.

Equally though, we note that the physical values of R_5 and R_{20} are extremely high (the baseline values are near 0.2 kPa.s.L^{-1} in Figure 5.2), which is the same level that would be expected for a healthy patient's entire lung resistance (Crim et al., 2011). This is despite the fact that the physical model contained less than 100 terminal branches, as opposed to the 100,000 or so in a normal adult lung. We believe that this discrepancy is primarily due to shunting resistance generated at the point of attachment of the 3D-printed structure to the FOT device, as this attachment was made using blue-tack. Another potential cause may have been a lack of appropriate lubrication in the structure, leading to an increase in resistance. While the virtual model does not directly incorporate lubrication, its approximation of 1D flow is built on an assumption of sufficient smoothness of the airway.

This conclusion is strengthened when considering the correlation of simulated

values with clinical measurements (Figure 5.4). No significant scaling is seen between the two datasets, and a reasonable ability of the model to separate high and low responses is illustrated. It can be noted that while the model is clearly capturing significant differences between asthmatic and healthy subjects, the R^2 values are quite low for both fits. For the resistance measures this can be seen to be driven by two significant outliers, both of which are severe asthmatic patients (GINA > 3). For the reactance measure, the variance is significantly higher.

It is not expected that the model would be able to perfectly recreate patient-specific resistance values. Creation of the virtual structures relies on algorithmic generation for the smaller airways, which is performed by propagating down airway sizes (with a constant scaling factor) from the last airways that could be segmented from the CT scans. This means that the lung structures inherently assume that levels of bronchoconstriction within generations 6-10 are indicative of levels of bronchoconstriction in generations 10-16. While this will be true for healthy patients, and for many asthmatics, it clearly does not hold in all cases. Considering the two outliers in resistance correlations in Figure 5.4, one may be a case where the algorithm over-predicted and the other where the algorithm under-predicted constriction severity of the terminal bronchioles. If this is the case, the correlation may potentially be improved by obtaining more specific structural information than is given through the CT segmentation process outlined in Chapter 2. This idea is briefly explored in Appendix B.

We also note that the model relies on constant contributions for tracheal, and chest

wall impedances, cheek shunting, and within the respiratory zone (the constant-phase model). In practice, all of these contributions are patient-specific (and in the case of shunting, measurement specific). However, without patient-specific experimental measurements to parameterise the contributions a constant model was deemed the most appropriate choice. Elasticity changes in the respiratory zone (as would be seen in COPD) have been shown to more strongly affect reactance than resistance (Crim et al., 2011). Considering this, the use of a non patient-specific constant-phase model may explain why the X_5 correlation is significantly worse than that of the resistance measures.

Importantly, we note that the studies contained within this thesis use the impedance model to investigate responses to bronchoconstriction primarily in a global population sense. Given this, achieving a perfect correlation with patient-specific values is not actually necessary. Rather, confidence that the model is capturing the most important underlying physical mechanisms accurately is needed. Thus, the strong correlation of the physical and virtual model responses to airway occlusion, alongside an ability of the model to separate responses of healthy and asthmatic subjects provides justification for the suitability of the computational model for the studies we have performed.

5.4.2 Validation of $R_5 - R_{20}$

The results in Figures 5.5-5.7 provide evidence that $R_5 - R_{20}$ responds strongly to bronchoconstriction in the small airways. Interestingly, in Figure 5.5 we note that the index reached its peak value under constriction of Strahler order 6. This is due to the

interplay of two different forces. As depth is increased, airways become progressively smaller, leading to an increase in the resistance of each branch (the dependence of resistance on diameter can be clearly seen in Equation (2.17)). However the number of branches also increases exponentially, creating many different pathways and leading to a reduction in overall resistance. So applying a constriction to a lower branch causes a larger change in local resistance than constriction of a more proximal branch, but may have less of an effect on total lung resistance, due to the large number of potential pathways that a signal can take (for an illustration of this, see Figure 5.8). The crossover point for these two opposing phenomena differs depending on the frequency, with lower frequencies considered to have deeper 'probing depths' (Bhatawadekar et al., 2015), leading to a more distal crossover point.

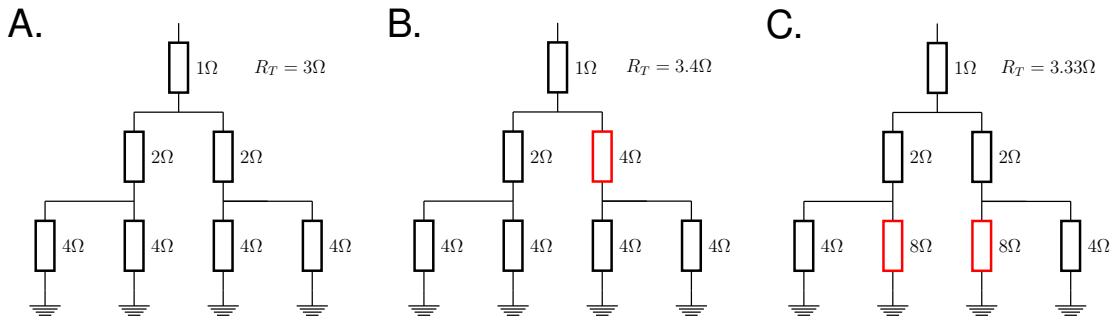

Figure 5.8: Illustration of the effect of constriction at different depths in a toy resistive circuit. The initial tree (A) has total resistance 3Ω. Constricting 50% of medial branches in the network (B) leads to a larger total resistance than constricting 50% of smaller branches (C), despite this leading to a lower local resistance increase.

This phenomenon is also responsible for the negative $R_5 - R_{20}$ values seen under severe constriction of the upper airways (orders 11-12). This occurs as, due to the assumed deeper probing depth of the 5 Hz signal, the 20 Hz signal appears to be more responsive to proximal constriction. It should be noted though, that as airway closure

is approached, the 5Hz signal will lose the ability to probe deeply, and thus $R_5 - R_{20}$ will become positive again. The start of this behaviour can be seen in Figure 5.6, and was also illustrated in the results of Chapter 4.

One point to note, is that homogeneous constriction was seen to consistently create a more positive response than heterogeneous constriction. This is in apparent contradiction to prior results in the literature (Campana et al., 2009). However, this is actually an artefact of constricting all airways of a given order. In the heterogeneous scheme, some constriction rates will be significantly higher or significantly lower than the mean. Since all pathways are being constricted, the addition of a small number of significantly milder constrictions leads to the existence of more relatively healthy pathways. This creates an overall reduction in resistance, relative to the homogeneous scheme, due to the parallel nature of resistance interactions. However, when there are already many healthy pathways (i.e. when constrictions are only applied partially to an order), the effect of a few significantly severe constrictions is more pronounced, and the effect of the milder constrictions is less pronounced, meaning the heterogeneity increases total resistance.

To illustrate this, we simulate $R_5 - R_{20}$ under varying degrees of homogeneous and heterogeneous constriction of different percentages of the small airways, in a healthy subject from the Bordas set. The results (averaged over 20 runs each) are given in Table 5.1. As the table shows, under partial constriction of the small airways, the heterogeneous scheme produces significantly higher index values than the homogeneous scheme. However, this difference lessens as the total percentage of airways being

Constriction severity	No. airways constricted	$R_5 - R_{20}$ (Homogeneous)	$R_5 - R_{20}$ (Heterogeneous)
10%	10%	0.119	0.145
	40%	0.153	0.193
	80%	0.214	0.242
50%	10%	0.178	0.210
	40%	0.467	0.469
	80%	1.498	1.428
90%	10%	0.172	0.203
	40%	0.476	0.555
	80%	2.219	2.183

Table 5.1: $R_5 - R_{20}$ values under partial constriction of the small airways. The heterogeneous scheme appears to produce larger values than the homogeneous scheme, except under constriction of nearly the entire airway tree. All simulations were performed in a healthy subject from the Bordas set.

constricted approaches 100%, as is expected.

5.4.3 Clinical significance

These results suggest that $R_5 - R_{20}$ may have sufficient sensitivity to be utilised as a detection tool for small airways disease such as asthma. Some clinical studies have explored the impact of small airways bronchoconstriction treatments, such as small particle corticosteroids, upon this index in asthmatics (Hoshino, 2010; Hozawa et al., 2011; Yamaguchi et al., 2009). However, to date there is a lack of randomised controlled trials investigating the effects of different particle size inhalers, and using $R_5 - R_{20}$ as an indicator. The results in this chapter provide evidence of the potential utility of such a study, and the broader use of $R_5 - R_{20}$ to detect and diagnose small airways disease.

A prior study by Campana et al. (2009) used imaging-derived functional modelling techniques to identify that significant heterogeneous small airways constrictions would

be needed to recreate ventilation defects as seen in the asthmatic lung. We extend upon this work by showing that even in the presence of shunting (which is known to influence frequency dependence of resistance (Smith et al., 2005)), significant proportions of the $R_5 - R_{20}$ response is due to small airways constriction, but the degree of airway constrictions needed to create this response is smaller.

Further to this, the results suggest that the level of constriction needed to create a significant response in $R_5 - R_{20}$ may be quite small. Considering the results in Table 5.1, the baseline response was nearly doubled from 10% closure of 40% of airways. This suggests that a significant response in the index may be detectable in subjects with early stage development of small airways disease or dysfunction.

The work in this chapter demonstrates strong potential clinical utility of $R_5 - R_{20}$ as a small airways dysfunction tool. Clearly, the computational results outlined in this chapter are not enough to fully justify the incorporation of $R_5 - R_{20}$ into clinical practice as a diagnosis tool. However, these results provide a foundation for interpretation of the index in terms of the underlying physiology. They give a strong justification upon which a meaningful clinical study could be formed.

Collaboration with Professor Siddiqui's research group is ongoing, to provide clinical data which can be used to test this hypothesis. Many of the computational results presented within this chapter form an underpinning to a more detailed clinical study, currently under review.

5.4.4 Comparing impedance with and without shunting

The clinical validation presented in this chapter relies on the incorporation of a shunting component to the model, unlike the results in Chapter 4. This adaptation was made to attempt to account for a clinically relevant source of noise in the data. However, since the model has been adapted from the original design, there is a need to illustrate that the results from Chapter 4 still hold after the incorporation of shunting. To do this, we perform a recreation of Figure 4.1, using the simulation protocol outlined in Chapter 4, with the model being updated to incorporate shunting effects. The recreation can be seen in Figure 5.9. As the figure shows, the incorporation of shunting causes a significant shift in model values, drastically increasing resistance, while reducing reactance (though to a lesser degree). However, the response to constriction severity is near identical to that seen in Figure 4.1. This gives us confidence that the results and conclusions from Chapter 4 would still hold with the updated and validated model.

5.4.5 Limitations

As discussed in the previous section, the main limitation of the model is the use of non patient-specific, constant contributions for shunting, tracheal and chest wall impedances, and the constant-phase respiratory zone model. Non patient-specific model components have primarily been used due to the lack of patient-specific information which could effectively inform the model parameters. Equally, while the airway impedance model was validated (Figure 5.2), the structures themselves rely on a degree of algorithmic generation. These two factors may explain a large proportion

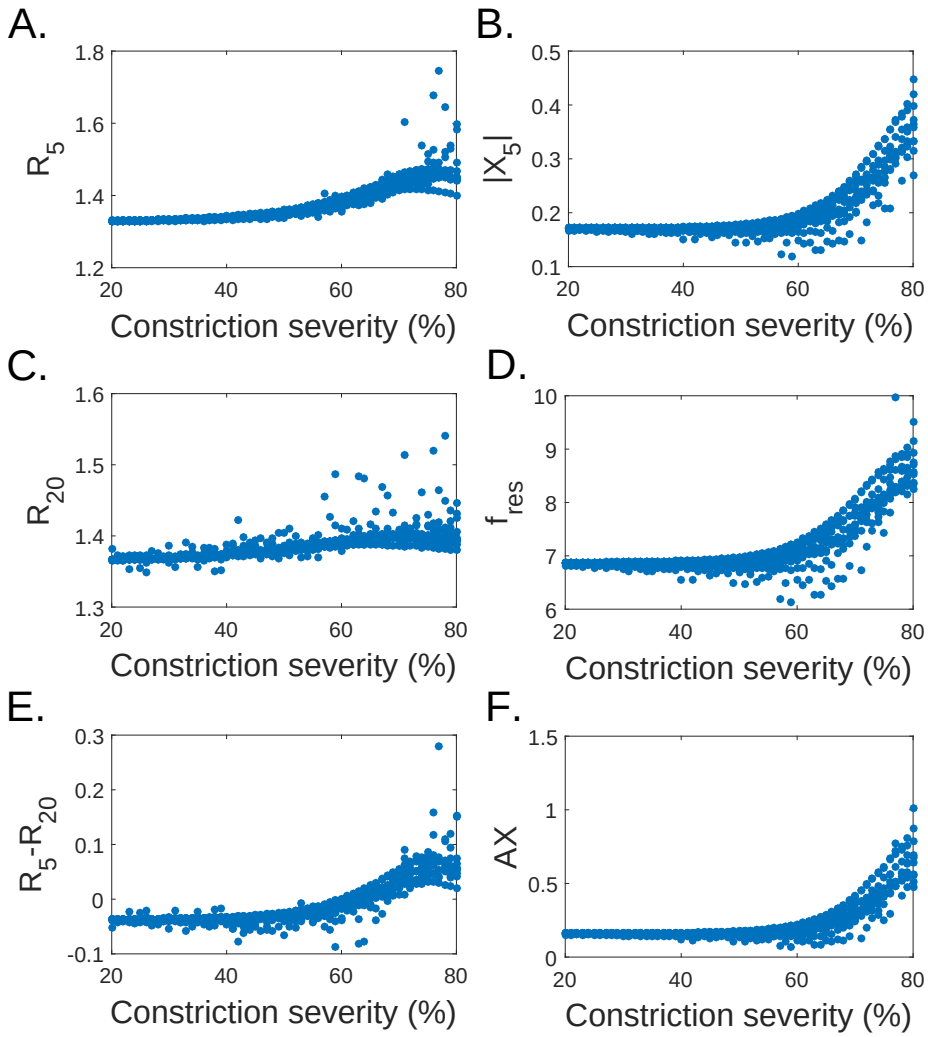

Figure 5.9: Simulated response of the resistance (A,C,E) and reactance (B,D,F) measures to constriction severity, with cheek shunting incorporation. Constrictions were applied homogeneously to 20% of airways at a given Strahler order (1-10).

of the variance seen in Figure 5.4.

While these represent limitations of the model, we do not believe that they represent limitations of the study itself. The results in this chapter illustrate the ability of the model to respond appropriately to changes in airway size and structure, and suggest its ability to effectively respond to bronchoconstriction. This gives strength to the conclusions about $R_5 - R_{20}$ derived from the model, which were inferred

based on simulations performed in a global sense, not relying on perfectly recreating patient-specific values, but rather investigating overall trends.

5.5 Summary

Within this chapter we have applied a computational model of lung impedance to investigate the utility of $R_5 - R_{20}$ as an indicator of small airways disease. The model was first validated using a combination of patient-specific clinical measurements, and physical measurements taken from a 3D-printed airway tree. Following validation, the response of the index was simulated under a variety of bronchoconstrictive scenarios. These simulations illustrated a consistent elevated response of the index under constriction of small airways, comparative to central airway constriction. This suggests potential utility of $R_5 - R_{20}$ as an indicator of small airways dysfunction, in diseases such as asthma. The results in this chapter form a foundation which could be used as a platform for future clinical studies.

6

Clinical validation and application of the washout model

In Chapters 3 and 4 we illustrated how computational models of the multiple-breath washout may help provide valuable clinical information about this test. However, similar to the impedance model, for these results to be meaningful, the ability of the model to capture clinical behaviour needs to be validated. Within this chapter, we perform this validation, by comparing model results to clinical data, as well as broader results in the literature. Following this, we show how the multiple-breath washout can be used to analyse a more meaningful clinical question.

Work within this chapter is based on the journal article:

- *Modelling the effects of gravity on inert-gas washout outputs*, published in *Physiological Reports*;

and conference papers:

- *Inert-gas washout and forced oscillation technique show sensitivity to the degree of regionalisation of bronchoconstriction*, presented at the *2*017 American Thoracic Society Congress;

- *Sacin responds to total compliance heterogeneity, and is less sensitive to regionalisation than scond*, presented at the *2*018 American Thoracic Society Congress.

This work relied heavily on clinical data collected by our collaborators. In particular, clinical data was collected and analysed by Dr Gonem, Professor Brightling, and Professor Siddiqui (University of Leicester). This clinical data was taken from the baseline values of a placebo-controlled trial of Fevipiprant, sponsored by Novartis UK (Gonem et al., 2016).

6.1 Rationale

In Chapter 2 of the thesis we outlined a model of the MBW, suitable for simulation of ^{3}He and SF_6 washouts in the lung. We followed this work in Chapters 3 and 4, by applying the model to investigate the response of MBW outputs to various types of bronchoconstriction, particularly in the small airways. Through this we illustrated that

LCI and s_{cond} showed strong sensitivity to constriction severity, but little sensitivity to constriction depth.

However, during model development, many other questions were raised about the underlying sensitivities of test outputs. In particular, while developing the gravitational gradient component of the model, it became clear that there is a lack of precision in understanding how gravity may effect inert-gas washout indices. It is well known in the literature that flow heterogeneity is affected by body position, due to the 'Slinky effect' (Hopkins et al., 2007), where the lung deforms unevenly under gravitational strain (see Figure 6.1). However, if flow heterogeneity is primarily driven by airway structure, and tissue properties (Horsfield and Cumming, 1968), it could be assumed that body position would have only minor effects on PFT test outputs.

There is an array of studies in the literature investigating the effect that body position and gravity have on PFT outputs, both in research and in clinical practice. In most studies relatively little difference is seen in healthy subject groups as gravitational forces are changed, or body position is altered (Behrakis et al., 1983; Grönkvist et al., 2002; Peces-Barba et al., 2004; Prisk et al., 1995; Rodríguez-Nieto et al., 2002). However, while the literature is more limited in studies of unhealthy patient groups, the results are inconsistent, noisy, and often contradictory. This has been illustrated in both clinical research studies (Attinger et al., 1956; Badr et al., 2002; Manning et al., 1999) and imaging studies (Petersson et al., 2007), meaning there is a lack of clarity as to how testing position affects outputs in unhealthy patient groups. This has potential ramifications for many clinical practices, such as mechanical ventilation,

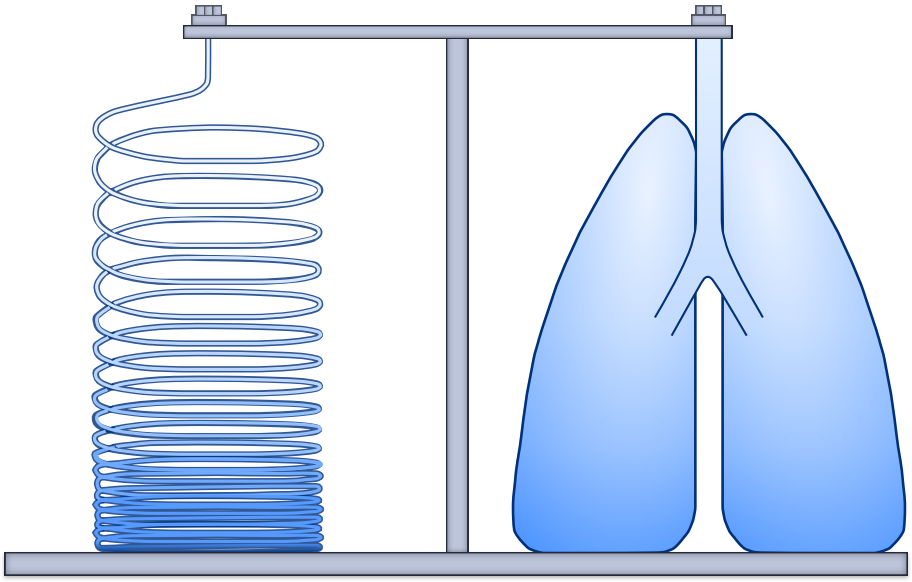

Figure 6.1: Simple illustration of the Slinky effect. Due to gravitational effects, the lungs are more compressed at the bottom than the top. This allows the lower regions to undergo a higher degree of ventilation, while the upper regions have less ability to expand/contract. Figure created with the assistance of Ms Sanjana Sharma.

where there is disagreement over the most appropriate positioning protocols for the procedure (Fessler and Talmor, 2010; Thomas and Paratz, 2007).

A variety of PFT outputs have been shown to be sensitive to the body position in which the test is performed. This sensitivity is particularly prominent for patients with unilateral disease (Gillespie and Rehder, 1987; Prokocimer et al., 1983; Zack et al., 1974), suggesting that the sensitivity may be driven more precisely by the gravitational ventilation gradient. Given the contradicting results within the literature, we believe that this is an appropriate phenomena to investigate using the previously developed computational model.

Within this chapter, we apply this rationale to analyse the response of LCI and s_{cond} to changes in body position. We first perform a detailed validation of the model,

using both clinical data, and broader results from the literature. This is performed both to provide strength to the interpretation of simulation results in Chapters 3 and 4, and to provide more confidence in the ability of the model to probe the more targeted clinical question within this chapter. Following this validation, we analyse the response of both MBW outputs to simulated body position changes within the Novartis set. Through this analysis, we show that body position has a significant, but consistent and quantifiable effect on the MBW. This is further illustrated by reverse-engineering this process to successfully classify disease regionalisation based on MBW output changes between opposing positions. We close with a comparison of results in sitting and supine positions, the two most common body positions used during clinical pulmonary function testing.

6.2 Validation of the washout model

Before the computational model can be applied to analyse the effect that gravity may have on washout indices, it should first be validated to ensure it is accurately capturing the underlying mechanisms of the test. However, given the focus of this chapter on investigating gravitational effects, we first briefly recap the gravitational component of the model.

6.2.1 Gravitational ventilation gradient

Full details of the MBW model have been given in Chapter 2, however, we briefly restate the gravitational component of the ventilation model here. In short, the simulated ventilation profile is driven by the pressure gradient from the trachea to the

pleural cavity, with pleural pressure given by the model

$$P_{pl}(t) = A_{pl} + R_{pl} \sin\left(\frac{2\pi t}{T}\right),$$

where A_{pl} and R_{pl} are the mean pleural pressure and pleural pressure range, t is time, and T is the breathing period. A gravitational gradient is incorporated into the model by directly applying a linear gradient to R_{pl}, meaning

$$P_{pl}(z,t) = A_{pl} + R_{pl} \sin\left(\frac{2\pi t}{T}\right) f(z),$$

where z is the spatial coordinate of the axis that gravity is acting in, and $f(z)$ is the linear gradient factor, give as:

$$f(z) = \left(1 - \frac{z - \bar{z}}{z_{\max} - z_{\min}} g_{\text{strength}}\right),$$

where z is vertical height from the ground, $\bar{z}, z_{\max}$ and $z_{\min}$ are the mean, maximum and minimum heights of the distal ends of the set of terminal bronchioles, g_{strength} is the strength of the gradient (set as 1.5%/cm).

Values for A_{pl} and R_{pl} are initially set at -1500Pa and 500Pa respectively, and iteratively updated to enforce the desired FRC and breathing depth (using the iterative procedure outlined in Chapter 2). Using this model, by modifying the axis and direction that gravity acts in, five different body positions can be simulated: orthostatic (cranio-caudal axis), supine and prone (anterior-posterior axis) and left and right-lateral (transverse axis), as well as simulation without gravity.

6.2.2 Clinical data collection

To validate the MBW model, outputs were directly compared to clinical data. Clinical data was collected prior to this study, with full details of collection summarised by Gonem et al. (2014), with the data from asthmatic subjects being derived from baseline data of a placebo-controlled trial of Fevipiprant (Gonem et al., 2016).

Washouts were performed by 31 subjects, 7 of which were healthy, and 24 of which were asthmatic (as classified by the GINA number (Global Initiative for Asthma, 2017)). Each washout was performed in triplicate using standard guidelines (Robinson et al., 2013), and the method described by Horsley et al. (2008). The washouts were performed in an upright sitting position, using SF_6 as the tracer gas, with s_{cond} and LCI being calculated from each. The clinical data presented in this chapter is the pooled average for each subject, over the three runs. All washouts were monitored by an Innocor photoacoustic gas analyser (Innovision A/S, Odense, Denmark).

Each of these 31 subjects also underwent inspiratory-expiratory CT imaging, in the supine position. Using the processes outlined in Chapter 2, these images were used to create patient-specific conducting zone structures, collectively referred to as the Novartis set (creation of the structures was performed by Dr Rafel Bordas). It should be noted, that while the same segmentation and algorithmic generation process was used, the structures in the Novartis set are completely distinct from those in the Bordas set, which is used in many other chapters in this thesis.

Similar to in previous chapters, all s_{cond} values are given in L^{-1}, and LCI in turnovers.

6.2.3 Clinical validation

Given the access to clinical MBW measurements for all 31 patient-specific structures, model validation was performed by simulating the clinical washout under similar conditions, allowing for direct comparison. For all 31 structures, an SF_6 washout was simulated with an orthostatic gravitational gradient (as clinical measurements were taken sitting). However, unlike in prior chapters, the washouts were simulated with the convection-diffusion model, instead of the pure convection model. This was done to minimise any potential sources of error within the clinical validation. We briefly present an analysis of the effect of diffusion at the end of this chapter.

The correlation between clinical and simulated values of s_{cond} and LCI can be seen in Figure 6.2. As the figure shows, both simulated measures have quite a strong correlation against the clinical data, with strong statistical significance ($p \ll 0.05$), and reasonable R^2 values (0.51 and 0.57 respectively). The recreation of clinical data is accurate for both healthy and asthmatic subjects, with both fits being close to the unity line, indicating no significant scaling of values by the model. The Bland Altman plots show low bias between the model and clinical data, with only one significant outlier. The strength of this correlation is particularly noteworthy given that the virtual structures rely on algorithmic generation to create many of the small airways. It should be noted that the only patient-specific information given to the model was structural information (branch-lengths, branching angles, and airway radii), and the subject FRC.

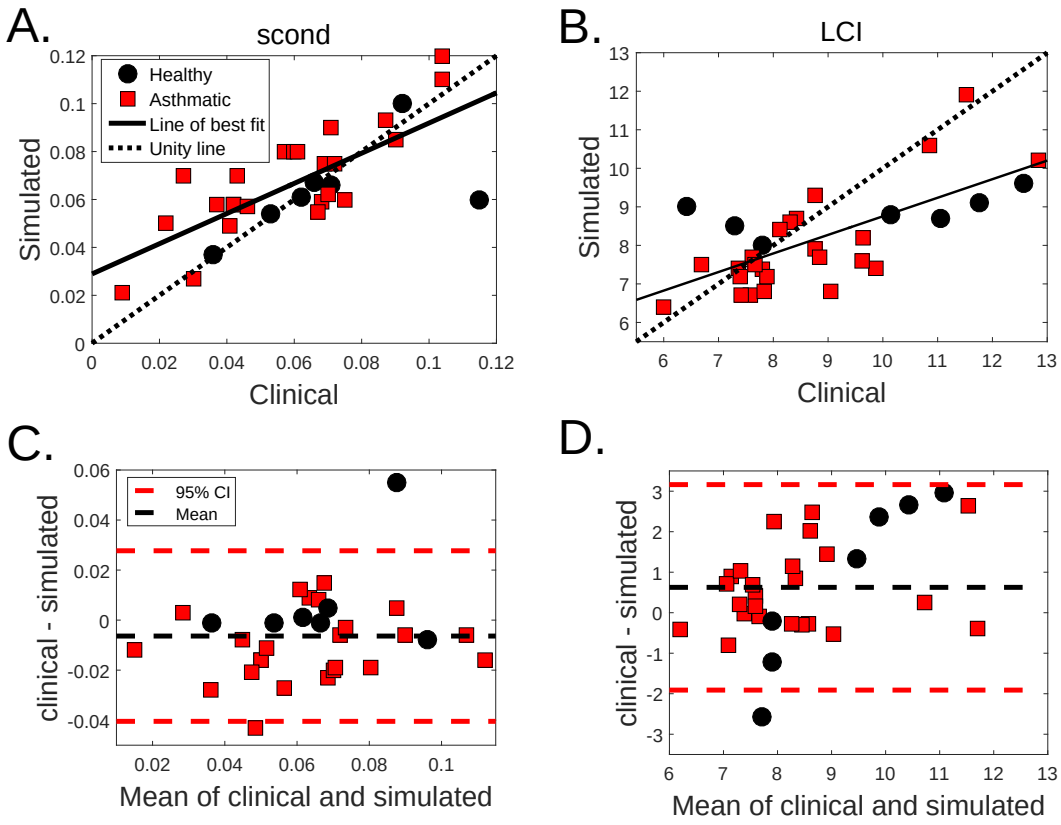

Figure 6.2: Comparison of clinical and simulated s_{cond} (A,C) and LCI (B,D) values for healthy and asthmatic subjects. Direct comparison is given (A,B), with a line of best fit, and the unity line, as well as a Bland Altman plot (C,D). Both fits are strongly statistically significant ($p \ll 0.05$), with R^2 values of 0.51 and 0.57 respectively, and low bias.

6.2.4 Validation against the broader literature

The clinical validation shown in Figure 6.2 is good, and provides strength to our ability to the use of the model to probe meaningful clinical questions. However, the validation was only performed in one body position. So while we can have confidence that the model is recreating clinical behaviours accurately, we cannot be sure that it is recreating ventilation changes (with respect to body position), as would be seen in real patients. Within the clinical study, MBW measurements were only taken in a single body position, meaning direct comparison of the virtual model to clinical

data in many different positions is not possible. We instead validate the gravitational component of the model by comparing model outputs to behaviours seen within the broader literature. To do this, we first simulate ventilation in a healthy lung structure from the Novartis set, across the five major body positions (orthostatic, supine/prone, left/right lateral), and without gravity. The relative ventilation during exhalation of each of the five lobes can be seen in Figure 6.3, with steeper curves indicating overall larger changes in ventilation.

We first note that the results in Figure 6.3 appear to accurately reproduce the 'Slinky' effect, with vertically higher lobes (relative to the gravitational axis) undergoing much larger changes in ventilation throughout the exhalation. Equally, we note that opposing axis distributions are not simple inversions of each other. For example, the prone distribution appears much more homogeneous than the supine distribution. This result is well known within the literature, having been illustrated in prior clinical studies (Mure et al., 2000). For more precise comparison, we note that the supine distribution creates a very similar pattern to what was illustrated in the work of Verbanck and Paiva (2016) (using data originally from (Jahani et al., 2015)), with the right-middle lobe changing the least during exhalation, and the lower lobes changing the most. Importantly, we note that the scales of exhalation are quite similar in both cases. As an example, the right-middle lobe reduces to approximately 80% of its maximum inhalation volume by end of exhalation in both Figure 6.3, and the work of Verbanck and Paiva (2016). The only major difference between the two profiles is that the physical data is more curved. This is most likely due to the linear nature of

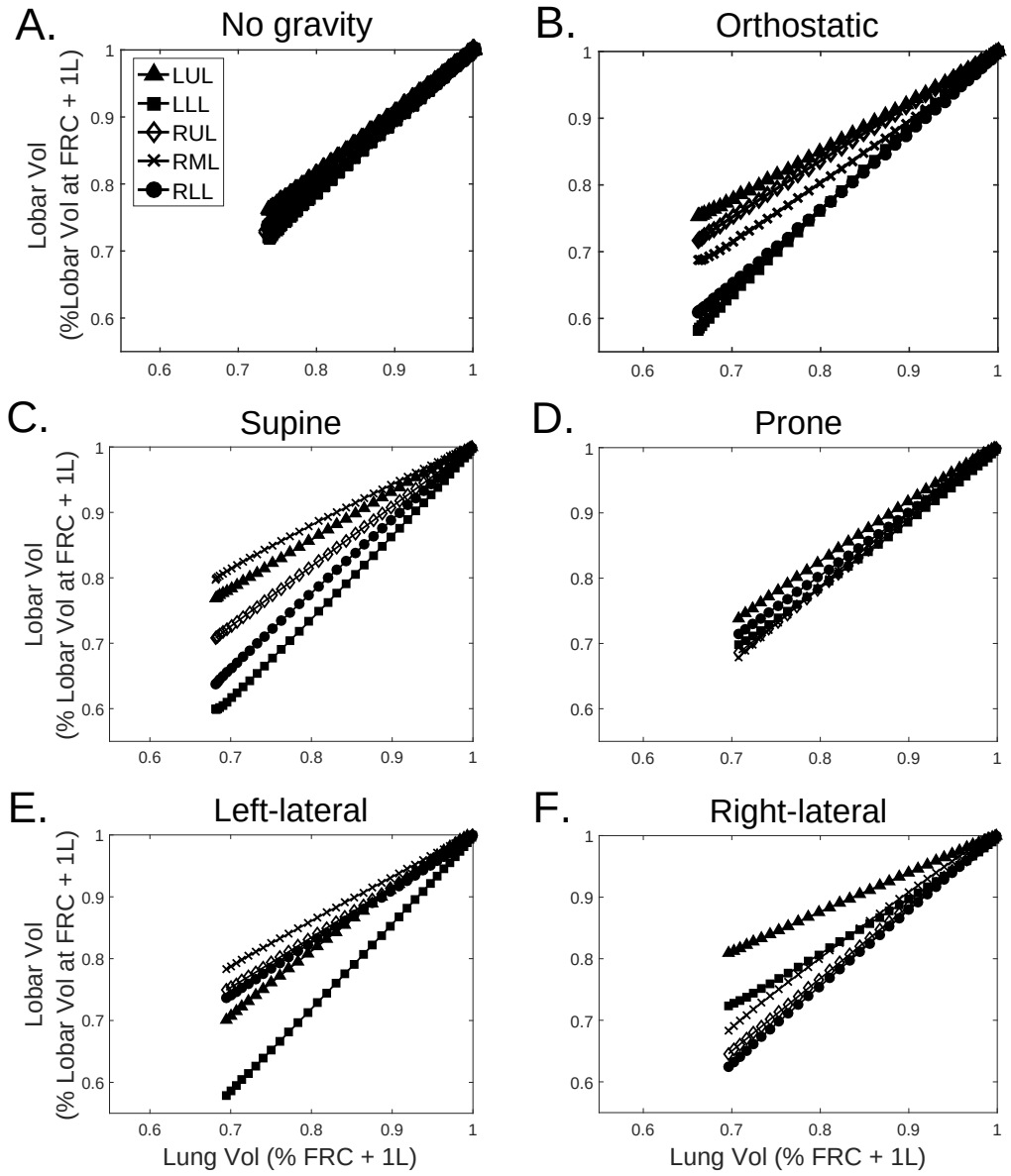

Figure 6.3: Relative ventilation of the five lobes during exhalation, in six positions. Ventilation profiles are given for the left-upper (LUL, triangle), left-lower (LLL, square), right-upper (RUL, diamond), right-middle (RML, cross), and right-lower lobe (RLL, circle). Profiles were simulated from a healthy lung without gravity (A), in orthostatic (B), supine (C), prone (D), left-lateral (E) and right-lateral (F). A flatter gradient indicates that the lobe experienced a relatively smaller change in volume over the exhalation.

our ventilation gradient, which is an efficient approximation, but not fully realistic. As discussed in Chapter 2, more complex tissue mechanics models exist for estimating gravitational gradients (Swan et al., 2012). Initially we investigated implementation

of these models, however, the overall changes to ventilation were considered too small to justify the extremely large increase in computational expense.

In Figure 6.4, we extend upon this validation by simulating ventilation maps (using the process outlined in Chapter 2) for the same healthy lung structure in the six scenarios. We see that these images also illustrate the 'Slinky' effect, with ventilation being greatest (denoted by brighter colours) in the lowest regions of the lungs (relative to the gravitational axis of each body position). Further to this, the results also match qualitatively to results seen in prior MRI studies in the literature (Hamedani et al., 2016; Petersson et al., 2007). In particular, the supine map strikingly resembles a clinical supine map from the work of Horn et al. (2014) (see Figure 3 in this paper). The ventilation ratio gradients (relative to the mean ventilation ratio) are 4.4, 2.8, 5.7, 5.4 and 4.9%.cm^{-1} for supine, prone, left-lateral, right-lateral and orthostatic respectively. We note that both the supine and prone gradients match to reported gradient values in the literature (Hamedani et al., 2016; Horn et al., 2014; Musch et al., 2002). This array of results gives us confidence in the ability of our gravitational model to realistically capture the effect that changes in body position may have on ventilation.

As a small note, care should be taken when interpreting Figures 6.3 and 6.4, to consider the positions of each lobe of the lung (see Figure 6.5 for a diagram). The upper and lower lobes are separated by oblique fissures, which are diagonal not horizontal, relative to the cranio-caudal axis (coronal plane). This means that the lower lobes are lowest to the ground in both supine and orthostatic positions. The

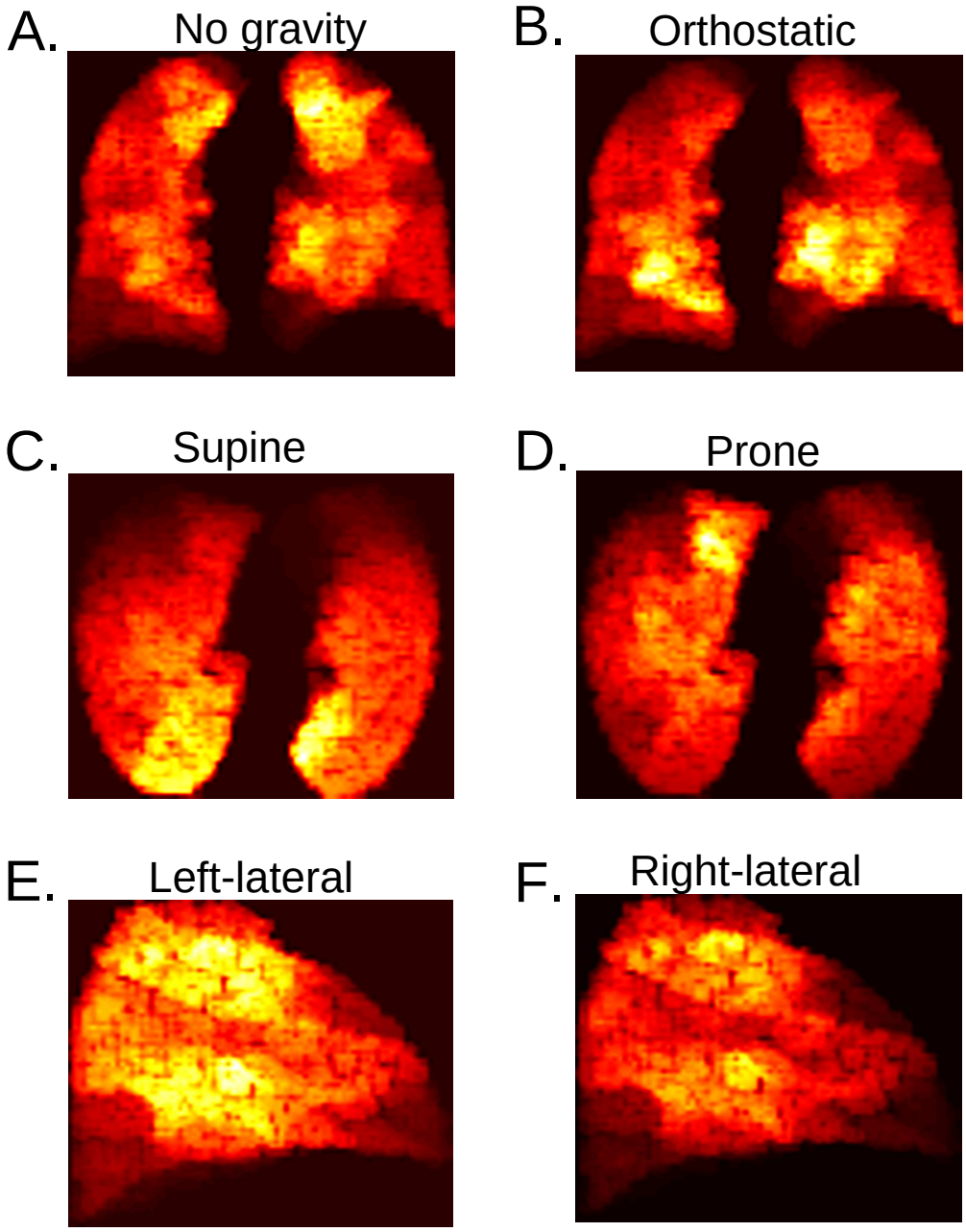

Figure 6.4: Specific ventilation ratios in a healthy lung in various body positions. Ventilation ratios in a central 3 cm lung slice. Ratios were calculated without gravity, and in orthostatic (A, B, coronal plane), supine and prone (C, D, transverse plane), and left and right-lateral (E, F, sagittal plane). Slices were taken directly from the centre of the lungs for coronal and transverse, and from the centre of the left lung for the sagittal plane. Brighter colours indicate higher ventilation, showing the magnitude of effect that body position can have. Panels A and B are oriented from base to head (bottom to top), Panels C and D from spine to sternum (bottom to top), and panels E and F from base to head (bottom to top). It should be carefully noted that panels E and F both originate from the left lung.

only significant change between the two positions occurs with the right-middle lobe, which is significantly smaller than the other lobes. Equally, the oblique fissure is more strongly vertical (relative to the cranio-caudal axis) in the left lung than in the right lung. This means that in a left-lateral position, the left-lower lobe is significantly lower than the left-upper lobe, while in a right-lateral position there is a much less pronounced difference between right-lower and right-upper lobes. Finally, both lungs are much larger towards the spine than the sternum. This combined with the precise position of the oblique fissures means lobar volumes are more even towards the sternum than the spine, leading to a more flat ventilation distribution when prone. We note that all of these phenomena are exhibited in Figures 6.3 and 6.4.

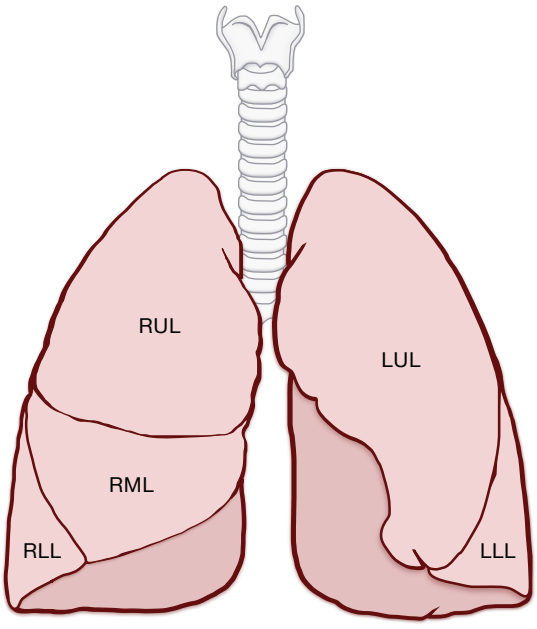

Figure 6.5: Diagram of the lung lobes. The diagonal nature of the oblique fissures can be seen. The left oblique fissure is also noticeably more vertical than the right oblique fissure. Figure created with the assistance of Ms Sanjana Sharma.

6.3 Investigation of the effect of body position

Figures 6.2-6.4 give validation of the MBW and ventilation model both in a direct clinical setting, and against broad patterns in the literature. Given the strength of this validation, we have confidence in the ability of the model to accurately capture the main driving mechanisms of the inert-gas washout, as well as the effect of gravity. This provides strength to the results in Chapters 3, and 4, and underpins the investigation of body position effects in the remainder of this chapter.

To investigate these effects, we start by considering the results in Figures 6.3 and 6.4 as a brief exploratory analysis of the data. They show that even in a healthy lung structure, changes in body position can have significant effects on ventilation heterogeneity. This response appears to be dominated by changes in relative lobar ventilation. Given these changes, the reason why healthy subject studies show stable results, while unhealthy results show stronger inconsistencies, can be hypothesised. In a healthy subject, all regions of the lungs should be well ventilated. This means that changes in relative ventilation of each lobe should only have mild effects on PFT outputs. However, in an unhealthy patient, disease heterogeneity would suggest that some regions of the lung ventilate more poorly than others. This means that body positions which increase ventilation to a specific lobe may mask lung disease which more dominantly affects that lobe. This is because the increase in gravitational ventilation may offset the decrease in ventilation caused by the disease process. Similarly, we hypothesise that a body position which decreases ventilation to a specific lobe may

exacerbate the response of a PFT to the disease.

To investigate this hypothesis, we first convert it to a series of more direct predictions. Considering the MBW, we hypothesise that s_{cond} and LCI will be decreased when changing to a position that better ventilates the area of most dominant disease. Thus, we take a significant change in either index when body position is altered, as indicative of regionalisation of lung disease. To be able to test whether this is the case, we first need a method for accurately classifying regionalisation of disease in an airway structure. Given the focus throughout the thesis on the investigation of bronchoconstriction, we choose to classify regionalisation by comparing mean terminal bronchiole sizes in different regions of the lungs. For a given structure, if the mean terminal airway size in the left lung was significantly larger ($> 10\%$) than in the right lung, the structure was classified as having 'Right' regionalisation, and vice versa as 'Left'. Similarly, if the mean small airway size in the lower lobes was significantly larger than in the upper lobes, the structure was classified as having 'Upper' regionalisation, and vice versa as 'Lower'. In either case, if no significant difference in airway size was seen, the structure was classified as having 'No' regionalisation in that axis.

If our hypothesis is correct, these classifications should be able to be consistently predicted through changes in MBW outputs. We expect both s_{cond} and LCI to be lowest (healthiest) when taken from a body position that best ventilates the most constricted region. Thus, we look at changes in these two indices between opposing positions, as indicators of regionalisation. For example, if LCI in supine is significantly greater ($> 10\%$) than LCI in prone, we take this as predictive of 'Upper' regionalisation

(as from Figures 6.3 and 6.4, supine best ventilates the lower lobes). We make similar predictions for 'Lower', 'Left', 'Right', and 'No', using LCI and s_{cond} between supine and prone, and left-lateral and right-lateral respectively.

To test this hypothesis, we simulate LCI and s_{cond} in all 31 of the patient-specific lung structures, in the four relevant body positions. We then compare predicted regionalisation (from MBW indices) to the actual regionalisation as measured by mean small airway sizes. To allow for simple evaluation of effectiveness, results were pooled from left-right classification, and supine-prone classification, leading to 62 data points. The accuracy of these classifications can be seen in Figure 6.6 and Table 6.1. As the figure and table show, both LCI and s_{cond} respond sensitively to the underlying regionalisation in the structure. Sensitivity and specificity are both high (100% and 68% for both LCI and s_{cond}), with a small number of false positives, and no false negatives. Interestingly, while both measures achieved identical classification rates, not all classifications were the same. It should be noted that in 12% (15/124) of classifications, an opposing classification was made (e.g. left regionalisation was predicted when right regionalisation had occurred), and that these were classified as false positives. The vast majority of these cases (11/15) occurred when classifying left and right regionalisation. We believe this may be due to the relative size differences between the left and right lung, meaning comparing mean small airway size in each lung isn't a perfectly balanced way of classifying regionalisation. Equally, this may partially be due to the limitations of classifying regionalisation using mean small airway size. In particular, s_{cond} is known to respond sensitively to sharp differences

	Upper	Lower	No upper or lower	Left	Right	No left or right
LCI	12 (16)	4 (5)	10 (10)	14 (15)	8 (9)	7 (7)
	75%	80%	100%	93.3%	88.9%	100%
s_{cond}	9 (11)	6 (10)	10 (10)	14 (15)	8 (9)	7 (7)
	81.8%	60%	100%	93.3%	88.9%	100%

Table 6.1: Classification accuracy of LCI and s_{cond} changes as detectors of bronchoconstriction. The results are presented for each category as: number of correct predictions for category (total number of predictions made for category).

in time constants between different lung regions, even when these regions are quite small. This means that if the right lung has the smallest mean airway size, but the left lung has a small group of severely constricted airways, s_{cond} may respond more sensitively to the left lung constriction than that in the right lung.

6.4 Discussion

In this chapter, the previously developed model of the multiple-breath washout (see Chapter 2) was validated against a combination of patient-specific clinical data, as well as broader behaviours in the literature. Following this, the model was used to investigate how MBW indices respond to changes in body position.

6.4.1 Dominant dynamics affecting the MBW

Considering the results in Figures 6.2-6.4, the correlation between the model and clinical data (both patient-specific and broader) is quite strong. As well as providing a validation of the model, this also highlights the system dynamics that the MBW appears to be most strongly affected by. The structural lungs are physically accurate to

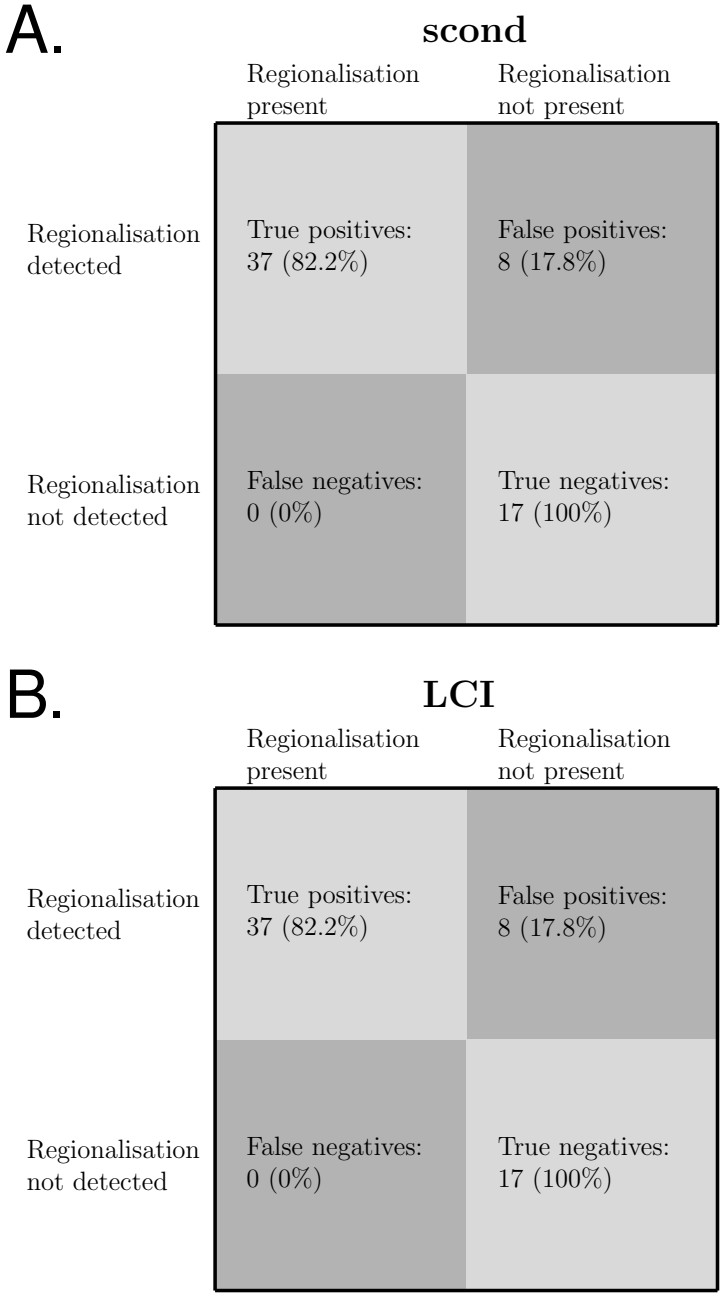

Figure 6.6: Sensitivity of s_{cond} (A) and LCI (B) as detectors of bronchoconstriction regionalisation. Data for lateral and vertical regionalisation classification has been combined into one pool. Both s_{cond} and LCI achieved high true positive rates and perfect true negative rates.

the patient up to generations 6-10, relying on algorithmic generation and extrapolation of the medial airway radii beyond this depth. Despite this algorithmic component, the asthmatic structures have previously been shown to have significantly higher total

resistance, as well as smaller and more varied homothety ratios (which are extrapolated down from the segmented airways), comparative to the healthy structures (Bordas et al., 2015). Given that the model only incorporates a simple respiratory zone approximation, this suggests that the responses of LCI and s_{cond} are most dominantly driven by central and medial airway sizes (and subsequent airflow rates), or equally, that the response to small airway sizes is more statistical than specific in nature.

6.4.2 Prediction of disease regionalisation

The results in Figure 6.6 and Table 6.1 show a strong and consistent interactive effect of gravity and disease regionalisation, on both LCI and s_{cond}. In particular, the results suggest that the gravitational ventilation gradient is strong enough to influence MBW outputs, particularly in unhealthy patient groups with regionalised or unilateral disease. The consistency of this response is noteworthy, suggesting that the response may be strong enough to reverse-engineer, and be used for disease classification. It also means that the response needs to be understood in clinical interpretation of the indices, as in the presence of strongly regionalised disease, the chosen testing position may either mask or exacerbate the MBW response.

This response may help explain the inconsistency of results in the literature, particularly in unhealthy patient groups. As body position is changed, relative changes in flow rates to different regions will occur, increasing ventilation to the lowest region (relative to the gravitational axis). In healthy subjects, flow rates into all the lobes are already quite high, meaning the change will have only a minimal effect on

LCI and s_{cond}. However, in a patient with highly regionalised bronchoconstriction, flow rates will be significantly lower in the constricted region than the rest of the lungs. This means that if a body position preferences flow to the constricted region, it will offset part of the flow reduction generated by the bronchoconstriction. In turn this will lead to a more fully ventilated lung, and a subsequent reduction in LCI. Equally, increasing flow to a constricted region will reduce the variance in time constants (Otis et al., 1956) across the lung, leading to a decrease in s_{cond}.

That body position affects MBW outputs is not on its own novel. As early as 1966, Bryan et al. (1966) illustrated that gravity creates a pleural pressure gradient, and subsequently affects relative ventilation of the lobes. However, studies in the literature have predominantly focused on healthy subject groups where the effects of these changes on test outputs are quite minimal. Equally, many of the studies which incorporate unhealthy patient groups illustrate drastic increases and decreases, with little explanation of why (Attinger et al., 1956; Badr et al., 2002; Manning et al., 1999). One unhealthy patient study that did outline the nature of the response more clearly was that of Zack et al. (1974), who showed a strong correlation between classification of right-lateral lung disease (by a physician) and increases in Pa_{O_2} (Partial pressure of oxygen) between left-lateral and right-lateral positions. The results that we have presented extend upon and broaden this idea, providing a more quantitative interpretation of the underlying phenomena.

Equally, to the best of our knowledge, no prior studies in the literature have utilised both computational and clinical data to investigate this phenomenon. The application

of a clinically validated computational model allows for more direct analysis of the function-form relationships between morphology, gravity, and MBW outputs. This in turn allows for more precision in understanding the effect that body position may have.

6.4.3 Comparison of orthostatic and supine

The two most commonly applied testing positions in clinical settings are orthostatic (for pulmonary function testing) and supine (for imaging). However, due to the diagonal nature of the oblique fissures, these two body positions generate quite similar ventilation distributions (as can be seen in Figure 6.3). Given the other results in this chapter, this suggests that both positions have quite similar biases, with higher sensitivity to constriction in the upper lobes than in the lower lobes. It can be reasoned that these biases would not be unique to the MBW, but an inherent property of the testing position. This interpretation is strengthened by the results in Figure 6.4, which show similar biases in simulated imaging data.

Further to this, while relative ventilation of the lobes is similar between both positions, it is not identical, with a large change occurring in ventilation of the right-middle lobe. This suggests that in specific disease cases, the response of LCI and s_{cond} may be quite different. To illustrate this, we consider the difference between LCI in orthostatic and supine over the entire subject group (Figure 6.7). As the figure shows, there is a strong correlation between the two outputs, with on average a small decrease from supine to orthostatic, consistent with prior results in the literature (Hanson

et al., 1962). However, while the correlation is strong, a few significant outliers can be seen, where the difference between the two indices is greater than 10%.

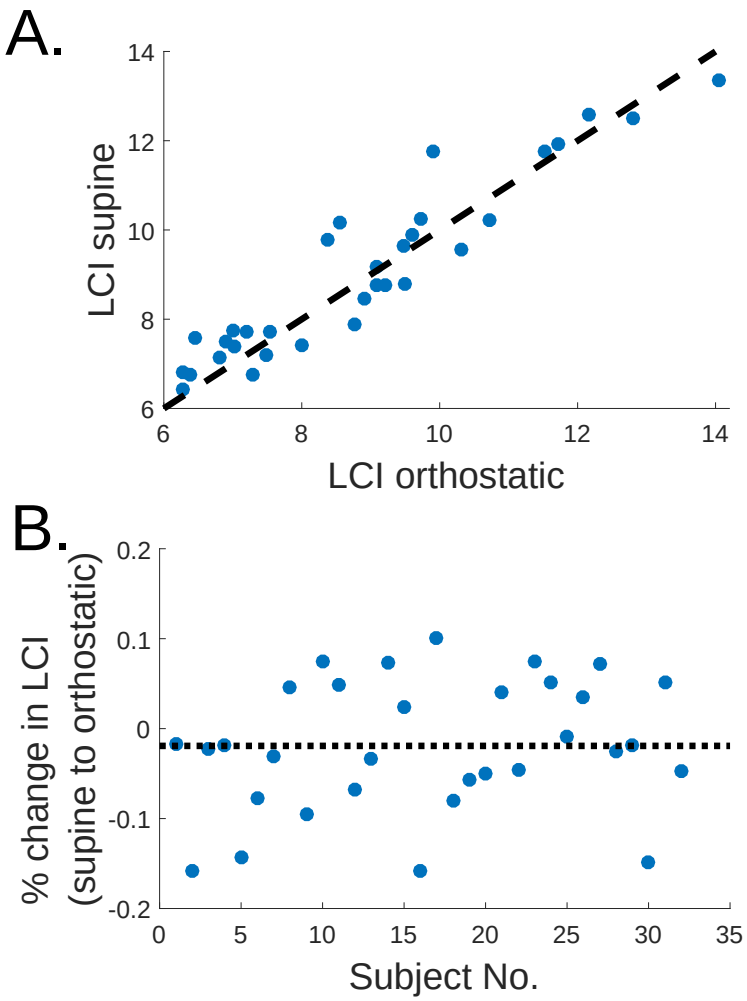

Figure 6.7: Comparison of LCI values between orthostatic and supine positions. Values are strongly, though not perfectly correlated (A), with an average decrease of 2% from supine to orthostatic (B). A few significant outliers can be seen, with changes between the two values being greater than 10%.

To illustrate why these changes occur, we highlight three distinct cases in Figure 6.8. In the first case, airway constriction is most severe in the right-middle lobe, leading to a significant increase in LCI in supine, relative to orthostatic (as orthostatic ventilates the RML more strongly than supine). In the second case, the right-middle lobe is

constricted, but so are the lower-lobes. This leads to a lower LCI (as both positions ventilate the lower lobes preferentially), and little change between the positions (as behaviour is dominated by the lower-lobes, not the middle-lobe). In the third case, the right-middle lobe is not constricted, but the right-upper lobe is. This leads to a raised LCI (as neither position preferentially ventilates the upper lobes), but little change between positions. These two figures further illustrate the consistency of LCI and s_{cond} response to body position, and highlight the importance of understanding this effect when interpreting test outputs.

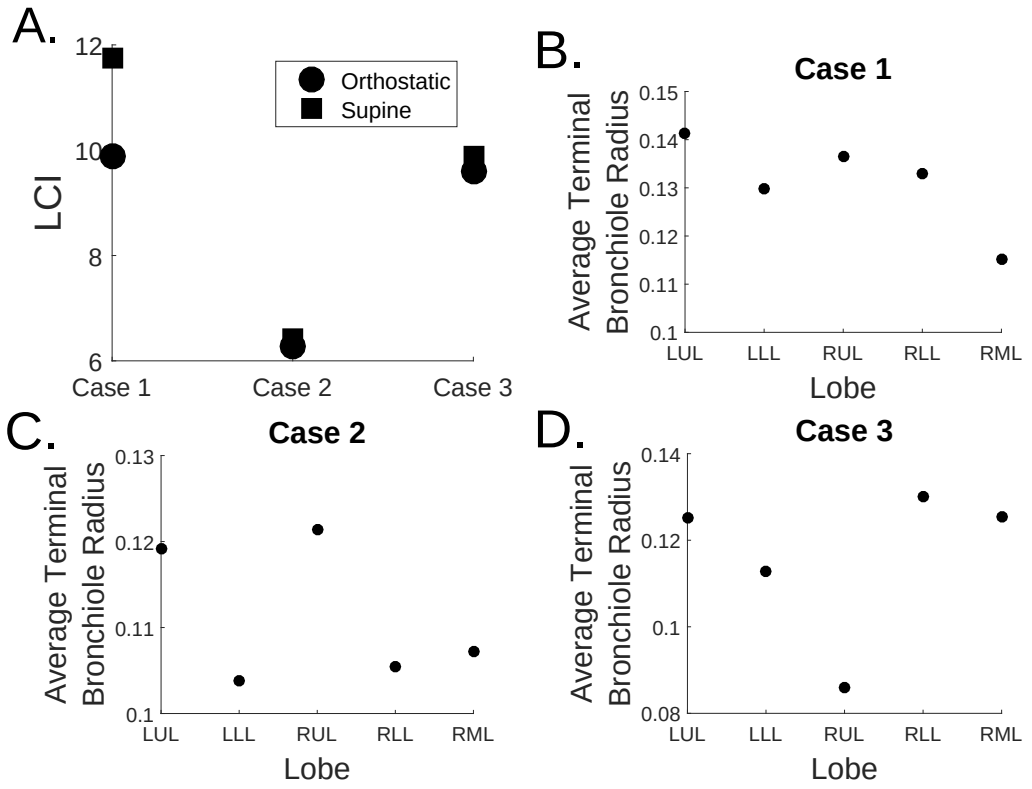

Figure 6.8: Comparison of LCI values between orthostatic and supine positions in 3 specific cases. In case 1 the right-middle-lobe is most constricted (leading to a large change in LCI), in case 2 the lower-lobes are most constricted (leading to a small change in LCI, and a lower overall value), and in case 3 the right-upper lobe is most constricted (leading to a small change in LCI, and a higher overall value). All values were simulated from patient-specific structures within the dataset.

6.4.4 Clinical significance

The results in this chapter illustrate that body position may have a clinically significant effect on the multiple-breath washout. This effect appears to be stable and noticeable, suggesting the ability to manipulate, or even reverse-engineer. Given the results in Figure 6.6 and Table 6.1, it may be possible to use washout indices from opposing positions to inform patient classifications in clinical trials, or even to infer treatment protocols. While clearly more direct clinical investigation of this phenomena is necessary, the potential utility is quite high. If classification of regionalisation through this comparison was sensitive enough, it could inform practices such as mechanical ventilation protocol during acute respiratory distress syndrome (over which there is currently strong disagreement in the literature (Fessler and Talmor, 2010; Thomas and Paratz, 2007)), or positioning protocols for physiotherapy chest clearance. This suggests a strong need for targeted clinical investigation of this phenomena.

Further to this, the results in Figure 6.7 illustrate the consistent similarity between the two most common testing positions, supine and orthostatic. Both of these test positions also appear to have similar biases, being more sensitive to disease in the upper lobes than the lower lobes. No testing position can be free of this bias, and so this does not represent an inherent flaw in testing in either of these positions. However, clearly the bias should be known and understood by clinicians when interpreting outputs from any PFT. Equally, given the results in Figure 6.4, these biases should also be understood when interpreting imaging outputs.

Finally, the validation of the computational model gives more strength to the

conclusions reached in Chapters 3 and 4. This increases the clinical relevance of taking both LCI and s_{cond} as global measures of ventilation heterogeneity, which respond more strongly to constriction severity than to constriction depth.

6.4.5 Analysing the role of diffusion

As noted in earlier sections, unlike in Chapters 3 and 4, the simulations in this chapter were performed using the convection-diffusion model. The primary rationale behind this was to reduce a potential source of error, as a way to improve the clinical validation (as clinically, diffusion does play a role in gas transport). However, since the primary validation of the MBW model within this thesis was performed using an updated model to that which was used within Chapters 3 and 4, there is a need to illustrate that the results from the previous chapters still hold. To illustrate this, we present a comparison of s_{cond} and LCI in the virtual lung structures (Bordas set) using a diffusion rate of 0.768 $\text{cm}^2.\text{s}^{-1}$ (the approximate diffusion rate of ^{3}He), and without diffusion. We chose to compare to ^{3}He instead of SF_6, as ^{3}He has a much larger diffusion rate in air, meaning the effect would be magnified. The results of this comparison can be seen in Figure 6.9.

As the figure shows, the incorporation of diffusion has only a minimal effect on outputs of the model, across all subjects. Diffusion leads to a small negative bias in both s_{cond} and LCI, presumably as it allows for slight increases in gas transport rates throughout constricted regions (where convection rates are lowest). However, this bias is not statistically significant, meaning we have confidence that the results illustrated

in Chapters 3 and 4 would still hold with the convection-diffusion model. We do note that for for LCI, there is one quite significant outlier that can be noticed. This occurs due to the discrete nature of LCI, as the index is calculated using a termination threshold. For this outlier, the introduction of diffusion caused the termination point to shift one exhalation earlier. We do not believe that this shift is significant enough to bias prior results, given all other structures exhibited minimal changes.

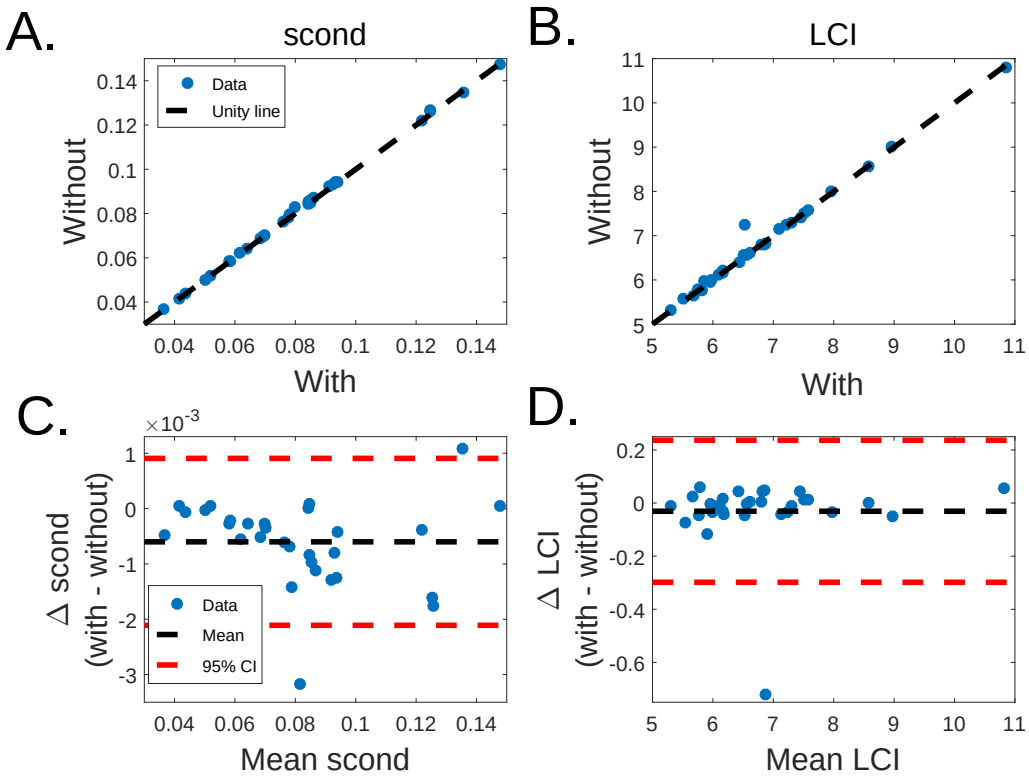

Figure 6.9: Comparison of MBW indices with and without diffusion. Direct comparison of s_{cond} (A) and LCI (B) is given, as well as Bland Altman plots (C,D).

6.4.6 Limitations

The MBW model which has been developed is intended as a tool to improve understanding of the function-form relationships between the MBW and underlying lung

morphology. While the results in this chapter give strong validation to this model, there are still some clear limitations which should be addressed and understood. As discussed in Chapter 2, the model does not incorporate airway dynamism throughout the breathing cycle, or a dynamic acinar compliance. Equally, the respiratory zone approximations are quite simplistic, and clearly not intended to represent actual acinar behaviour. All of these factors may lead to an overestimation of flow rates, and in turn may have slightly magnified the strength of effect shown in the results.

The virtual structures also relied on algorithmic generation for the small airways, meaning radii below generation 6-10 are not specifically representative of the subject, but instead are an extrapolation from the last CT-measurable airway size for that region. Given the strong correlations of the model with clinical data, we do not believe this represents a flaw in interpretation of the key results. However, the consistency of airway decrease in the small airways may have reduced noise in the data, leading to clearer results than would be seen in a clinical setting.

Considering the clinical data, the study incorporated a much larger number of asthmatic patients (24) than healthy subjects (7). This means that the conclusions are clearest for unhealthy groups. However, given the wide array of literature which illustrates the minimal effects of gravity on ventilation in healthy subjects, we do not believe that this detriments the study.

Finally, as noted in results in Chapter 3, the MBW is not able to assess regions of the lung which have undergone airway closure. This means that the results in this study may not hold for incredibly severe bronchoconstriction, where airways remain

closed regardless of body position. However, within the literature this is a well-known limitation of the MBW, which is why it is often targeted as a sensitive detector of early stage disease (Robinson et al., 2013), comparative to tests such as spirometry.

The results here are intended as a groundwork for future investigation. They suggest two major ideas; that MBW outputs may under or over-predict lung disease in patients with strong disease regionalisation; and that information about regionalisation may be gained by comparing outputs measured from opposing positions. The bias of different positions in detection is a phenomenon that should be carefully understood in clinical scenarios. Equally, the potential to manipulate this bias to classify regionalisation is an interesting idea that should be more directly investigated in a clinical study.

6.5 Summary

Within this chapter we have used a combination of clinical data and computational modelling to better quantify the effect that body position may have on outputs from the multiple-breath washout. The previously developed models of the MBW (see Chapter 2) were validated against patient-specific data, as well as broader trends from the literature. The model was then used to illustrate that body position can significantly affect MBW outputs, due to the fact that it directly affects relative ventilation of the lobes through the 'Slinky' effect. These changes in relative ventilation appear to have minimal effect in healthy subject groups, but create bias towards detection of disease in specific lung regions. This in turn can magnify or mask the response in LCI and s_{cond}, particularly in patients with significant disease regionalisation. However,

the effect of gravity on test outputs appears to be consistent and interpretable. This means that the biases of each testing position can be understood and accounted for in clinical settings. It also suggests the potential to classify lung disease regionalisation by comparing test outputs in opposing positions; though clearly this hypothesis would need to be investigated further in a clinical study.

7

A model of the pulmonary system

Within Chapters 2-6, we developed, implemented, validated, and analysed models for lung impedance and the inert-gas washout. Through this, we have provided more detailed information of the sensitivities of both tests to bronchoconstriction, and small airways disease. More broadly, these chapters serve to illustrate the potential beneficial role that computational models of the lungs can provide. Within Chapter 7 we extend upon this idea, showing how the models within Chapter 2 can be adapted to simulate the entire pulmonary system, allowing for more holistic simulations of respiratory processes.

7.1 Rationale

So far within this thesis we have analysed computational models of pulmonary function tests within the conducting zone of the lungs. The models have been shown to accurately recreate clinical behaviours, and to be of utility in analysis of function-form relationships within the system. However, they are still significantly limited by the simplifying approximations made during their construction. While airflow rates are highest in the conducting zone of the lungs, many significant respiratory functions occur peripherally in the respiratory zone. Equally, the lungs do not operate independently of the remainder of the human body, being strongly influenced by the behaviour of other organs and systems. In particular, the primary function of the lungs is to allow for the exchange of O_2 and CO_2 into and out of the bloodstream, and so the lack of pulmonary gas exchange presents a key limitation to the suite of developed models.

This is not the only extension that could be made to the models within this thesis, however, we believe that it is the most significant. A detailed discussion of other potential model improvements (such as airway dynamism and multi-scale modelling) is given in Chapter 9. Within Chapters 7 and 8, we instead address the bloodstream limitation, by adapting the gas transport models in Chapter 2 to incorporate simulation of the entire pulmonary system.

The rationale for this choice is to allow for exploration of a much wider variety of respiratory scenarios. The two most abundant gases in Earth's atmosphere are

N_2 (78%) and O_2 (21%), both of which have significant vascular permeability. Thus, without effective incorporation of pulmonary gas exchange the vast majority of real-life respiratory scenarios, and clinical PFTs cannot be meaningfully simulated. Further to this, specifically considering the MBW, we have constrained investigations within this thesis to ^3He and SF_6 washouts only. However, due to cost the majority of washouts are performed using N_2 (Robinson et al., 2013), meaning a more detailed model is needed to investigate the MBW in its most commonly applied form.

Modelling of pulmonary blood flow, and associated gas transfer is a rich area of computational biology with entire books dedicated to model design and implementation (Tu et al., 2012), and with many review papers having been published in recent years (Burrowes et al., 2014; Tawhai and Burrowes, 2008). Most commonly, blood flow and artery cross-sectional area profiles are simulated using the Navier-Stokes equations. Depending on the underlying motivation for the model, these equations have been applied in a 1D setting (Olufsen et al., 2000), or using a collapsed 3D-1D model (Smith et al., 2002), alongside various adaptations for phenomena such as gravity (Burrowes and Tawhai, 2006).

Initial work involved the application of computational models on fractal based pulmonary geometries (Glenny and Robertson, 1991; Krenz et al., 1992), derived from earlier morphological studies (Horsfield, 1978). Similar to airway models, as improvements in computational power, and imaging were made, modelling approaches started to make use of patient-specific vasculature structures (Burrowes et al., 2005; Tawhai et al., 2004). Due to the scale of patient-specific structures, and the nature of

Navier-Stokes equations, the resulting models are typically extremely large, highly non-linear and stiff. For this reason solutions have most commonly been generated through application of explicit methods, such as the two-step Lax Wendroff scheme (Smith et al., 2002; Olufsen et al., 2000). However, recent work in the literature has explored more complex, semi-implicit schemes (Tavelli et al., 2013).

While there has been a large degree of work in modelling pulmonary flow, and investigating pulmonary disease, there is substantially less work which connects airflow and blood flow models together, to achieve full pulmonary simulation. While detailed models of alveolar-capillary gas exchange have been derived (Ben-Tal, 2006), they have usually only been applied as compartmental models, limiting many potential avenues for analysis. This in part is driven by the significant computational constraint of building a full pulmonary model. As a way of overcoming this limitation, some researchers have investigated multi-scale modelling approaches (Burrowes et al., 2014). However, to the best of our knowledge, to date, no tractable model of gas transfer across the entire pulmonary system exists, particularly in reference to the inert-gas washout.

Within this chapter, we aim to partially address this literature gap, by outlining an effective model of gas transport within the conducting zone of the lungs, the pulmonary arterial network, and across the alveolar-capillary membrane. We build upon prior work in the literature and previous chapters, to design the model and implement it numerically. Following this, we show how the use of parallel computing architectures can significantly reduce computational strain, allowing for tractable simulations of the

entire system to a fine resolution. We end the chapter with a more detailed analysis of computational constraints, alongside a discussion of potential future work.

7.2 Model outline

In early work within this thesis we outlined a model suitable for simulating ventilation and gas transfer within the conducting zone of the lungs. In brief, the flow rate Q within each airway was driven by the pressure gradient ΔP, over the branch. Each terminal bronchiole was subtended by a spherical acinar region V_{acin}, whose expansion and contraction was proportional to the terminal bronchiole flow rate. Acinar volumes were also constrained by local tissue compliance $\mathbb{C}$ and the pressure difference between the pleural cavity (P_{pl}) and the distal end of the terminal bronchiole. This was expressed by the equation system:

$$\Delta P = R(Q)Q, \qquad \text{for each branch,} \tag{7.1}$$

$$Q_{\text{upper}} = \sum Q_{\text{lower}}, \qquad \text{for each bifurcation,} \tag{7.2}$$

$$\frac{d}{dt}V_{\text{acin}} = Q, \qquad \text{for each terminal branch,} \tag{7.3}$$

$$P_T - P_{pl}(t) = \frac{1}{\mathbb{C}}V_{\text{acin}}, \qquad \text{for each terminal branch.} \tag{7.4}$$

where $R(Q)$ is Poiseuille branch resistance, with a modification for energy dissipation (Pedley et al., 1970). In the absence of bloodstream interactions, this ventilation model was used to drive a gas transport model first proposed by Paiva (1973):

$$\frac{\partial C}{\partial t} = D\frac{\partial^2 C}{\partial x^2} + \frac{D}{A}\frac{\partial A}{\partial x}\frac{\partial C}{\partial x} - u\frac{\partial C}{\partial x}, \tag{7.5}$$

where $C(x,t)$ is the gas concentration at position x and time t, A the airway cross-sectional area, $u = Q/A$ the air velocity, and D the diffusion coefficient for the gas in air.

To expand upon this model to incorporate gas transfer between the airways and bloodstream, four components are needed: a structural representation of the pulmonary arterial (and venous) network, a model for blood flow within the network, a model for gas transfer within the network, and a model for gas exchange between the airways and capillaries.

7.2.1 Virtual arterial structure

To simulate gas transfer within the pulmonary system, a physiologically realistic structural representation of the pulmonary arterial network is needed. We construct this network through modification of the previously created virtual conducting zone structures (see Chapter 2). Typically, the structure of the arteries mimics the structure of the airways, tracking alongside them, and decreasing with similar ratios when they bifurcate (Horsfield et al., 1976; Horsfield, 1978). However, this similarity ends proximally at the distal ends of the left and right main bronchi, where the arterial network splits away into the left and right pulmonary artery, which join together at the pulmonary trunk. To mimic this structure, we first take the conducting zone airway structure, and truncate it at the proximal end of the left and right main bronchi. We then artificially create the left and right pulmonary artery, by extending a centreline directly away from the mid-point where the two inferior pulmonary arteries meet.

Instead of creating an artificial pulmonary trunk, we leave the artery network as two distinct structures, for the left and right lung respectively.

Arteries and veins fluctuate in size throughout the heartbeat, due to drastic changes in pressure. However, these changes can typically be defined relative to the radius under standard pleural pressure. We define this resting radii of the artery network by reducing the associated airway radii by 25%, which approximates histological data for healthy subjects (Horsfield, 1978). Length and radii of the pulmonary arteries were calculated by extrapolating the average length and radii of the two daughter arteries by the average branching ratios for their corresponding bifurcations.

The corresponding vein network was assumed to be symmetrical to the arterial network. Each terminal artery was connected to the associated terminal vein by a single capillary branch, with equal radius to the artery. The capillaries were assumed to wrap around the acinar regions, covering approximately 1/5 of their surface area (a detailed justification of this is given in Appendix C). This leads to a capillary length of

$$l_{\text{cap}} = \frac{2\pi R_{\text{acin}}^2}{5R_{\text{cap}}^0}, \tag{7.6}$$

where R_{acin} is the radius of the associated acinar region, and R_{cap}^0 is the resting radius of the capillary. An illustration of the structural representation of the pulmonary network can be seen in Figure 7.1.

We note that the construction of the arterial network is based on significant simplifying assumptions about branch lengths and radii. However, the modelling techniques outlined in the remainder of this chapter do not rely on the specific nature of

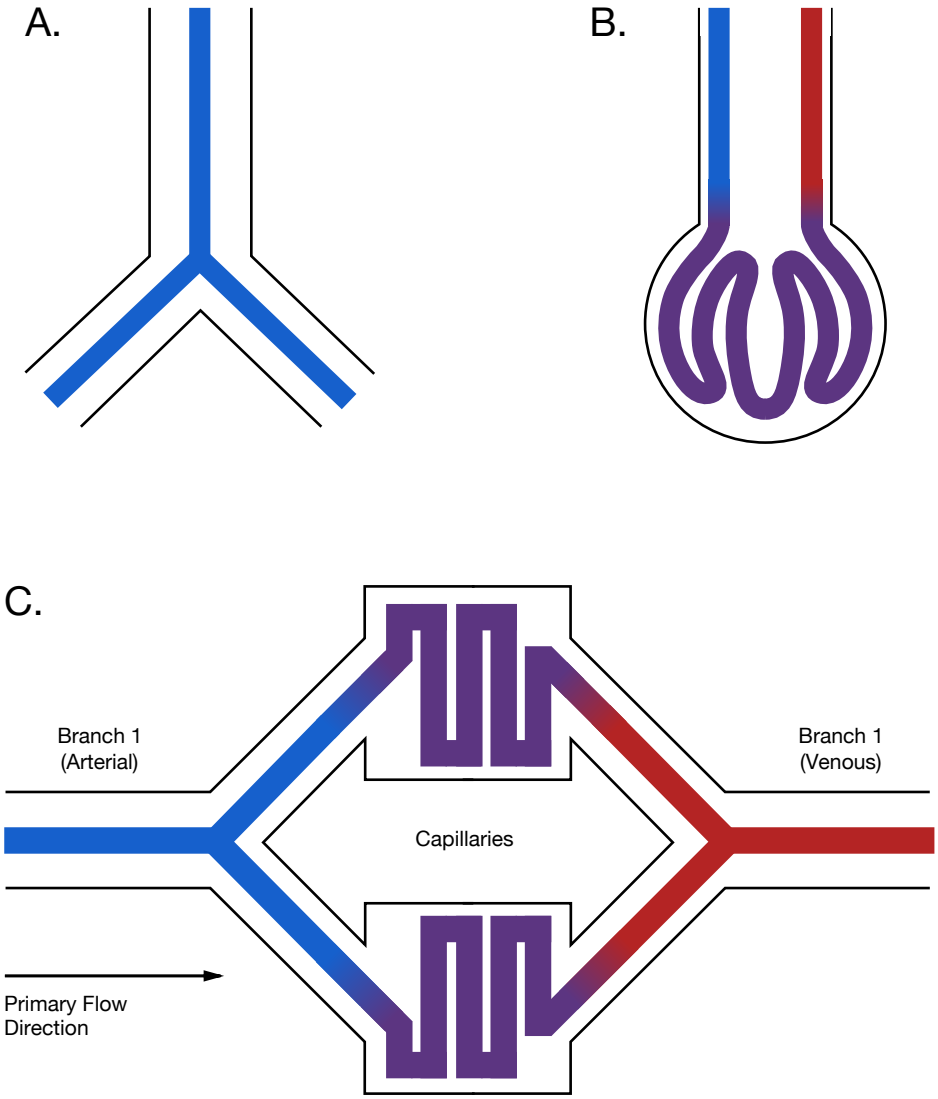

Figure 7.1: Diagram of the arterial network. A cross-section of the arteries against the airways can be seen (A), as well as a 2D representation of the capillaries wrapping around the acinus (B). An unravelled 2D schematic of the symmetry between artery and vein networks is also given (C). Figure created with the assistance of Ms Sanjana Sharma.

the structure, and would be suitable for application to any appropriately formatted 1D representation of the pulmonary network. Clearly, the investigation of imaging-based patient-specific structural models of the veins and arteries is an avenue for future research.

7.2.2 Blood flow model

To model blood flow and oscillation of the arteries and veins, we adapt the body of work outlined in detail by Olufsen (1998). However, to ease explanation, we first note some notation choices. From this point onwards, we use the word arteries to refer to arteries, veins and capillaries collectively, only making distinctions when necessary. We introduce a subscript b to refer to variables relating to the bloodstream (e.g. Q_b, A_b). This is to distinguish them from similar variables in the airway network (which have no associated subscript).

To model flow in the network, we first consider the compliance of each arterial wall, which can be approximated as (Olufsen, 1998):

$$\mathbb{C}_b = \frac{3A_b^0 L_b}{2} \frac{R_b^0}{Eh},$$

where R_b^0 is the resting radius, A_b^0 the resting cross-sectional area, L_b is the artery length, h is the wall thickness, and E is the Young's Modulus for the artery walls. In prior work in the literature (Olufsen, 1998) it has been shown that there is an apparent function relationship between wall thickness, vessel radius and stiffness, with experimental data following the model

$$\frac{Eh}{R_b^0} = k_1 \exp(k_2 R_b^0) + k_3,$$

with $k_1 = 2 \times 10^7 g/s^2 cm, k_2 = -22.53 cm^{-1}$, and $k_3 = 8.65 \times 10^5 g/s^2 cm$. Given this, and the compliance model we can calculate the relationship between vessel pressure P_b (relative to external pressure) and cross-sectional area using a linear stress-strain

relationship as

$$P_b = \frac{4}{3}\frac{Eh}{R_b^0}\left(1 - \sqrt{\frac{A_b^0}{A_b}}\right) = f\left(1 - \sqrt{\frac{A_b^0}{A_b}}\right).$$

Using this pressure model, and considering a flux-driven 1D Navier Stokes equation, a full 1D model for blood flow and arterial area changes can be derived (with full details of derivation given by Olufsen (1998)) as

$$\frac{\partial A_b}{\partial t} + \frac{\partial Q_b}{\partial x} = 0, \tag{7.7}$$

$$\frac{\partial Q_b}{\partial t} + \frac{\partial}{\partial x}\left(\frac{Q_b^2}{A_b} + B\right) = -\frac{2\pi\nu_b Q_b R_b}{\delta A_b} + \frac{\partial B}{\partial R_b^0}\frac{\partial R_b^0}{\partial x}, \tag{7.8}$$

where Q_b is the flow rate in the vessel, ν_b is the dynamic viscosity of blood, δ is the boundary layer thickness, $B = f\sqrt{A_b^0 A_b}/\rho_b$ is a term constructed to allow the equations to be written in conservative form, and ρ_b is the density of blood. All general parameter values are given in Table 7.1.

To simplify mathematical manipulations, we introduce the notation

$$\mathbf{U} = \begin{bmatrix} A_b \\ Q_b \end{bmatrix}, \mathbf{T} = \begin{bmatrix} \mathcal{T}_1 \\ \mathcal{T}_2 \end{bmatrix} = \begin{bmatrix} Q_b \\ \frac{Q_b^2}{A_b} + B \end{bmatrix}, \mathbf{S} = \begin{bmatrix} \mathcal{S}_1 \\ \mathcal{S}_2 \end{bmatrix} = \begin{bmatrix} 0 \\ -\frac{2\pi\nu_b Q_b R_b}{\delta A_b} + \frac{\partial B}{\partial R_b^0}\frac{\partial R_b^0}{\partial x} \end{bmatrix},$$

meaning the system can be written as

$$\frac{\partial}{\partial t}\mathbf{U} + \frac{\partial}{\partial x}\mathbf{T} = \mathbf{S}.$$

We solve this equation system using a two-step Lax-Wendroff explicit scheme (Olufsen et al., 2000). We first discretise each arterial branch separately into M evenly spaced nodes (with spacing Δx), at N evenly spaced points in time (with time step Δt). We denote the value of the variable U_b at node M, and time step n as U_M^n, and

define intermediate step values as

$$\mathbf{U}_j^{n+1/2} = \frac{\mathbf{U}_{j+1/2}^n + \mathbf{U}_{j-1/2}^n}{2} + \frac{\Delta t}{2}\left(-\frac{\mathbf{T}_{j+1/2}^n - \mathbf{T}_{j-1/2}^n}{\Delta x} + \frac{\mathbf{S}_{j+1/2}^n + \mathbf{S}_{j-1/2}^n}{2}\right), \quad (7.9)$$

for $j = m \pm 1/2$. The full step solution is then defined from the intermediate step values as

$$\mathbf{U}_m^{n+1} = \mathbf{U}_m^n - \frac{\Delta t}{\Delta x}\left(\mathbf{T}_{m+1/2}^{n+1/2} - \mathbf{T}_{m-1/2}^{n+1/2}\right) + \frac{\Delta t}{2}\left(\mathbf{S}_{m+1/2}^{n+1/2} + \mathbf{S}_{m-1/2}^{n+1/2}\right). \quad (7.10)$$

Bifurcation conditions

The model outlined above can only be used to advance the solution at nodes within a single branch. To account for bifurcations, each bifurcation node is decomposed into its parent node, and corresponding daughter nodes, as shown in Figure 7.2. Equations at the branch bifurcations must be solved simultaneously to ensure conservation is upheld.

Considering a three branch bifurcation, enforcing conservation of flow and continuity of pressure gives

$$Q_{b,j}^{p,M} = Q_{b,0}^{d_1,j} + Q_{b,0}^{d_2,j}, \quad (7.11)$$

$$P_{b,M}^{p,j} = P_{b,0}^{d_1,j} = P_{b,0}^{d_2,j}, \quad (7.12)$$

where p, d_1 and d_2 denote the parent and daughter nodes of the bifurcation, and $j = n + 1/2, n + 1$.

Given P_b is a function of A_b, the pressure continuity equation can be re-written as

$$f_M^p\left(1 - \sqrt{\frac{A_{b,M}^{p,0}}{A_{b,M}^{p,n+1}}}\right) = f_0^{d_1}\left(1 - \sqrt{\frac{A_{b,0}^{d_1,0}}{A_{b,0}^{d_1,n+1}}}\right),$$

Parameter	Value	Interpretation	Value taken from:
$\mathcal{C}_T$	1.3×10^{-6} cm^{4}s^2/g	Windkessel parameter	(Olufsen, 1998)
$\mathcal{D}_{\text{cap}}$	5×10^{-4} L/s/mmHg	Diffusing capacity of N_2	Average for O_2 and CO_2 (Ben-Tal, 2006)
δ	0.1cm	Artery boundary layer size	(Olufsen et al., 2000)
f_{loss}	0%	Percentage of N_2 lost to body during 1 circulation	N_2 loss is minimal and ignored (Katz, 2010)
H_T	1s	Heartbeat period	Standard value
k_1	2×10^7 g/s^{2}cm	Fit parameter for $f(R_b^0)$	(Olufsen, 1998)
k_2	-22.53 /cm	Fit parameter for $f(R_b^0)$	(Olufsen, 1998)
k_3	8.65×10^5 g/s^2 cm	Fit parameter for $f(R_b^0)$	(Olufsen, 1998)
ρ_b	1060 kg/m^3	Density of blood	(Saladin and Porth, 1998)
$\bar{Q}_b$	20cm^3/s	Maximum inlet flow rate	(Olufsen, 1998)
$\mathcal{R}_1$	25300 g/(s cm^4)	Windkessel parameter	(Olufsen, 1998)
$\mathcal{R}_2$	13900 g/(s cm^4)	Windkessel parameter	(Olufsen, 1998)
σ_b	1.7×10^{-5}/mmHg	Solubility of N_2 in blood	(Sander, 2015)
τ	0.1s	Time of peak inlet flow (during each heartbeat)	(Olufsen, 1998)
$t_{\text{circulation}}$	60s	Average time taken for blood to circulate the body	(Katz, 2010)
ν_b	0.046 cm^2/s	Dynamic viscosity of blood	(Olufsen et al., 2000)

Table 7.1: Pulmonary model parameters

and similar for d_2. These six continuity equations can be taken alongside the Lax-Wendroff scheme equations

$$A_{b,m}^{i,n+1} = A_{b,m}^{i,n} + \frac{\Delta t}{\Delta x}\left(\mathcal{T}_{1,m+1/2}^{i,n+1/2} + \mathcal{T}_{1,m-1/2}^{i,n+1/2}\right), \tag{7.13}$$

$$Q_{b,m}^{i,n+1} = Q_{b,m}^{i,n} + \frac{\Delta t}{\Delta x}\left(\mathcal{T}_{2,m+1/2}^{i,n+1/2} - \mathcal{T}_{2,m-1/2}^{i,n+1/2}\right) + \frac{\Delta t}{2}\left(\mathcal{S}_{2,m+1/2}^{i,n+1/2} + \mathcal{S}_{2,m-1/2}^{i,n+1/2}\right), \tag{7.14}$$

where $i = p, d_1, d_2$, and $m = M$ for p, and $m = 0$ for d_1 and d_2.

This gives 12 equations, which govern the 12 state variables $Q_{b,m}^{i,j}, A_{b,m}^{i,j}$ for $i =$

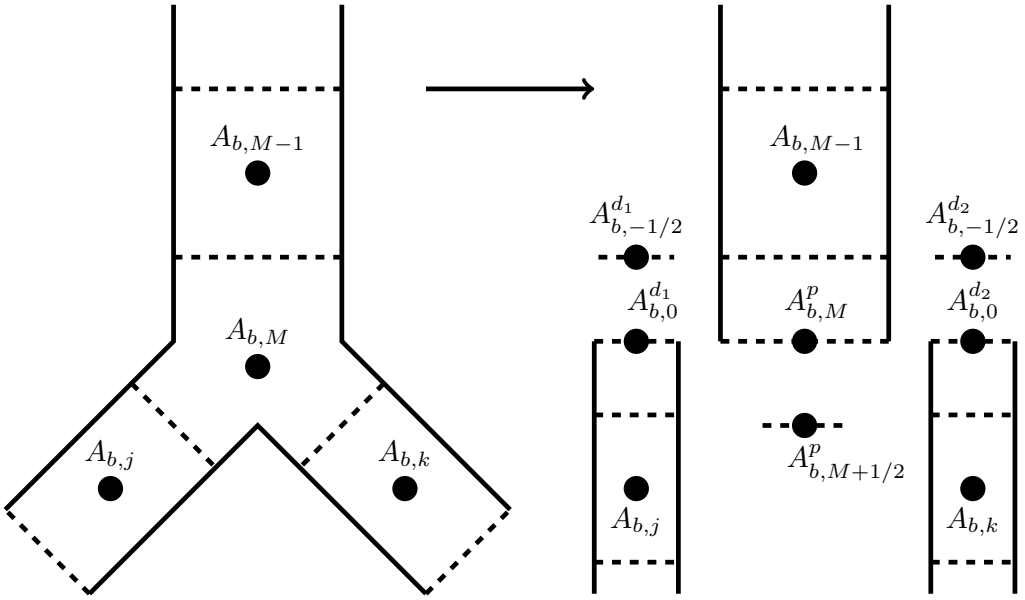

Figure 7.2: Diagram of 3-branch bifurcation decomposition. The schematic shows a bifurcation before (left) and after (right) separation. New nodes d_1 and d_2 are created, alongside ghost node values $A^{d_1}_{b,-1/2}$, $A^{d_2}_{b,-1/2}$, and $A^{p}_{b,M+1/2}$. Similar nodes are also created for all corresponding Q_b values.

p, d_1, d_2, and $j = n, n+1$. However, these equations also require 6 variables which exist only as ghost nodes: $A^{p,n+1/2}_{b,M+1/2}, A^{d_1,n+1/2}_{b,-1/2}, A^{d_2,n+1/2}_{b,-1/2}$, and similar for Q_b. This requires 6 more equations to close the system, which are created, by defining the ghost points through averaging, such that

$$Q^{i,n+1/2}_{b,m} = \frac{Q^{i,n+1/2}_{b,m-1/2} + Q^{i,n+1/2}_{b,m+1/2}}{2}, \tag{7.15}$$

$$A^{i,n+1/2}_{b,m} = \frac{A^{i,n+1/2}_{b,m-1/2} + A^{i,n+1/2}_{b,m+1/2}}{2}, \tag{7.16}$$

where $i = p, d_1, d_2$, and $m = M$ for p and $m = 0$ for d_1 and d_2.

This gives rise to a closed system of 18 non-linear equations. However, 8 of the 18 equations are linear, and many of the other 10 are linear in some of the variables. This means the system can actually be collapsed into two systems of 3 non-linear equations, the first of which can be solved independently of the second. Full details of

this are presented in Appendix D, however, in brief, the non-linear equation system was collapsed, and solved using a vector Newton Method (as described in Chapter 2). Due to the small size of the system, the Jacobian can be directly formed with low computational cost, allowing for efficient solution of the system at each bifurcation.

While we have presented the bifurcation equations for a single parent node bifurcating into two daughter nodes, the procedure can easily be expanded to deal with other types of bifurcations. In the case of one parent node and three daughters, the same equations are derived, but the resulting Jacobian is of size 24×24. Following the procedure outlined for two daughters in Appendix D, the system can be collapsed into two systems of 4 non-linear equations. Equally, when considering the reversed direction bifurcations in the venous network, the appropriate equations can be derived by taking the bifurcation as having multiple parent nodes, and a single daughter node.

Finally, particular note should be made of the capillaries. The capillaries change length throughout the simulations (due to the expansion and contraction of the associated acinar region). Due to this length change, the connection between each capillary and the associated terminal vein and terminal artery must be treated as a bifurcation with a single parent and single daughter. This leads to a 12×12 Jacobian, which decomposes into a pair of 2×2 non-linear equation systems.

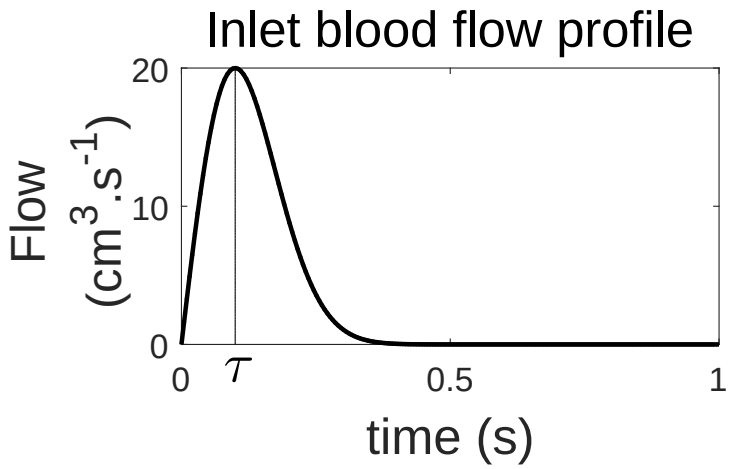

Figure 7.3: Inlet blood flow profile. A plot of the prescribed inflow boundary condition. The plot was generated with $\tau = 0.1$ seconds, $\bar{Q}_b = 20$ cm^3/s and $T = 1$s

Inlet boundary condition

At the two inlet boundaries (the left and right pulmonary arteries), a flow rate boundary condition is prescribed such that

$$Q_b(0,t) = \frac{\bar{Q}_b t}{\tau} \exp\left(\frac{1}{2}(1 - t^2/\tau^2)\right), \qquad 0 \le t < H_T, \tag{7.17}$$

$$Q_b(0, t + jH_T) = Q_b(0,t), \qquad j = 1, 2, 3, \ldots$$

where $\bar{Q}_b$ is the maximum flow, τ is the time of maximum flow, and H_T is the heartbeat period. A diagram of the inlet flow rate can be seen in Figure 7.3

We calculate the inflow boundary cross-sectional area, by first introducing a ghost point $Q^{n+1}_{b,-1/2}$ which satisfies

$$Q^{n+1/2}_{b,0} = \frac{Q^{n+1/2}_{b,-1/2} + Q^{n+1/2}_{b,1/2}}{2},$$

where $Q^{n+1/2}_{b,0}$ is the inflow rate, evaluated at time step $n + 1/2$. Using this ghost point, the inflow area A^0_b can be calculated as

$$A^{n+1}_{b,0} = A^n_{b,0} - \frac{\Delta t}{\Delta x}\left(\mathcal{T}^{n+1/2}_{1,1/2} - \mathcal{T}^{n+1/2}_{1,-1/2}\right) + \frac{\Delta t}{2}\left(\mathcal{S}^{n+1/2}_{1,1/2} + \mathcal{S}^{n+1/2}_{1,-1/2}\right),$$

where $\mathcal{T}^{n+1/2}_{1,-1/2} = Q^{n+1/2}_{b,-1/2}$ and $\mathcal{S}^{n+1/2}_{1,-1/2} = 0$.

Outlet boundary condition

At each outlet boundary, we model the out of domain resistance and compliance using a 3-element Windkessel model (Wesseling et al., 1993) with parameters $\mathcal{R}_1, \mathcal{R}_2, \mathcal{C}_t$ (see Figure 7.4). This leads to the model

$$\frac{\partial P_b}{\partial t} = \mathcal{R}_1 \frac{\partial Q_b}{\partial t} - \frac{P_b}{\mathcal{R}_2 \mathcal{C}_T} + \frac{Q_b(\mathcal{R}_1 + \mathcal{R}_2)}{\mathcal{R}_2 \mathcal{C}_T},$$

which is discretised as

$$P^{n+1}_{b,M} = P^n_{b,M} + \mathcal{R}_1(Q^{n+1}_{b,M} - Q^n_{b,M}) + \Delta t \left(-\frac{P^n_{b,M}}{\mathcal{R}_2 \mathcal{C}_T} + \frac{Q^n_{b,M}(\mathcal{R}_1 + \mathcal{R}_2)}{\mathcal{R}_2 \mathcal{C}_T} \right),$$

where

$$P^{n+1}_{b,M} = \frac{f_M}{\rho_b} \left(1 - \sqrt{\frac{A^0_{b,M}}{A^{n+1}_{b,M}}} \right).$$

A second equation is constructed through an upwind discretisation of Equation 7.7:

$$A^{n+1}_{b,M} = A^n_{b,M} - \frac{\Delta t}{\Delta x}(Q^{n+1}_{b,M} - Q^{n+1}_{b,M-1}).$$

These two equations are solved iteratively using Jacobi's method until a convergent solution is reached (to within a given tolerance).

Computational implementation

The model outlined in the previous section is both highly non-linear and extremely large. At a minimum, each branch in the system requires three nodes (one at each end, and a central node), both with two unknown variables (A_b, Q_b). This means at the lowest resolution for a full conducting airway zone structure (approximately

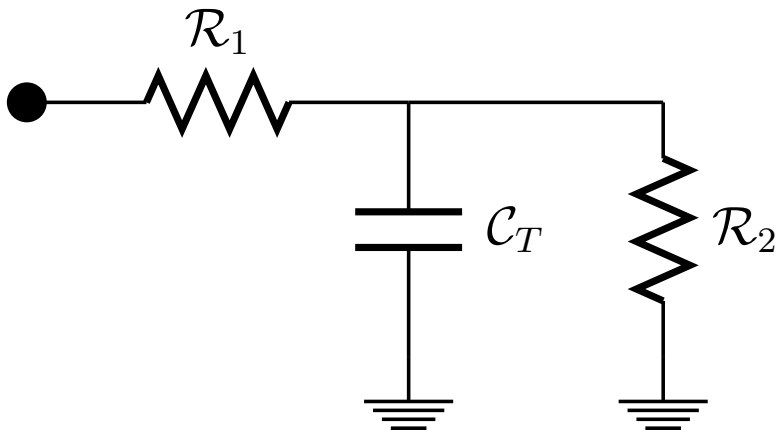

Figure 7.4: 3-Element Windkessel model. The outlet boundary condition is parameterised by a 3-element Windkessel model, with a resistance $\mathcal{R}_1$ in series with parallel resistance and compliance $\mathcal{R}_2$ and $\mathcal{C}_T$.

100,000 branches, 50,000 of which are terminal), the corresponding vasculature system has 250,000 arterial branches, and thus 1,500,000 variables. While the Lax-Wendroff scheme is explicit, due to conservation constraints, each bifurcation (of which there are approximately 200,000) is constrained by 18 non-linear equations. In Appendix D, we illustrate how the computational challenges of the bifurcation conditions can be reduced through careful algebraic manipulation; however, even with these simplifications, the resulting system is incredibly large and computationally intensive.

This is further exacerbated by the time step constraints imposed by the explicit solution scheme. Assuming a uniform spatial discretisation over each branch, it can be shown that the Lax-Wendroff method is stable (Olufsen et al., 2000) if the associated Courant Friedrichs Lewy (CFL) condition is fulfilled:

$$\frac{\Delta t}{\Delta x} \leq \left| \frac{Q_b}{A_b} \pm c \right|^{-1},$$

for both choices of sign, where

$$c = \sqrt{\frac{A_b}{\rho_b}\frac{\partial P_b}{\partial A}},$$

is the pulse wave speed.

In standard implementation on a full conducting zone structure, we have found this leads to an average constraint condition of

$$\Delta t \leq 10^{-6}.$$

For non-trivial simulations of ventilation and gas transfer, a stable blood profile is needed for at least the duration of a breathing cycle. In practice, this means blood flow needs to be simulated for a duration of 3 breathing cycles (to allow for solution stabilisation), equating to 12 seconds at a standard breathing rate. Thus, total solution of the system requires explicit iteration of a system of approximately 1,500,000 variables more than 10^7 times with the Lax-Wendroff scheme.

In a standard CPU architecture this would be computationally intractable, with estimated runtime being greater than 1 year per profile. However, given that the solution scheme is explicit, the calculations (within each time step) are highly parallelisable. To exploit this structure, we solve the blood flow model in a GPU environment. A standard GPU (as of 2018) has between 1000-4000 cores. This means that the incorporation of GPU computing could be expected to decrease runtime by an order of $10^3 - 10^4$ (for a sufficiently large system). This was one of the primary motivations for the use of an explicit solution scheme. The explicit scheme introduces a harsh time constraint penalty, but the use of high-performance computing greatly offsets

this effect. Equally, given the highly non-linear nature of the system (particularly the continuity constraints across each bifurcation), for a stable and accurate solution, an implicit scheme would also be expected to require quite a small time step. However, an implicit scheme would not be able to be implemented in a GPU environment with the same degree of ease or effectiveness as the explicit scheme.

GPU implementation of the blood flow model was performed using *gpuArray* structures within MATLAB's *Parallel Computing Toolbox*. All simulations of blood flow performed within this thesis were computed using an Alienware 17 R2 laptop (i7 processor, NVIDIA GTX970 GPU). In later results within this chapter, we illustrate how this solution architecture makes the problem computationally tractable.

7.2.3 Blood gas transport model

Following calculation of blood flow and arterial area changes, a model is needed to drive gas transport throughout the network. Unlike in the airways, the entire vasculature network is convection-dominated. This is in part due to the lower rates of diffusion of standard gases in blood, and partially due to the strong pulsatile nature of blood flow. However, unlike in the airways, volumes of branches change over time. To account for this, a mass transport equation was implemented, of the form

$$\frac{\partial A_b C_b}{\partial t} = \frac{Q_b}{A_b}\frac{\partial A_b C_b}{\partial x}, \tag{7.18}$$

where C_b is the gas concentration.

This model was implemented using a standard backward Euler discretisation, with appropriate upwinding and downwinding, similar to that outlined in Chapter

2. Importantly though, we note that while A_b is a function of time, it is solved for independently of C_b within the blood flow model, meaning the only variable in Equation (7.18) is C_b.

We briefly note that while blood flow is dominantly one-directional, many smaller branches can experience small amounts of negative flow, immediately following the heartbeat driven pulse. This is particularly true as, unlike most human vasculature, pulmonary veins do not have valves to prevent back flow. For this reason both up and down-winding are necessary for stable implementation.

Boundary conditions

At each outflow branch, during outward flow, concentration is removed from the branch, proportional to the flow rate, meaning

$$\frac{\partial C_b}{\partial \mathbf{n}} = -\frac{Q_b}{A_b} C_b,$$

where $\mathbf{n}$ is the outward normal vector to the boundary. During inward flow, it is assumed that no concentration of gas re-enters the system, such that

$$\frac{\partial C_b}{\partial \mathbf{n}} = 0.$$

At each inflow boundary, flow is only positive (due to the prescribed inflow rate, given in Equation 7.17). Thus, there is one inflow condition of the form

$$\frac{\partial C_b}{\partial \mathbf{n}} = -\frac{Q_b}{A_b} C_{\text{in}},$$

where C_{in} is the upstream gas concentration.

Physically, as gas circulates the body some may be absorbed into tissues, or converted into another gas through processes such as aerobic respiration. To account for this process, we use a simple loss function, of the form

$$C_{\text{in}}(t) = (1 - f_{\text{loss}})\bar{C}_{\text{out}}(t - t_{\text{circulation}}), \tag{7.19}$$

where $\bar{C}_{\text{out}}$ is the averaging outflow gas concentration, and $t_{\text{circulation}}$ is the average time it takes the gas to circulate the body (to get from the outflow point back to the model inlet). The loss fraction f_{loss} is the percentage of the gas lost on average through absorption by body tissues, or through chemical reactions (such as respiration).

7.2.4 Alveolar-capillary gas transfer model

To close the full pulmonary model outlined in this chapter, a model for gas transfer between acinar regions and the capillaries is needed. Physiologically, transfer across the alveolar-capillary membrane is driven by the partial pressure gradient between the two regions, leading to the equations (Ben-Tal, 2006):

$$\frac{\partial V_{\text{acin}} C_{\text{acin}}}{\partial t} = \mathcal{D}_{\text{cap}}(P_{p,b} - P_{p,\text{acin}}), \tag{7.20}$$

$$\frac{\partial V_b C_b}{\partial t} = -\mathcal{D}_{\text{cap}}(P_{p,b} - P_{p,\text{acin}}), \tag{7.21}$$

where C_b is the concentration in the centre of the capillary, C_{acin} is the concentration in the associated acinar region, and $\mathcal{D}_{\text{cap}}$ is the diffusing capacity (not to be confused with diffusion rate) of the gas across the alveolar-capillary membrane. $P_{p,b}$ and $P_{p,\text{acin}}$ are the partial pressures of the gas in blood and the acinus respectively, calculated as

$$P_{p,b} = \frac{1}{\sigma_b} C_b,$$

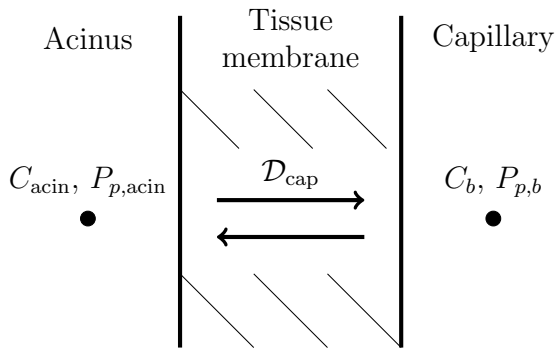

Figure 7.5: Schematic of the alveolar-capillary transfer model.

$$P_{p,\text{acin}} = P_{\text{acin}} C_{\text{acin}},$$

where σ_b is the solubility of the gas in blood, and P_{acin} is the gas pressure inside the acinus, which is the total pressure, minus the water vapour pressure (typically 47mmHg). A basic schematic of the alveolar-capillary model is given in Figure 7.5. Values for $\mathcal{D}_{\text{cap}}$ and σ_b can be found in Table 7.1.

The model for gas transfer across the alveolar-capillary membrane is solved using a backward Euler discretisation, with equal time step size to both gas concentration models. Under this discretisation, this leads to a series of 2×2 linear systems, which can be efficiently solved through direct manipulation.

7.2.5 Pulmonary model

Combining the models outlined in the previous sections, we can achieve simulation of gas transport throughout the entire pulmonary system. The process for this is described in Algorithm 1 and Figure 7.6. Firstly, the ventilation profile and associated acinar volumes are calculated using System (7.1)-(7.4). The acinar volumes are then used to calculate capillary lengths using Equation (7.6), meaning the blood flow

profile and arterial areas can be simulated through System (7.7)-(7.8). Once the ventilation and blood flow distributions are calculated, gas transfer is simulated using Equation (7.5) for the airways and Equation (7.18) for the bloodstream. Both of these equations are discretised using the same time step size, and at each time step are solved independently of each other. Between time steps, System (7.20)-(7.21) is used to account for gas transfer across the alveolar-capillary membrane.

Algorithm 1: Solution process for the pulmonary model

Data: Airway structure

Result: Concentration profiles for the airways ($\mathbf{C}$) and arterial network ($\mathbf{C}_b$).

if *Arterial structure doesn't exist* **then**

  Construct arterial structure from airway structure.

end

Calculate $\mathbf{Q}$ and $\mathbf{V}_{\text{acin}}$ from (7.1)-(7.4) (until stable over one breathing cycle).

Calculate capillary lengths from (7.6).

Calculate $\mathbf{Q}_b$ and $\mathbf{A}_b$ from (7.7)-(7.8) (until stable over one breathing cycle).

Set $t_{\text{simulation}} = 0$.

Set $\mathbf{C}_b^0 = \mathbf{0}$, $\mathbf{C}^0 = \mathbf{0}$.

while $t_{\text{simulation}} < t_{\text{end}}$ **do**

  Calculate $\mathbf{C}^{n+1}$ from (7.5).

  Calculate $\mathbf{C}_b^{n+1}$ from (7.18).

  Update $\mathbf{C}_b^{n+1}$ and $\mathbf{C}^{n+1}$ using (7.20)-(7.21).

  $t_{\text{simulation}} = t_{\text{simulation}} + \Delta t$.

end

Ventilation and blood flow profiles are simulated over consecutive breathing cycles until stability (within 1%) is reached (typically taking 3 periods). These profiles are then repeatedly used to simulate gas transfer for as long as necessary. While in many

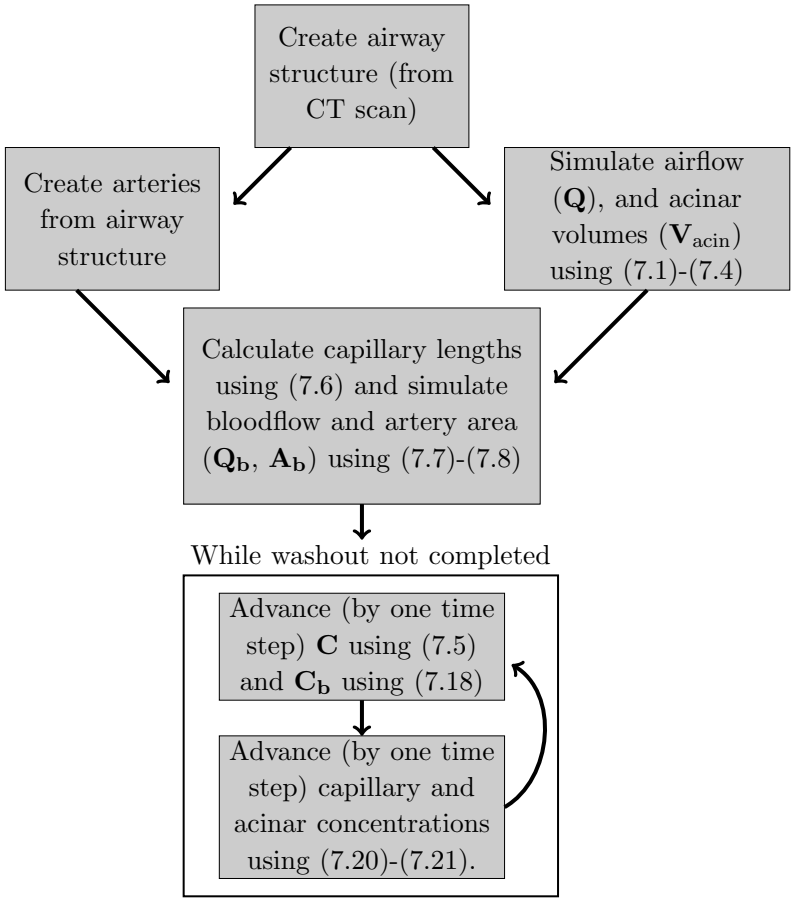

Figure 7.6: Flow diagram for the pulmonary model solution procedure.

applications gas transfer is simulated for a substantially longer period than blood flow, the solution speed is still dominated by the time taken to calculate the blood flow profile. This is because all other components of the model are solved implicitly, meaning time step sizes can be much larger ($\approx 10^{-2}$) than that of the explicit blood flow scheme ($\approx 10^{-6}$).

7.2.6 Error convergence

Error convergence was analysed under simultaneous temporal and spatial refinement of the model, using the fine mesh error metric in Equation (2.10). Due to computational constraints, to allow for a significant number of data points, error was analysed in a

3 generation pulmonary network and a 5 generation pulmonary network. The small airway structures were created by randomly growing a tree to the desired depth, starting with a healthy trachea with radius (1 cm) and length (10 cm). At each new generation, each daughter branch was grown from its parent, using a branch angle of 30°, and radius and branch length reduction factors of 0.8 and 0.6 respectively. However, to add inherent randomness into the tree structure, each instance of the reduction factors was scaled by a normal-random number, drawn from the distribution $\mathcal{N}(1, 0.05)$.

Blood flow and cross-sectional area profiles (over 12 seconds) for the 3 generation network were calculated at the centre node of each branch (in arteries, capillaries and veins) with 1, 3, 7, 15, and 31 nodes per branch, and corresponding dt values of $0.002, 0.001, 0.0005, 0.00025, 0.000125$. Error was calculated as the maximum relative difference between the solution and the corresponding fine mesh solution at all branch bifurcations, and centre nodes. The fine mesh solution was created using 63 nodes per branch, and $dt = 0.0000625$. A similar process was applied to analyse error in the 5 generation network, using $dt = 0.0002, 0.0001, 0.00005, 0.000025$ and 1, 3, 7, and 15 nodes per branch, and a fine mesh solution created with 31 nodes per branch, and $dt = 0.0000125$. The convergence of error in the structures can be seen in Figure 7.7. The convergence appears linear, as is expected from the Lax-Wendroff scheme.

A similar approach was applied to analyse convergence of the gas transport model. Simulations of a 30s N_2 washout (preceded by a 30s N_2 wash-in) were performed in a 3 and 5 generation network, with the same pairs of dt and number of nodes as

above. The discretisation was applied to both the blood flow and concentration model, across the airways and arterial network. The error convergence is shown in Figure 7.8, appearing linear as expected.

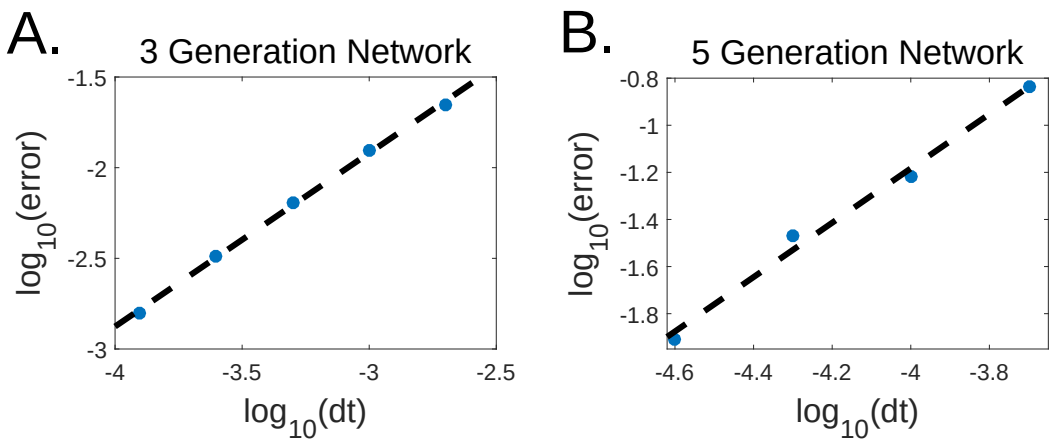

Figure 7.7: Error convergence of the blood flow model in a 3 generation network (A), and a 5 generation network (B). Both error plots have slopes of approximately 1, indicating linear convergence (as expected).

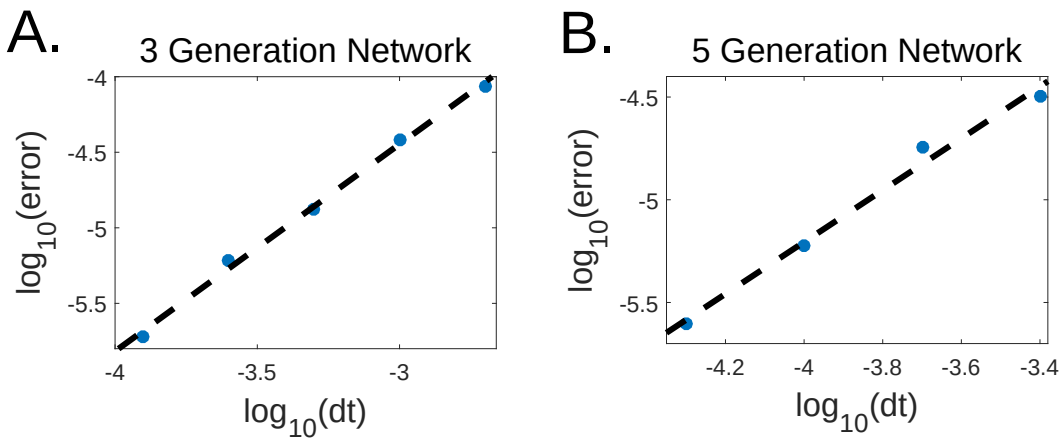

Figure 7.8: Error convergence of the pulmonary model in a 3 generation network (A), and a 5 generation network (B), over the arteries, acinar regions and airways. The two error plots have slopes of approximately 1.2-1.4, indicating linear convergence (as expected).

7.3 Simulation of a washout

Given the detail required in model development within this chapter, we do not apply the model to a clinically meaningful question. Instead, we simply provide some basic behaviours of solution profiles, leaving more detailed analysis to Chapter 8. Since the focus of this thesis has primarily been on the analysis of pulmonary function tests, we apply the pulmonary model to simulate a multiple breath nitrogen washout. The washout is simulated using N_2 as the tracer gas, with a wash-in concentration of 78% (standard concentration of N_2 in air), and a wash-in length of 120 s. Both wash-in and washout are simulated using parameters given in Table 7.1. The simulation was performed on one of the healthy structures from the Bordas set.

In Figure 7.9, we give basic profiles of blood flow and arterial area in a pulmonary vein and a capillary. As the figure shows, blood flow throughout the network follows a pattern quite similar to the prescribed inlet flow shown in Figure 7.3. Interestingly, we see a sinusoidal alternation in peak flow values every four heartbeats, with the relative amplitude being greatest in the capillaries. This is due to the expansion and contraction of the capillaries (in response to the expansion and contraction of the alveoli), which sends small shock-waves in both directions throughout the system. Considering the arterial area profiles, we note that they behave similarly to the blood flow profiles, expanding in response to each heartbeat, though with a slower return to resting size. The arterial area is actually very slightly offset from the blood flow, experiencing a delay of a few fractions of a second. This is logical, as the blood

flow rate is primarily driven by the upstream flow, while arterial cross-sectional areas change in direct response to flow rates.

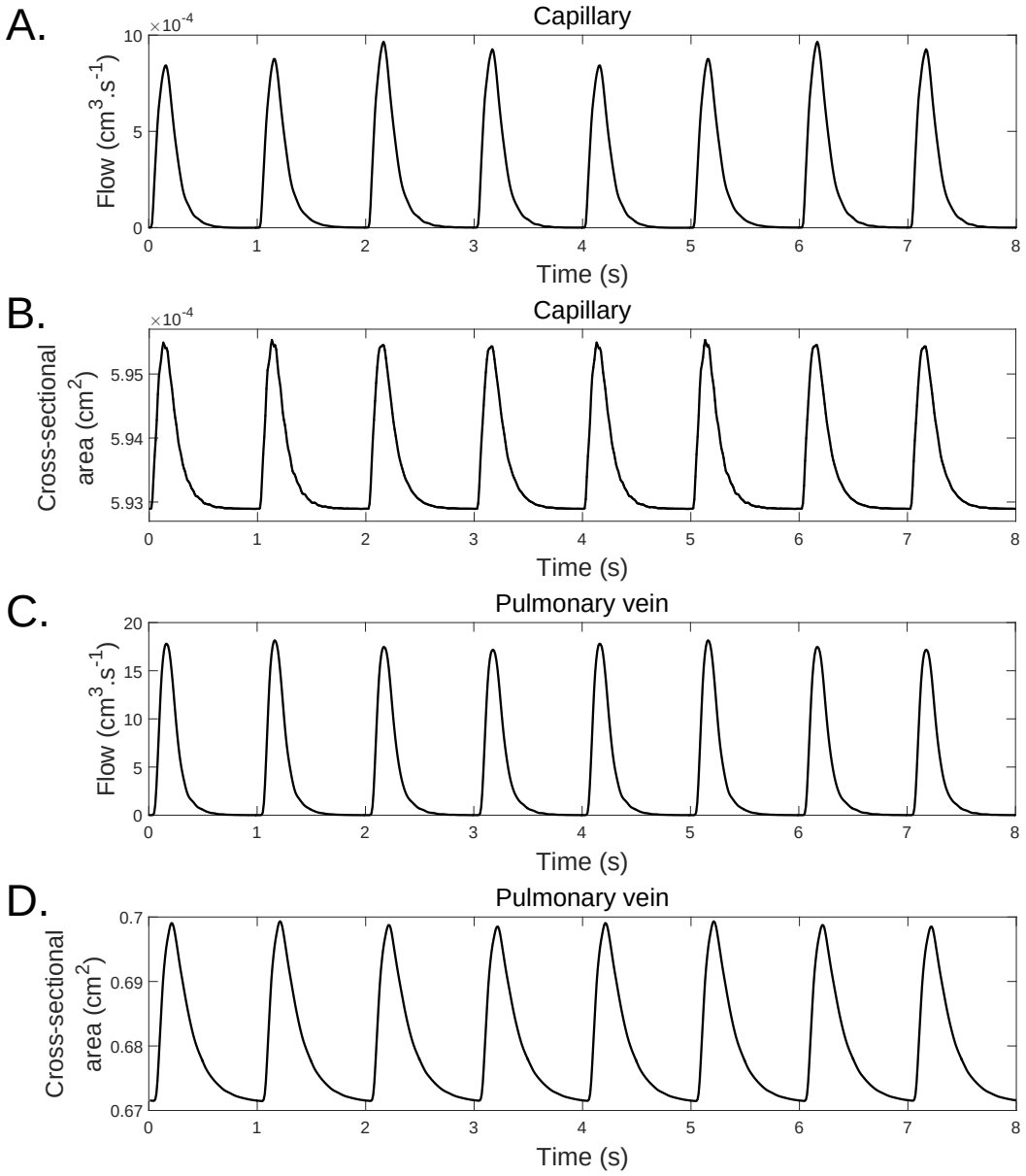

Figure 7.9: Blood flow and cross-sectional area profiles in a capillary (A,B) and pulmonary vein (C,D). The capillaries undergo a strong sinusoidal pattern in peak values, driven by the expansion and contraction of the acinus. Flow is significantly larger in the pulmonary arteries, which also undergo a more significant cross-sectional area deformation.

In Figure 7.10, we show the more detailed washout profiles. No immediately obvious

effect of the bloodstream can be seen in the tracheal N_2 concentration profile. This is to be expected though, given that the individual contributions from the capillaries will be smoothed out by the time they reach the trachea. Effects of the exchange can be more clearly seen in the washout profiles for the acinus and capillary. During each exhalation the concentrations between capillary and acinus stabilise, as N_2 is a perfusion-limited gas, and the acinus does not change gas concentration since it loses mass proportional to its volume contraction.

However, once an inhalation starts, both the acinar region and capillary experience a small increase in gas concentration. This may seem counter-intuitive at first, but is driven by the out of sync relationship between flow rates and volume. If flow is approximately sinusoidal (as assumed in our model), when an inhalation starts the flow rate is increasing rapidly, while the volume is changing slowly. Thus, for the acinus, the inflow concentration is initially high enough to overcome the increase in volume (which would drive a decrease in concentration). As the acinus concentration increases, the capillary concentration is seen to increase too, maintaining equilibrium. Shortly after though, the rate of increase of flow into the acinus slows while the rate of change of volume still increases. This change leads to the volume change becoming the dominant process, leading to a decrease in acinar concentration. As this occurs, N_2 starts transferring from the capillary into the acinus, causing a reduced rate of concentration decrease, and significant emptying from the capillary.

Considering the gas concentration in the left pulmonary artery, we see expected behaviour. Given the arterial network started with no gas concentration, it takes

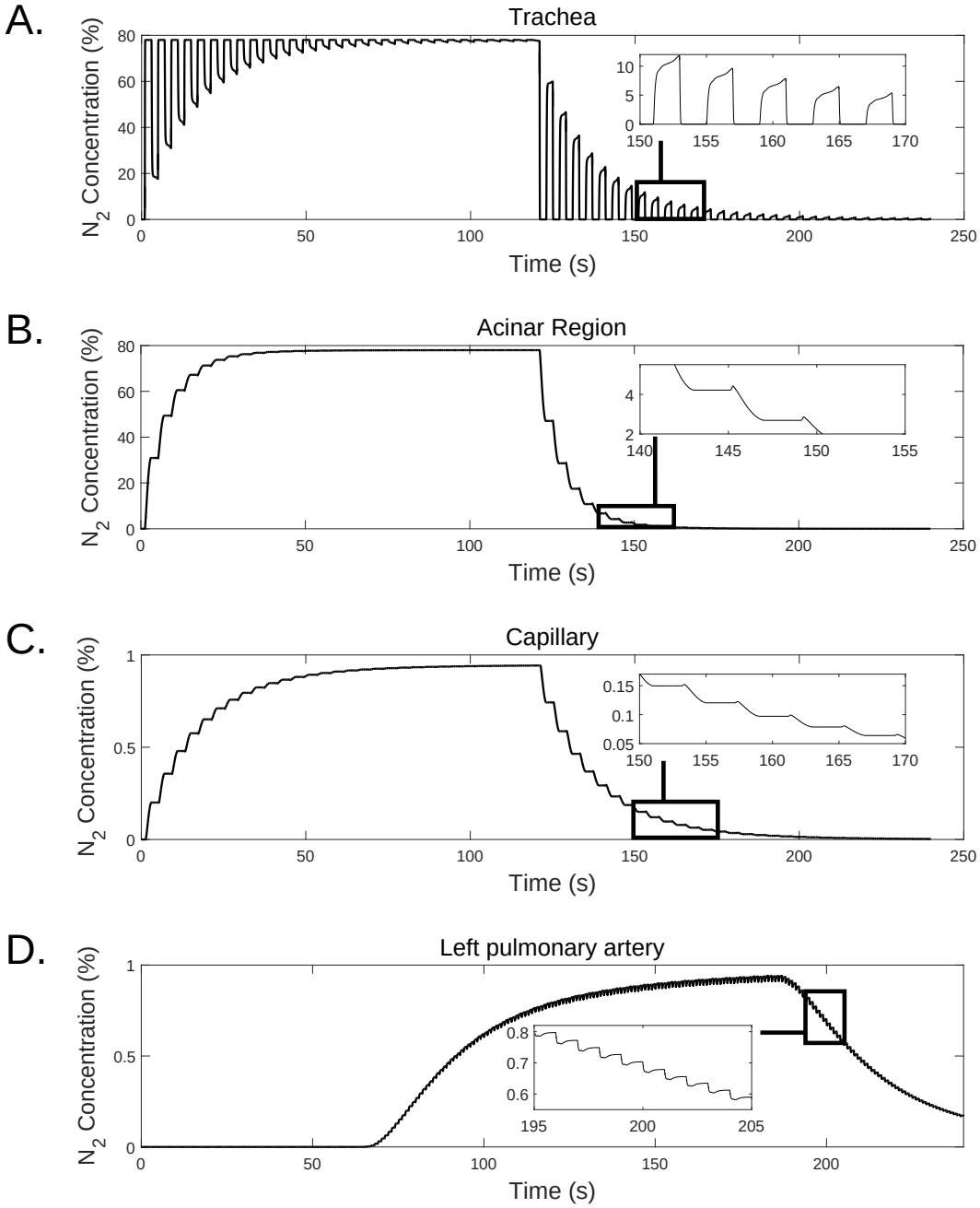

Figure 7.10: Concentration profiles at various locations in the pulmonary network. Nitrogen concentrations can be seen during wash-in and washout at the trachea (A), in an acinar region (B) and its associated capillary (C), and in the left pulmonary artery (D). For each washout profile, a zoom in is given to show behaviour over a few breaths.

slightly more than 60 seconds (the chosen $t_{\text{circulation}}$) for the left pulmonary artery to experience gas transfer. Gas enters the pulmonary artery equal to the mean venous

outflow concentration, stabilising to approximately the same concentration as the capillary (though with more variance, due to it being the average value over multiple outlets). Given the assumed blood circulation time, the pulmonary artery does not begin emptying til more than 60 seconds after the washout has begun. Interestingly, the pulmonary artery empties at a much slower rate than the shown capillary. This is due to cumulative effects, and that the capillaries are not perfectly in sync with each other (similar to the acinar regions).

As a final point, we note that before the washout began, gas concentrations in the capillaries stabilised to just under 1%, while concentrations in the acinus stabilised at 78%. This is in line with the normal physiological concentration of nitrogen in the bloodstream, when breathing standard air (78% nitrogen).

7.4 Discussion

In this chapter we have presented the design and implementation of a gas transport model for the entire pulmonary system, alongside preliminary results from simulation of a multiple-breath nitrogen washout. Further analysis of the inert-gas washout using the full pulmonary model will be presented in Chapter 8. We instead close this chapter with a discussion of computational considerations, limitations, and potential future work.

7.4.1 Computational constraints

As outlined previously, the computational scale of the model is quite large. For the simulations performed in this thesis, to calculate the blood flow and arterial

cross-sectional area profiles over 12 seconds, a system of approximately 1,500,000 variables was iteratively solved 10^7 times. More generally, if we have an N generation network, the number of branches can be approximated by 2^N, leading to 2^{N+1} branches in the associated arterial network (excluding the capillaries). Assuming that only bifurcations occur (no trifurcations), and using the most coarse discretisation possible, each arterial branch contains 14 variables (two at the branch centre, 4 at each branch end, and 2 ghost nodes at each branch end). If each terminal bronchiole is subtended by a single acinus with a single capillary, there are 2^{N-1} total capillaries, each also having 14 variables. This leads to a total system complexity of

$$\mathcal{O}\left(14(2^{N+1} + 2^{N-1})\right).$$

Further to this, the time step constraint on the Lax-Wendroff scheme scales linearly with the branch length (which directly relates to Δx). Assuming a branch length scaling factor of 0.6 (approximated from histological data (Horsfield, 1978)), as the tree grows, the total number of time steps scales according to 1.65^N. For a 2 generation system, with a physically realistic geometry, we estimated a necessary step size of $\Delta t = 10^{-3}$, leading to approximately 10^4 steps per solution (of a 12 second blood profile). Given this, the total complexity of the model (expressed as number of necessary variable-iterations) is

$$\mathcal{O}\left(14(2^{N+1} + 2^{N-1}) \times 10^4 1.65^N\right) \approx \mathcal{O}\left(10^5 \times 2^{1.72N+1}\right).$$

For a full respiratory system ($N \approx 23$), this would lead to approximately 10^{17} variable iterations. In practice, this number is much greater, as beyond generation 16-17 the

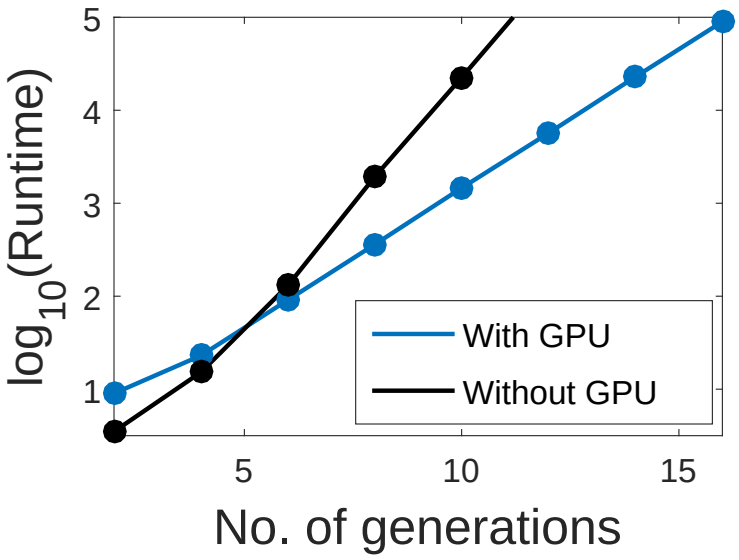

Figure 7.11: Comparison of runtimes when simulating blood flow with and without a GPU architecture. Run times are given for arterial trees with generation sizes 2-16, times are in seconds

.

assumption of each branch being subtended by a single acinus fails to hold. Regardless, this presents significant computational strain, which we illustrate by comparing run times with and without GPU implementation, for various tree sizes (Figure 7.11).

7.4.2 Limitations

Within this chapter we have presented a detailed computational model for simulation of gas transport within the entire pulmonary system. Through application of efficient numerical methods and the use of high-performance computing environments, this model was shown to be tractable to a degree where clinical research utility is possible. As mentioned at the start of the chapter, models for pulmonary blood flow are not a completely recent development within the literature. However, most applications have been strongly limited by available computing power, and as such use simple

approximations for flow in the capillaries and small arteries, and often exclude any venous component. As we have shown, through the embedding of the blood flow models in efficient parallel environments, many of these computational limitations may be overcome, allowing for effective simulation of the pulmonary system to much deeper levels.

Clearly though, this model still applies a variety of simplifying approximations, to make simulation at this depth computationally tractable. Similar to the airway models outlined in Chapter 2, the strongest limitation of the pulmonary model is the simplicity of the respiratory zone approximation. Representation of all veins and arteries below the structural resolution by a single capillary is clearly not physically realistic. However, as with the ventilation model this is primarily driven by a lack of realistic structural information and computational constraints. With access to more powerful HPC environments, and improvements in imaging techniques (such as micro-CT (Litzlbauer et al., 2010)), these limitations may be overcome.

Beyond this, the model is 1D in nature, meaning it cannot account for turbulent effects in both air and blood flow. Again, this choice is primarily made due to computational constraints. Given that both airflow and blood flow drastically slow as airway and artery radii decrease, we do not believe that the 1D approximation significantly affects accuracy. However, in the blood flow modelling literature, some groups have taken a multi-scale approach, whereby the largest branches are modelled using a full 3D Navier-Stokes, before transitioning to 1D, past a certain point (Formaggia et al., 2001). This approach could be explored in future work through adaptation of the

model outlined in this chapter.

Further to this, the model uses parameterised inflow and outflow boundary conditions for blood flow. While we have applied a simplistic model for inflow in this chapter (Equation 7.17), this could clearly be replaced with patient-specific data, or used to represent more complex scenarios (as would be caused by various heart conditions). Equally, the outlet boundary is parameterised by a Windkessel model, with 3 degrees of freedom ($\mathcal{R}_1, \mathcal{R}_2, \mathcal{C}_T$). For results within this thesis, we have parameterised this model with values taken from a prior study in the literature (Olufsen, 1998). However, in future work, investigations could be undertaken to improve the outlet boundary condition, and create more accurate estimations of downstream resistance and compliance.

Considering the arterial boundaries, the model for gas transfer also uses a simplistic approximation of gas loss throughout circulation (see Equation 7.19), parameterised by $t_{\text{circulation}}$ and f_{loss}. These were simple approximations made to allow for closure of the model. More complex models for f_{loss} could be implemented by approximating the diffusion of a given gas into body tissues, and equally, each outlet boundary could be approximated by a unique $t_{\text{circulation}}$, if relevant experimental information was available.

Another simplification made within the model was the lack of gravitational effects on the bloodstream, which would lead to blood pooling. This simplification was made due to a combination of time and computational constraints. However, in the literature blood flow models which incorporate gravitational effects have been implemented and

analysed (Burrowes and Tawhai, 2006). Thus, we believe that these effects could easily be incorporated in future work.

Finally, the models were applied using pulmonary networks which were directly modelled based off of the CT-generated airway structures, as opposed to an independent CT-generated artery/vein network. While the pulmonary arteries and veins closely follow the airway structure, this is not a perfect correspondence. We note though, that while this represents a limitation underpinning some of the results in the thesis, it does not represent a limitation of the model itself, which in the presented form may be applied to any given 1D airway and pulmonary structure.

While the outlined limitations may seem significant, they should be interpreted in context of the computational considerations. The majority of these limitations are not inherent to the model, but simply chosen factors (termination depths, etc.) based on computational constraints. Given the parallelisable nature of the model, advancements in computing power may allow many of these limitations to be overcome. Equally, the constant approximation of many factors ($f_{\text{loss}}, \mathcal{R}_1$, etc.) was chosen because the primary motivation for the pulmonary model within this thesis is to perform an exploratory analysis of the MBW. The investigation of more complex and physically realistic approximations is a clear avenue for future work.

7.4.3 Future work

While we have applied the full pulmonary model to the simulation of N_2 washouts, the adaptation to a wider range of scenarios can be easily achieved with simple

modifications.

The model outlined in this chapter is suitable for modelling transport of gases which cross the alveolar-capillary membrane, but which otherwise do not strongly interact with body tissues, or do so through a simple diffusive process. This means that the model in its current form cannot be applied to model the two gases of highest interest in respiration; oxygen and carbon dioxide. However, adaptation of the model into this scenario is fairly straightforward, by building on prior work in the literature, such as that of Ben-Tal (2006). For the simulation of oxygen transport, the alveolar-capillary exchange model can be modified to account for haemoglobin binding and saturation such that

$$\frac{\partial V_b C_b}{\partial t} = \mathcal{D}_{\text{cap}} \left(P_{p,b} - P_{p,\text{acin}} \right) - N_0 T_h V_b \frac{dS}{dt},$$

where C_b is the oxygen concentration, N_0 is the maximum number of molecules of O_2 that can bind to haemoglobin, T_h is the haemoglobin concentration, and $S(T)$ is the saturation function of oxygen in haemoglobin. Various different forms for the saturation function exist within the literature (Ben-Tal, 2006).

Ben-Tal (2006) also presented similar models for transport of CO_2 in the blood. However, to simulate both O_2 and CO_2 transfer across the pulmonary system, the model would need to be further expanded to incorporate a respiration model, which decomposes O_2 into CO_2. This could be incorporated by making the O_2 and CO_2 loss functions dependent on CO_2 and O_2 concentration, with parameters inferred from the aerobic respiration chemical reaction.

If these adaptations were applied to the model, it would potentially be capable of realistically simulating a much larger variety of physical scenarios, and to more precisely probe disease processes, and pulmonary function tests. The potential uses for such a model are quite vast, as there is still a strongly limited understanding of how different morphological changes across both the airway and veins/arteries affect the overall function of the pulmonary system. The model could be applied to a variety of questions such as investigating how pulmonary arterial wall thickness increases (as can be seen due to high cholesterol) affect the O_2 distribution across the lungs, or how an elevated heart rate may affect clinical respiratory measurements. This array of questions forms an exciting direction for future research within the field of computational modelling of the human body and the pulmonary system.

7.5 Summary

Within this chapter we have presented a detailed model of blood flow, and gas transport within the entire pulmonary system. To achieve computational tractability, this model has been embedded within a high-performance parallel computing environment, allowing for efficient simulation within a practical time frame. Following the design, implementation, and error analysis of the model, brief results of blood flow, and an N_2 MBW profile were presented. The chapter was then closed with a discussion of computational considerations, potential limitations, and of potential avenues for future research.

8

Applications of the pulmonary model

In the previous chapter we extended upon the models from Chapter 2 to allow for efficient and detailed simulation of the pulmonary system. Within this chapter, we apply this pulmonary model to analyse how the choice of tracer gas can affect the inert-gas washout. This is intended as a brief concluding study, to highlight the potential value that full pulmonary simulation may add, comparative to airways simulation.

8.1 Rationale

The primary purpose of the lungs is to facilitate the exchange of gases between the outside world and the body, and thus to allow for cellular respiration. Given the transport role that the pulmonary arteries and veins play, it seems natural that

pulmonary system health should be defined in relation to both the airways and the bloodstream. However, many pulmonary function tests analyse mechanics of the two systems in effective isolation, through measurements of airflow (as in spirometry), or of blood properties (e.g. blood pressure measurement). This is done for a variety of reasons, often relating to ease of performance and interpretation of the tests. However, due to the highly interactive nature of the systems, tests which monitor only one of the systems in isolation may not be as effective in diagnosing true pulmonary health.

Considering the inert-gas washout in particular, the test is performed in one of two ways. Either an inert gas with low pulmonary permeability (such as ^{3}He or SF_6) is first washed-in at a set concentration, and then washed out; or, since N_2 exists naturally in air, it is washed out by switching a subject to an air mixture without nitrogen gas (typically pure oxygen). Due to the differences in pulmonary permeability, these two types of washout work in opposing ways, with N_2 washouts being heavily influenced by interactions from the bloodstream, while ^{3}He and SF_6 washouts effectively ignore these effects.

However, within the literature there is relatively little comparative analysis of different washout gas choices. It is assumed that SF_6 probes the lung more deeply than ^{3}He, due to its higher molar mass, and larger diffusion rate in air (Robinson et al., 2013), leading to an expected small elevation in LCI and s_{cond}. However, this has also been shown to reverse under various lung pathologies, particularly for disease within the respiratory zone (Ljungberg and Gustafsson, 2003; Van Muylem et al., 2005).

Within clinical practice, N_2 washouts are typically more commonly performed than other types. This is primarily due to the low cost, and wide availability of pure oxygen (comparative to wash-in gas mixtures), and the lower time requirements for performing N_2 washouts, due to the lack of a wash-in phase. It is well known that bloodstream interactions may affect the nitrogen washouts. However, as Robinson et al. (2013) noted, 'Estimation and correction of tissue N_2 contribution is difficult due to limited available data to base correction on, and adjustment for tissue N_2 is not currently recommended'.

This is further exacerbated by the fact that different research groups predominantly use one gas over all others (most likely due to supply and implementation ease). Consequently, within the literature SF_6 and ^3He are heavily used in studies of cystic fibrosis (Aurora et al., 2005b; Horsley et al., 2008; Kent et al., 2014), while N_2 has been more commonly applied to studies of asthma (Downie et al., 2007; King et al., 2005; Strömberg and Gustafsson, 2000), making direct comparison quite challenging. The lack of standardisation in application, and the lack of good comparative data between different gas choices illustrates a clear gap within the literature.

Within this chapter we aim to help address this literature gap, by investigating the effect that gas choice may have on both LCI and s_{cond}. In particular, we apply the pulmonary model developed in Chapter 7, to simulation of the multiple breath nitrogen washout. Indices derived from these washouts are then compared to washouts performed using SF_6 and ^3He, outlining the potential effect that bloodstream interactions may have on test outputs. We close the chapter with a brief discussion of the

clinical relevance of the results.

8.2 Simulation protocol

To investigate the effect that gas choice may have on the inert-gas washout, we perform two different sets of simulations. Within the first batch, the MBW was simulated on 26 of the 31 virtual structures within the Bordas set. Washouts were simulated for each structure in the set, using three tracer gases: ^{3}He and SF_6, (without bloodstream effects), and N_2 (with bloodstream effects). Simulations were not performed on the 5 largest structures within the set, due to an 8Gb RAM limitation on the laptop used for simulations.

In the second simulation batch, we investigated the effect of the bloodstream in a more granular setting. Firstly, a healthy structure (subject 1), and two asthmatic structures (subjects 2 and 3) were selected from the Bordas set. For each structure, nitrogen washouts were simulated after artificially blocking gas transfer across a percentage p ($p = 10, 20, \ldots, 100$) of the alveolar-capillary membranes. Blockages were applied to a uniformly random percentage of acinar regions across the lung, by setting the local diffusing capacity ($\mathcal{D}_{\text{cap}}$) to 0. For each simulation s_{cond} and LCI were calculated. It should be noted that for the nitrogen washouts, an artificial wash-in phase was simulated, at 78% nitrogen, to simulate the effects of breathing normal air.

8.3 Results

As in prior chapters, all s_{cond} values are presented in L^{-1}, and LCI in turnovers.

8.3.1 Comparing different tracer gases

In Figures 8.1 and 8.2, we compare simulated s_{cond} and LCI responses across the Bordas set, using the three different tracer gases. Considering the non-bloodstream washouts first, we note that there is small negative bias in both LCI and s_{cond}, when performing ^{3}He washouts relative to SF_6. This could potentially be due to the higher diffusivity of helium, allowing constricted areas to washout slightly faster than with SF_6. However, the confidence intervals for this difference greatly overlap zero, meaning the inference is quite weak.

Comparing N_2 washouts to ^{3}He and SF_6 washouts, we see more consistent results. In both cases, s_{cond} has a noticeable negative bias when using N_2, with the effect size increasing as s_{cond} increases. Conversely, LCI has a positive bias with N_2, again with magnitude increasing with the index value. For both indices the difference is consistent, with the 95% confidence intervals excluding zero, and only one slight outlier.

8.3.2 Gradual reduction of alveolar-capillary transfer

In Figure 8.3, we illustrate the effect that gradual closure of the bloodstream may have, by considering this reduction in three structures, a healthy (subject 1), and two asthmatics (subjects 2 and 3). In all three cases, the overall changes in s_{cond} and LCI are fairly small (particularly for LCI). However, the transitions are consistent and smooth for both indices, with LCI decreasing, and s_{cond} increasing as bloodstream contributions are reduced. We note that for 2 of the cases, the transition is not linear, but strongly logistic, with maximum change occurring at approximately 50% blockage.

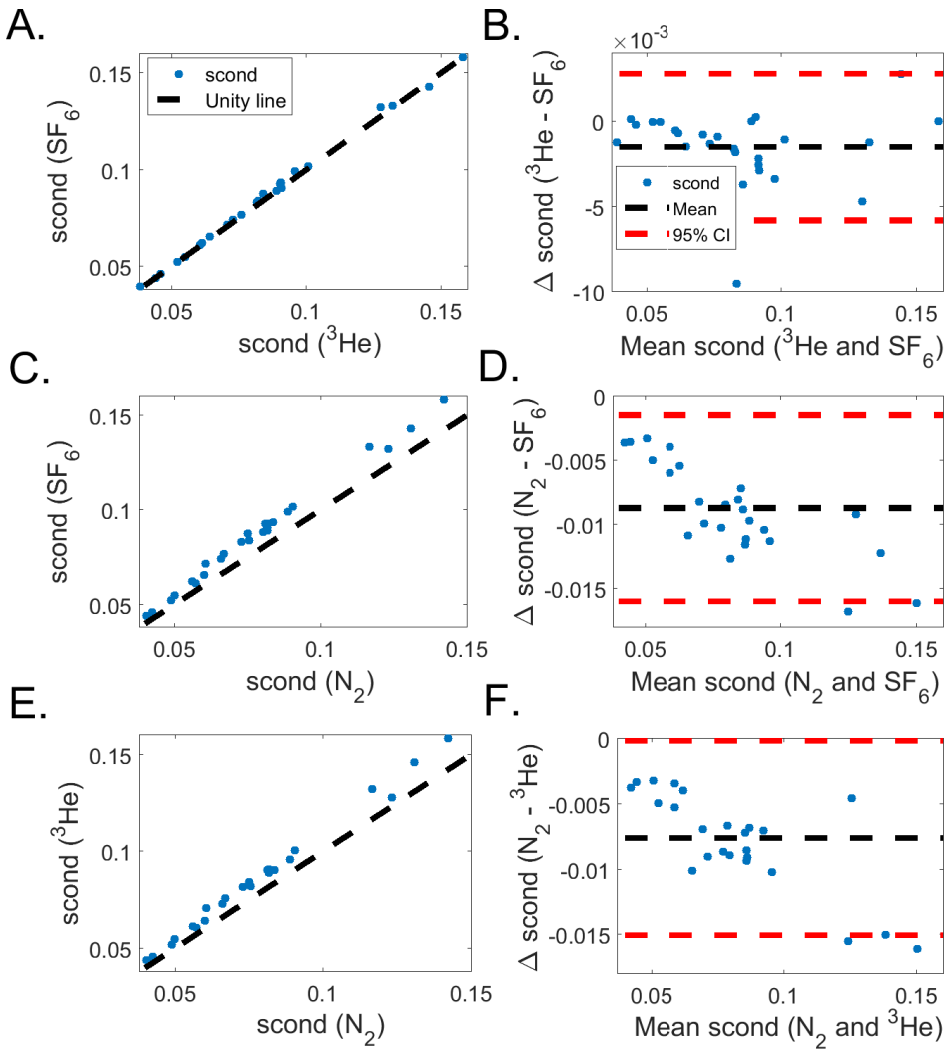

Figure 8.1: Comparison of simulated s_{cond} with different tracer gases. Results comparing ^{3}He, SF_6 and N_2 are given, with corresponding Bland Altman plots.

8.4 Discussion

In this chapter we have applied the previously developed pulmonary model (see Chapter 7) to analysis of the effect that tracer gas choice has on the multiple-breath washout. While the analysis performed in this chapter is only exploratory, the results still provide potentially meaningful insight.

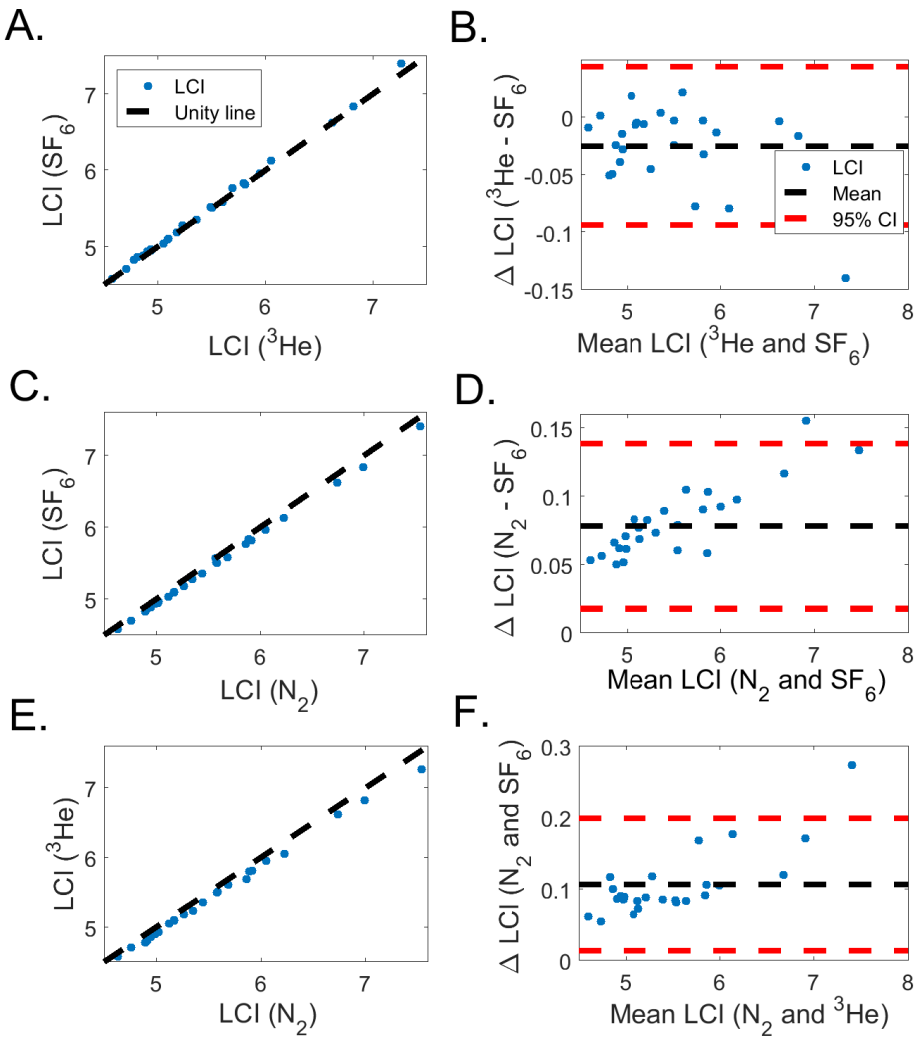

Figure 8.2: Comparison of simulated LCI with different tracer gases. Results comparing SF_6 to ^3He (A), SF_6 to N_2 (C) and N_2 to ^3He (E) are given, with corresponding Bland Altman plots (B,D,F).

8.4.1 Effect of gas choice on MBW outputs

As the results in Figure 8.1 and 8.2 show, gas choice appears to have a small, but consistent effect on MBW outputs. ^3He washouts were shown to produce slightly smaller indices than corresponding SF_6 washouts. This is most likely due to the higher diffusivity of Helium, allowing gas to more easily exit constricted areas, particularly in the small airways. This effect size was quite small though, and would most likely

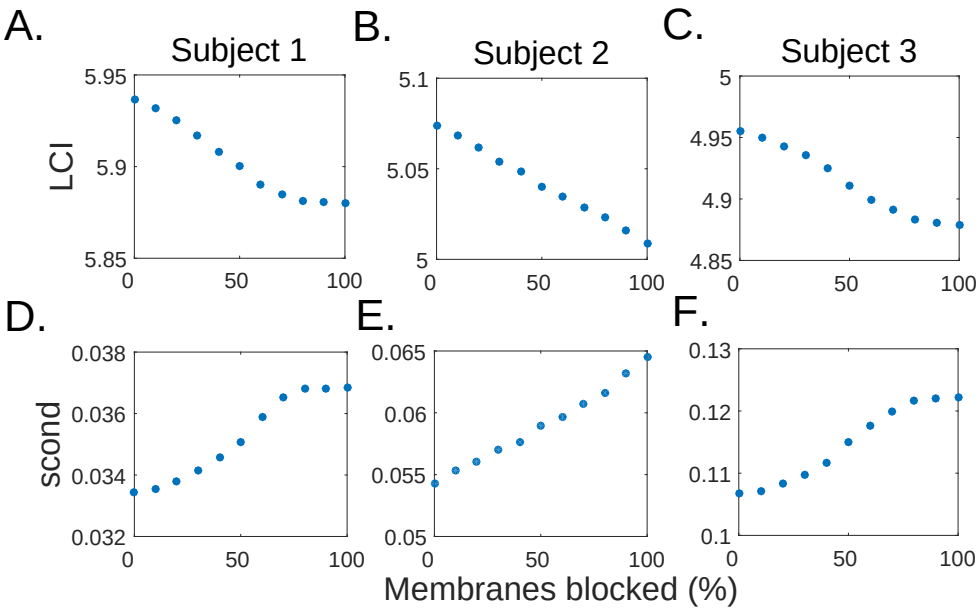

Figure 8.3: Effect of alveolar-capillary membrane blockage on LCI and s_{cond}. Results are given for three cases, representing a healthy subject (A, D), and two asthmatics (B,C,E,F). Consistent changes in both LCI (A-C) and s_{cond} (D-F) can be seen as more membranes are blocked.

be overpowered by random noise in clinical data.

However, the differences were more significant when analysing the influence of pulmonary permeability. s_{cond} was seen to be significantly reduced (by 5-20%) when simulating the washout with N_2, comparative to the other gases. Conversely, LCI was seen to by increased (by 2-7%) by gas transfer from the bloodstream. It can be noted that the same differences were seen when comparing to ^{3}He (which has higher diffusivity than N_2), and SF_6 (which has lower diffusivity than N_2). Thus, we can be confident that these differences are primarily driven by the incorporation of gas transfer across the alveolar-capillary membrane.

Why the bloodstream contributions lead to a reduction in s_{cond} but an increase in LCI, can be understood by considering how each index is calculated. s_{cond} is calculated

as the rate of change of exhaled concentration gradients throughout the washout (see Chapter 1 for more precise details). When performing an N_2 washout, gas from the capillary will enter the acinus as it empties, and help to smooth out the airflow driven concentration front. This in turn will lead to a slight reduction in concentration slope over each exhalation. Furthermore, this effect will grow as the washout progresses (thus reducing s_{cond}), as the bloodstream takes significantly longer to empty than the airways, due to the circulation time of pulmonary blood.

Conversely though, the movement of nitrogen from the bloodstream into the acinus, will increase the maximum exhaled concentration over each breath. Similarly, this effect will become more significant as the washout progresses, due to the relative reduction in alveolar gas concentration. This will in turn mean that more time is needed to washout nitrogen to below the 2.5% (1/40th) threshold, increasing the LCI.

Given the results in Figure 8.3, the transitions appear to occur smoothly, with the decrease in LCI and increase in s_{cond} (as more membranes are blocked) occuring logistically. Due to this logistic transition, it appears that 10-20% of the alveolar-capillary membranes may be able to be blocked, before significant changes in MBW outputs occur.

8.4.2 Clinical significance

It is well known within clinical practice and literature that nitrogen interacts with the bloodstream (Robinson et al., 2013). However, current standard practice when performing washouts is to not correct for this phenomenon (Robinson et al., 2013).

The results within this chapter suggest that this phenomenon is both strong enough and consistent enough to influence interpretation of MBW outputs, particularly with reference to s_{cond}. This study on its own may not provide enough clinical confidence to allow for this correction. However, it provides a foundation for future work to be built upon. The results suggest that when using N_2, s_{cond} is a less sensitive measure, and LCI a slightly more sensitive measure, than when using other inert gases.

8.4.3 Limitations

To the best of our knowledge, the results in this chapter are quite novel, representing the first detailed computational analysis of the inert-gas washout with multiple gases, and bloodstream interactions. However, the pulmonary model we have developed should be considered as an initial step towards more holistic mechanistic modelling of human respiration. The majority of limitations of the pulmonary model have been detailed within Chapter 7; however, we briefly touch on some of the most pertinent ones for the results within this chapter.

It has been noted in prior work in the literature that helium is both more diffusive, and heavier, meaning it may penetrate the lungs more deeply than SF_6, and subsequently produce slightly elevated LCI values (Robinson et al., 2013). This appears to be in direct contradiction to the results illustrated in Figure 8.2. This is most likely due to the simplicity of our respiratory zone approximations, meaning that differences in probing depths of the two gases could not be explored (as these differences are most pronounced in the respiratory zone).

Considering the pulmonary model, it was assumed that no nitrogen was lost to, or gained from body tissue throughout the washout. In practice, nitrogen gas diffuses between the two media, dependent on the concentration gradient (Saladin and Porth, 1998). However, comparative to the alveolar-capillary diffusion, this effect was considered minimal. To more accurately incorporate tissue absorption, specific experimental information would be needed.

Equally, the simulations assumed a perfectly steady heart rate (60 bpm) over the entire washout. In standard practice, subjects are required to breathe tidally at 1 L per breath, but heart rate cannot be controlled so easily. The effect that heart rate has on washouts may be assumed minimal, but more experimental or computational data would be needed to have confidence in this.

8.5 Summary

Within this chapter we have applied the pulmonary model developed in Chapter 7, to the analysis of how tracer gas choice affects the inert-gas washout. Through this analysis, N_2 washouts were shown to have small but consistent bias, with s_{cond} being reduced, but LCI being increased, relative to other gas choices. This work presents a foundation which can be built upon in the future, to better quantify and correct for this bias.

9 Conclusion

Within this thesis, a series of different mathematical and computational models were developed to capture the key physical mechanisms underpinning a variety of different pulmonary function tests. This was performed with the aim of improving understanding of the function-form relationships within the lungs, and in particular to better quantify test responses to morphological changes in lung structure, as occurs in different types of lung disease. The models were also used to generate a series of clinical hypotheses, suggesting potential benefit to more targeted application of certain PFTs.

Within Chapter 2, we described in detail the development and computational implementation of a variety of models relating to different physical processes within the lungs. As an initial step, a model for pressure-driven ventilation was presented, and used to drive a gas transport model across the conducting zone. Alongside this, a

circuit analogous technique was used to approximate impedance across the entirety of the lungs. Collectively, these methods allowed for simulation of tidal ventilation, the inert-gas washout, imaging techniques, and the FOT and IOS. Each model was implemented in a computationally efficient environment, with error convergence analysis presented where appropriate.

Following this work, Chapters 3 and 4 were dedicated to performing an exploratory analysis of outputs derived from the inert-gas washout, MR imaging, and lung impedance. In particular, the responses of each output were explored in relation to constriction of airways within the conducting zone of the lungs. Through this analysis, certain indices were shown to predominantly respond to the severity of applied constrictions, while other indices responded quite differently to equivalent severities, depending on whether the constrictions were distal or proximal. Further to this, certain outputs were shown to be sensitive to airway closure, while other measures could not adequately detect the phenomena. Given these differences, we outlined a series of ways in which joint interpretation of different PFT outputs may be of clinical benefit. In particular, we illustrated the potential utility of joint interpretation of MBW outputs alongside lung reactance measures, and low-high frequency resistive difference ($R_5 - R_{20}$).

For more detailed analysis to be performed there needed to be confidence that the models were accurately capturing the key physiological processes driving each test. Within Chapters 5 and 6 we provided this confidence, by performing a detailed validation of the lung impedance and inert-gas washout models. The lung impedance

model was validated using a combination of experimental data from a 3D-printed lung, and clinical data. Following this, the model was used to provide strength to the interpretation of $R_5 - R_{20}$ as a detector of small airways dysfunction. In Chapter 6, the inert-gas washout model was validated using clinical data, as well as data from the broader literature. The model was then used to improve understanding of how gravity and body position may affect test outputs. Through this, the potential value of comparing MBW outputs taken from opposing positions was illustrated, showing how it may help classify regionalisation of disease.

Within Chapters 7 and 8, the thesis was concluded with an ambitious extension of the models from Chapter 2. The models for ventilation and gas transfer were adapted to incorporate gas transport and flow within the pulmonary arteries, veins and capillaries, as well as across the alveolar-capillary membrane. Within Chapter 7, we presented a detailed description of the model, alongside a series of techniques to improve computational tractability, including implementation in a HPC environment, using GPU computations. Within Chapter 8, this model was used to simulate multiple-breath nitrogen washouts, providing a comparative analysis of how the choice of tracer gas affects the sensitivity of the test, showing the small consistent bias that N_2 creates.

9.1 Clinical significance

The majority of work within this thesis has focused on the development and implementation of computational models. However, the underlying aim has primarily been to improve clinical understanding of pulmonary function test outputs. Below we

summarise the clinically relevant findings within this body of work.

In Chapter 3, the MBW outputs s_{cond} and LCI were shown to consistently respond to increases in severity of bronchoconstriction, but to show no consistent response to changes in the the depth at which the constrictions were applied. The global imaging index σ_r was shown to respond similarly, though unlike the MBW indices, it did not collapse under airway closure. Conversely, the local imaging index σ_{local} appeared to have much more consistent responses to depth, peaking distally, though was deeply sensitive to the neighbourhood size used in its calculation. Interestingly, MBW indices were seen to have a similar sensitivity to constriction as σ_r, with significant increases starting around 40% constriction. This gives justification to the use of PFTs such as the MBW in place of more expensive imaging techniques. Beyond highlighting the different sensitivities of the four indices, these results also suggest that σ_r and σ_{local} may be able to be jointly used to provide more direct quantitative interpretation of MR images.

LCI and s_{cond} were shown to have similar responses to depth and severity within Chapter 4 as in Chapter 3, despite a change in constriction protocol. In the parallel analysis of lung impedance, R_5 was shown to respond mostly to severity, R_{20} to proximal constriction (meaning $R_5 - R_{20}$ responded mostly to distal constriction), and the reactance measures to both severity and depth. Through this analysis we showed that joint interpretation of LCI or s_{cond} alongside either X_5, AX, f_{res} or $R_5 - R_{20}$ may allow for more accurate identification of disease severity and location.

Within Chapters 5 and 6, detailed validations of both models were provided, to

allow for more strength in interpretation of the key results in Chapters 3 and 4. This on its own has clinical significance, as it adds strength to prior results in the literature based on similar models. Within Chapter 5, we also provided a series of analyses to highlight that $R_5 - R_{20}$ sensitively and specifically responds to constrictions within the small airways, suggesting its potential value as a marker of small airways dysfunction in future clinical trials.

Within Chapter 6, we analysed the effect that body position may have on PFT outputs. In particular, it was illustrated that each position has a detection bias, due to the uneven gravitational distribution of ventilation. These biases are inherently present in all positions, and as such, should be accounted for when clinicians are interpreting outputs. Further to this, we illustrated that the response of the inert-gas washout to changes in body position may be sensitive enough to reverse engineer, allowing for classification of disease regionalisation. This in turn could be used to inform ventilation protocols, or underpin a future clinical study.

Finally, in Chapter 8 we analysed the effect that tracer gas choice has on both LCI and s_{cond}. Both indices were seen to change consistently to different disease states, regardless of gas choice. However, the magnitude of response in LCI was larger when simulating N_2 washouts than with SF_6, and conversely for s_{cond}. Both effects were also seen to grow with the index size. This suggests that when performing N_2 washouts, LCI may be a slightly more sensitive indicator of lung disease than s_{cond}, comparative to washouts with ^3He or SF_6.

9.2 Future research

Computational modelling of the human pulmonary system is by no means a recent pursuit. The work within this thesis builds upon, both directly and indirectly, decades of work within the literature. We believe that the models contained within this thesis present a step forward in our ability to accurately, and with computational tractability, simulate the pulmonary system. However, while providing more clarity to a variety of clinical questions, the results within this thesis also raise further questions, forming a series of clear pathways for future research. Within this section we give an overview of potential future research pathways that form natural extensions to the work within this thesis. This is by no means an exhaustive list, but rather illustrates the most clear and potentially fruitful next steps.

9.2.1 Improvements to structural resolution

As noted in many of the chapters, each of the models is inherently limited by the detail and resolution of the lung structure that it is simulated upon. All of the simulations within this thesis were performed on conducting zone lung structures that were patient-specific to generations 6-10, and were algorithmically generated to the depth of the terminal bronchioles. This accuracy is currently limited by imaging resolution, as well as computational constraints. However, as illustrated within Chapter 7, the use of HPC environments may allow for efficient simulation of the lungs under greater structural resolution. Equally, recent advances in imaging such as the advent of micro-CT (Litzlbauer et al., 2010; Nakamura et al., 2016), may allow for the creation

of virtual lung structures that remain physically accurate to much more distal depths. The creation of more detailed and accurate virtual lungs may allow for the exploration of more detailed clinical questions.

9.2.2 Improvements to the ventilation model

The main limitations of the ventilation model are the assumption of constant compliance, and 1D flow, and the lack of airway dynamism. Each of these limitations presents a potential area for future development. Regarding compliance, Swan et al. (2012) presented a detailed lung compliance model based on tissue mechanics calculations. While it was deemed computationally infeasible for the studies within this thesis, techniques to improve computational efficiency of the model could be explored, allowing for dynamic compliance, and ventilation simulation outside of a tidal breathing range. Similarly, models for dynamic airway motion (of a similar form to that of the bloodstream in Chapter 7), were not implemented due to computational constraints, and the relatively small range of motion in conducting zone airways. However, as was illustrated within Chapter 7, the use of HPC environments may allow for tractable simulation of this phenomenon.

The assumption of unidirectional flow within each airway is also primarily made due to computational constraints. The solution of a full 3D Navier-Stokes problem across the conducting zone is far beyond current computational ability. However, many recent methods have investigated the potential for 3D-1D hybrid models (Lin et al., 2013), where 3D effects are accounted for in the upper airways (where turbulence is

most dominant), before transitioning to a 1D model in the small airways.

9.2.3 Improvements to the impedance model

Considering the lung impedance model, as noted throughout this thesis, its strongest limitation is the assumption of a homogeneous respiratory zone impedance. Within Appendix B, we briefly explored how outputs derived from CT images could be used to provide more detailed information about small airway sizes in each lobe. A natural extension of this idea is to use CT images to gain high-resolution information about local elastance, and thus to parameterise the constant-phase model more accurately.

9.2.4 Improvements to the pulmonary model

The pulmonary model in Chapter 7 presents a significant advancement on other models seen within the literature. However, it can still be greatly improved upon. As discussed briefly within the chapter, the most straightforward improvement of the model would be to incorporate haemoglobin binding, and thus to allow for simulation of carbon dioxide and oxygen transport. This in turn would allow for simulation of a much wider variety of pulmonary function tests, as well as other broader clinical scenarios.

Further research into computational efficiency of the model could also be undertaken. While many techniques to improve tractability were explored in Chapter 7, investigations could be made into the use of different simplifying approximations, multi-scale techniques, or operator splitting methods. For a model to be widely used, it must be able to be implemented with enough ease and efficiency to allow for truly

broad exploration.

9.2.5 Further clinical questions

Throughout the thesis we have outlined a series of different results which have direct and meaningful clinical significance. However, the developed models can easily be applied to a much broader range of questions than those investigated within this thesis. The list of potential clinical research questions is too broad to be meaningfully covered here, but below we give a few key examples.

We have so far limited ourselves to investigations of PFT responses to bronchoconstriction in the conducting zone, and in particular to small airways dysfunction. However, clearly other disease states could be investigated, by analysing model responses to elasticity changes (such as in COPD), or airway obstructions. In particular, if improvements to structural resolution of the models were made, more effective investigation of respiratory zone disease could be performed.

Equally, the models have only been applied to the analysis of PFTs within standard clinical scenarios. However, the ventilation and pulmonary models in particular could easily be used to investigate much broader scenarios, outside of the clinic. In theory, these models could be applied to the analysis meaningful questions in other fields, such as sports science.

Finally, many of the results within this thesis have been predominantly derived from insights relating to the computational models. Given this, a clear direction for future research is the development of clinical studies to attempt to confirm the

hypotheses derived from model results.

9.3 Concluding remarks

Computational modelling can be of immense value to all fields of science, including clinical medicine. However, for this to be true, there need to be strong communication channels between clinical and computational researchers, throughout the entire research process. Computational models cannot be effectively designed or analysed in isolation from current clinical practice. Neither should models be developed completely in line with current clinical dogma though; as one of the strongest advantages of inter-disciplinary collaboration is the challenge to conventional wisdom within a field.

Within this thesis, we have aimed to apply this philosophy to the sub-field of pulmonary medicine. The models within this thesis have been built in continual collaboration with clinical researchers, imaging specialists, and biomedical engineers. The results have been generated with direct and meaningful input from clinical collaborators, but also occasionally in direct contrast to current clinical thinking and practice. We believe that this simultaneously adds strength to the results, and also highlights the value of this underlying philosophy. This thesis represents a small stone in a truly vast river of research. But we hope it's a good stone.

A

Clinical summary statistics

Within this appendix, we briefly provide clinical details of the patient groups which formed the basis of the Bordas and Novartis sets.

The results within this thesis rely on two different sets of clinical data, the *Bordas set*, and the *Novartis set*. We provide a brief clinical summary of the subjects in both groups in Table A.1.

	Bordas		Novartis	
	Healthy (n = 11)	Asthmatic (n = 24)	Healthy (n = 7)	Asthmatic (n = 24)
Age (years)	54.2 (13.8)	56.3 (13.8)	52.6 (13.5)	50.3 (13.2)
Sex (% male)	45	42	57	64
BMI ($kg.m^2$)	28.3 (4.5)	26.2 (4.5)	30 (6.32)	30.4 (5.6)
GINA (no. with 0, 1-3, 4-5)	11, 0, 0	0, 17, 7	7, 0, 0	0, 5, 19
FRC (L)	2.4 (0.7)	2.5 (0.6)	2.3 (0.4)	2.5 (0.7)

Table A.1: Clinical summary statistics of the Bordas and Novartis sets. Unless otherwise stated, numbers are given as mean (std).

B

Improving patient-specific virtual structures

Within Chapter 5, we validated the computational model of lung impedance against clinical measurements (Figure 5.4). While there is a clear correlation between clinical measurements and simulated indices, there is also a significant degree of variability. Within this appendix, we investigate a potential explanation for this noise.

This work formed the basis of the conference paper *Low frequency lung resistance is a global bronchoconstriction detection measure, but is still sensitive to small airways*, presented at the *2018 American Thoracic Society Congress*.

This work was created in collaboration with Professor Siddiqui's research group at the University of Leicester. In particular, analysis of the CT images, and subsequent calculation of the ΔHU values for each lobe in the patient-specific structures was performed by Mr Alex Bell. The idea for this work was created collaboratively by myself, Mr Bell, Professor Siddiqui and Professor Kay.

Modification of small airway sizes

As noted in Chapter 5, the correlation of simulated and clinical impedance measures (seen in Figure 5.4) is quite noisy. We hypothesise that the correlation may be partially reduced due to the algorithmic generation of the small airways in the patient-specific structures. The small airway radii (generations 10-16) are generated by propagating down the airway radii that are measurable from the CT-scan, after scaling by an appropriate branching factor.

For each of the subjects in the Bordas set, inspiratory-expiratory CT scans were taken at TLC-FRC. While these scans were primarily used to segment the central airways and lobar boundaries, they may also be used to provide more granular ventilation information. In particular, the Housfield units (HU, a quantitative measure of radio-density in a CT scan) can be calculated in different regions of the lungs. By examining the difference between Hounsfield units at inspiration and expiration (ΔHU), estimation of ventilation in different regions can be made. In particular, the ΔHU values can be calculated for each of the five lung lobes, and taken as

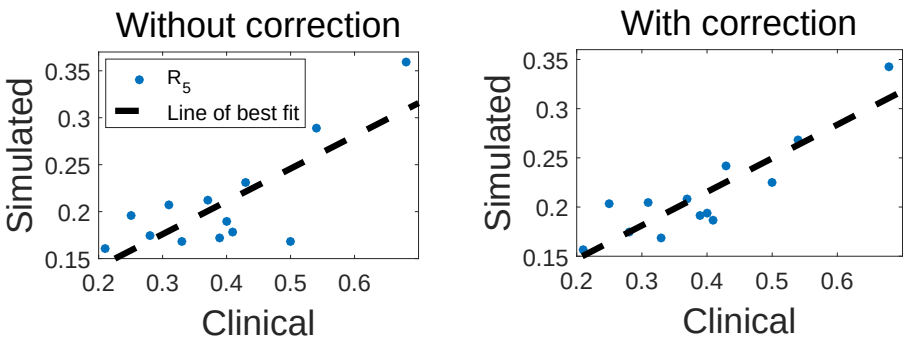

Figure B.1: Comparison of clinical and simulated R_5 pre and post adjustment using ΔHU. The adjustment of small airway sizes leads to an increase in correlation strength, with R^2 improving by 15% (from 0.61 to 0.78). Values are given in kPa.s.L^{-1}.

approximations of local ventilation.

By using this ventilation information, hypothetically, more accurate prediction of small airway sizes in different regions can be made. These predictions are made using a simple scaling factor, where a small airway radius in lobe a (denoted r_a) is modified such that

$$r_a^{\text{new}} = \frac{\Delta HU}{\mathbf{\Delta HU}} r_a^{\text{old}},$$

where $\mathbf{\Delta HU}$ is the volume-weighted average of ΔHU over the lobes.

As a brief illustration of this idea, we simulate R_5 in 13 of the structures, pre and post adjustment (see Figure B.1). As can be seen, the adjustment of airway radii significantly improves the correlation between clinical and simulated R_5 values. The p-value for the linear fit decreased by a factor of 5, while the R^2 value increased by 15% (from 0.61 to 0.78).

This is a very brief illustration of the concept, on a subset of the total data (due to time constraints). However, it suggests that some of the variation in Figure 5.4

may be due to the algorithmic nature of small airway generation within the structures. This in turn helps provide validation to the model, as it means that some of the loss in correlation is not due to the model, but rather to a lack of sufficient structural resolution.

In future work, more detailed investigations of this phenomenon could be performed. Equally, the incorporation of information at a more granular level (rather than just at a lobar level), could be performed.

C

Derivation of formula for capillary length

Within Chapter 7, we presented the formula for length of each capillary as

$$l_{\text{cap}} = \frac{2\pi R_{\text{acin}}^2}{5R_{\text{cap}}^0}.$$

Within this appendix, we briefly derive and analyse this equation.

Physiologically, the capillaries form a bed around each acinus, dividing into an extremely small, dense network of branches, with slow bloodflow. Accounting for each branch in this network is computationally infeasible, and so we aim to approximate the entire bed by a single capillary. For this to be a reasonable approximation, we need the mass of blood in a single capillary to approximate the mass of blood in the corresponding capillary bed. To achieve this, we assume that the single capillary

wraps around the surface area of the acinus, covering a fraction f. This means that the capillary length is proportional to surface area, but also limited by its own diameter (which determines how much of the surface any piece of the capillary covers). Combining these two dependencies gives

$$l_{\text{cap}} = f\frac{4\pi R_{\text{acin}}}{2R^0_{\text{cap}}} = f\frac{2\pi R_{\text{acin}}}{2R^0_{\text{cap}}}.$$

The fraction f of covered surface can be estimated by assuming a healthy adult lung (FRC= 2.5L) is surrounded by 60mL of capillary blood (a normal healthy adult value). Using a healthy lung from the Bordas set, this gives $f \approx 1/5$, meaning

$$l_{\text{cap}} = \frac{2\pi R^2_{\text{acin}}}{5R^0_{\text{cap}}}.$$

For this approximation to be appropriate, the ratio of lung volume to capillary blood should be independent of the number of generations in the airway tree. This is because this ratio significantly determines how strongly gas concentrations in the blood can affect concentrations in the airway (due to relative mass differences). To analyse whether this holds within our model, we first note that

$$V_{\text{cap}} = l_{\text{cap}} \times A_{\text{cap}} = \frac{2}{5}\pi^2 R^2_{\text{acin}} R^0_{\text{cap}},$$

where V_{cap} is the volume of the capillary, and A_{cap} is its cross-sectional area.

For a structure with a given FRC, approximated using an N-generation network, we assume there is an average ratio between capillary volume and acinus volume, such that

$$V_{\text{cap},N} \approx kV_{\text{acin},N},$$

where the subscript N denotes that the variable is from the N-generation network. If we take this structure, and add another generation, but hold FRC constant we have

$$V_{\text{acin},N+1} \approx \frac{1}{2} V_{\text{acin},N},$$

$$R_{\text{acin},N} \approx \left(\frac{1}{2}\right)^{1/3} R_{\text{acin},N},$$

as the number of acinar regions should approximately double in the new network.

If we assume that at each generation, the capillary and airway radii decrease with a branching factor b_f, we also have

$$R_{\text{cap},N+1} \approx b_f R_{\text{cap},N},$$

which means that the new capillary volume can be approximated as

$$V_{\text{cap},N+1} \approx \frac{2}{5}\pi^2 b_f \left(\frac{1}{2}\right)^{2/3} R^2_{\text{acin},N} R^0_{\text{cap},N}.$$

$$V_{\text{cap},N+1} \approx b_f \left(\frac{1}{2}\right)^{2/3} V_{\text{cap},N}.$$

If we assume the ratio between capillary volume and acinar volume is the same for both sized networks, we have that

$$b_f \left(\frac{1}{2}\right)^{2/3} = \frac{1}{2},$$

which means that the branching factor must be

$$b_f = 2^{-1/3} \approx 0.79.$$

This number is the well-known optimal branching factor (Mauroy et al., 2004) for the human lung, also known as the Hess-Murray law.

This illustrates that in an idealised branching network, this model holds, and accurately maintains an appropriate ratio (which we have set from standard physiological values as 2500L: 60mL) between FRC and capillary blood volume. In an actual lung, average branching factors are usually slightly higher than the optimal factor, usually being around 0.81-0.86 (Weibel, 1963). Thus in practice for airway networks significantly larger or smaller than 16 generations, the surface area factor f should be modified to maintain this ratio. However, all of the major investigations in this thesis use airway structures of similar sizes, meaning the approximation is appropriate.

D

Simplification of pulmonary bifurcation equations

In Chapter 7, an explicit model for simulating blood flow and arterial area changes was outlined. At each bifurcation a system of 18 equations define the continuity of pressure, conservation of flow, and advancement of flow and area through time. In this appendix, we provide more explicit details of the system, and show how it can be more efficiently implemented numerically.

We first introduce the simplifying notation for the variables:

$$
\begin{aligned}
x_1 &= Q_{b,M}^{p,n+1}, & x_2 &= Q_{b,M}^{p,n+1/2}, & x_3 &= Q_{b,M+1/2}^{p,n+1/2},\\
x_4 &= Q_{b,0}^{d_1,n+1}, & x_5 &= Q_{b,0}^{d_1,n+1/2}, & x_6 &= Q_{b,-1/2}^{d_1,n+1/2},\\
x_7 &= Q_{b,0}^{d_2,n+1}, & x_8 &= Q_{b,0}^{d_2,n+1/2}, & x_9 &= Q_{b,-1/2}^{d_2,n+1/2},\\
x_{10} &= A_{b,M}^{p,n+1}, & x_{11} &= A_{b,M}^{p,n+1/2}, & x_{12} &= A_{b,M+1/2}^{p,n+1/2},\\
x_{13} &= A_{b,0}^{d_1,n+1}, & x_{14} &= A_{b,0}^{d_1,n+1/2}, & x_{15} &= A_{b,-1/2}^{d_1,n+1/2},\\
x_{16} &= A_{b,0}^{d_2,n+1}, & x_{17} &= A_{b,0}^{d_2,n+1/2}, & x_{18} &= A_{b,-1/2}^{d_2,n+1/2}.
\end{aligned}
$$

We then introduce the definitions

$$
\begin{aligned}
B_{M+1/2}(x) &= \frac{R_{b,M+1/2}^0 f}{\rho_b}\sqrt{A_{b,M+1/2}^0},\\
F_{M+1/2}(x_1,x_2) &= -\frac{2\pi\nu_b R_{b,M+1/2}^0}{\delta}\frac{x_1}{x_2},\\
\frac{dB_{M+1/2}}{dx}(x) &= \left(\frac{\partial B}{\partial R_b^0}\frac{dR_b^0}{dx}\right)_{M+1/2}^{n+1/2}\\
&= \left(2\sqrt{x}\left(\sqrt{\pi}fR_b^0 + \sqrt{A_b^0}\frac{df}{dR_b^0}\right) - A\frac{df}{dR_b^0}\right)_{M+1/2}\left(\frac{dR_{b,M+1/2}^0}{dx}\right),\\
\theta_i &= \frac{\Delta t}{\Delta x_i},\\
\gamma &= \frac{\Delta t}{2}.
\end{aligned}
$$

Using this notation, we can rewrite Equations (7.11)-(7.16) in the form

$$\mathbf{H}(\mathbf{X}) = \mathbf{0},$$

where $\mathbf{X} = (x_1, x_2, \ldots, x_{18})^T$, and $\mathbf{H} = (h_1, h_2, \ldots, h_{18})^T$. The vector $\mathbf{H}$ comprises the

18 residual functions, with the equations for conservation of flow (7.11):

$$h_1 = x_1 - x_4 - x_7, \tag{D.1}$$

$$h_2 = x_2 - x_5 - x_8, \tag{D.2}$$

the ghost node approximations (7.15)-(7.16):

$$h_{3,4,5} = x_{2,5,8} - \frac{x_{3,6,9}}{2} + k_{1a,1b,1c}, \tag{D.3}$$

$$h_{6,7,8} = x_{11,14,17} - \frac{x_{12,15,18}}{2} + k_{2a,2b,2c}, \tag{D.4}$$

$$\begin{aligned} k_{1a} &= -\frac{Q^{p,n+1/2}_{b,M-1/2}}{2}, \\ k_{1b} &= -\frac{Q^{d_1,n+1/2}_{b,1/2}}{2}, \quad k_{1c} = -\frac{Q^{d_2,n+1/2}_{b,1/2}}{2}, \\ k_{2a} &= -\frac{A^{p,n+1/2}_{b,M-1/2}}{2}, \\ k_{2b} &= -\frac{A^{d_1,n+1/2}_{b,1/2}}{2}, \quad k_{2c} = -\frac{A^{d_2,n+1/2}_{b,1/2}}{2} \end{aligned}$$

advancement of A_b in time (7.13):

$$h_9 = x_{10} + \theta_p x_3 - k_{3a}, \tag{D.5}$$

$$h_{10,11} = x_{13,16} - \theta_{d_1,d_2} x_{6,9} - k_{3b,3c}, \tag{D.6}$$

$$k_{3a} = A^{p,n}_{b,M} + \theta_p Q^{p,n+1/2}_{b,M-1/2},$$

$$k_{3b} = A^{d_1,n}_{b,0} - \theta_{d_1} A^{d_1,n}_{b,1/2}, \quad k_{3c} = A^{d_2,n}_{b,0} - \theta_{d_2} A^{d_2,n}_{b,1/2}$$

continuity of pressure (7.12):

$$h_{12,13} = \frac{k_{4a}}{\sqrt{x_{10}}} - \frac{k_{4b,4c}}{\sqrt{x_{13,16}}} + k_{5a,5b}, \tag{D.7}$$

$$h_{14,15} = \frac{k_{4a}}{\sqrt{x_{11}}} - \frac{k_{4b,4c}}{\sqrt{x_{14,17}}} + k_{5a,5b}, \tag{D.8}$$

$$k_{4a} = \left(f_M^p \sqrt{A_{b,M}^p}\right),$$

$$k_{4b} = \left(f_0^{d_1} \sqrt{A_{b,0}^{d_1}}\right), \quad k_{4c} = \left(f_0^{d_2} \sqrt{A_{b,0}^{d_2}}\right),$$

$$k_{5a} = -f_M^p + f_0^{d_1}, \qquad k_{5b} = -f_M^p + f_0^{d_2},$$

and advancement of Q_b in time (7.14):

$$\begin{aligned} h_{16} &= k_{6a} - x_1 - \theta_p \left(\frac{x_3^2}{x_{12}} + B_{M+1/2}(x_{12})\right) + \\ &\quad \gamma \left(F_{M+1/2}(x_3, x_{12}) + \frac{dB_{M+1/2}}{dx}(x_{12})\right) \\ &= k_{6a} - x_1 + G_1(x_3, x_{12}), \end{aligned} \tag{D.9}$$

$$\begin{aligned} h_{17,18} &= k_{6b,6c} - x_{4,7} + \theta_{d_1,d_2} \left(\frac{x_{6,9}^2}{x_{15,18}} + B_{-1/2}(x_{15,18})\right) + \\ &\quad \gamma(F_{-1/2}(x_{6,9}, x_{15,18}) + \frac{dB_{-1/2}}{dx}(x_{15,18})) \\ &= k_{6b,6c} - x_{4,7} + G_{2,3}(x_{6,9}, x_{15,18}), \end{aligned} \tag{D.10}$$

$$k_{6a} = Q_{b,M}^{p,n} + \theta_p \mathcal{T}_{2,M-1/2}^{p,n+1/2} + \gamma \mathcal{S}_{2,M-1/2}^{p,n+1/2},$$

$$k_{6b} = Q_{b,0}^{d_1,n} - \theta_{d_1} \mathcal{T}_{2,1/2}^{d_1,n+1/2} + \gamma \mathcal{T}_{2,1/2}^{d_1,n+1/2},$$

$$k_{6c} = Q_{b,0}^{d_2,n} - \theta_{d_2} \mathcal{T}_{2,1/2}^{d_2,n+1/2} + \gamma \mathcal{T}_{2,1/2}^{d_2,n+1/2}.$$

Equations (D.1)-(D.10) form a system of 18 non-linear equations, for 18 variables. However, we note that Equations (D.1)-(D.6) are linear in the variables. We can use this linearity to collapse the system significantly.

Given we are solving $h_i = 0$, (for $i = 1 \dots 18$), we first rearrange Equation (D.3) for x_2, x_5 and x_8, and substitute into Equation (D.2), to give (after rearrangement),

$$h_{a1} = x_3 - x_6 - x_9 + k_7 = 0, \tag{D.11}$$

$$k_7 = k_{1a} - k_{1b} - k_{1c}.$$

We then rearrange Equations (D.5) and (D.6) for x_{10}, x_{13} and x_{16}, and substitute into Equation (D.7), to give

$$h_{a2,a3} = \frac{k_{4a}}{\sqrt{k_{3a} - \theta_p x_3}} - \frac{k_{4b,4c}}{\sqrt{k_{3b,3c} + \theta_{d_1,d_2} x_{6,9}}} + k_{5a,5b} = 0. \tag{D.12}$$

Equations (D.11) and (D.12) form a system of 3 non-linear equations with 3 unknowns. These can be solved for x_3, x_6 and x_9 using vector Newton method iterations, of the form

$$\mathbf{X}_a^{i+1} = \mathbf{X}_a^i - \mathcal{J}_a^{-1} \mathbf{H}_a(\mathbf{X}_a^i),$$

where $\mathbf{X}_a = (x_3, x_6, x_9)^T$ and $\mathbf{H}_a = (h_{a1}, h_{a2}, h_{a3})^T$. $\mathcal{J}_a$ is the Jacobian matrix of $\mathbf{H}_a$ and can be computed as

$$\mathcal{J}_a = \begin{bmatrix} 1 & -1 & -1 \\ \xi_1 & \xi_2 & 0 \\ \xi_1 & 0 & \xi_3 \end{bmatrix},$$

where

$$\xi_1 = \frac{1}{2} k_{4a} \theta_p (k_{3a} - \theta_p x_3)^{-3/2},$$

$$\xi_{2,3} = \frac{1}{2} k_{4b,4c} \theta_{d_1,d_2} (k_{3b,3c} + \theta_{d_1,d_2} x_{6,9})^{-3/2}.$$

Due to the small size of the system, the Jacobian inverse-product against $\mathbf{H}_a$ can be calculated explicitly, though is only updated once each time step.

This system collapse allows us to efficiently solve for x_3, x_6 and x_9. By substituting these values into Equations (D.3), (D.5) and (D.6) we can also easily calculate $x_2, x_5, x_8, x_{10}, x_{13}$, and x_{16}.

To solve for the remaining variables we first rearrange Equations (D.4) for x_{11}, x_{14}, and x_{17} and substitute into Equations (D.8) to give

$$h_{b1,b2} = \frac{k_{4a}}{\sqrt{\frac{x_{12}}{2} + k_{2a}}} - \frac{k_{4b,4c}}{\sqrt{\frac{x_{15,18}}{2} + k_{2b,2c}}} + k_{5a,5b} = 0. \tag{D.13}$$

We then rearrange Equations (D.9) and (D.10) for x_1, x_4, and x_7, and substitute into Equation (D.1) to give

$$h_{b3} = k_8 + G_1(x_3, x_{12}) - G_2(x_6, x_{15}) - G_3(x_9, x_{18}) = 0 \tag{D.14}$$

$$k_8 = k_{6a} - k_{6b} - k_{6c}.$$

Since we have already solved for x_3, x_6, and x_9, Equations (D.13) and (D.14) form a non-linear system with 3 unknowns. As with the first system, we solve these equations for x_{12}, x_{15}, and x_{18} using vector Newton method iterations of the form

$$\mathbf{X}_b^{i+1} = \mathbf{X}_b^i - \mathcal{J}_b^{-1}\mathbf{H}_b(\mathbf{X}_b^i),$$

where $\mathbf{X}_b = (x_{12}, x_{15}, x_{18})^T, \mathbf{H}_b = (h_{b1}, h_{b2}, h_{b3})^T$ and

$$\mathcal{J}_b = \begin{bmatrix} \xi_1 & \xi_2 & 0 \\ \xi_1 & 0 & \xi_3 \\ \xi_4 & \xi_5 & \xi_6 \end{bmatrix},$$

is the Jacobian of $\mathbf{H}_b$, with

$$
\begin{aligned}
\xi_1 &= -\frac{1}{4}\left(\frac{x_{12}}{2} + k_{2a}\right)^{-3/2}, \\
\xi_{2,3} &= \frac{1}{4}\left(\frac{x_{15,18}}{2} + k_{2b,2c}\right)^{-3/2}, \\
\xi_4 &= \frac{\partial G_1}{\partial x_{12}}, \\
&= -\theta_p\left(-\left(\frac{x_3}{x_{12}}\right)^2 + \frac{1}{2} f R^0_{b,M+1/2}\sqrt{A^0_{b,M+1/2}}\, x_{12}^{-3/2}\right) + \\
&\quad \gamma\left(\frac{2\pi R^0_{b,M+1/2}}{\delta}\frac{x_3}{x_{12}^2} - \frac{1}{2x_{12}}\frac{dB_{M+1/2}}{dx}(x_{12})\right), \\
\xi_{5,6} &= -\frac{\partial G_{2,3}}{dx_{15,18}}, \\
&= -\theta_{d_1,d_2}\left(-\left(\frac{x_{6,9}}{x_{15,18}}\right)^2 + \frac{1}{2} f R^0_{b,-1/2}\sqrt{A^0_{b,-1/2}}\, x_{15,18}^{-3/2}\right) + \\
&\quad \gamma\left(\frac{2\pi R^0_{b,-1/2}}{\delta}\frac{x_{6,9}}{x_{15,18}} - \frac{1}{2x_{15,18}}\frac{dB_{-1/2}}{dx}(x_{15,18})\right).
\end{aligned}
$$

As with the other 3×3 system, the size allows for efficient direct calculation of the Jacobian inverse-product against $\mathbf{H}_b$. Once a convergent solution (to within a desired tolerance) is reached, all remaining unsolved variables in $\mathbf{X}$ can be solved through simple substitutions into the remaining equations of System (D.1)-(D.10).

Bibliography

Altes, T. A., Powers, P. L., Knight-Scott, J., Rakes, G., Platts-Mills, T. A., de Lange, E. E., Alford, B. A., Mugler, J. P., and Brookeman, J. R. (2001). Hyperpolarized 3he mr lung ventilation imaging in asthmatics: preliminary findings. *Journal of Magnetic Resonance Imaging*, 13(3):378–384.

Attinger, E. O., Herschfus, J. A., and Segal, M. S. (1956). The mechanics of breathing in different body positions. II. In cardiopulmonary disease. *The Journal of Clinical Investigation*, 35(8):912–920.

Aurora, P., Bush, A., Gustafsson, P., Oliver, C., Wallis, C., Price, J., Stroobant, J., Carr, S., and Stocks, J. (2005a). Multiple-breath washout as a marker of lung disease in preschool children with cystic fibrosis. *American Journal of Respiratory and Critical Care Medicine*, 171(3):249–256.

Aurora, P., Gustafsson, P., Bush, A., Lindblad, A., Oliver, C., Wallis, C., and Stocks, J. (2004). Multiple breath inert gas washout as a measure of ventilation distribution in children with cystic fibrosis. *Thorax*, 59(12):1068–1073.

Aurora, P., Kozlowska, W., and Stocks, J. (2005b). Gas mixing efficiency from birth

to adulthood measured by multiple-breath washout. *Respiratory Physiology & Neurobiology*, 148(1):125–139.

Badr, C., Elkins, M. R., and Ellis, E. R. (2002). The effect of body position on maximal expiratory pressure and flow. *Australian Journal of Physiotherapy*, 48(2):95–102.

Barnas, G. M., Yoshino, K., Fredberg, J., Kikuchi, Y., Loring, S. H., and Mead, J. (1990). Total and local impedances of the chest wall up to 10 Hz. *Journal of Applied Physiology*, 68(4):1409–1414.

Bates, J., Rossi, A., and Milic-Emili, J. (1985). Analysis of the behavior of the respiratory system with constant inspiratory flow. *Journal of Applied Physiology*, 58(6):1840–1848.

Bauman, G., Puderbach, M., Deimling, M., Jellus, V., Chefd'hotel, C., Dinkel, J., Hintze, C., Kauczor, H., and Schad, L. (2009). Non-contrast-enhanced perfusion and ventilation assessment of the human lung by means of fourier decomposition in proton MRI. *Magnetic Resonance in Medicine*, 62(3):656–664.

Behrakis, P. K., Baydur, A., Jaeger, M. J., and Milic-Emili, J. (1983). Lung mechanics in sitting and horizontal body positions. *Chest*, 83(4):643–646.

Ben-Tal, A. (2006). Simplified models for gas exchange in the human lungs. *Journal of Theoretical Biology*, 238(2):474–495.

Benade, A. H. (1968). On the propagation of sound waves in a cylindrical conduit. *Journal of the Acoustical Society of America*, 44(2):616–623.

Bhatawadekar, S. A., Leary, D., and Maksym, G. N. (2015). Modelling resistance and reactance with heterogeneous airway narrowing in mild to severe asthma. *Canadian Journal of Physiology and Pharmacology*, 93(3):207–214.

Biederer, J., Beer, M., Hirsch, W., Wild, J., Fabel, M., Puderbach, M., and Van Beek, E. (2012). Mri of the lung (2/3). why when how? *Insights into Imaging*, 3(4):355–371.

Bordas, R., Lefevre, C., Veeckmans, B., Pitt-Francis, J., Fetita, C., Brightling, C. E., Kay, D., Siddiqui, S., and Burrowes, K. S. (2015). Development and analysis of patient-based complete conducting airways models. *PLoS One*, 10(12):e0144105.

British Lung Foundation (2016). Lung disease in the UK. https://statistics.blf.org.uk/. Accessed: 2016-05-06.

British Thoracic Society (2016). British guideline on the management of asthma. https://www.brit-thoracic.org.uk/standards-of-care/guidelines/btssign-british-guideline-on-the-management-of-asthma/. Accessed: 25-01-2018.

Bryan, A., Milic-Emili, J., and Pengelly, D. (1966). Effect of gravity on the distribution of pulmonary ventilation. *Journal of Applied Physiology*, 21(3):778–784.

Burrowes, K. S., Doel, T., and Brightling, C. (2014). Computational modeling of the obstructive lung diseases asthma and copd. *Journal of Translational Medicine*, 12(2):S5.

Burrowes, K. S., Hunter, P. J., and Tawhai, M. H. (2005). Anatomically based finite element models of the human pulmonary arterial and venous trees including supernumerary vessels. *Journal of Applied Physiology*, 99(2):731–738.

Burrowes, K. S. and Tawhai, M. H. (2006). Computational predictions of pulmonary blood flow gradients: gravity versus structure. *Respiratory Physiology & Neurobiology*, 154(3):515–523.

Campana, L., Kenyon, J., Zhalehdoust-Sani, S., Tzeng, Y.-S., Sun, Y., Albert, M., and Lutchen, K. R. (2009). Probing airway conditions governing ventilation defects in asthma via hyperpolarized MRI image functional modeling. *Journal of Applied Physiology*, 106(4):1293–1300.

Capaldi, D., Bluemke, E., Paulin, G., Davis, C., Sheikh, K., McCormack, D., Parraga, G., and Svenningsen, S. (2015). Lung clearance index and hyperpolarized 3He MRI ventilation heterogeneity measurements in non-CF bronchiectasis and COPD. *American Journal of Respiratory and Critical Care Medicine*, 191:A2255.

Cauberghs, M. and Van de Woestijne, K. (1983). Mechanical properties of the upper airway. *Journal of Applied Physiology*, 55(2):335–342.

Cavalcanti, J. V., Lopes, A. J., Jansen, J. M., and Melo, P. L. (2006). Detection of changes in respiratory mechanics due to increasing degrees of airway obstruction in asthma by the forced oscillation technique. *Respiratory Medicine*, 100(12):2207–2219.

Cotes, J. E., Chinn, D. J., and Miller, M. R. (2009). *Lung function: Physiology, measurement and application in medicine*. John Wiley & Sons.

Crim, C., Celli, B., Edwards, L. D., Wouters, E., Coxson, H. O., Tal-Singer, R., Calverley, P. M., investigators, E., et al. (2011). Respiratory system impedance with impulse oscillometry in healthy and COPD subjects: ECLIPSE baseline results. *Respiratory Medicine*, 105(7):1069–1078.

Cruz, J. C., Jeng, D.-R., Han, D., Wu, G., and Flores, X. F. (1997). Ventilation inhomogeneities and mixed venous blood N2 in multibreath N2 washout. *Respiration Physiology*, 110(1):47–56.

Downie, S. R., Salome, C. M., Verbanck, S., Thompson, B., Berend, N., and King, G. G. (2007). Ventilation heterogeneity is a major determinant of airway hyperresponsiveness in asthma, independent of airway inflammation. *Thorax*, 62(8):684–689.

DuBois, A. B., Brody, A. W., Lewis, D. H., and Burgess, B. F. (1956). Oscillation mechanics of lungs and chest in man. *Journal of Applied Physiology*, 8(6):587–594.

Dutrieue, B., Vanholsbeeck, F., Verbanck, S., and Paiva, M. (2000). A human acinar structure for simulation of realistic alveolar plateau slopes. *Journal of Applied Physiology*, 89(5):1859–1867.

Fain, S. B., Korosec, F. R., Holmes, J. H., O'Halloran, R., Sorkness, R. L., and Grist, T. M. (2007). Functional lung imaging using hyperpolarized gas MRI. *Journal of Magnetic Resonance Imaging*, 25(5):910–923.

Fessler, H. E. and Talmor, D. S. (2010). Should prone positioning be routinely used for lung protection during mechanical ventilation? *Respiratory Care*, 55(1):88–99.

Fetita, C. I., Prêteux, F., Beigelman-Aubry, C., and Grenier, P. (2004). Pulmonary airways: 3-D reconstruction from multislice CT and clinical investigation. *Medical Imaging*, 23(11):1353–1364.

Fingerlin, T. E., Murphy, E., Zhang, W., Peljto, A. L., Brown, K. K., Steele, M. P., Loyd, J. E., Cosgrove, G. P., Lynch, D., Groshong, S., et al. (2013). Genome-wide association study identifies multiple susceptibility loci for pulmonary fibrosis. *Nature genetics*, 45(6):613.

Formaggia, L., Gerbeau, J.-F., Nobile, F., and Quarteroni, A. (2001). On the coupling of 3D and 1D Navier–Stokes equations for flow problems in compliant vessels. *Computer Methods in Applied Mechanics and Engineering*, 191(6-7):561–582.

Foy, B. H., Gonem, S., Brightling, C., Siddiqui, S., and Kay, D. (2018). Modelling the effect of gravity on inert-gas washout outputs. *Physiological reports*, 6(10):e13709.

Foy, B. H. and Kay, D. (2017). A computational comparison of the multiple-breath washout and forced oscillation technique as markers of bronchoconstriction. *Respiratory Physiology & Neurobiology*, 240:61–69.

Foy, B. H., Kay, D., and Bordas, R. (2017). Modelling responses of the inert-gas washout and mri to bronchoconstriction. *Respiratory Physiology & Neurobiology*, 235:8–17.

Galetke, W., Feier, C., Muth, T., Ruehle, K.-H., Borsch-Galetke, E., and Randerath, W. (2007). Reference values for dynamic and static pulmonary compliance in men. *Respiratory Medicine*, 101(8):1783–1789.

Gibson, R. L., Burns, J. L., and Ramsey, B. W. (2003). Pathophysiology and management of pulmonary infections in cystic fibrosis. *American Journal of Respiratory and Critical Care Medicine*, 168(8):918–951.

Gillespie, D. J. and Rehder, K. (1987). Body position and ventilation-perfusion relationships in unilateral pulmonary. *Chest*, 91(1):75–79.

Glenny, R. W. and Robertson, H. T. (1991). Fractal modeling of pulmonary blood flow heterogeneity. *Journal of Applied Physiology*, 70(3):1024–1030.

Global Initiative for Asthma (2017). Global Initiative for Asthma. http://ginasthma.org/. Accessed: 09-03-2017.

Goldman, M. D., Saadeh, C., and Ross, D. (2005). Clinical applications of forced oscillation to assess peripheral airway function. *Respiratory Physiology & Neurobiology*, 148(1):179–194.

Gonem, S., Berair, R., Singapuri, A., Hartley, R., Laurencin, M. F., Bacher, G., Holzhauer, B., Bourne, M., Mistry, V., Pavord, I. D., et al. (2016). Fevipiprant, a prostaglandin D2 receptor 2 antagonist, in patients with persistent eosinophilic asthma: A single-centre, randomised, double-blind, parallel-group, placebo-controlled trial. *The Lancet Respiratory Medicine*, 4(9):699–707.

Gonem, S., Natarajan, S., Desai, D., Corkill, S., Singapuri, A., Bradding, P., Gustafsson, P., Costanza, R., Kajekar, R., Parmar, H., et al. (2014). Clinical significance of small airway obstruction markers in patients with asthma. *Clinical & Experimental Allergy*, 44(4):499–507.

Gould, M. K., Maclean, C. C., Kuschner, W. G., Rydzak, C. E., and Owens, D. K. (2001). Accuracy of positron emission tomography for diagnosis of pulmonary nodules and mass lesions: a meta-analysis. *Journal of the American Medical Association*, 285(7):914–924.

Grimby, G., Takishima, T., Graham, W., Macklem, P., and Mead, J. (1968). Frequency dependence of flow resistance in patients with obstructive lung disease. *Journal of Clinical Investigation*, 47(6):1455.

Grönkvist, M., Bergsten, E., and Gustafsson, P. M. (2002). Effects of body posture and tidal volume on inter-and intraregional ventilation distribution in healthy men. *Journal of Applied Physiology*, 92(2):634–642.

Gustafsson, P. M. (2007). Peripheral airway involvement in CF and asthma compared by inert gas washout. *Pediatric Pulmonology*, 42(2):168–176.

Hahn, C., Black, A., Barton, S., and Scott, I. (1993). Gas exchange in a three-compartment lung model analyzed by forcing sinusoids of N2O. *Journal of Applied Physiology*, 75(4):1863–1876.

Hamedani, H., Clapp, J. T., Kadlecek, S. J., Emami, K., Ishii, M., Gefter, W. B., Xin, Y., Cereda, M., Shaghaghi, H., Siddiqui, S., et al. (2016). Regional fractional ventilation by using multibreath wash-in 3He MR imaging. *Radiology*, 279(3):917–924.

Hamid, Q., Song, Y., Kotsimbos, T. C., Minshall, E., Bai, T. R., Hegele, R. G., and Hogg, J. C. (1997). Inflammation of small airways in asthma. *Journal of Allergy and Clinical Immunology*, 100(1):44–51.

Han, D., Jeng, D.-R., Cruz, J. C., Flores, X. F., and Mallea, J. (2001). New method to calculate the n2 evolution from mixed venous blood during the N2 washout. *Annals of Biomedical Engineering*, 29(8):701–706.

Hanson, J. S., Tabakin, B. S., and Caldwell, E. J. (1962). Response of lung volumes and ventilation to posture change and upright exercise. *Journal of Applied Physiology*, 17(5):783–786.

Henry, F., Llapur, C., Tsuda, A., and Tepper, R. (2012). Numerical modelling and analysis of peripheral airway asymmetry and ventilation in the human adult lung. *Journal of Biomechanical Engineering*, 134(6):061001.

Holgate, S. T. (2008). Pathogenesis of asthma. *Clinical & Experimental Allergy*, 38(6):872–897.

Hopkins, S. R., Henderson, A. C., Levin, D. L., Yamada, K., Arai, T., Buxton, R. B., and Prisk, G. K. (2007). Vertical gradients in regional lung density and

perfusion in the supine human lung: The Slinky effect. *Journal of Applied Physiology*, 103(1):240–248.

Horn, F., Marshall, H., Siddiqui, S., Horsley, A., Smith, L., Aldag, I., Brightling, C., Kay, R., Taylor, C., Parra-Robles, J., et al. (2015). Comparison of ventilation heterogeneity (VH) measured with multiple breath washout (MBW) imaging to whole lung MBW LCI and FEV1 in asthma and cystic fibrosis (CF). *Poster presented at: European Respiratory Society International Congress*, 46(suppl 59):OA2946.

Horn, F. C., Deppe, M. H., Marshall, H., Parra-Robles, J., and Wild, J. M. (2014). Quantification of regional fractional ventilation in human subjects by measurement of hyperpolarized 3He washout with 2D and 3D MRI. *Journal of Applied Physiology*, 116(2):129–139.

Horsfield, K. (1978). Morphometry of the small pulmonary arteries in man. *Circulation Research*, 42(5):593–597.

Horsfield, K. and Cumming, G. (1968). Functional consequences of airway morphology. *Journal of applied physiology*, 24(3):384–390.

Horsfield, K., Relea, F. G., and Gumming, G. (1976). Diameter, length and branching ratios in the bronchial tree. *Respiration Physiology*, 26(3):351–356.

Horsley, A., Marshall, H., Smith, L., Hughes, D., Horn, F., Armstrong, L., Parra-Nobles, J., Cunningham, S., Aldag, I., Wild, J., et al. (2014). Visualising ventilation

heterogeneity in mild CF using hyperpolarised 3He MRI, and comparison with lung clearance index (LCI). *Journal of Cystic Fibrosis*, 13:S28.

Horsley, A. R., Gustafsson, P. M., Macleod, K., Saunders, C., Greening, A. P., Porteous, D., Davies, J., Cunningham, S., Alton, E., and Innes, J. A. (2008). Lung clearance index is a sensitive, repeatable and practical measure of airways disease in adults with cystic fibrosis. *Thorax*, 63(2):135–140.

Hoshino, M. (2010). Comparison of effectiveness in ciclesonide and fluticasone propionate on small airway function in mild asthma. *Allergology International*, 59(1):59–66.

Hozawa, S., Terada, M., and Hozawa, M. (2011). Comparison of budesonide/formoterol turbuhaler with fluticasone/salmeterol diskus for treatment effects on small airway impairment and airway inflammation in patients with asthma. *Pulmonary Pharmacology & Therapeutics*, 24(5):571–576.

Jahani, N., Choi, S., Choi, J., Iyer, K., Hoffman, E. A., and Lin, C.-L. (2015). Assessment of regional ventilation and deformation using 4D-CT imaging for healthy human lungs during tidal breathing. *Journal of Applied Physiology*, 119(10):1064–1074.

Johns, D. P. and Crockett, A. J. (2005). Lung function testing. *Evidence-based Respiratory Medicine*, page 25.

Johnson, M., Birch, M., Carter, R., Kinsella, J., and Stevenson, R. (2005). Use of reactance to estimate transpulmonary resistance. *European Respiratory Journal*, 25(6):1061–1069.

Kaczka, D. W., Ingenito, E. P., Israel, E., and Lutchen, K. R. (1999). Airway and lung tissue mechanics in asthma: Effects of albuterol. *American Journal of Respiratory and Critical Care Medicine*, 159(1):169–178.

Kaczka, D. W., Ingenito, E. P., Suki, B., and Lutchen, K. R. (1997). Partitioning airway and lung tissue resistances in humans: Effects of bronchoconstriction. *Journal of Applied Physiology*, 82(5):1531–1541.

Kaczka, D. W., Massa, C. B., and Simon, B. A. (2007). Reliability of estimating stochastic lung tissue heterogeneity from pulmonary impedance spectra: A forward-inverse modeling study. *Annals of Biomedical Engineering*, 35(10):1722–1738.

Kaneko, K., Milic-Emili, J., Dolovich, M., Dawson, A., and Bates, D. (1966). Regional distribution of ventilation and perfusion as a function of body position. *Journal of Applied Physiology*, 21(3):767–777.

Katz, A. M. (2010). *Physiology of the Heart*. Lippincott Williams & Wilkins.

Katzenstein, A.-L. A. and Myers, J. L. (1998). Idiopathic pulmonary fibrosis: Clinical relevance of pathologic classification. *American Journal of Respiratory and Critical Care Medicine*, 157(4):1301–1315.

Kelley, C. T. (2003). *Solving nonlinear equations with Newton's method*, volume 1. Siam.

Kent, L., Reix, P., Innes, J., Zielen, S., Le Bourgeois, M., Braggion, C., Lever, S., Arets, H., Brownlee, K., Bradley, J., et al. (2014). Lung clearance index: Evidence for use in clinical trials in cystic fibrosis. *Journal of Cystic Fibrosis*, 13(2):123–138.

King, G. G., Downie, S. R., Verbanck, S., Thorpe, C. W., Berend, N., Salome, C. M., and Thompson, B. (2005). Effects of methacholine on small airway function measured by forced oscillation technique and multiple breath nitrogen washout in normal subjects. *Respiratory Physiology & Neurobiology*, 148(1-2):165–177.

King, P. (2011). Pathogenesis of bronchiectasis. *Paediatric Respiratory Reviews*, 12(2):104–110.

Kraft, M. (1999). The distal airways: are they important in asthma? *European Respiratory Journal*, 14(6):1403–1417.

Krenz, G. S., Linehan, J. H., and Dawson, C. A. (1992). A fractal continuum model of the pulmonary arterial tree. *Journal of Applied Physiology*, 72(6):2225–2237.

Lambert, R., Baile, E., Moreno, R., Bert, J., and Pare, P. (1991). A method for estimating the Young's modulus of complete tracheal cartilage rings. *Journal of Applied Physiology*, 70(3):1152–1159.

Leary, D., Bhatawadekar, S. A., Parraga, G., and Maksym, G. N. (2012). Modeling

stochastic and spatial heterogeneity in a human airway tree to determine variation in respiratory system resistance. *Journal of Applied Physiology*, 112(1):167–175.

Levitzky, M. G. (2003). *Pulmonary Physiology (Lange Physiology Series)*. McGraw-Hill, New York.

Lin, C.-L., Tawhai, M. H., and Hoffman, E. A. (2013). Multiscale image-based modeling and simulation of gas flow and particle transport in the human lungs. *Wiley Interdisciplinary Reviews: Systems Biology and Medicine*, 5(5):643–655.

Litzlbauer, H. D., Korbel, K., Kline, T. L., Jorgensen, S. M., Eaker, D. R., Bohle, R. M., Ritman, E. L., and Langheinrich, A. C. (2010). Synchrotron-based micro-CT imaging of the human lung acinus. *The Anatomical Record*, 293(9):1607–1614.

Ljungberg, H. K. and Gustafsson, P. M. (2003). Peripheral airway function in childhood asthma, assessed by single-breath he and sf6 washout. *Pediatric Pulmonology*, 36(4):339–347.

Lumb, A. B. (2016). *Nunn's applied respiratory physiology*. Elsevier Health Sciences.

Lutchen, K. R. and Gillis, H. (1997). Relationship between heterogeneous changes in airway morphometry and lung resistance and elastance. *Journal of Applied Physiology*, 83(4):1192–1201.

Macleod, K. A., Horsley, A. R., Bell, N. J., Greening, A. P., Innes, J. A., and Cunningham, S. (2009). Ventilation heterogeneity in children with well controlled

asthma with normal spirometry indicates residual airways disease. *Thorax*, 64(1):33–37.

MacNee, W. (2005). Pathogenesis of chronic obstructive pulmonary disease. *Proceedings of the American Thoracic Society*, 2(4):258–266.

Mallory, T. B. (1948). Pathology of pulmonary fibrosis, including chronic pulmonary sarcoidosis. *Radiology*, 51(4):468–476.

Manning, F., Dean, E., Ross, J., and Abboud, R. T. (1999). Effects of side lying on lung function in older individuals. *Physical Therapy*, 79(5):456.

Marchal, F. and Hall, G. (2010). Forced oscillation technique. *European Respiratory Monograph*, 47:121–136.

Mauroy, B., Filoche, M., Weibel, E., and Sapoval, B. (2004). An optimal bronchial tree may be dangerous. *Nature*, 427(6975):633.

Milic-Emili, J., Torchio, R., and DAngelo, E. (2007). Closing volume: A reappraisal (1967–2007). *European Journal of Applied Physiology*, 99(6):567–583.

Miller, M. R., Hankinson, J., Brusasco, V., Burgos, F., Casaburi, R., Coates, A., Crapo, R., Enright, P., Van Der Grinten, C., Gustafsson, P., et al. (2005). Standardisation of spirometry. *European Respiratory Journal*, 26(2):319–338.

Mitchell, J. H., Hoffman, E. A., and Tawhai, M. H. (2012). Relating indices of inert gas washout to localised bronchoconstriction. *Respiratory Physiology & Neurobiology*, 183(3):224–233.

Mittman, C., Edelman, N. H., Norris, A. H., and Shock, N. W. (1965). Relationship between chest wall and pulmonary compliance and age. *Journal of Applied Physiology*, 20(6):1211–1216.

Möller, H. E., Chen, X. J., Saam, B., Hagspiel, K. D., Johnson, G. A., Altes, T. A., de Lange, E. E., and Kauczor, H.-U. (2002). MRI of the lungs using hyperpolarized noble gases. *Magnetic Resonance in Medicine*, 47(6):1029–1051.

Mure, M., Domino, K. B., Lindahl, S. G., Hlastala, M. P., Altemeier, W. A., and Glenny, R. W. (2000). Regional ventilation-perfusion distribution is more uniform in the prone position. *Journal of Applied Physiology*, 88(3):1076–1083.

Murphy, T. F. and Sethi, S. (2002). Chronic obstructive pulmonary disease. *Drugs & aging*, 19(10):761–775.

Musch, G., Layfield, J. D. H., Harris, R. S., Melo, M. F. V., Winkler, T., Callahan, R. J., Fischman, A. J., and Venegas, J. G. (2002). Topographical distribution of pulmonary perfusion and ventilation, assessed by PET in supine and prone humans. *Journal of Applied Physiology*, 93(5):1841–1851.

Nagels, J., Landser, F., Van der Linden, L., Clement, J., and Van de Woestijne, K. (1980). Mechanical properties of lungs and chest wall during spontaneous breathing. *Journal of Applied Physiology*, 49(3):408–416.

Nakamura, S., Mori, K., Okasaka, T., Kawaguchi, K., Fukui, T., Fukumoto, K., and Yokoi, K. (2016). Micro-computed tomography of the lung: Imaging of alveolar

duct and alveolus in human lung. *Poster presented at: American Thoracic Society Congress*, pages A7411–A7411.

Olufsen, M. S. (1998). *Modeling the arterial system with reference to an anestesia simulator*. PhD thesis, Roskilde Universitetscenter, Institut for Studiet af Matematik og Fysik samt deres Funktioner i Undervisning, Forskning og Anvendelser.

Olufsen, M. S., Peskin, C. S., Kim, W. Y., Pedersen, E. M., Nadim, A., and Larsen, J. (2000). Numerical simulation and experimental validation of blood flow in arteries with structured-tree outflow conditions. *Annals of Biomedical Engineering*, 28(11):1281–1299.

Oostveen, E., MacLeod, D., Lorino, H., Farre, R., Hantos, Z., Desager, K., Marchal, F., et al. (2003). The forced oscillation technique in clinical practice: Methodology, recommendations and future developments. *European Respiratory Journal*, 22(6):1026–1041.

Oppenheimer, B. W., Goldring, R. M., and Berger, K. I. (2009). Distal airway function assessed by oscillometry at varying respiratory rate: Comparison with dynamic compliance. *Journal of Chronic Obstructive Pulmonary Disease*, 6(3):162–170.

Otis, A. B., McKerrow, C. B., Bartlett, R. A., Mead, J., McIlroy, M., Selverstone, N., and Radford, E. (1956). Mechanical factors in distribution of pulmonary ventilation. *Journal of Applied Physiology*, 8(4):427–443.

Paiva, M. (1973). Gas transport in the human lung. *Journal of Applied Physiology*, 35(3):401–410.

Peces-Barba, G., Rodríguez-Nieto, M. J., Verbanck, S., Paiva, M., and González-Mangado, N. (2004). Lower pulmonary diffusing capacity in the prone vs. supine posture. *Journal of Applied Physiology*, 96(5):1937–1942.

Pedley, T., Schroter, R., and Sudlow, M. (1970). The prediction of pressure drop and variation of resistance within the human bronchial airways. *Respiration Physiology*, 9(3):387–405.

Peslin, R., Duvivier, C., Gallina, C., and Cervantes, P. (1985). Upper airway artifact in respiratory impedance measurements 1, 2. *American Review of Respiratory Disease*, 132(3):712–714.

Petersson, J., Rohdin, M., Sánchez-Crespo, A., Nyrén, S., Jacobsson, H., Larsson, S. A., Lindahl, S. G., Linnarsson, D., Neradilek, B., Polissar, N. L., et al. (2007). Posture primarily affects lung tissue distribution with minor effect on blood flow and ventilation. *Respiratory Physiology & Neurobiology*, 156(3):293–303.

Prisk, G. K., Elliott, A. R., Guy, H. J., Verbanck, S., Paiva, M., and West, J. B. (1998). Multiple-breath wash-in of helium and sulfur hexafluoride in sustained microgravity. *Journal of Applied Physiology*, 84(1):244–252.

Prisk, G. K., Guy, H., Elliott, A. R., Paiva, M., and West, J. B. (1995). Ventila-

tory inhomogeneity determined from multiple-breath washouts during sustained microgravity on spacelab SLS-1. *Journal of Applied Physiology*, 78(2):597–607.

Prokocimer, P., Garbino, J., Wolff, M., and Regnier, B. (1983). Influence of posture on gas exchange in artificially ventilated patients with focal lung disease. *Intensive Care Medicine*, 9(2):69–72.

Qing, K., Ruppert, K., Jiang, Y., Mata, J. F., Miller, G. W., Shim, Y. M., Wang, C., Ruset, I. C., Hersman, F. W., Altes, T. A., et al. (2014). Regional mapping of gas uptake by blood and tissue in the human lung using hyperpolarized Xenon-129 MRI. *Journal of Magnetic Resonance Imaging*, 39(2):346–359.

Quanjer, P. H., Stanojevic, S., Cole, T. J., Baur, X., Hall, G. L., Culver, B. H., Enright, P. L., Hankinson, J. L., Ip, M. S., Zheng, J., et al. (2012). Multi-ethnic reference values for spirometry for the 3–95-yr age range: the global lung function 2012 equations.

Robinson, P., Latzin, P., and Gustafsson, P. (2010). Multiple-breath washout. *European Respiratory Monograph*, 47:87–104.

Robinson, P. D., Latzin, P., Verbanck, S., Hall, G. L., Horsley, A., Gappa, M., Thamrin, C., Arets, H. G., Aurora, P., Fuchs, S. I., et al. (2013). Consensus statement for inert gas washout measurement using multiple-and single-breath tests. *European Respiratory Journal*, 41(3):507–522.

Rodríguez-Nieto, M. J., Peces-Barba, G., Mangado, N. G., Paiva, M., and Verbanck, S. (2002). Similar ventilation distribution in normal subjects prone and supine during tidal breathing. *Journal of Applied Physiology*, 92(2):622–626.

Rosenblueth, A. and Wiener, N. (1945). The role of models in science. *Philosophy of science*, 12(4):316–321.

Sá, R. C., Cronin, M. V., Henderson, A. C., Holverda, S., Theilmann, R. J., Arai, T. J., Dubowitz, D. J., Hopkins, S. R., Buxton, R. B., and Prisk, G. K. (2010). Vertical distribution of specific ventilation in normal supine humans measured by oxygen-enhanced proton MRI. *Journal of Applied Physiology*, 109(6):1950–1959.

Saladin, K. S. and Porth, C. M. (1998). *Anatomy & physiology*. McGraw-Hill.

Sander, R. (2015). Compilation of henry's law constants (version 4.0) for water as solvent. *Atmospheric Chemistry & Physics*, 15(8).

Simon, B. A. (2005). Regional ventilation and lung mechanics using X-Ray CT. *Academic Radiology*, 12(11):1414–1422.

Smith, G. D. (1985). *Numerical solution of partial differential equations: finite difference methods*. Oxford university press.

Smith, H., Reinhold, P., and Goldman, M. (2005). Forced oscillation technique and impulse oscillometry. *European Respiratory Monograph*, 31:72.

Smith, N., Pullan, A., and Hunter, P. J. (2002). An anatomically based model of transient coronary blood flow in the heart. *SIAM Journal on Applied Mathematics*, 62(3):990–1018.

Stavngaard, T., Søgaard, L. V., Mortensen, J., Hanson, L. G., Schmiedeskamp, J., Berthelsen, A. K., and Dirksen, A. (2005). Hyperpolarised ^{3}He MRI and ^{81m}Kr SPECT in chronic obstructive pulmonary disease. *European Journal of Nuclear Medicine and Molecular Imaging*, 32(4):448–457.

Strahler, A. N. (1957). Quantitative analysis of watershed geomorphology. *Transactions American Geophysical Union*, 38(6):913–920.

Strömberg, N. and Gustafsson, P. M. (2000). Ventilation inhomogeneity assessed by nitrogen washout and ventilation-perfusion mismatch by capnography in stable and induced airway obstruction. *Pediatric Pulmonology*, 29(2):94–102.

Swan, A. J., Clark, A. R., and Tawhai, M. H. (2012). A computational model of the topographic distribution of ventilation in healthy human lungs. *Journal of Theoretical Biology*, 300:222–231.

Tajik, J. K., Chon, D., Won, C., Tran, B. Q., and Hoffman, E. A. (2002). Subsecond multisection CT of regional pulmonary ventilation. *Academic Radiology*, 9(2):130–146.

Tavelli, M., Dumbser, M., and Casulli, V. (2013). High resolution methods for scalar

transport problems in compliant systems of arteries. *Applied Numerical Mathematics*, 74:62–82.

Tawhai, M. H. and Burrowes, K. S. (2008). Modelling pulmonary blood flow. *Respiratory Physiology & Neurobiology*, 163(1-3):150–157.

Tawhai, M. H., Hunter, P., Tschirren, J., Reinhardt, J., McLennan, G., and Hoffman, E. A. (2004). CT-based geometry analysis and finite element models of the human and ovine bronchial tree. *Journal of Applied Physiology*, 97(6):2310–2321.

Tawhai, M. H. and Hunter, P. J. (2001). Multibreath washout analysis: Modelling the influence of conducting airway asymmetry. *Respiration Physiology*, 127(2):249–258.

Thomas, P. and Paratz, J. (2007). Is there evidence to support the use of lateral positioning in intensive care? a systematic review. *Anaesthesia and Intensive Care*, 35(2):239.

Thorpe, C. W. and Bates, J. H. (1997). Effect of stochastic heterogeneity on lung impedance during acute bronchoconstriction: A model analysis. *Journal of Applied Physiology*, 82(5):1616–1625.

Thurlbeck, W. M. (1967). The internal surface area of nonemphysematous lungs. *American Review of Respiratory Disease*, 95(5):765–773.

Thurston, G. B. (1952). Periodic fluid flow through circular tubes. *The Journal of the Acoustical Society of America*, 24(6):653–656.

Timmerman, B., Gibbons, G., and Bryanston-Cross, P. (2013). Study of flows in physiologically realistic patient specific airway models. In *PIV13; 10th International Symposium on Particle Image Velocimetry, Delft, The Netherlands, July 1-3, 2013*. Delft University of Technology, Faculty of Mechanical, Maritime and Materials Engineering, and Faculty of Aerospace Engineering.

Tu, J., Inthavong, K., and Ahmadi, G. (2012). *Computational fluid and particle dynamics in the human respiratory system*. Springer Science & Business Media.

Tzeng, Y.-S., Lutchen, K., and Albert, M. (2009). The difference in ventilation heterogeneity between asthmatic and healthy subjects quantified using hyperpolarized ^{3}He MRI. *Journal of Applied Physiology*, 106(3):813–822.

Usmani, O. S., Singh, D., Spinola, M., Bizzi, A., and Barnes, P. J. (2016). The prevalence of small airways disease in adult asthma: A systematic literature review. *Respiratory Medicine*, 116:19–27.

van Beek, E. J., Wild, J. M., Kauczor, H.-U., Schreiber, W., Mugler, J. P., and de Lange, E. E. (2004). Functional MRI of the lung using hyperpolarized 3-helium gas. *Journal of Magnetic Resonance Imaging*, 20(4):540–554.

Van Muyleim, A., De Vuyst, P., Yernault, J.-C., and Paiva, M. (1992). Inert gas single-breath washout and structural alteration of respiratory bronchioles. *American Review of Respiratory Disease*, 146(5_pt_1):1167–1172.

Van Muylem, A., Verbanck, S., and Estenne, M. (2005). Monitoring the lung periphery of transplanted lungs. *Respiratory Physiology & Neurobiology*, 148(1-2):141–151.

Verbanck, S. and Paiva, M. (1990). Model simulations of gas mixing and ventilation distribution in the human lung. *Journal of Applied Physiology*, 69(6):2269–2279.

Verbanck, S. and Paiva, M. (2016). Could lobar flow sequencing account for convection-dependent ventilation heterogeneity in normal humans? *Journal of Applied Physiology*, 121(2):589–591.

Verbanck, S., Schuermans, D., Noppen, M., Van Muylem, Alainand Paiva, M., and Vincken, W. (1999). Evidence of acinar airway involvement in asthma. *American Journal of Respiratory and Critical Care Medicine*, 159(5):1545–1550.

Verbanck, S., Schuermans, D., Paiva, M., and Vincken, W. (2003). Nonreversible conductive airway ventilation heterogeneity in mild asthma. *Journal of Applied Physiology*, 94(4):1380–1386.

Verbanck, S., Schuermans, D., Van Muylem, A., Melot, C., Noppen, M., Vincken, W., and Paiva, M. (1998). Conductive and acinar lung-zone contributions to ventilation inhomogeneity in COPD. *American Journal of Respiratory and Critical Care Medicine*, 157(5):1573–1577.

Verbanck, S., Schuermans, D., Van Muylem, A., Paiva, M., Noppen, M., and Vincken, W. (1997). Ventilation distribution during histamine provocation. *Journal of Applied Physiology*, 83(6):1907–1916.

Vyshedskiy, A. and Murphy, R. (2012). Pendelluft in chronic obstructive lung disease measured with lung sounds. *Pulmonary Medicine*, 2012.

Weibel, E. R. (1963). *Geometry and dimensions of airways of conductive and transitory zones*. Springer.

Wesseling, K., Jansen, J., Settels, J., and Schreuder, J. (1993). Computation of aortic flow from pressure in humans using a nonlinear, three-element model. *Journal of Applied Physiology*, 74(5):2566–2573.

Yamaguchi, M., Niimi, A., Ueda, T., Takemura, M., Matsuoka, H., Jinnai, M., Otsuka, K., Oguma, T., Takeda, T., Ito, I., et al. (2009). Effect of inhaled corticosteroids on small airways in asthma: Investigation using impulse oscillometry. *Pulmonary Pharmacology & Therapeutics*, 22(4):326–332.

Zack, M. B., Pontoppidan, H., and Kazemi, H. (1974). The effect of lateral positions on gas exchange in pulmonary disease: A prospective evaluation. *American Review of Respiratory Disease*, 110(1):49–55.